分 类 号： O572　　　　单位代码： 10422
密　　级： 公开　　　　学　　号： 201812163

SHANDONG UNIVERSITY

博士学位论文

Dissertation for Doctoral Degree

（学术学位）

论文题目：　利用 ATLAS 探测器在 13 TeV 质心能量下采集的质子质子对撞数据寻找顶夸克衰变过程中的重型右手马约拉纳中微子

Search for heavy right-handed Majorana neutrinos in $t\bar{t}$ decays in proton-proton collisions at $\sqrt{s} = 13$ TeV with the ATLAS detector

作者姓名　赵桐彬

培养单位　前沿交叉科学青岛研究院

培养方式　全日制

专业名称　粒子物理与原子核物理

指导老师　张学尧 教授

合作导师　马连良 教授

合作导师　Markus Cristinziani 教授

2025 年 5 月 27 日

原 创 性 声 明

本人郑重声明：所呈交的学位论文，是本人在导师指导下，独立进行研究所取得的成果。除文中已经注明引用的内容外，本论文不包含任何其他个人或集体已经发表或撰写过的科研成果。对本论文的研究作出重要贡献的个人和集体，均已在文中以明确方式标明。本声明的法律责任由本人承担。

论文作者签名：________________ 日 期：________________

关于学位论文使用授权的声明

本人完全了解山东大学有关保留、使用学位论文的规定，同意学校保留或向国家有关部门或机构送交论文的复印件和电子版，允许论文被查阅和借阅；本人授权山东大学可以将本学位论文全部或部分内容编入有关数据库进行检索，可以采用影印、缩印或其他复制手段保存论文和汇编本学位论文。

（保密的论文在解密后应遵守此规定）

论文作者签名：________ 导师签名：________ 日 期：________

Contents

List of Figures

List of Tables

摘 要

在粒子物理标准模型中，中微子最初被假设为无质量粒子，但中微子振荡实验证实其具有非零质量，这一发现挑战了标准模型的基本假设。为了解释中微子的低质量问题，物理学家提出了许多超出标准模型的理论，如跷跷板机制。该机制引入了大质量的重型右手中微子来解释标准模型下中微子的低质量问题。而无中微子双贝塔衰变过程是寻找重型中微子的重要研究过程。

本论文利用大型强子对撞机 LHC 上 ATLAS 探测器采集的全部 Run-2 数据，通过顶夸克对衰变过程来寻找右手马约拉纳中微子。全部 Run-2 数据是指质心能量 $\sqrt{s} = 13\,\text{TeV}$，积分亮度为 $140.1\,\text{fb}^{-1}$ 的质子-质子碰撞数据。物理目标是研究顶夸克对衰变末态中的一个 W 玻色子的无中微子双贝塔衰变过程，即 W 衰变产生一个电子（或缪子）和一个重型的右手中微子。随后重型中微子衰变为同味同电荷的另一个带电轻子和一个离壳的 W 玻色子，最终可以得到具有相同电荷的双电子和双缪子末态。

在分析过程中，本论文使用基于增强决策树的多变量分析方法来区分信号和本底，对输入变量和训练参数进行了深入优化，极大增强了分析的灵敏度以及分析的稳定性。此外，本论文通过分析顶夸克蒙特卡洛模拟样本的真值信息 (truth information) 对轻子进行分类，针对不同来源的轻子定义控制区间，并利用模板拟合方法估算其中主要本底的贡献。随后对分析中的不同系统误差进行详细估计，并将这些误差纳入拟合过程，以提高结果的可靠性。最终，本论文使用最大似然估计方法对重型中微子的信号强度进行拟合估计。

在实验数据中未观测到显著超出背景预期的事例，因此可以对质量范围在 15–75 GeV 的马约拉纳中微子分别设定其与电子和缪子的耦合参数上限，针对信号质量为 40 GeV 的电子和缪子马约拉纳中微子，最终结果为 $|V_{e,N}|^2 < 2.0\times10^{-4}$ 和 $|V_{\mu,N}|^2 < 6.8\times10^{-5}$。本研究将 ATLAS 对重型中微子质量的搜索范围扩展至 75 GeV，并且首次通过顶夸克对衰变事例来寻找重型右手马约拉纳中微子。该实验结果为未来重型中微子的研究以及新物理探索提供了可靠的实验依据。

关键词: LHC；ATLAS；重型中微子; $t\bar{t}$ 衰变; 跷跷板机制；BSM

ABSTRACT

In the Standard Model of particle physics, neutrinos are considered massless. However, neutrino oscillation experiments have demonstrated that neutrinos have non-zero mass. This discovery challenges the fundamental assumptions of the Standard Model. To explain the smallness of neutrino masses, physicists have proposed theories beyond the Standard Model, such as the seesaw mechanism. This mechanism introduces the concept of heavy right-handed neutrinos to account for the low mass of neutrinos in the Standard Model. The neutrinoless double beta decay process serves as a crucial research avenue for investigating heavy neutrinos.

This thesis uses the full Run-2 data collected by the ATLAS detector at the Large Hadron Collider to search for right-handed Majorana neutrinos through top quark pair decay processes. The full Run-2 data refers to proton-proton collision data at a center-of-mass energy of $\sqrt{s} = 13\,\text{TeV}$, with an integrated luminosity of $140.1\,\text{fb}^{-1}$. The physical target is to investigate the neutrinoless double beta decay of a W boson in the final state of top quark pair events, where the W boson decays to produce either an electron or muon and a heavy right-handed Majorana neutrino. Subsequently, the heavy neutrino further decays into another charged lepton of the same flavor and charge, along with an off-shell W boson, resulting in a final state with same-sign di-electrons or di-muons.

This thesis employs a multivariate analysis approach based on boosted decision trees to distinguish signal from background. The analysis achieves significant enhancements in sensitivity and stability through comprehensive optimization of input variables and hyperparameters. Additionally, by comparing truth-level information, leptons from different sources are classified. This information is used to define control regions, and template fit methods are applied to estimate the contributions of dominant backgrounds. Subsequently, all systematic uncertainties in the analysis are estimated and incorporated into the fitting process to enhance the reliability of the results. Finally, the thesis uses a maximum likelihood estimation method to fit the signal and control regions to estimate the signal strength of the heavy neutrinos at different mass points.

No significant excess over the expected background is observed in the data. Therefore, upper limits on the coupling parameters to electrons and muons are set for Majorana neutrinos in the mass range of 15–75 GeV. For a heavy neutrino

with the mass of 40 GeV, the final results are $|V_{e,N}|^2 < 2.0 \times 10^{-4}$ and $|V_{\mu,N}|^2 < 6.8 \times 10^{-5}$. This thesis extends the ATLAS search for heavy neutrinos to a mass range of up to 75 GeV and is the first search for heavy right-handed neutrinos through top quark pair decay events. These results provide reliable evidence for future searches of heavy neutrinos and the exploration of new physics.

Key words: LHC, ATLAS, Majorana neutrino, BSM, $t\bar{t}$, seesaw mechanism

Chapter 1 Introduction

The detection of flavor oscillations in neutrinos from the sun, atmosphere, nuclear reactors, and particle accelerators provides compelling evidence that neutrinos have a non-zero mass. This discovery strongly suggests the presence of physics beyond the Standard Model (SM), which originally treated neutrinos as massless particles.

Several theoretical models can accommodate the Majorana mass, including SO(10) Supersymmetric (SUSY) grand unification theories [1–3], along with other Grand Unified Theories (GUTs) [4–6]. These models naturally link the small masses of neutrinos to new physics at the GUT scale. Therefore, within the framework of GUTs, the mass of heavy Majorana neutrinos, M_N, is typically of the order of the GUT scale.

Among the various seesaw mechanisms, the Type-I seesaw is the most straightforward, introducing three heavy neutral leptons [7–10]. This model involves three right-handed (RH) neutrinos, $(N_{R\alpha})$, and the full mass term for neutrinos is given by:

$$-\mathcal{L}_M = y_{i\alpha}\bar{L}_{Li}\widetilde{\Phi}N_{R\alpha} + \frac{1}{2}\left(M_N\right)_{\alpha\beta}\bar{N}^C_{R\alpha}N_{R\beta} + \text{ H.c. }, \tag{1.1}$$

where $i = 1, 2, 3$ is the generation index, $\alpha = e, \mu, \tau$ is the RH neutrino flavor index. The Lagrangian $\mathcal{L}_M$ is given here, the Matrix elements $y_{i\alpha}$ representing the strength of interactions between left-handed quark doublet index and right-handed neutrino index, the conjugate of the left-handed lepton doublet $\bar{L}_{Li}$, the conjugate of the Higgs field $\widetilde{\Phi}$ and Hermitian conjugate H.c. are shown in the right side. After the electroweak symmetry breaking, the neutrino mass matrix in the flavor basis $\left\{\nu^C_{Li}, N_{R\alpha}\right\}$ is given by,

$$\mathcal{M}_\nu = \begin{pmatrix} 0 & M_D \\ M_D^\top & M_N \end{pmatrix}. \tag{1.2}$$

Diagonalizing the mass matrix above results in a mixing between light and heavy neutrinos. Here, M_N and M_D correspond to the Majorana and Dirac mass matrices, respectively. Consequently, the light-flavor neutrinos ν_{iL} can be expressed as a superposition of both light and heavy mass eigenstates:

$$\nu_{iL} = \sum_{m=1}^{3} U_{im}\nu_{mL} + \sum_{m=4}^{6} V_{im}N_{mL}^{c}. \tag{1.3}$$

In this framework, ν_{mL} denotes the left-handed neutrino mass eigenstates, and N_{mL}^c represents the charge-conjugated right-handed neutrino states. The mixing matrices U and V satisfy the unitarity condition $UU^\dagger + VV^\dagger = I$. When the Majorana mass matrix M_N is on the order of the GUT scale, the mixing parameters between light and heavy neutrinos, $V_{iN}^2 \sim M_D/M_N$, are generally too small to significantly affect physical processes. However, if M_N is much smaller, the influence of these heavy Majorana neutrinos could potentially be observable in existing experiments. Thus, exploring the viability of the seesaw mechanism at lower energy scales is crucial, both theoretically and experimentally.

Recently, several low-scale Type-I seesaw models have been proposed (see examples, e.g., [11–16]), where the mass scale of M_N may be within reach of future experiments. This opens a unique opportunity to investigate the connection between the origin of neutrino masses and the observed matter-antimatter asymmetry via leptogenesis at colliders (for a review, see e.g., [17]).

As shown in Equation (1.1), generating Majorana neutrino masses also leads to lepton number violation with $|\Delta L| = 2$. The lepton-number-violating (LNV) processes serve as a potential signature to probe the mechanism of neutrino mass generation. One promising probe for Majorana neutrinos is neutrinoless double beta decay ($0\nu\beta\beta$) [18–20].

Multiple experiments are investigating heavy neutrinos through the Drell-Yan process at the Large Hadron Collider (LHC), particularly via W boson decays. The CMS Collaboration has recently performed searches for heavy Majorana neutrinos via the Drell-Yan process $q\bar{q} \to W^* \to N\ell$ and the photon-induced process $\gamma q \to W^* q' \to N\ell q'$ in trilepton and same-sign dilepton final states. These results provide stringent limits on $|V_{eN,\mu N}|^2$ ranging from $\mathcal{O}(10^{-5})$ to unity for heavy neutrino masses between 20 GeV and 1600 GeV [21, 22]. The ATLAS Collaboration also set constraints on the heavy neutrino mixing with muon and electron neutrinos for HNL masses from W boson decays in the range of 4.5-50 GeV [23]. Additionally, ATLAS recently conducted a search for HNLs in W boson decays through displaced dilepton vertices in the mass range of 3–15 GeV [24]. More recent ATLAS analyses have searched for Majorana neutrinos in same-charge WW scattering events, probing their interaction with electrons and muons in the HNL mass range of 50 GeV–20 TeV [25, 26].

The Large Hadron Collider can produce copious top quark events and give a good opportunity to test the low-scale seesaw models [27, 28] . In this work, we will demonstrate that the top quark neutrinoless double beta decay process $t \to bjj\ell^{\pm}\ell^{\pm}$ provides a new way to search for the [15,75] GeV heavy Majorana neutrino, which will give the signature of the same-sign same-flavor dilepton plus multi-jet through $t\bar{t}$ production at the LHC.

This thesis presents the first search for a heavy neutrino using the $t\bar{t}$ process. After performing the statistical treatment on our signal region and control regions, we will set the limit on the mixing parameters $|V_{eN}|^2$ and $|V_{\mu N}|^2$ in the mass range of 15 GeV $< m_N <$ 75 GeV at 13 TeV LHC with the luminosity of 140.1 fb^{-1}, which extends the ATLAS results from 50 GeV to 75 GeV.

In this analysis, I was fully involved in all stages, contributing significantly to key components of the study. My contributions include:

- Monte Carlo production for all the signal samples and CxAODs production for all the background samples.
- Design and development of a comprehensive analysis framework.
- Optimization of event selection and categorization.
- Definition of signal and control regions.
- Implementation and optimization of multivariate analysis techniques.
- Estimation of systematic uncertainties for major background processes.
- Data analysis, including background estimation, template fitting, and statistical treatment.
- Setting upper limits on mixing parameters.
- Presenting all approval talks at different stages

This thesis is structured as follows: Chapter 2 presents a concise overview of the theoretical background, encompassing both the standard model and beyond standard model theories. Chapter 3 offers a brief introduction to the Large Hadron Collider and the ATLAS detector. The procedures for reconstructing and identifying various physics objects within the ATLAS detector are outlined in Chapter 4. Chapter 5 provides an in-depth discussion of the search for the heavy neutrino.

- Section 5.1 details the signal process and background processes
- Section 5.2 describes object selection, event selection, and event reconstruction.
- Section 5.3 provides definitions of signal and control regions.
- Section 5.4 describes the multivariate analysis
- Section 5.5 summarizes systematic uncertainties.
- Section 5.6 presents different fit results from the statistical treatment.
- Section 5.7 presents the upper limit results for the mixing parameters

Finally, Chapter 6 summarizes the conclusions of this thesis.

Chapter 2 Theoretical Overview

This chapter provides an overview of the theoretical foundations. Section 2.1 briefly describes the Standard Model of particle physics, followed by an overview of the heavy neutrino mechanism in Section 2.1. The physics involved in hadron colliders is discussed in Section 2.2

2.1 The Standard Model of Particle Physics

The Standard Model of particle physics [29, 30] is a widely accepted theory that describes all fundamental forces in the universe and classifies all known elementary particles. Quantum Field Theory (QFT) serves as the mathematical framework for the SM. Developed during the latter half of the 20^{th} century, the SM has successfully explained experimental observations in particle physics. In 2012, the ATLAS and CMS experiments [31, 32] at the LHC observed the Higgs boson, the final particle predicted by the SM, further solidifying the model's validity.

In the Standard Model, elementary particles are categorized into two groups: fermions and bosons. Fermions, which have spin 1/2, are the fundamental constituents of matter, while bosons, with spin 1, mediate the interactions between these particles. Additionally, the masses of these particles are determined by the scalar Higgs boson, which has spin 0.

The fermions are classified into leptons and quarks, and both are divided into three generations, with mass increasing across generations, as shown in Figure 2.1. The leptons are further categorized into charged leptons (e^-, μ^-, τ^-), which interact via weak and electromagnetic interactions, and corresponding neutral leptons, called neutrinos (ν_e, ν_μ, ν_τ), which interact only through the weak interaction.

The SM contains six types of quarks: up quark(u), down quark(d), charm quark(c), strange quark(s), top quark(t), and bottom quark (b). They each carry a fractional charge Q in units of the positron charge: +2/3 charge for the up, charm, and top quarks, and -1/3 charge for the down, strange, and bottom quarks. They can interact strongly, weakly, and electromagnetically. They also carry a color charge with three flavors: red (r), green (g), and blue (b). In nature, only colorless particles exist due to the color confinement phenomenon. This means that free quarks are always confined to uncolored particles called hadrons. Hadrons composed of three quarks are classified as baryons, which have half-integer spin, while hadrons composed of a quark-antiquark pair are mesons, which are integer spin particles.

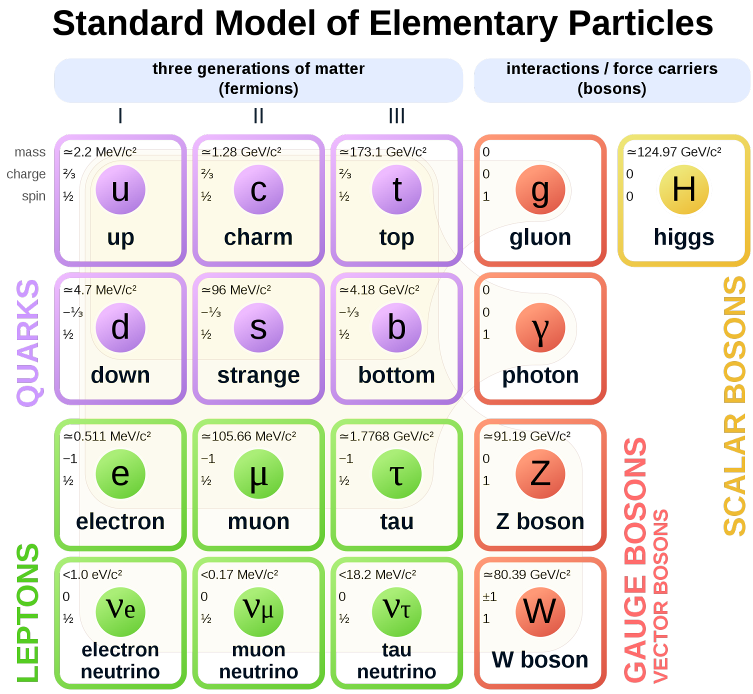

Figure 2.1: Elementary particles and their properties in the Standard Model. The twelve fermions and five fundamental bosons (the eight gluons and the two W bosons are shown in a single g and W box, respectively) are shown.[33]

The Standard Model includes twelve spin-1 bosons: the photon, which carries the electromagnetic force between charged particles; three bosons (W^+, W^-, and Z) that mediate the weak force; and eight gluons that mediate the strong force.

The Standard Model (SM) comprehensively describes three fundamental interactions: electromagnetic (governing charged particle behavior), weak (responsible for nuclear decay processes), and strong (binding nucleons in atomic nuclei and confining quarks within hadrons). Notably absent from the SM is gravity, which remains described by Einstein's general relativity; its negligible strength at particle interaction scales makes it irrelevant for most SM phenomena.

The SM is based on the gauge symmetry: $SU(3)_c \times SU(2)_L \times U(1)_Y$. The

$SU(3)_c$ describes color symmetry and strong interactions, while $SU(2)_L \times U1(_Y)$ represents electroweak interactions proposed by Glashow, Salam, and Weinberg in the 1960s [34, 35]. Consider the Lagrangian density for a free spin 1/2 particle:

$$\mathcal{L} = \overline{\psi}(i\gamma^\mu \partial_\mu - m)\psi, \tag{2.1}$$

where the $\psi = \psi(x)$ means the Dirac spinor of a spin $\frac{1}{2}$ fermison. Consider the $U(1)$ gauge transformation, where m is the mass of the particle, γ^μ are the Dirac gamma matrices, $\partial_\mu = \partial/\partial x^\mu$ is the derivative, $\bar{\psi} = \psi^\dagger \gamma^0$ is the Dirac adjont of the spinor. Under a local $U(1)$ transformation, the spinor field transforms as:

$$\psi \to \psi^{'} = e^{i\alpha(x)}\psi, \tag{2.2}$$

the Dirac Lagrangian could be expressed:

$$\mathcal{L} \to \mathcal{L}^{'} = \mathcal{L} - \overline{\psi}\gamma^\mu \partial_\mu \alpha(x)\psi. \tag{2.3}$$

To keep gauge invariance under the $U(1)$ changes, the derivative ∂_μ could be replaced by the covariant derivative D_μ. The covariant derivative D_μ must satisfy the following condition:

$$D_\mu \psi(x) \to D_\mu^{'} \psi(x)^{'} = e^{i\alpha(x)} D_\mu \psi(x), \tag{2.4}$$

Equation 2.4 is satisfied for:

$$D_\mu \psi(x) = \partial_\mu + ieA_m\mu, \tag{2.5}$$

$$A_\mu \to A_\mu^{'} = A_\mu - \frac{1}{e}\partial_\mu \alpha(x). \tag{2.6}$$

In Quantum Electrodynamics (QED), the gauge field A_μ can be interpreted as the gauge field of the electromagnetic interaction with the interaction strength denoted by e. The QED Lagrangian can then be given by:

$$\mathcal{L}_{QED} = \bar{\psi}\left(i\gamma^\mu D_\mu - m\right)\psi - \frac{1}{4}F_{\mu\nu}F^{\mu\nu}, \tag{2.7}$$

where $F_{\mu\nu} = \partial_\mu A_\nu - \partial_\nu A_\mu$ and $F_{\mu\nu}F^{\mu\nu}$ is the kinetic energy term of the photon.

Quantum Electrodynamics is invariant under $U(1)$ gauge transformations, whereas Quantum Chromodynamics (QCD) is based on the gauge symmetry group $SU(3)$, which is a non-abelian group[1]. Due to the $SU(3)$ gauge symmetry, the spinor field can be transformed as follows:

$$\psi_A(x) \rightarrow \psi'_A(x) = \exp(i\alpha_s \overrightarrow{\lambda} \cdot \overrightarrow{\beta}(x))\, \psi_A(x), \tag{2.8}$$

where ψ_A is the spinor for a quark with color A, α_s is the strong coupling constant, $\overrightarrow{\lambda}$ presents the eight Gell-Mann matrices and $\overrightarrow{\beta}(x)$ are the eight angles. Then the QCD Lagrangian could be written as:

$$\mathcal{L}_{QCD} = -\frac{1}{4} G^A_{\alpha\beta} G^{\alpha\beta}_A + \sum_{flavours} \bar{\psi}_A (i\gamma^\mu D_\mu - m)_{AB} \psi_B, \tag{2.9}$$

where $-\frac{1}{4} G^A_{\alpha\beta} G^{\alpha\beta}_A$ represents the kinematic term for the gluons, with the $G^A_{\alpha\beta}$ being the gluonic field strength tensor.

QED and QCD are associated with $U(1)$ and $SU(3)$ local gauge symmetry, respectively. The weak interactions under $SU(2)$ local gauge transformations could be defined as:

$$\psi(x) \rightarrow \psi'(x) = \exp\left[\frac{g_W}{2} \overrightarrow{\alpha}(x) \cdot \overrightarrow{\sigma}\right] \psi(x), \tag{2.10}$$

where $\overrightarrow{\sigma}$ are the three Pauli spin matrices, the generators of the $SU(2)$ group. The g $\overrightarrow{\alpha}(x) = (\alpha_1(x), \alpha_2(x), \alpha_3(x))$ are the three functions that specify the local phase at each point in space-time, and g_W is the gauge coupling constant. Three gauge fields $W^{(k)}_\mu$ with $k = 1, 2, 3$ which are the analogous of A_μ in QED are introduced to conserve the symmetry. These gauge fields correspond to gauge bosons $W^{(1)}$, $W^{(2)}$ and $W^{(3)}$. The charged currents are expressed as a linear combination of $W^{(1)}_\mu$ and $W^{(2)}_\mu$:

$$W^{\pm}_\mu = \frac{1}{\sqrt{2}} \left(W^{(1)}_\mu \mp i W^{(2)}_\mu\right) \tag{2.11}$$

The wave function $\psi(x)$ has two components since the generators of the $SU(2)$ gauge transformations are the 2×2 Pauli matrices, which is called weak isospin doublet. The weak isospin doublet contains flavors differing by one unit of electric charge, i.e., the neutrino-electron isospin doublet:

$$\psi_L(x) = \begin{pmatrix} \nu_e(x) \\ e^-(x) \end{pmatrix}_L . \tag{2.12}$$

[1] A non-abelian gauge symmetry group is a gauge group where the group operations do not commute, meaning the order of transformations affects the result.

The weak isospin quantum number I_W is used to describe the weak interaction. Left-handed fermions are in weak isospin doublets with $I_W = \frac{1}{2}$, while right-handed fermions form weak isospin singlets with $I_W = 0$. The coupling of particle wave functions to these bosons depends on the third component from the weak isospin charge, I_W^3. For example:

$$e_R^-, \quad u_R, \quad d_R. \tag{2.13}$$

Experimental evidence demonstrates that the Z boson interacts with both left-handed and right-handed states, indicating that it cannot be identified as the $W^{(3)}$ boson associated with the $SU(2)_L$ local gauge symmetry. Similarly, photons couple to both left-handed and right-handed particles. In the electroweak model formulated by Glashow, Salam, and Weinberg, the $U(1)$ of QED is replaced by a $U(1)_Y$ local gauge symmetry governed by the weak hypercharge Y. The weak hypercharge is defined as:

$$Y = 2Q - 2I_W^{(3)}, \tag{2.14}$$

where Q is the electromagnetic charge of the particle and W_3^μ is the third component from the weak isospin. The B^μ is defined based on the electroweak mixing Weinberg angle θ_W:

$$\begin{pmatrix} Z_\mu \\ A_\mu \end{pmatrix} = \begin{pmatrix} \cos\theta_W & -\sin\theta_W \\ \sin\theta_W & \cos\theta_W \end{pmatrix} \begin{pmatrix} W_\mu^3 \\ B_\mu \end{pmatrix} \tag{2.15}$$

and the angle is defined as:

$$\frac{g_W}{\sin\theta_W} = \frac{g'}{\cos\theta_W} = e, \tag{2.16}$$

where e represents the charge of the electron, g_W corresponds to the coupling constant of the $SU(2)_L$ local gauge transformation, and g' denotes the coupling constant of the $U(1)_Y$ local gauge transformation. The SM described so far does not include the mass of the bosons and fermions. However, the masses of these particles are introduced into the SM through the Higgs mechanism.

2.2 Beyond the Standard Model: Incorporating Majorana neutrinos

The Standard Model needs to be extended to incorporate a neutrino mass term, as the original SM does not provide a mechanism for neutrino masses. A common method is to extend the SM by introducing m sterile neutrinos, denoted as ν_s. With the inclusion of these sterile neutrinos, two different mass terms can be constructed.

The first is the Dirac mass term, which introduces a coupling between the sterile and the SM neutrinos:

$$\mathcal{L}_{M_\nu,\,\text{Dirac}} = -M_{Dij}\bar{\nu}_{si}\nu_{Lj}. \tag{2.17}$$

Here, M_D is a complex $3 \times m$ matrix, where 3 corresponds to the three generations of left-handed SM neutrinos, and m corresponds to the number of sterile neutrinos. This Lagrangian introduces a Yukawa coupling for neutrinos, allowing them to gain mass similarly to the charged leptons via the Higgs mechanism. Also, the Dirac mass term conserves the lepton number, but not the lepton flavour number, which means the neutrino oscillations remain possible. However, this mechanism alone does not explain why the observed neutrinos are significantly lighter than the charged leptons. The discrepancy suggests the need for additional mechanisms or mass terms, such as the Majorana mass term, to explain the smallness of neutrino masses.

Alternatively, one can postulate that the sterile neutrinos are Majorana particles, meaning they are their antiparticles. In this case, the Lagrangian can include a Majorana mass term:

$$\mathcal{L}_{M_\nu,\,\text{Majorana}} = -\frac{1}{2}M_{Nij}\bar{\nu}_{si}\nu^C_{sj}. \tag{2.18}$$

The Majorana mass term involves two sterile neutrino fields and a symmetric $m \times m$ matrix M_N. This term explicitly breaks lepton number conservation by two units, allowing for processes that are forbidden in the Standard Model if the lepton number is conserved.

Both the Dirac and Majorana mass terms can be combined into a single Lagrangian:

$$\mathcal{L}_{M_\nu} = -\frac{1}{2}\begin{pmatrix} \bar{\nu}_L^C & \overline{\nu_s} \end{pmatrix}\begin{pmatrix} 0 & M_D^T \\ M_D & M_N \end{pmatrix}\begin{pmatrix} \nu_L \\ \nu_s^C \end{pmatrix} + \text{ h.c. }, \tag{2.19}$$

where $\left(\nu^C, \bar{\nu}_s\right)^T$ is a $3+m$-dimensional vector and $h.$ c. is the hermitian conjugate of the previous expression. The matrix M_ν is symmetric and complex, and it can be diagonalised to get the mass eigenstates.

2.3 The Seesaw Mechanism

The eigenvalues of M_ν in Equation 2.19 determine the masses of the observable neutrinos. The eigenvalue problem associated with M_ν has two solutions:

$$m_\pm = \frac{M_N}{2} \pm \frac{1}{2}\sqrt{M_N^2 + M_D^2} = \frac{1}{2}\left(M_N \pm M_N\sqrt{1 + \frac{4M_D^2}{M_N^2}}\right). \tag{2.20}$$

Assuming $M_N \gg M_D$, the two solutions correspond to a light (ν) and a heavy (N) neutrino state:

$$|m_\nu| \approx \frac{M_D^2}{M_N} \text{ and } m_N \approx M_N. \tag{2.21}$$

This relationship is where the name ”seesaw mechanism” originates: the heavier the heavy neutrino N is, the lighter the light neutrino ν becomes.

Assuming the existence of the Majorana term, the seesaw mechanism predicts that there is a light and a heavy neutrino for each neutrino generation. The light neutrino will have masses significantly smaller than the other fermions in the SM, while the heavy neutrino will be very massive.

For illustration, if we take $|m_\nu| \approx 0.1\text{eV}$, which is compatible and consistent with the current experimental limits on neutrino masses. If the Dirac mass is on the order of magnitude of the electron mass, i.e. $M_D = \mathcal{O}(1\text{MeV})$, Equation 2.21 would postulate that $m_N = \mathcal{O}(10\text{TeV})$. Alternatively, if the Dirac mass was closer to the mass of the τ lepton or quarks, i.e.. $m_D = \mathcal{O}(1\text{GeV})$, the resulting heavy neutrino mass would be $m_N = \mathcal{O}\left(10^7\text{TeV}\right)$.

2.4 Physics at Hadron Colliders

The presence of hadrons, which are composite particles, adds layers of complexity to hadron-hadron collisions in contrast to collisions at lepton colliders, where elementary particles interact. This complex situation can be broken down into various sub-processes and stages, as detailed in Section 2.4.1. An overview of cross-section and parton density functions is presented in Section 2.4.2. The process of event simulation is discussed in Section 2.4.3.

2.4.1 Proton-proton Collisions

In proton-proton collisions, the primary hard scattering process involves interactions between two constituent partons, while the remaining proton constituents contribute to additional activity as shown in Figure 2.2. The different colored elements in the figure mean the different energy scales in the event evolution, which are sequentially modeled in Monte Carlo simulations. The hard scattering process (upper purple circle) involves one parton from each colliding proton. Both the incoming partons and the produced particles in the hard scattering could sustain radiation processes (red lines), described theoretically through parton shower models. Radiation emitted by the incoming partons is classified as initial state radiation (ISR), while that from outgoing partons constitutes final state radiation (FSR). These partons evolve through successive emissions until they reach the hadronization phase (light green circles), where they combine into color-neutral hadrons that subsequently decay into stable particles (dark green circles). The resulting collimated sprays of hadrons form what we observe as jets. Meanwhile, interactions between the proton remnants (bottom purple circle) contribute to what is known as the underlying event activity.

2.4.2 Cross-section and Parton Density Function

As discussed in Section 2.4.1, In a proton-proton collision, the interaction can be treated as the sum of individual interactions from any two constituents from each proton. As a result, only a portion of the total center-of-mass energy ($\sqrt{s}$) is available for the hard scattering process.

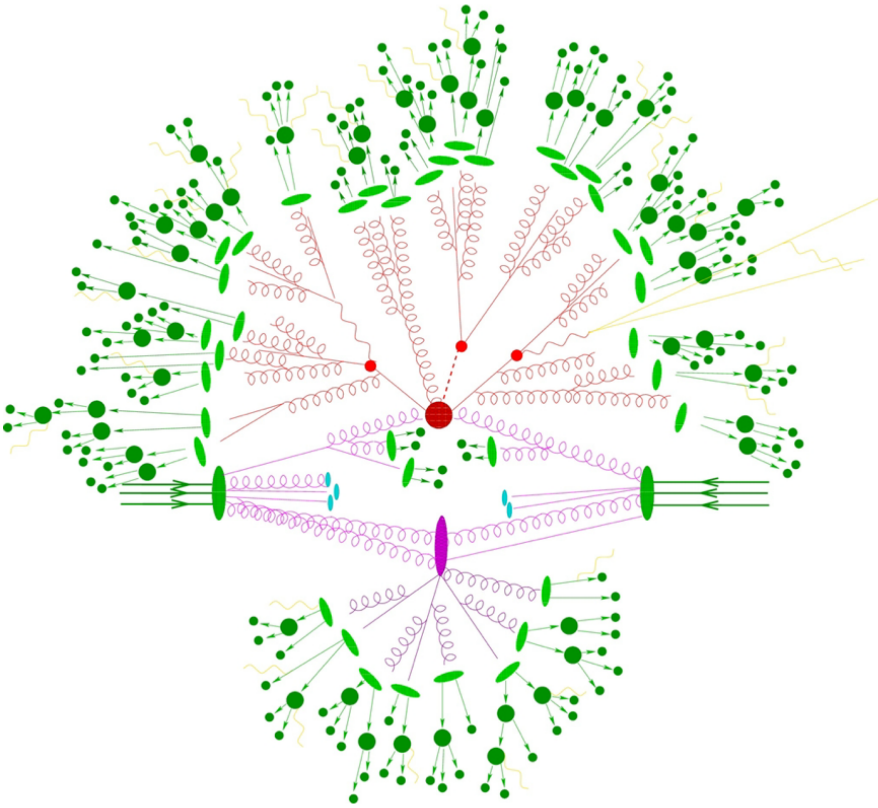

Figure 2.2: Schematic view of the interaction at a pp collider.

This portion is referred to as the partonic center-of-mass energy, $\sqrt{\hat{s}} = \sqrt{x_1 x_2 s}$. Here, x_1 and x_2 are the Bjorken x-variables, which represent the fractions of the proton's momentum interacted by the two partons. The cross-section for a specific process can then be written as:

$$\sigma = \sum_{i,j} \int dx_1 dx_2 \cdot f_i(x_1, \mu_F) f_j(x_2, \mu_F) \cdot \hat{\sigma}(\hat{s}, \mu_R, \mu_F), \tag{2.22}$$

where i and j represent different parton types.

The partonic cross-section $\hat{\sigma}$ describes proton-proton (pp) interactions at a given partonic center-of-mass energy $\sqrt{\hat{s}}$, calculated through perturbative methods. The theoretical prediction of $\hat{\sigma}$ involves two arbitrary scales: the renormalization scale μ_R and factorization scale μ_F, whose exact values cannot be uniquely determined at finite orders of perturbation theory. A conventional approach to estimate this theoretical uncertainty involves varying both scales by factors between 0.5 and 2 relative to their central values and examining the resulting variations. For most processes, Next-to-Leading Order (NLO) calculations are available, which incorporate $\mathcal{O}(\alpha_s)$ virtual corrections and real emission contributions. Current theoretical developments are progressively advancing toward Next-to-Next-to-Leading Order (NNLO) precision, where two-loop virtual corrections are included, yielding significantly improved prediction accuracy.

Figure 2.3 shows a summary plot of cross-section measurement results from different SM processes by the ATLAS experiment, and all of them are consistent with the theory predictions within uncertainties, respectively.

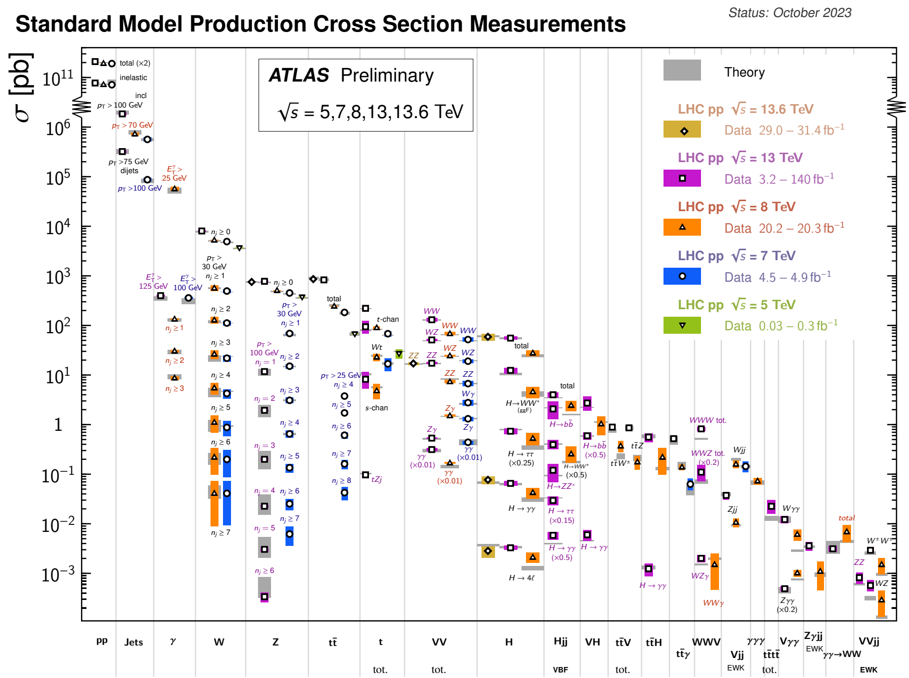

Figure 2.3: Several Standard Model total and fiducial production cross-section measurements by ATLAS are listed here. The measurements are compared to the respective SM theory predictions. [36]

The parton distribution function (PDF), denoted as $f_p(x)$, means the probability density of finding a parton with a momentum fraction x inside a proton. The factorization scale μ_F serves as a regulator for collinear divergences that emerge from soft gluon emissions and parton splitting processes. Experimental determinations of proton PDFs primarily rely on data from deep inelastic scattering experiments (e.g., HERA) combined with precision measurements at hadron colliders. These measurements are vital for constraining PDF parameters and advancing our knowledge of proton substructure [37].

Multiple PDF sets exist in the literature, differing in their theoretical approaches and experimental inputs. These distributions are initially determined at a reference energy scale and can be evolved to other scales through the Dokshitzer-

Gribov-Lipatov-Altarelli-Parisi (DGLAP) equations. The DGLAP framework describes the energy dependence of both the strong coupling constant α_s and parton radiation patterns, enabling reliable PDF predictions across various energy scales. This scale evolution is crucial for theoretical predictions at energies beyond those directly accessible in experiments. A representative set of PDFs extracted from ATLAS data is shown in Figure 2.4 [38].

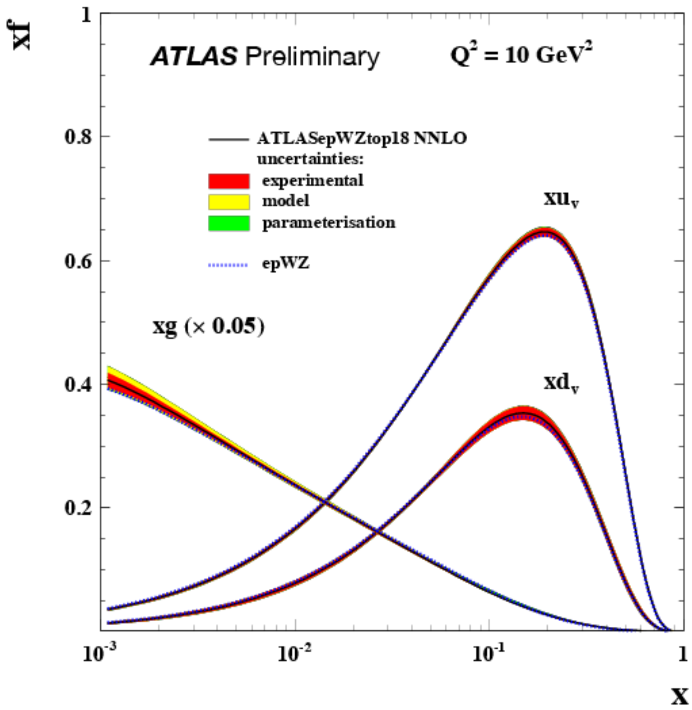

Figure 2.4: An example of the PDFs extracted from a fit to ATLAS data.

2.4.3 Event Simulation

To compare observed data with theoretical predictions, it is essential to simulate both the physics processes and the detector response. The simulation process involves several key steps: first, the generation of the final state particles resulting from a collision; then, the interaction between these particles and the detector; and finally, the digitization of the simulated data. This sequence ensures that the simulated events closely resemble the actual data collected by the detector, allowing for accurate comparisons between theory and experiment.

Various Monte Carlo (MC) methods are utilized to simulate distinct phases of particle collisions listed on Section 2.4.1. The hard scattering process is calculated perturbatively, where initial-state radiation is incorporated through exact matrix element (ME) computations at fixed order. When determining the hadronic cross-section, decisions must be made regarding the factorization and renormalization scales, as well as the choice of the PDF set. These choices are critical for the theoretical calculations and can significantly influence the accuracy and precision of the results. Therefore, it is essential to carefully consider and evaluate these parameters to ensure reliable and meaningful predictions for hadronic processes.

Parton showers (PS) are vital for accounting for higher-order effects that go beyond the fixed-order matrix element calculation. They capture soft and collinear emissions, providing a more comprehensive understanding of particle interactions in high-energy collisions by including additional layers of complexity that are not covered by the fixed-order calculations alone.

Several general-purpose event generators are available to address the physics at LHC experiments [39], and below list the most commonly used generators:

Sherpa excels in the perturbative event phase, providing automated generation of tree-level matrix elements through its two comprehensive ME generators. It features advanced phase-space integration methods and extends its capabilities to support next-to-leading order accuracy via automated subtraction methods. Additionally, SHERPA includes a default parton-shower algorithm that relies on the Catani-Seymour dipole factorization formalism, its own hadronization model, and various enhancements such as a detailed model of hadron and τ decays, QED final-state radiation, and a simulation of the underlying event based on multiple-parton scattering.

Powheg interfaces parton-shower Monte Carlo generators with fixed NLO QCD computations. Its key features include NLO accuracy for infrared-safe observables, summation of collinear emissions at the leading-logarithmic level, and proper treatment of the double logarithmic region (i.e., soft and collinear gluon emission).

Pythia is a general-purpose generator with over 30 years of development. It offers more than 200 hard-coded subprocesses, primarily covering $2 \to 1$ or $2 \to 2$ interactions, and a few $2 \to 3$ interactions. Unlike other generators such as SHERPA, PYTHIA does not automate new process code generation but instead reads Les Houches Event files, ensuring compatibility with a range of external programs, including general-purpose matrix-element programs like MADGRAPH and many processes within the POWHEG framework for NLO calculations. PYTHIA is renowned for its modeling of Multiple Parton Interactions (MPI) and provides an inclusive description of the total proton-proton cross-section, incorporating elastic, single and double diffractive, and non-diffractive soft processes.

MadGraph functions as the matrix element generator in this analysis. It generates matrix elements for processes such as decays or $2 \rightarrow$ n scatterings. By specifying the desired initial and final state particles, MadGraph produces Feynman diagrams and corresponding code for calculating the matrix element at specific phase space points. This code is used for cross-section or decay width calculations and event generation. The output is then passed to external programs like Pythia for simulating parton showers, underlying events, and other phenomena.

Herwig++ builds on the original Herwig (Hadron Emission Reactions With Interfering Gluons) framework. It features angular-ordered parton showers to capture color coherence effects accurately and includes unique physics features such as automatic generation of hard processes and decays with full spin correlations for many BSM models, NLO matching with the Powheg method, and advanced models for hadronic decays, particularly for bottom hadrons and τ leptons. It also includes models for hard and soft multiple partonic interactions to simulate the underlying event and inclusive interactions.

The event generation process produces final-state particles from the primary interaction vertex. These particles are subsequently propagated through the detector using Geant4 simulation. To optimize computational efficiency, a fast simulation approach (Atlfast-II) [40] is employed, which utilizes parameterized response models for calorimeter showers. The simulated events are then combined with inelastic pile-up interactions, and a reweighting technique is applied to match the distribution of interactions per bunch crossing to the observed data.

Following detector simulation, the Monte Carlo events undergo identical reconstruction and analysis chains as applied to collision data. Additional corrections are implemented to align the simulation with the actual detector performance, particularly for object reconstruction efficiencies and identification criteria, thereby minimizing residual discrepancies between simulation and data.

Chapter 3 The Large Hadron Collider and the ATLAS Detector

The Large Hadron Collider (LHC) [41] represents the highest-energy hadron accelerator and collider facility worldwide. With a circumference of 26.7 km buried approximately 100 m underground across the Franco-Swiss border, the LHC repurposes the underground infrastructure originally constructed for its predecessor, the Large Electron-Positron Collider (LEP), decommissioned in 2000.

The LHC complex houses seven principal detector systems: the general-purpose ATLAS and CMS detectors, the heavy-ion focused ALICE experiment, the flavor physics LHCb detector, and the specialized LHCf, TOTEM, and MoEDAL installations. ATLAS holds the distinction as the largest detector by physical dimensions, while CMS ranks as the most massive. Both ATLAS and CMS serve as multipurpose detectors capable of precision Standard Model measurements and searches for new physics phenomena. Their joint discovery of the Higgs boson in 2012 remains the LHC's most celebrated scientific breakthrough to date.

This section is organized as follows: a brief overview of the LHC in Section 3.1, followed by a description of the ATLAS detector in Section 3.2.

3.1 The Large Hadron Collider

3.1.1 Accelerator Complex

The accelerator complex is a sequence of machines designed to progressively increase particle beams' energy. Each unit in this chain accelerates the particles further before injecting them into the next stage. The LHC represents the final stage in this series. During LHC Run-2, the particle beams were accelerated to an energy of 6.5 TeV per beam. The layout of the accelerator complex is illustrated in Figure 3.1.

Linear Accelerator 4 (Linac 4) replaced Linear Accelerator 2 (Linac 2) as the new injector for the Proton Synchrotron Booster (PSB) in 2020, marking the beginning of the proton acceleration chain. Linac 2 was decommissioned in 2018 after 40 years of service. Linac 4 accelerates negative hydrogen ions (H^- ions), which contain a hydrogen atom and an extra electron, to 160 MeV before injecting them into the PSB.

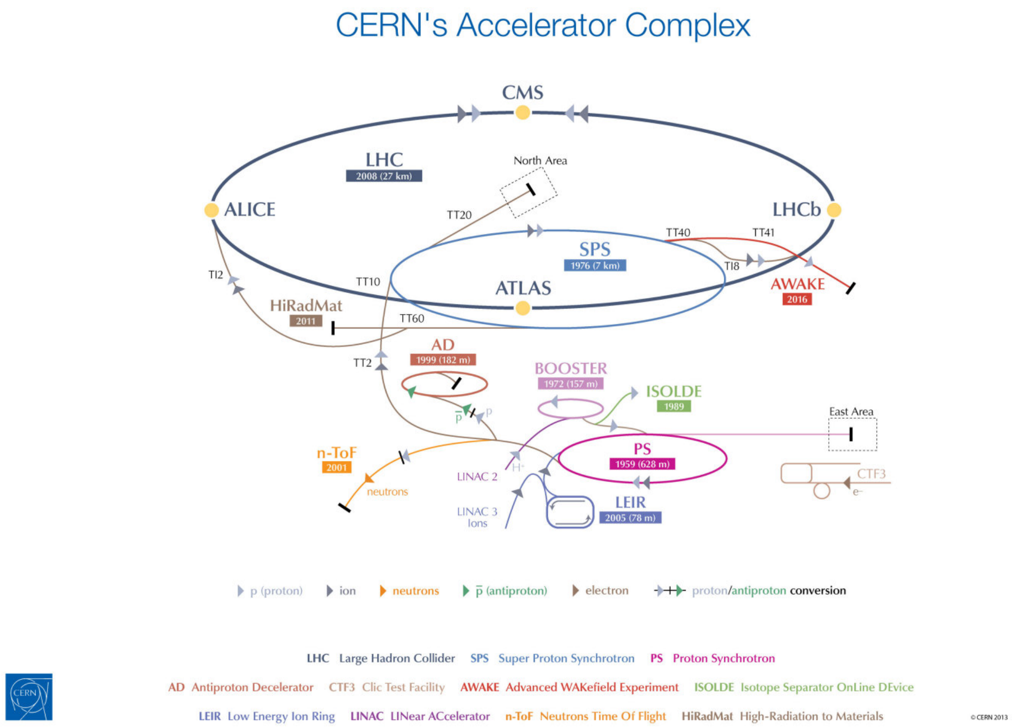

Figure 3.1: Complex chain of the LHC accelerator.

The H^- ions are initially extracted from the ion source at 45 keV. The acceleration chain comprises successive stages: first, the radio-frequency quadrupole (RFQ) accelerates the beam to 3 MeV; then drift tube linacs (DTLs) increase the energy to 50 MeV; followed by coupled-cavity drift tube linacs (CCDTLs) reaching 100 MeV; and finally Pi-mode structures (PIMS) achieving 160 MeV. During injection into the Proton Synchrotron Booster (PSB), the H^- ions are stripped of their electrons, converting them to protons. This stripping process doubles the beam brightness and plays a crucial role in achieving the high luminosity of the LHC.

The Proton Synchrotron Booster, with a circumference of 25 meters, increases the proton energy to 1.4 GeV in 1.2 seconds. The protons are then transferred to the 628-meter circumference Proton Synchrotron, where their energy is elevated to 25 GeV. At this stage, the protons are organized into bunches with the same frequency and spacing as those used in the LHC, and the beam is split into two bunches, each containing approximately 1.1×10^{11} protons. The protons are subsequently directed to the 7 km-long Super Proton Synchrotron (SPS), where they can be accelerated to 450 GeV.

Finally, the two proton beams arrive at the LHC, the last unit in the acceleration chain. Filling each LHC ring takes 4 minutes and 20 seconds, followed by an additional 20 minutes to accelerate the beams to 6.5 TeV using a 400 MHz Radio-Frequency (RF) system. In the LHC, one beam circulates clockwise while the other circulates counterclockwise. To ensure that both beams travel the same path length, their positions are alternated between the inside and outside of the ring during experiments. The beams are separated by 194 mm, which is the nominal distance between the coil axes, and 420 mm in the RF cavities.

Thousands of magnets of various types and sizes are employed to guide the beams around the accelerator. The 27 km underground tunnel of the LHC is predominantly occupied by superconducting magnets. This includes 1,232 main dipole magnets, which are responsible for bending the beam, and 392 main quadrupole magnets, which focus the beam. Additionally, several insertion quadrupole magnets further contribute to beam focusing and control.

3.1.2 Luminosity and Pile-up

The expected event yield in proton-proton collisions is given by:

$$N = L \times \sigma = \sigma \int \mathcal{L}\, dt, \tag{3.1}$$

where L represents the integrated luminosity, σ denotes the process cross-section, and $\mathcal{L}$ is the instantaneous luminosity determined by beam parameters:

$$\mathcal{L} = \frac{N_b^2 n_b f_{\text{rev}}}{4\pi\sigma_x\sigma_y} \cdot F, \tag{3.2}$$

with f_{rev} being the LHC revolution frequency, N_b the number of protons per bunch, n_b the number of bunches per beam, and σ_x, σ_y the transverse bunch dimensions. The geometric reduction factor F accounts for the crossing angle effect:

$$F = \left[1 + \left(\frac{\theta_c\sigma_z}{2\sigma^*}\right)^2\right]^{-1/2}, \tag{3.3}$$

where θ_c is the crossing angle, σ_z the longitudinal bunch size, and σ^* the transverse beam size at the interaction point.

Figure 3.2 displays the integrated luminosities sent by the LHC and recorded by ATLAS during the 2015-2018 data-taking periods at $\sqrt{s} = 13$ TeV. The ATLAS detector maintained data-taking efficiencies consistently above 90% throughout these operations.

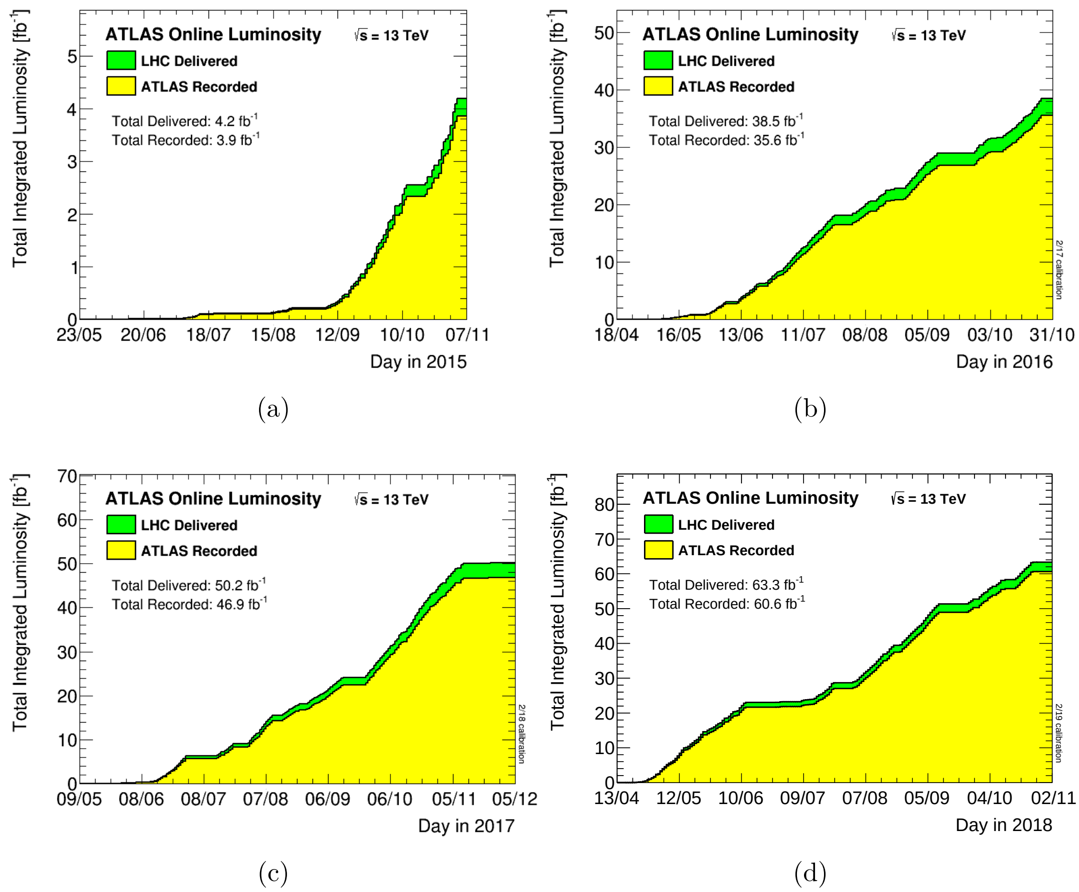

Figure 3.2: Cumulative luminosity versus time sent by LHC (with green color) and recorded by ATLAS (with yellow color) during stable beams for *pp* collisions at $\sqrt{s} = 13$TeV for the years: 2015 (a), 2016 (b), 2017 (c) and 2018 (d).

To sustain the target luminosity and collision rate at the LHC, proton bunches are collided, resulting in multiple concurrent interactions per bunch crossing. These additional collisions are known as pile-up interactions, whose characteristics and frequency depend on both the collision energy and instantaneous luminosity. Figure 3.3 displays the evolution of the mean number of interactions per bunch crossing ($\langle\mu\rangle$) during the 2015-2018 data-taking period, with values of 13.4 (2015), 25.1 (2016), 37.8 (2017), and 36.1 (2018), yielding an overall Run 2 average of $\langle\mu\rangle = 33.7$.

The parameter $\langle\mu\rangle$ is the mean of the Poisson distribution describing the number of interactions per bunch crossing and for each individual bunch as:

$$\langle\mu\rangle = \frac{L_{\text{bunch}} \times \sigma_{\text{inel}}}{f_r}, \tag{3.4}$$

where L_{bunch} denotes the per-bunch instantaneous luminosity, σ_{inel} the inelastic pp cross-section, and f_r the LHC revolution frequency [42].

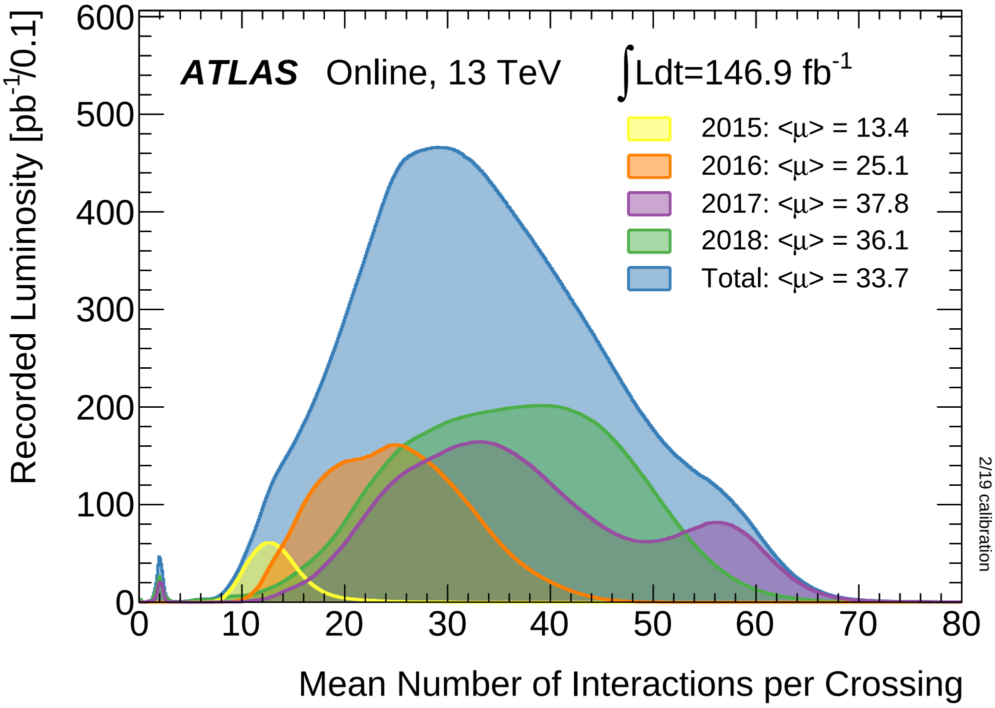

Figure 3.3: Distribution of the mean number of interactions per bunch crossing ($\langle\mu\rangle$) for ATLAS pp collision data collected during 2015-2018 at $\sqrt{s} = 13$ TeV.

3.2 The ATLAS Detector

ATLAS is one of the two general-purpose detectors at the LHC, designed to investigate a wide range of physics phenomena from Higgs boson studies to searches for extra dimensions and dark matter candidates. The detector features a cylindrical structure with perfect symmetry about the interaction point, measuring 46 meters in length and 25 meters in diameter. With a total weight of 7,000 tons, it is installed 100 meters underground at Point 1 of the LHC ring, making it the largest particle detector ever constructed. The overall layout of the ATLAS detector is displayed in Figure 3.4, while Figure 3.5 illustrates characteristic particle interaction signatures within the detector.

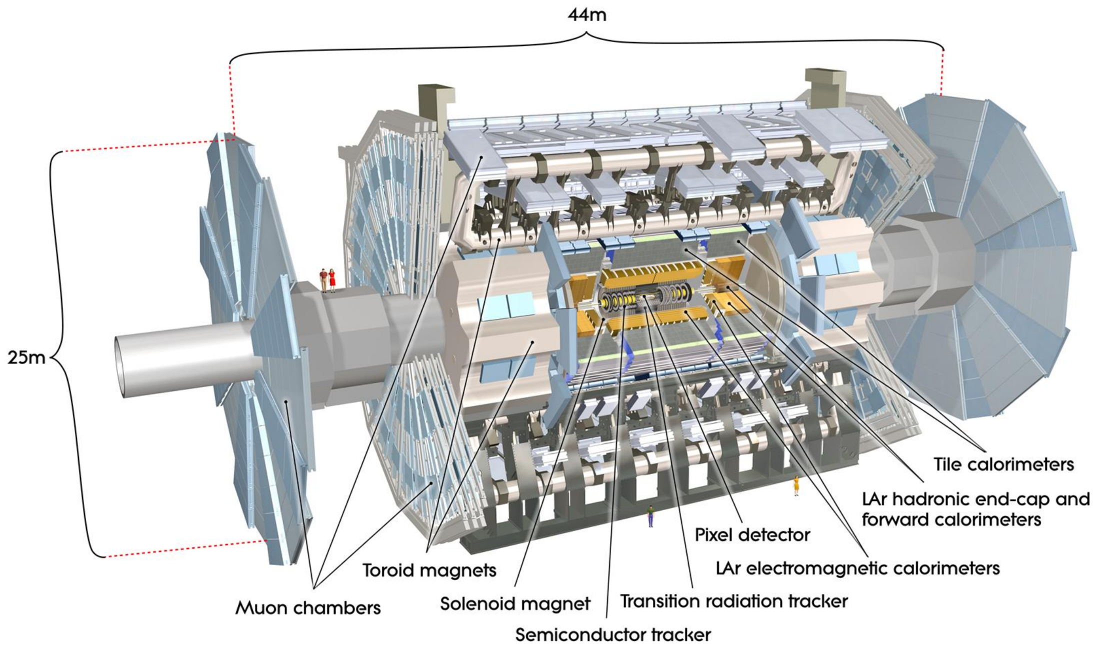

Figure 3.4: Cut-away view showing the internal structure of the ATLAS detector.

This sophisticated detector system is specifically engineered to identify and measure the most energetic particles produced in terrestrial experiments. It consists of four primary detection systems arranged concentrically around the collision point, each optimized for specific measurement tasks. The innermost tracking system precisely reconstructs charged particle trajectories and measures their momenta. Surrounding this, the electromagnetic calorimeter accurately measures energy deposits from electrons and photons, while the adjacent hadronic calorimeter performs similar measurements for hadronic particles. The outermost muon spectrometer specializes in identifying muons and measuring their momenta. An integrated superconducting magnet system generates the strong magnetic field required to bend charged particle trajectories, enabling precise momentum measurements throughout the entire detector volume.

The detector components are described in detail throughout this document: Section 3.2.1 presents the three-layer inner detector system, comprising the pixel detector, Semi-Conductor Tracker (SCT), and Transition Radiation Tracker (TRT). Section 3.2.2 discusses the calorimeter system, with its external hadronic calorimeter and internal electromagnetic calorimeter. The muon spectrometer is detailed in Section 3.2.3, while the magnet system specifications are covered in Section 3.2.4. Finally, Section 3.2.5 introduces the trigger and data acquisition system.

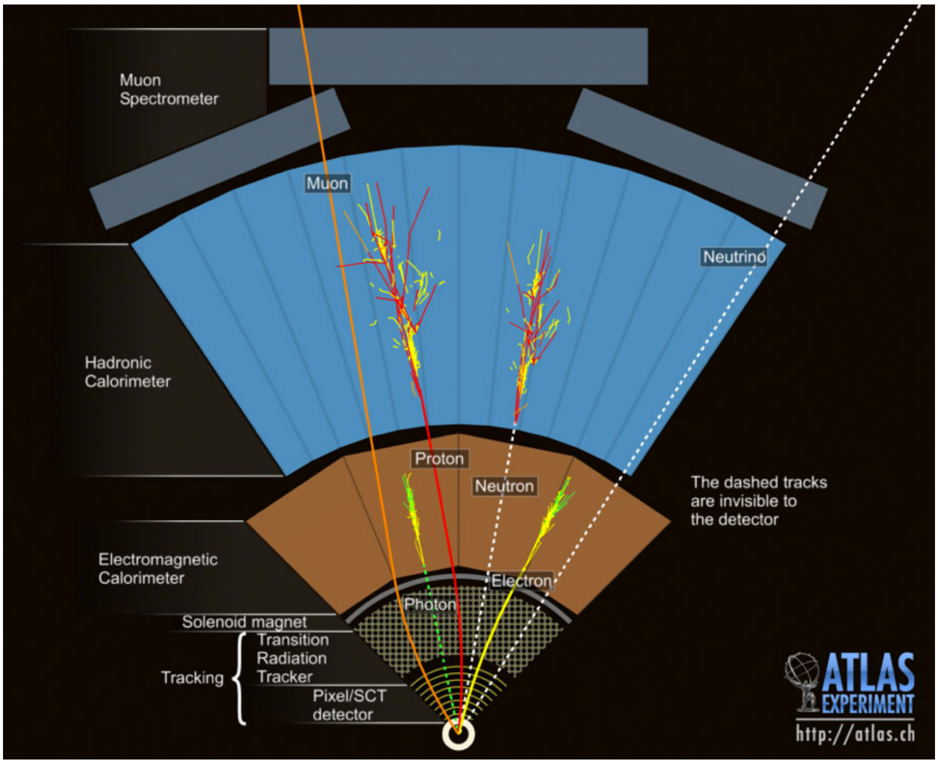

Figure 3.5: Schematic representation of particle interactions and signatures in the ATLAS detector subsystems.

3.2.1 Inner Detector

The Inner Detector (ID) [43] provides precise tracking of charged particles in high-radiation environments, operating within a 2 T magnetic field from the barrel solenoid. This system comprises three complementary subdetectors with barrel and end-cap configurations: the pixel detector, SemiConductor Tracker (SCT), and Transition Radiation Tracker (TRT).

Closest to the beam pipe, the pixel detector enables high-precision vertex reconstruction. The SCT delivers accurate momentum measurements, while the TRT provides up to 36 hits per track for improved momentum resolution and pattern recognition across a broad energy range. Combined, these systems achieve precise tracking for charged particles within $|\eta| < 2.5$ and $p_T > 0.5$ GeV. Figure 3.6 shows the ID's internal structure.

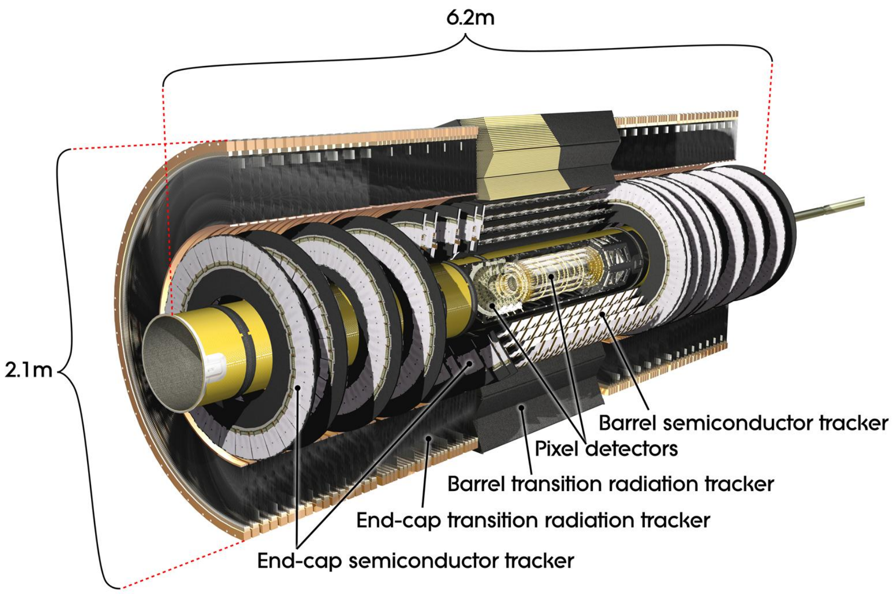

Figure 3.6: Cross-sectional view of the ATLAS Inner Detector showing its three-layer architecture.

Pixel Detector Upgrade: During LHC's first long shutdown, the Insertable B-Layer (IBL) [44] was installed at 33.2 mm radius, becoming ATLAS's innermost tracking layer. The IBL enhances tracking performance by 40% for low-p_T ($\sim$0.5 GeV) particles and improves b-tagging efficiency by 10% compared to Run 1. Its 6 million pixels (50×250 μm^2 each) provide exceptional granularity, achieving 8×40 μm^2 spatial resolution in the r-ϕ plane.

The transverse momentum resolution of the Inner Detector is designed as:

$$\sigma\left(\frac{1}{p_T}\right) = 0.036\% \cdot p_T \oplus 1.3\%, \tag{3.5}$$

where p_T is measured in GeV.

The pixel detector system consists of the IBL plus three barrel layers (at radii of 50.5 mm, 88.5 mm, and 122.5 mm) and three end-cap disks on each side. The barrel region contains 1,456 modules (67 million channels) while the end-caps have 288 modules (13 million channels), totaling approximately 80 million readout channels. Each 50×400 μm^2 pixel provides intrinsic resolutions of:

- Barrel: 10 μm (r-ϕ) × 115 μm (z)
- End-caps: 14 μm (r-ϕ) × 115 μm (z)

Silicon Microstrip Tracker: The SCT contains four barrel layers (at 299 mm, 371 mm, 443 mm, and 514 mm radii) plus nine end-cap wheels per side, covering 60 m^2 with 4,088 double-layer modules. With 6 million channels, it provides:

- 8 hits per track in barrel (2 hits/layer)
- 9 hits per track in end-caps
- Intrinsic resolution: 16 μm (r-ϕ) × 580 μm (z)

Each module measures 6.36×6.40 cm^2.

Transition Radiation Tracker: The TRT's outermost subsystem comprises:

- Barrel: 144 cm straw tubes (73 layers, 50,000 straws, 563–1066 mm radius)
- End-caps: 37 cm straws (320 layers, 25,000 straws)
- Total: ∼350,000 channels

With 36 hits/track capability, it enhances pattern recognition and momentum resolution for 1–200 GeVparticles, achieving 130 μm resolution in r-ϕ for $|\eta| < 2.0$.

3.2.2 Calorimeters

The ATLAS calorimeter system measures particle energies through interactions with detector materials, with specialized subsystems for different particle types:

- **Electromagnetic Calorimeter (EMAL)**: Used to measure electrons and photons via electromagnetic interactions, using liquid argon and lead absorber technology

- **Hadronic Calorimeter (HCAl)**: Detects energy deposits from quark-containing hadrons, providing essential data for strong interaction studies

Figure 3.7 shows the integrated calorimeter system layout.

Electromagnetic Calorimeter: The LAr electromagnetic calorimeter [45] comprises:

- Barrel region ($|\eta| < 1.475$)

- Endcap region ($1.375 < |\eta| < 3.2$)

This sampling calorimeter combines liquid argon (active medium) with lead absorbers. The barrel's unique accordion geometry (Figure 3.8) ensures complete ϕ-coverage without dead regions. Incident electrons/photons create EM showers in the lead, with ionization signals collected by electrodes. The total charge provides a direct energy measurement with resolution:

$$\frac{\sigma_E}{E} = \frac{10\%}{\sqrt{E}} \oplus 0.3\% \tag{3.6}$$

Hadronic Calorimeter: Unlike electromagnetic particles, hadrons interact through both strong and electromagnetic forces, producing fundamentally different shower patterns. The hadronic calorimeter [46] utilizes:

- Steel absorber plates for hadronic interactions

- Scintillator tiles for energy sampling

This design optimally captures the complex energy deposition patterns characteristic of hadronic showers.

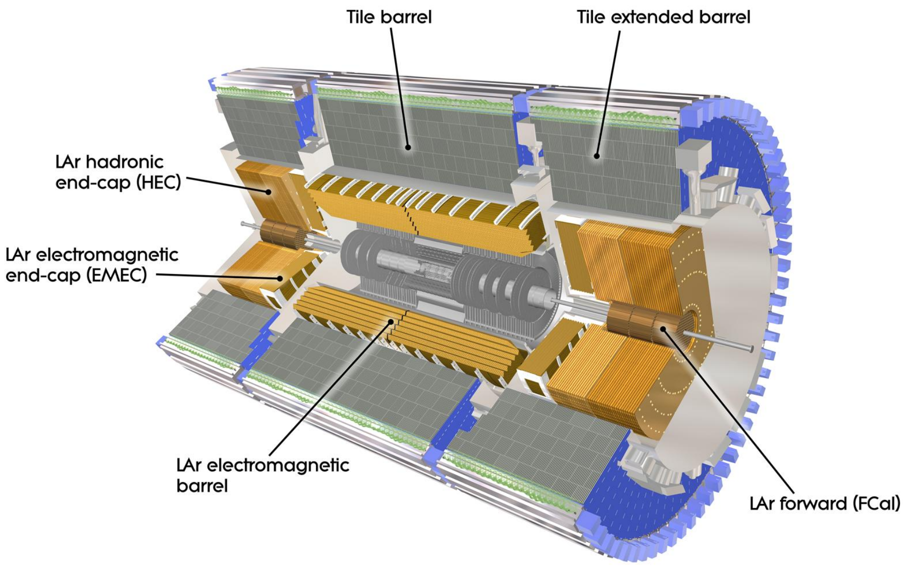

Figure 3.7: Cross-sectional view of the ATLAS calorimeter system showing the electromagnetic and hadronic calorimeter components.

The hadronic calorimeter system features a barrel region with a central section covering $|\eta| < 1.0$ and two extended barrels covering $0.8 < |\eta| < 1.7$. Additional coverage is provided by the hadronic end-cap calorimeter ($1.5 < |\eta| < 3.2$) with copper absorbers and the forward calorimeter ($3.1 < |\eta| < 4.9$), which uses one copper and two tungsten absorber layers. Both the end-cap and forward calorimeters employ liquid argon technology.

The energy resolution for the barrel/end-cap and forward calorimeters is described by Equations 3.7 and 3.8 respectively.

$$\frac{\sigma_E}{E} = \frac{50\%}{\sqrt{E}} \oplus 3\%, \tag{3.7}$$

$$\frac{\sigma_E}{E} = \frac{100\%}{\sqrt{E}} \oplus 10\%. \tag{3.8}$$

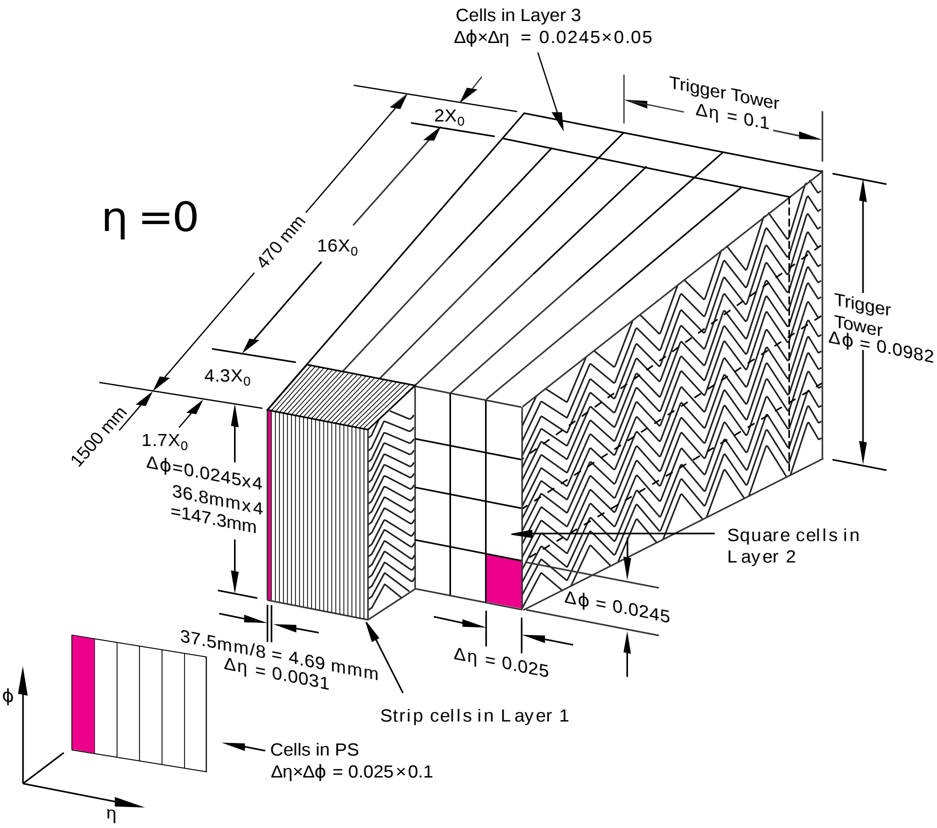

Figure 3.8: Schematic view of the EM barrel modules.

3.2.3 Muon Spectrometer

The muon spectrometer (MS) is the outermost part of the ATLAS detector, defining its overall dimensions. It spans a radial distance from 4.25 meters to 11 meters. The primary function of the MS is to identify and measure the momentum of muons and provide triggers for muons with varying transverse momentum thresholds down to a few GeV.

The MS is divided into 16 sectors in the x-y plane, based on their coverage in ϕ. These sectors include 8 large and 8 small sectors in both the barrel and end-cap regions. Each sector is further subdivided into three sections: Inner, Middle, and Outer, depending on their distance from the Interaction Point.

The muon spectrometer comprises four distinct parts utilizing different technologies to cover different η ranges. The Monitored Drift Tubes (MDTs) are placed in the central regions ($|\eta| < 2.7$), while the Cathode Strip Chambers (CSCs) are located in the end-caps ($2.0 < |\eta| < 2.7$) for precise muon measurement. The other two components are designed for the fast trigger system with a time resolution of less than 25 ns, enabling the identification of the corresponding bunch crossing ID of a hit. The Resistive Plate Chambers (RPCs) are installed in the barrel ($|\eta| < 1.05$), and the Thin-Gap Chambers (TGCs) are used in the end-caps ($1.05 < |\eta| < 2.7$).

Figure 3.9 illustrates the geometry of the muon spectrometer. The barrel MDT chambers are marked in green color, while the end-cap MDT chambers are marked in blue color. In the barrel and end-caps, the RPCs and TGCs are represented in purple, and the CSCs are highlighted in yellow.

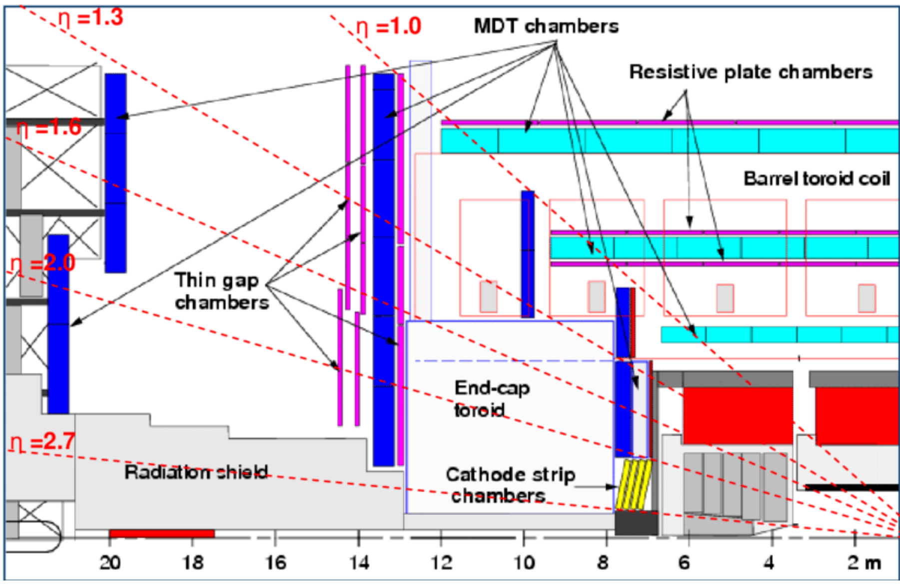

Figure 3.9: A schematic side-view of the ATLAS Muon Spectrometer.

The Monitored Drift Tube (MDT) chambers, covering most of the Muon Spectrometer (MS) acceptance, consist of two MultiLayers (ML), with each containing three or four tube layers. These tubes feature a 30 mm diameter with a central 50 μm anode wire, achieving a single-hit resolution of approximately 80 μm. For high-background regions in the end-caps, Cathode Strip Chambers (CSCs) provide enhanced performance through their four-layer design with 70,000 channels and improved 60 μm resolution.

The trigger system employs Resistive Plate Chambers (RPCs) in two configurations: middle barrel chambers for low-p_T triggers and outer barrel chambers for high-p_T triggers. These RPCs additionally measure the η-ϕ position parallel to MDT wires with 5-10 mm spatial resolution. Similarly, Thin Gap Chambers (TGCs) handle end-cap background conditions through a system of 1,171 chambers containing 354,240 tubes (3 cm diameter, 0.85-6.5 m length), providing both trigger signals and complementary η-ϕ position measurements with 80 μm resolution.

To enhance coverage in the transition region ($1.0 < |\eta| < 1.4$), four special MDT chambers equipped with RPCs were installed, incorporating smaller-radius tubes for improved rate capability. The muon momentum measurement relies on trajectory reconstruction in the toroidal magnetic field (Section 3.2.4), where the bending from Lorentz force enables momentum determination with resolutions of 3% at 100 GeV and 10% at 1 TeV.

3.2.4 Magnet System

The ATLAS magnet system comprises three superconducting components: a central solenoid, a barrel toroid, and two end-cap toroids, as illustrated in Figure 3.10.

The solenoid magnet, positioned between the inner detector (Section 3.2.1) and electromagnetic calorimeter (Section 3.2.2), produces a 2 Tesla axial magnetic field for precise momentum measurement of charged particles through trajectory bending. This critical component measures 5.3 meters in length with 2.46/2.56 meter inner/outer diameters, featuring a 4.5 cm thick superconducting coil structure with a total mass of approximately 5 tonnes.

The superconducting air-core toroids consist of one barrel toroid and two end-cap toroids, positioned around the calorimeters and extending to the muon detectors. These toroids operate at a temperature of 4.5 K.

The barrel toroid, which covers $|\eta| < 1.05$, is composed of 8 separate coils. Each coil has a length of 25.3 meters, an inner diameter of 9.4 meters, an outer diameter of 20.1 meters, and the total weight of the assembly is 830 tonnes. This toroid can store 1.08 gigajoules (GJ) of energy and provides a magnetic field of about 4 Tesla.

The end-cap toroids, which cover the range $1.05 < |\eta| < 2.7$, each contain 8 coils housed in a common cryostat. Each end-cap toroid has an axial length of 5.0 meters, an inner diameter of 1.65 meters, an outer diameter of 10.7 meters, and weighs 240 tonnes. It can store 0.25 GJ of energy and provides a magnetic field of approximately 4 Tesla.

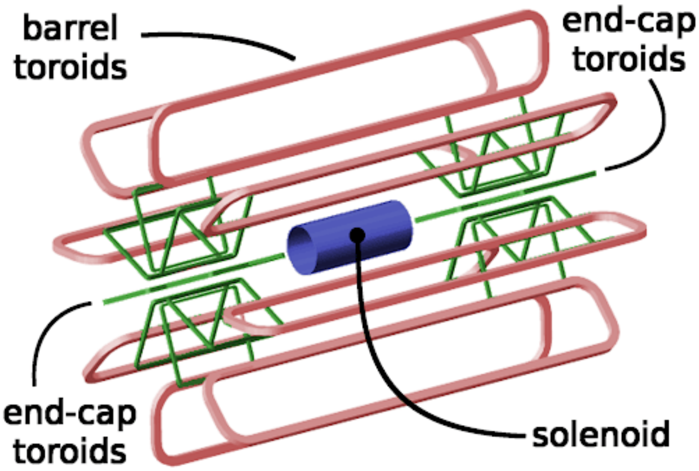

Figure 3.10: The schematic view of magnet system.

3.2.5 Data Acquisition System

Due to limitations in bandwidth and storage capacity, the ATLAS Trigger and Data Acquisition system (TDAQ) cannot record all collision events. Additionally, only a subset of these events contains the physics of interest. Consequently, it is impractical to record every event at the collision rate of 40 MHz.

To manage the data rate, ATLAS employs a specialized two-level trigger system, as illustrated in Figure 3.11.

The ATLAS trigger system is comprised of a two-level trigger architecture. The Level-1 Trigger (L1) [47] is hardware-based, while the High-Level Trigger (HLT) [48] is software-based and includes the Level-2 Trigger (L2) and the Event Filter. The L1 Trigger must make a decision on whether to keep an event within 2.5 ms of its occurrence, during which time the event data is held in storage buffers. The peak data rate at this stage is 6 TB per second. The L1 Trigger processes a subset of information from the calorimeters and muon spectrometer to identify events with high transverse momentum or large missing transverse energy exceeding predefined thresholds. It then records the Region of Interest (ROI), which contains the η and ϕ coordinates, along with full granularity data from the inner detector. Following the L1 Trigger, the event rate is reduced to 100 K events per second and the peak data rate is approximately 160 GB per second.

The High-Level Trigger (HLT) processes events using the complete detector granularity, with an average execution time of 40 ms per event. Building upon the Regions of Interest (ROIs) identified by the Level-1 Trigger, the HLT performs progressively refined object reconstruction. This system reduces the event rate to approximately 1.5 kHz while sustaining a peak data throughput of 160 GB/s. Accepted events are subsequently stored for detailed offline analysis.

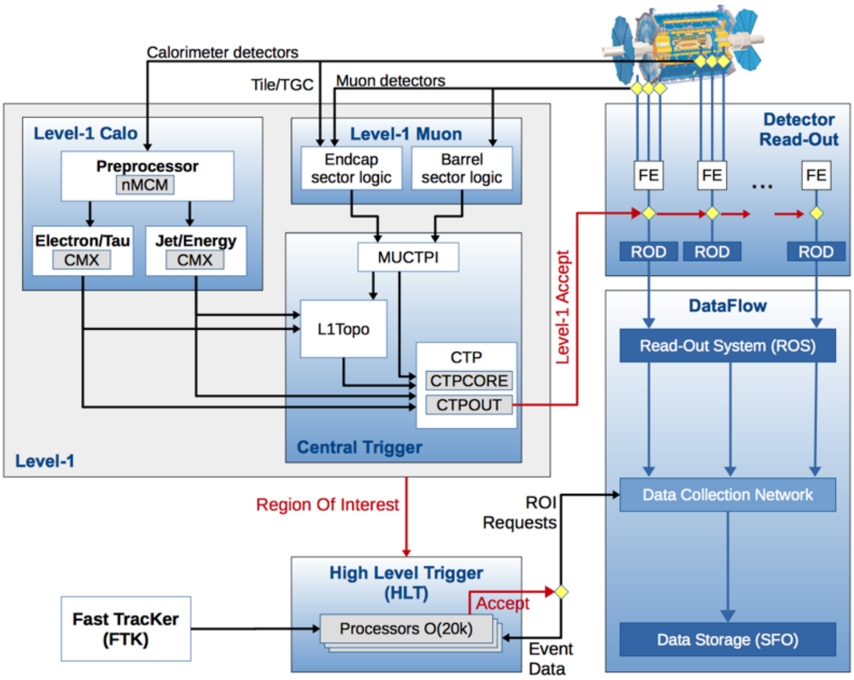

Figure 3.11: Schematic diagram of the ATLAS trigger and data acquisition architecture during Run-2 operations, showing the data flow from Level-1 Trigger through High-Level Trigger processing.

Chapter 4 Object Reconstruction

The accurate reconstruction and identification of physical objects represent a fundamental requirement for physics analysis. These processes rely on a detailed understanding of particle-detector interactions, as visualized in Figure 3.5, which shows characteristic particle signatures across ATLAS subsystems. Basic quantities like tracks and calorimetric clusters are formed by combining output information from sub-detectors. These quantities are then used for reconstructing the final physics objects. This section describes the procedures for the reconstruction and identification of all physics objects. These procedures are applied to both simulated events and real data events.

4.1 Tracks, Vertices and Clusters

4.1.1 Tracks

Charged particle track reconstruction is performed by the Inner Detector (ID) within the 2 T solenoid magnetic field, providing precise position measurements for charged particles within $|\eta| < 2.5$. The ID employs two complementary reconstruction algorithms [49]: (1) The standard *inside-out* approach for primary charged particles (defined as particles with mean lifetime $> 3 \times 10^{-11}$ s, produced either directly in *pp* collisions or from decays of shorter-lived particles) begins with cluster formation in Pixel/SCT detectors and drift circle identification in TRT, converts these to 3D space-points, creates seeds from three Pixel/SCT hits, propagates tracks outward using a combinatorial Kalman filter [50] for selected seeds meeting p_T and impact parameter requirements, and finally extends tracks to TRT for a complete refit; (2) The *outside-in* algorithm specifically reconstructs secondary particles from primary decays, initiating the process from TRT information.

As shown in Figure 4.1, charged particle tracks in a magnetic field require five parameters:

The track parameters are defined as follows: d_0 represents the signed transverse impact parameter, corresponding to the minimum distance between the

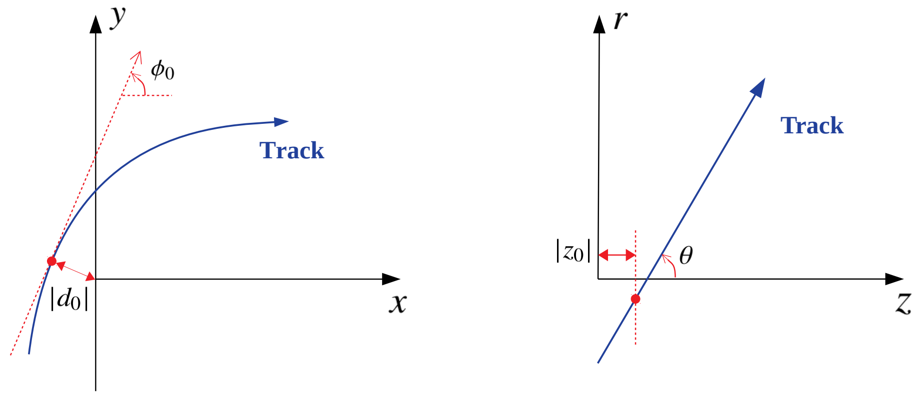

Figure 4.1: Track parameters in the transverse (left) and the $r-z$ (right) planes.

track's closest approach and the interaction point in the transverse plane; Z_0 denotes the longitudinal impact parameter, given by the z-coordinate of the closest approach; ϕ_0 is the azimuthal angle of the track direction at closest approach, defined in the range $[-\pi, \pi]$ in the $x-y$ plane; θ indicates the polar angle of the track direction at the interaction point, spanning $[0, \pi]$ in the $z-R$ plane; and q/p represents the ratio of particle charge to momentum.

The increasing detector occupancy due to pile-up can lead to nearby hits from other particles, potentially confusing the pattern recognition algorithm. To mitigate this and reduce the number of fake tracks, stricter criteria are applied to reconstructed tracks. Specifically, the selection criteria require each track to have at least 9 hits in the silicon detectors (Pixel and SCT), no holes[1] in the Pixel detectors, and a transverse momentum (p_T) greater than 400 MeV.

4.1.2 Vertices

Primary vertices are the spatial locations where p-p interactions occur [51]. These vertices are essential for reconstructing the full kinematic properties of an event. The process of primary vertex reconstruction is divided into two stages: vertex finding and vertex fitting. In the vertex finding stage, reconstructed tracks are associated with potential vertices, with the selection of tracks originating from the hard scatter vertex primarily based on the impact parameters d_0 and z_0. The vertex fitting procedure determines the precise vertex position through

[1] A hole refers to an expected measurement point along a track's trajectory where a hit is missing.

an iterative process. After establishing the vertex position, incompatible tracks are removed and may be reassigned to alternative vertices. The primary vertex means the vertex with the largest scalar sum of squared transverse momenta ($\sum p_{\mathrm{T}}^2$) of its associated tracks. All other reconstructed vertices predominantly originate from pile-up interactions or secondary particle production processes.

4.1.3 Clusters

Topological clusters (topo-clusters) are constructed by closely tracking the spatial patterns of signal significance from the particle showers. The basic observable in cluster formation is cell signal significance S_{cell}, defined as:

$$S_{cell} = \frac{E_{cell}}{\sigma_{noise,cell}}, \tag{4.1}$$

in this formulation, E_{cell} represents the deposited energy while $\sigma_{\mathrm{noise,\ cell}}$ denotes the average cell noise from pile-up or electronic sources. Both measurements are performed using the electromagnetic energy scale (EM scale), which provides accurate energy reconstruction for electrons and photons. However, this calibration does not compensate for the energy loss effects characteristic of hadronic showers in the ATLAS calorimeter system, due to its inherently non-compensating nature. The clustering algorithm implements the "4-2-0" reconstruction scheme: seed cells must first satisfy $S_{\mathrm{cell}} > 4$, then neighboring cells with $S_{\mathrm{cell}} > 2$ are collected (with qualifying cells becoming new seeds), and finally adjacent cells meeting $S_{\mathrm{cell}} > 0$ are included to complete the proto-cluster formation.

The clustering algorithm merges proto-clusters under two conditions: either when a direct neighbor cell is itself a seed cell, or when two seed cells share a common neighboring cell with significance greater than two standard deviations. The clustering process terminates when no additional neighboring cells meet the inclusion criteria. While this approach effectively preserves shower tails, it can produce oversized clusters that potentially contain energy deposits from multiple particles. To mitigate this effect, proto-clusters exhibiting two or more local maxima undergo a splitting procedure. In this refinement step, each local maximum serves as a new seed for reclustering, considering only cells contained within the original proto-cluster boundary. The resulting clusters after this splitting process are designated as *topo-clusters*.

Track-Calo Cluster (TCC) provides an enhanced reconstruction method by merging tracking and calorimeter information to improve jet energy resolution. While standard topo-clusters rely solely on calorimeter data, the TCC approach [52] combines the precise spatial information from tracks with the energy measurements from topo-clusters. The TCC construction algorithm establishes associations between tracks and topo-clusters when they meet the following matching criteria:

$$\sigma_{\text{trk}} < \sigma_{\text{clus}} \ , \ \Delta R < \sqrt{\sigma_{\text{clus}}^2 + \sigma_{\text{trk}}^2} \ , \tag{4.2}$$

where σ_{clus} represents the spatial width of the topo-cluster, σ_{trk} denotes the extrapolation uncertainty of the track to the calorimeter cluster position, and ΔR measures the angular separation between the track direction and the topo-cluster axis. The algorithm constructs TCC 4-vectors using successfully matched track-topo-cluster pairs. The various categories of TCC objects are illustrated in Figure 4.2, with complete descriptions available in Ref. [52].

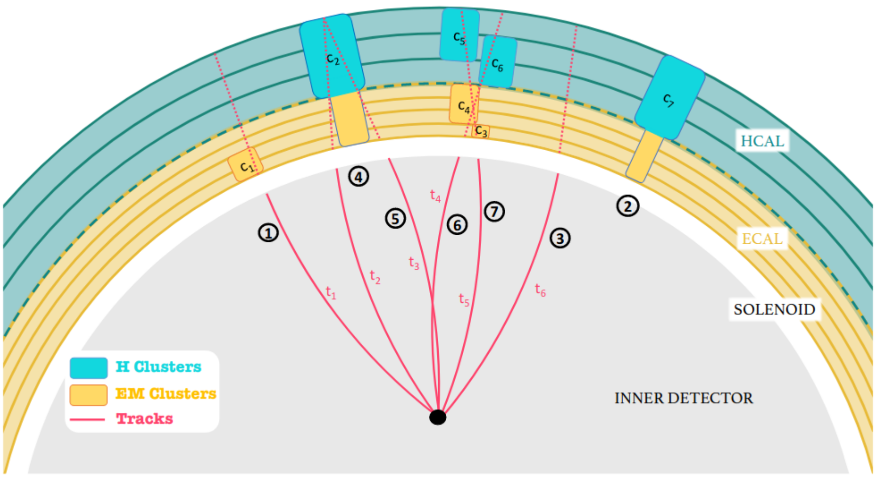

Figure 4.2: Schematic representation of the seven TCC object types. Track trajectories are shown in red, electromagnetic calorimeter clusters in orange, and hadronic calorimeter clusters in blue. The diagram illustrates the spatial relationships between different detector components in the reconstruction of topological clusters.

For every track acting as a seed to build a Track-Calo-Cluster (TCC) object, the energy of matched topo-clusters is distributed among associated tracks proportionally to their momentum fractions. This distribution accounts for cases where multiple clusters match a single track by incorporating a weighted cluster energy fraction. The weighting factor is determined through the following expression:

$$w_\tau^{c_i} = \frac{p_{\mathrm{T}}^{c_i}}{p_{\mathrm{T}}\left[\sum_{c_k} \boldsymbol{p}^{c_k}\right]}. \tag{4.3}$$

In the preceding equation, the summation includes all clusters (c_k) linked to a given track τ, where c_i denotes the particular topo-cluster involved in energy sharing. The transverse momentum fraction p_{T} of track τ that determines the energy contribution from topo-cluster c_i to a Track-Calo-Cluster (TCC) object is expressed as:

$$f^{\tau,c_i} = \frac{p_{\mathrm{T}}^{\tau} \cdot w_\tau^{c_i}}{p_{\mathrm{T}}\left[\sum_{t_j} \boldsymbol{p}^{t_j} \cdot w_{t_j}^{c_i}\right]}, \tag{4.4}$$

where the sum takes all the tracks (t_j) matched to topo-cluster c_i. Finally, the 4-vector of a TCC object built from track τ is:

$$\mathrm{TCC}_\tau : (\sum_{c_i} \boldsymbol{p}_{\mathrm{T}}^{c_i} \cdot f^{\tau,c_i}, \eta^\tau, \phi^\tau, m = 0), \tag{4.5}$$

where the sum takes all the topo-clusters matched to the track τ.

Particle Flow (PFlow) [53] represents an alternative reconstruction method that integrates both tracking and calorimeter information. This technique works by first removing calorimeter energy deposits that correspond to extrapolated tracks, then combining the remaining topo-clusters with track data to form complete PFlow objects.

The algorithm handles several distinct cases: if a single charged particle matches with one topo-cluster, the cluster is entirely removed and replaced by the corresponding track information. For cases where particle showers distribute energy across multiple topo-clusters (typically two), the procedure identifies all related clusters before performing the subtraction, with tracks ultimately replacing the clusters as in the single-cluster scenario. Topo-clusters that show no track matches are preserved unchanged as they likely originate from neutral particles.

More complex situations occur when multiple particles contribute to a single topo-cluster; only the portions corresponding to charged particles are removed. The energy from charged particles is calculated through the formula:

$$\langle E_{\mathrm{dep}} \rangle = p^{\mathrm{trk}} \langle E_{\mathrm{ref}}^{\mathrm{clus}} / p_{\mathrm{ref}}^{\mathrm{clus}} \rangle, \tag{4.6}$$

where $E_{\text{ref}}^{\text{clus}}/p_{\text{ref}}^{\text{clus}}$ is the ratio of energy deposits to the momentum measured, determined from single pion samples. The final Particle Flow object is modified with the estimated energy replaced by the track.

The cluster energy reconstruction is performed by summing the energy deposits from individual calorimeter cells. Both the signal measurements and average noise levels for each cell are calibrated using the electromagnetic energy scale, which provides accurate energy reconstruction for electrons and photons. To account for the reduced calorimeter response to hadronic showers, the algorithm applies a *local hadronic cell weighting* (LCW) calibration procedure [54]. This correction compensates for the non-compensating nature of the calorimeter system when measuring hadronic energy deposits.

Clusters are classified as either electromagnetic or hadronic based on their characteristic energy deposition patterns observed in the calorimeter systems. The energy measurement of these clusters is subsequently calibrated using correction factors derived from detailed Monte Carlo simulations of single pion interactions, with additional validation from test-beam data. These corrections address three primary effects: the non-compensating response of the calorimeter to hadronic showers, signal losses caused by the noise thresholds inherent in the clustering algorithm, and energy deposition in passive detector materials. The moment-dependent correction framework ensures accurate energy reconstruction by systematically accounting for these detector-specific effects.

4.2 Electrons

The electron is an elementary particle and stable, belonging to the first generation of the lepton particle family, with a negative one elementary charge and an intrinsic angular momentum of a half-integer value and a mass of about $0.51\text{MeV}/c^2$.

The electron is involved in many decay processes and is measured as the final state of proton-proton collisions at the LHC. The reconstruction, identification and isolation of prompt electrons with a high efficiency is an important goal of the ATLAS detector, with the information mainly provided by the ID and EM calorimeters. Hence, the ability to effectively reconstruct electrons originating from the prompt decay of particles such as the Z boson, to identify them as such with high efficiency, and to isolate them from misidentified hadrons, electrons from photon conversions, and non-isolated electrons originating from heavy-flavour decays are all essential steps to a successful scientific programme.

The reconstruction and identification of the electron in the precise central region ($|\eta| < 2.47$) and the acceptance of the ID are considered in the thesis. Over the region devoted to precision measurements ($|\eta| < 2.47$, excluding the transition regions).

4.2.1 Electron Reconstruction

Electron signatures in the ATLAS detector comprise both charged particle tracks in the Inner Detector (ID) and energy deposits predominantly in the electromagnetic calorimeter (EMCal) [55, 56]. The electron reconstruction algorithm integrates three fundamental components: topo-cluster reconstruction in the EMCal, charged track identification in the ID, and precise $\eta \times \phi$ spatial matching between tracks and clusters. Reconstructed electron candidates must satisfy vertex compatibility requirements, including transverse impact parameter significance $d_0/\sigma_{d_0} < 5$ and longitudinal displacement $|z_0 \sin\theta| < 0.5$ mm, where σ_{d_0} quantifies the d_0 measurement uncertainty. The complete reconstruction chain is visualized in Figure 4.3, demonstrating the interplay between tracking and calorimetric components.

To reconstruct the electromagnetic clusters, the $\eta\times\phi$ space of the EM calorimeter is divided into a grid of 200×250 elements, referred to as *towers*, each with dimensions $\Delta\eta \times \Delta\phi = 0.025 \times 0.025$. The energy of each tower is the total energy collected in the presampler and the additional calorimeter layers. Electromagnetic-energy cluster candidates are seeded from localized energy deposits using a sliding-window algorithm [57] with a combined transverse energy exceeding 2.5 GeV. This algorithm clusters calorimeter cells within rectangles of size 3×5 towers in the $\eta - \phi$ space[1]. A removal algorithm is then applied to nearby seed clusters. Additionally, energy corrections account for leakages and fluctuations in the energy deposits.

[1]The cluster window is larger in ϕ than in η because the magnetic field bends charged particles in the $R - \phi$ plane, causing the resulting shower to spread more in that direction.

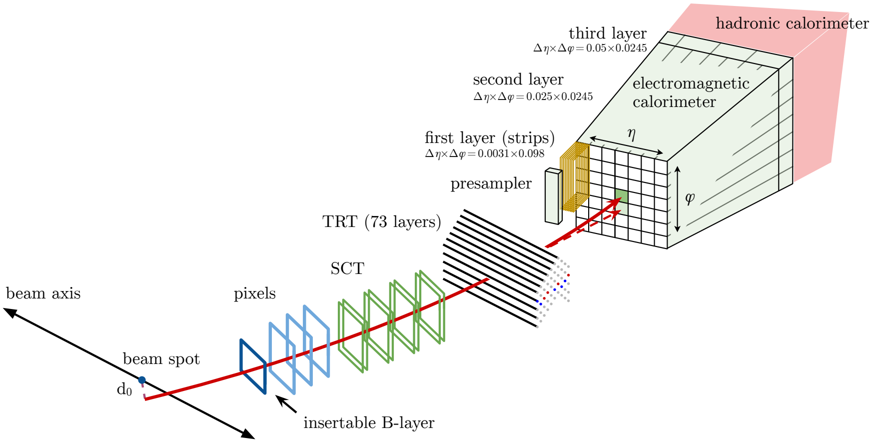

Figure 4.3: Schematic illustration of the path of an electron through the detector. The red trajectory shows the path of an electron, while the dashed red trajectory indicates the path of a photon produced by the interaction of the electron with the material of the tracking system [56].

4.2.2 Electron Identification

The electron reconstruction algorithm inevitably captures background objects alongside genuine prompt electrons. These background sources primarily include hadronic jets misidentified as electrons, photon conversions, and electrons from semileptonic decays of heavy-flavor hadrons. To distinguish signal electrons from these backgrounds, the electron identification algorithm [58] employs a likelihood-based (LH) technique that has served as the baseline method for Run-2 analyses.

This multivariate approach simultaneously evaluates multiple electron candidate properties through probability density functions constructed separately for signal and background hypotheses. The method computes a composite discriminant $d_{\mathcal{L}}$ representing the relative likelihood of an electron candidate being signal-like versus background-like. The discriminant takes the form:

$$d_{\mathcal{L}} = \frac{\mathcal{L}_S}{\mathcal{L}_S + \mathcal{L}_B}, \tag{4.7}$$

$$\mathcal{L}_{S(B)}(\vec{x}) = \prod_{i=1}^{n} P_{s(b),i}(x_i). \tag{4.8}$$

Here, $\vec{x}$ is the vector of discriminating variable values, while $P_{s(b),i}(x_i)$ is the probability function with the i^{th} variable, either for signal (s) or background (b), evaluated at x_i.

The electron identification employs three progressively stricter working points (WP) - *Loose*, *Medium*, and *Tight* - which share identical likelihood discriminant variables but apply increasingly stringent selection criteria to enhance background rejection. The identification efficiencies are measured in both data and simulation by computing the fraction of electrons passing each WP selection relative to those with matched tracks satisfying quality requirements. As shown in Figure 4.4, these efficiencies exhibit dependence on both the electron transverse energy (E_T) and pseudorapidity (η), with measurements derived from $Z \to ee$ events using the tag-and-probe technique [58]. Notably, the efficiency decreases in the transition from the barrel region ($|\eta| < 1.2$) to the end-caps. Physics analyses account for data-simulation discrepancies by applying scale factors derived from efficiency ratios.

4.2.3 Electron Isolation

The high-luminosity environment of proton-proton (p-p) collisions presents significant challenges for separating prompt electrons from background sources. To enhance background suppression, an isolation requirement is applied using dedicated variables that quantify the energy deposition near electron candidates.

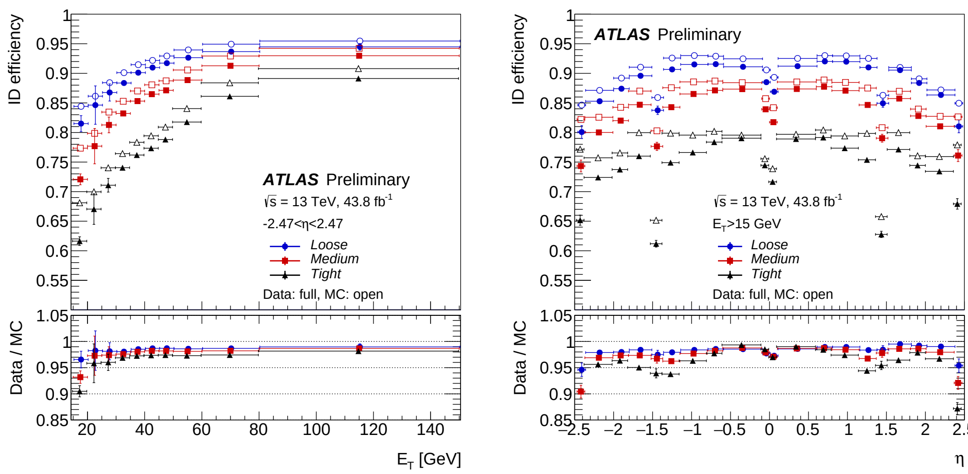

Figure 4.4: Electron identification efficiencies in $Z \to ee$ events as a function of transverse energy E_T (left) and as a function of pseudo-rapidity η (right). [59].

The algorithm employs two key discriminating variables [58]:

- Track-based isolation variable $p_T^{\text{varcone20}}$: Calculated by adding the transverse momentum p_T of selected tracks, where $p_T > 1$ GeV and $|\eta| < 2.5$, within a cone centered on the electron track direction, excluding the electron track itself. The cone size ΔR is defined as $\Delta R = \min\left(\frac{10}{p_{\mathrm{T}}[\mathrm{GeV}]}, 0.2\right)$;

- Calorimeter-based isolation variable $E_T^{\mathrm{topocone20}}$: Formed by summing the transverse energy of topological clusters within a cone of size $\Delta R = 0.2$ around the electron, while subtracting the energy contribution from the electron itself. This variable is sensitive to pile-up effects, underlying events, and potential leakages. Corrections are applied to address these effects.

Four electron isolation working points are defined and presented in Table 4.1.

working point	Calorimeter isolation	Track isolation
Gradient	$\epsilon = 0.11 * p_T + 92.14\%$ (with E_T^{cone20})	$\epsilon = 0.11 * p_T + 92.14\%$ (with $p_T^{varcone20}$)
HighPtCaloOnly	$E_T^{cone20} <$ max (0.015 x p_T, 3.5 GeV)	-
Loose	$E_T^{cone20}/p_T < 0.20$	$p_T^{varcone20}/p_T < 0.15$
Tight	$E_T^{cone20}/p_T < 0.06$	$p_T^{varcone20}/p_T < 0.06$

Table 4.1: Electron isolation working points.

4.3 Muons

The muon (μ) is an elementary particle described by the Standard Model. It carries an electric charge of $-1\,e$, has a spin of $\frac{1}{2}$, and a mass of $105.66\,\mathrm{MeV}/c^2$, which is approximately 207 times greater than that of the electron. The muon is unstable, with a mean lifetime of $2.2\,\mu$s, and its decay occurs via the weak interaction, which is why the decay is relatively slow. A muon can travel approximately 658 meters before decaying at rest. The reconstruction and identification of muons in the ATLAS detector are discussed in this section.

4.3.1 Muon Reconstruction

Muon reconstruction combines tracking information from both the Inner Detector (ID) and Muon Spectrometer (MS) [60]. The MS employs a χ^2 fitting algorithm using hit positions, while the ID reconstructs muon tracks identically to other charged particles. The final muon candidates are classified into four categories based on their reconstruction method:

Combined Muons (CB) Result from a global track fit incorporating hits from both ID and MS systems, providing the most precise momentum measurement.

Segment-Tagged Muons (ST) Identified through matching ID tracks with at least one MS segment after extrapolation. This method efficiently recovers low-p_T muons ($p_T < 5$ GeV) and those in regions with partial MS coverage.

Calorimeter-Tagged Muons (CT) Reconstructed by associating ID tracks with minimum-ionizing energy deposits in the calorimeters, particularly useful in non-instrumented MS regions.

Extrapolated Muons (ME) Derived from MS tracks with relaxed vertex constraints, extending coverage to $2.5 < |\eta| < 2.7$ beyond ID acceptance.

All muon candidates must satisfy vertex compatibility requirements: $|d_0/\sigma_{d_0}| < 3$ and $|\Delta z_0 \sin\theta| < 0.5$ mm relative to the primary vertex.

4.3.2 Muon Identification

Prompt muons are distinguished from those originating from pion and kaon decays using specific identification criteria. Muon candidates resulting from charged hadron decays in the Inner Detector can be identified by examining the poor fit quality of the combined track and inconsistencies between the momentum measurements in the ID and the Muon Spectrometer. To further differentiate between muons produced in hard scattering events and those from semi-leptonic decays, particularly within hadronic jets, isolation criteria and cuts on the impact parameters d_0 and z_0 are applied.

Muon identification is performed through a cut-based approach with three distinct selections: *Loose*, *Medium*, and *Tight*, each providing increasing rejection power against pion and kaon decays. The identification efficiency for muons in the transverse momentum range $20\,\text{GeV} < p_T < 100\,\text{GeV}$ and $|\eta| < 2.5$ is approximately 98%, 96%, and 92% for the Loose, Medium, and Tight requirements, respectively [61], as illustrated in Fig. 4.5. These measurements are obtained using the tag-and-probe method [60] on $Z \to \mu\mu$ events. The efficiency for the Medium and Tight working points decreases in the region around $\eta \sim 0$, where the MS has partial coverage with muon chambers.

4.3.3 Muon Isolation

Similar to electrons, muon isolation criteria are imposed to suppress non-prompt muon backgrounds. Three distinct variables [60] are utilized for isolation:

Calorimeter isolation: The parameter $E_T^{\text{cone}0.2}$ quantifies the total transverse energy of topological clusters within a cone of $\Delta R = 0.2$ around the muon candidate.

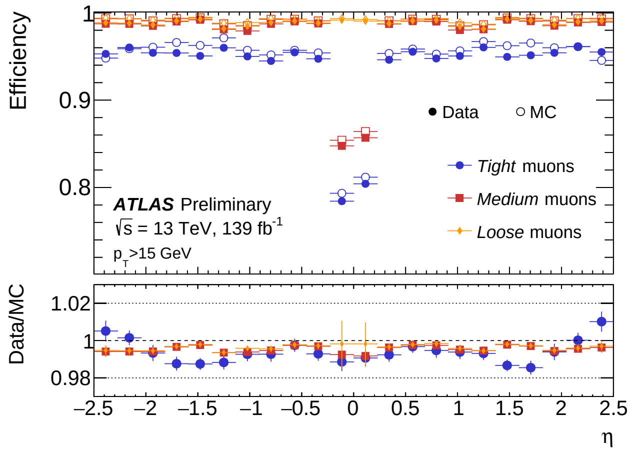

Figure 4.5: The muon identification efficiencies for the Loose, Medium, and Tight identification algorithms is measured in $Z \to \mu\mu$ events as a function of η_{muon} with $p_\mathrm{T} > 15$ GeV. The bottom panel displays the ratio between expected and observed efficiencies [61].

Track Isolation Criteria: Two complementary isolation measures are employed:

- **Adaptive cone isolation** ($p_T^{\text{varcone}0.3}$): Sum of track p_T within $\Delta R = \min(0.3,\ 10\ \text{GeV}/p_T^\mu)$
- **Fixed cone isolation** ($p_T^{\text{cone}0.2}$): Sum of track p_T within $\Delta R = 0.2$

where p_T^μ denotes the muon transverse momentum and $\Delta R \equiv \sqrt{(\Delta\eta)^2 + (\Delta\phi)^2}$ is the angular distance metric.

The efficiency of muon isolation is assessed through the tag-and-probe method. Seven distinct working points are specified, with further details summarized in Table 4.2. The calibration of isolation efficiency is performed using $Z \to \mu\mu$ events with $\Delta R_{\mu\mu} > 0.3$, as depicted in Figure 4.6.

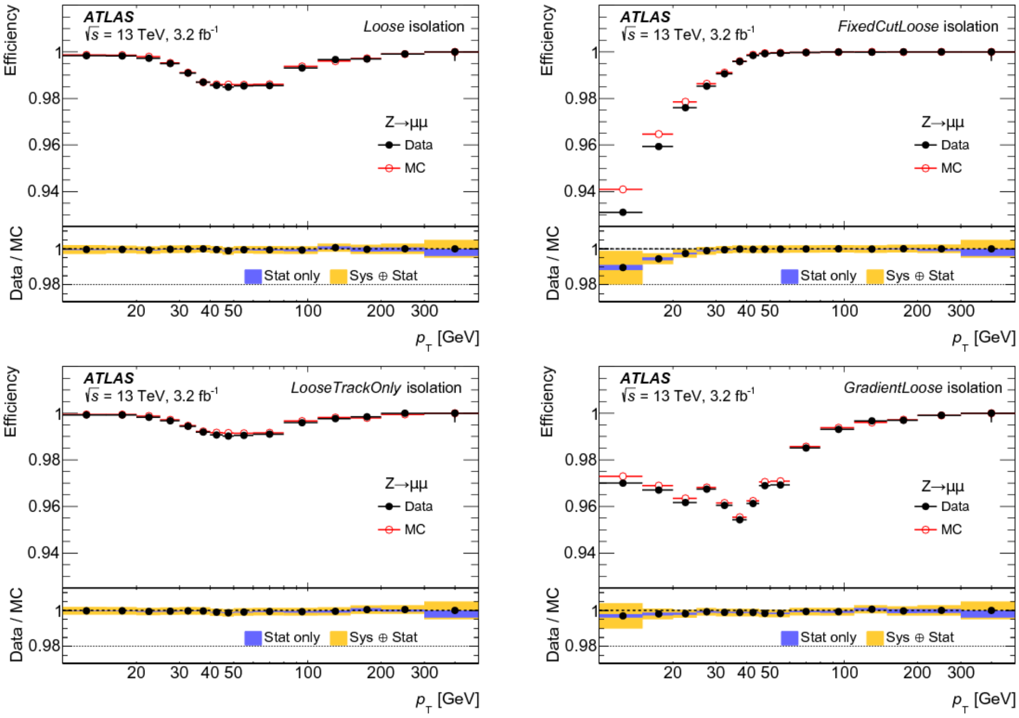

Figure 4.6: Isolation efficiencies for muons at different working points [60].

Isolation WP	Discrimination	Definition
LooseTrackOnly	$p_T^{varcone30}/p_T$	99% efficiency constraint in η and p_T
Loose	$p_T^{varcone30}/p_T$, E_T^{cone20}/p_T	99% efficiency constraint in η and p_T
Tight	$p_T^{varcone30}/p_T$, E_T^{cone20}/p_T	99% efficiency constraint in η and p_T
Gradient	$p_T^{varcone30}/p_T$, E_T^{cone20}/p_T	$\geq 90(99\%)$ efficiency at 25 (60) GeV
GradientLoose	$p_T^{varcone30}/p_T$, E_T^{cone20}/p_T	$\geq 90(99\%)$ efficiency at 25 (60) GeV
FixedCutTightTrackOnly	$p_T^{varcone30}/p_T$	$p_T^{varcone30}/p_T < 0.06$
FixCutLoose	$p_T^{varcone30}/p_T$, E_T^{cone20}/p_T	$p_T^{varcone30}/p_T < 0.15$, $E_T^{cone20}/p_T < 0.30$

Table 4.2: Definition of the seven isolation working points. The discriminating variables are listed in the second column and the criteria used in the definition are reported in the third column. [60].

4.4 Jets

In a hadron collider, quarks and gluons rapidly undergo fragmentation and hadronization upon production. The resultant particles appear as collimated sprays of tracks and energy deposits in the calorimeter, commonly known as jets. Two categories of jets are reconstructed: calorimeter jets and track jets, both employing the anti-k_t algorithm [62]. For calorimeter jets, the algorithm utilizes topo-clusters or PFlow objects as inputs, whereas for track jets, tracks serve as the inputs. The subsequent section elaborates on the procedures for jet reconstruction and calibration.

4.4.1 Jet Reconstruction

Calibrated clusters and tracks are used as inputs for the jet reconstruction algorithm. The anti-k_t algorithm determines clustering based on the distance measure d_{ij} between two objects i and j, as well as the distance d_{iB} between an object i and the beam B, defined as:

$$d_{ij} = \min\left(k_{ti}^{2p}, k_{tj}^{2p}\right) \cdot \Delta R_{ij}^2, \tag{4.9a}$$

$$d_{iB} = k_{ti}^{2p} \cdot R_i^2, \tag{4.9b}$$

where ΔR_{ij} represents the angular distance between two objects i and j, defined as

$$\Delta R_{ij} = \sqrt{(\eta_i - \eta_j)^2 + (\phi_i - \phi_j)^2}. \tag{4.10}$$

Here, $k_{t_{i/j}}$, $\eta_{i/j}$, and $\phi_{i/j}$ denote the transverse momenta, rapidity, and azimuthal angles of particles i and j, respectively. The parameter R_i corresponds to the radius parameter of object i. The exponent p regulates the balance between energy and geometrical scales. The anti-k_t algorithm is specified by $p = -1$, while the cases $p = 0$ and $p = 1$ correspond to the inclusive Cambridge/Aachen algorithm and the k_t algorithm, respectively [63].

The implementation of the anti-k_t algorithm proceeds through the following steps:

1. Compute d_{iB} and all d_{ij} distances.

2. Identify the smallest of the distances:

- If the smallest distance is d_{ij}, merge objects i and j into a single new object.
- If the smallest distance is d_{iB}, consider i to be a jet and remove it from the list of objects.

3. Repeat the procedure until all the clusters/tracks are clustered into jets.

Once this clustering procedure is completed, the jet's four-momentum is obtained as the sum of the four-momenta of the clusters/tracks.

4.4.2 Jet Calibration

Jet energy calibration addresses two key requirements: (1) correcting the reconstructed jet energy scale (JES) to match the truth-particle level, and (2) reconciling differences between data and Monte Carlo (MC) simulations. The calibration procedure involves four sequential steps:

1. Jet direction correction to align with the primary vertex
2. Pile-up mitigation through area-based subtraction
3. MC-derived energy calibration
4. In situ correction using data-driven techniques

The in situ calibration utilizes well-measured standard processes:

- Z+jets events for jets with $20 < p_T < 500$ GeV
- γ+jets events for jets with $36 < p_T < 950$ GeV
- Multi-jet balance techniques for high-p_T jets (950 GeV$< p_T < 2$ TeV)

The calibration exploits the transverse momentum balance between the well-modeled γ/Z boson decay products and the recoiling jet system. For the highest-p_T jets, the calibration employs a system of reference jets with lower transverse momenta.

4.4.3 Jets Cleaning and Pile-up Removal

The jet cleaning tool [64] is designed to classify jets based on their origin. Additionally, the jet-vertex-tagger (JVT) method [65] employs a combination of two track-based variables to further suppress pile-up jets.

Three working points are defined for jets within $|\eta| < 2.4$ and $20 < p_T < 60$ GeV. The corresponding cut values and the average efficiencies for hard-scatter jets are provided in Table 4.3.

Working Points	JVT Cut	Hard scatter jets average efficiency
Loose	> 0.11	97%
Medium	> 0.59	92%
Tight	> 0.91	85%

Table 4.3: Summary of the cut values and average efficiencies for the different Jet Vertex Tagger working points.

Forward Jet Vertex Tagging: The standard JVT method is inapplicable to forward jets ($2.5 < |\eta| < 4.5$) due to limited tracking coverage. For these jets with $p_{\mathrm{T}} < 120$ GeV, a dedicated forward Jet Vertex Tagger (fJVT) [66] is employed. Two working points have been optimized for jets in the $20 < p_{\mathrm{T}} < 50$ GeV range:

Table 4.4: Performance characteristics of forward Jet Vertex Tagger working points, showing selection efficiencies for hard-scatter and pile-up jets.

Working Point	fJVT Cut	Hard-Scatter Eff.	Pile-up Rejection
Loose	< 0.5	92%	40%
Tight	< 0.4	85%	50%

4.4.4 Flavour Tagging

Jets play a fundamental role in proton-proton collisions. The identification of b-jets, referred to as b-tagging, exploits the unique properties of b-quarks. These properties include their relatively large mass (~ 5 GeV), long lifetime (~ 1.5 ps), and high decay multiplicity, typically producing around five charged particles. As a result, b-jets frequently contain at least one *secondary vertex* that is spatially displaced from the *primary vertex*, as illustrated in Figure 4.7. Additionally, muons originating from the semileptonic decays of b- and c-hadrons provide a distinct signature that enhances the performance of b-tagging.

Flavor tagging algorithms exploit these features to efficiently differentiate b-jets from jets initiated by light-flavor hadrons. The low-level b-tagging algorithms encompass secondary vertex-based methods (SV1, JetFitter), impact parameter-based approaches (IP2D, IP3D, and RNNIP), and the Muon-based algorithm. Each of these low-level taggers targets specific characteristics to optimize the identification of b-jets while maintaining discrimination against c-jets and light-flavor jets.

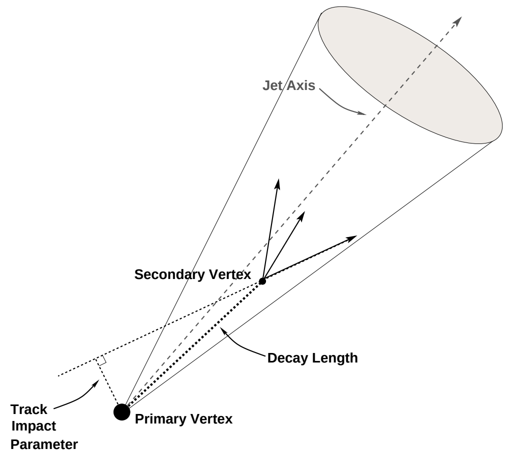

Figure 4.7: Illustration of a b-hadron decay within a jet. [67].

- **IP2D/IP3D/RNNIP** [68] These algorithms are based on impact parameter measurements. IP2D utilizes the significance of the transverse impact parameter along with charge information, whereas IP3D extends this by incorporating both transverse and longitudinal impact parameter significance. The RNNIP tagger, a Recurrent Neural Network Impact-Parameter tagger, exploits correlations among tracks within the jet to enhance b-jet identification.

- **SV1** [69] This algorithm identifies secondary vertices by reconstructing vertex candidates from tracks that do not originate from the decays of long-lived particles, photon conversions, or interactions with detector material. The optimal secondary vertex is selected using a χ^2 minimization fit.

- **Jet Fitter** [70] A multi-vertex algorithm that employs a topological approach to reconstruct the full decay chain of a b-quark. It adapts the

Kalman filter technique to model weak decay chains such as $b \to c \to s$. This method reconstructs multiple vertices, even in cases where only a single track is available.

- **Soft Muon Tagger (SMT)** [71] This tagger identifies b-jets by leveraging the presence of muons originating from the semileptonic decays of heavy-flavor hadrons. The frequency of muons in b-jets is significantly higher compared to c-jets and light-flavor jets, mainly due to the substantial semileptonic decay branching ratios of b-hadrons ($BR(b \to \mu\nu X) \approx 11\%$) and secondary c-hadrons from b-hadron decays (sequential semileptonic decay, $BR(b \to c \to \mu\nu X) \approx 10\%$). The associated muon variables provide strong discriminating power for rejecting light-flavor jets.

DL1 tagger

To improve the flavor-tagging performance in Run-2, deep-learning classifiers are employed to combine the output quantities from low-level tagging algorithms. These classifiers, based on neural networks (NN), constitute the DL1 algorithm series. The training of these algorithms utilizes a hybrid dataset composed of 70% jets from $t\bar{t}$ events and 30% from $Z' \to q\bar{q}$ events.

The DL1 algorithm takes as inputs the outputs from the IP2D, IP3D, SV1, and JetFitter algorithms. An extended version, DL1r, further incorporates the jet RNNIP output to enhance discrimination performance. Additionally, jet kinematic properties, such as p_{T} and $|\eta|$, are included in the training process.

The final DL1r output discriminant is constructed by combining the probabilities for b-jets, c-jets, and light-flavor jets:

$$D_{DL1r} = \ln\left(\frac{p_b}{f_c \cdot p_c + (1 - f_c) \cdot p_u}\right), \tag{4.11}$$

where p_b, p_c, and p_u represent the probabilities for b-jets, c-jets, and light-flavor jets, respectively, and f_c denotes the effective c-jet fraction in the background hypothesis. The outputs of the DL1r b-tagging algorithm are depicted in Figure 4.8. Four operating points, corresponding to different b-jet efficiencies (60%, 70%, 77%, and 85%), are defined using different cut values, as listed in Table 4.5.

The performance of b-tagging algorithms is evaluated using both Monte Carlo simulations and real collision data. Data-to-simulation scale factors (SFs) are measured as a function of jet transverse momentum (p_T) in dedicated calibration analyses, utilizing data samples enriched in b-, c-, or light-flavor jets [72–76]. These SFs correct for discrepancies in the detector modeling and the description of underlying physics processes in the MC simulation.

The DL1r b-tagging efficiency SFs, shown in Figure 4.9, are specifically for $R = 0.4$ PFlow jets or VR track jets.

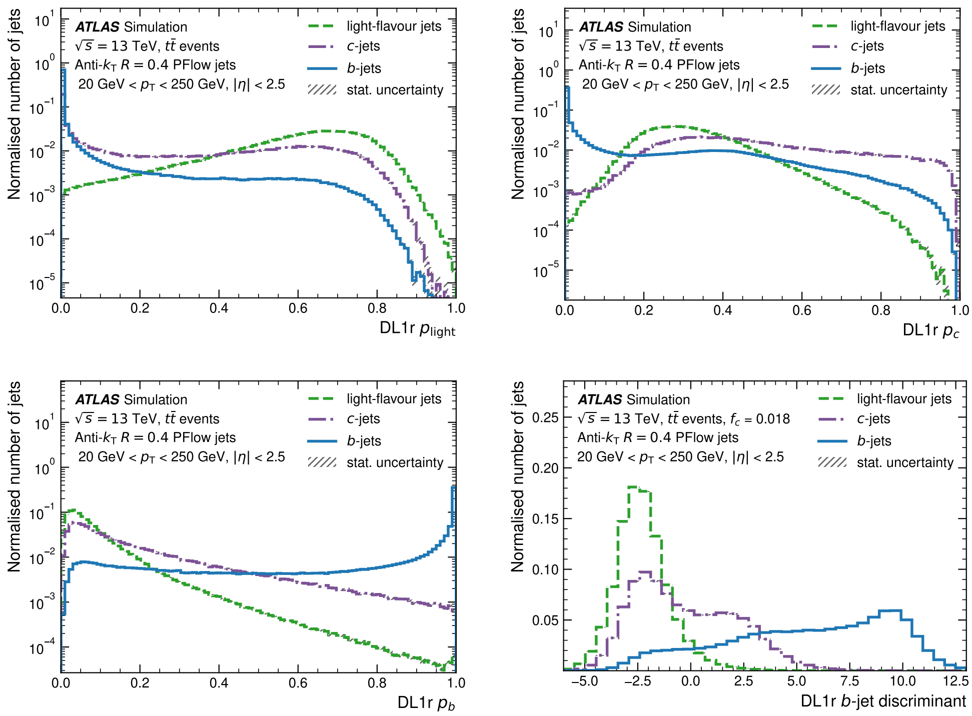

Figure 4.8: Distributions of the outputs of the DL1r b-tagging algorithm for b-jets, c-jets and light-flavour jets in $t\bar{t}$ simulated events: p_u (top left), p_c (top right), p_b (bottom left), and D_{DL1r} (bottom right).

Working point	60%	70%	77%	85%
Threshold value	2.97	1.83	1.07	0.08

Table 4.5: The DL1r tagger threshold values for all WPs with $f_c = 0.08$.

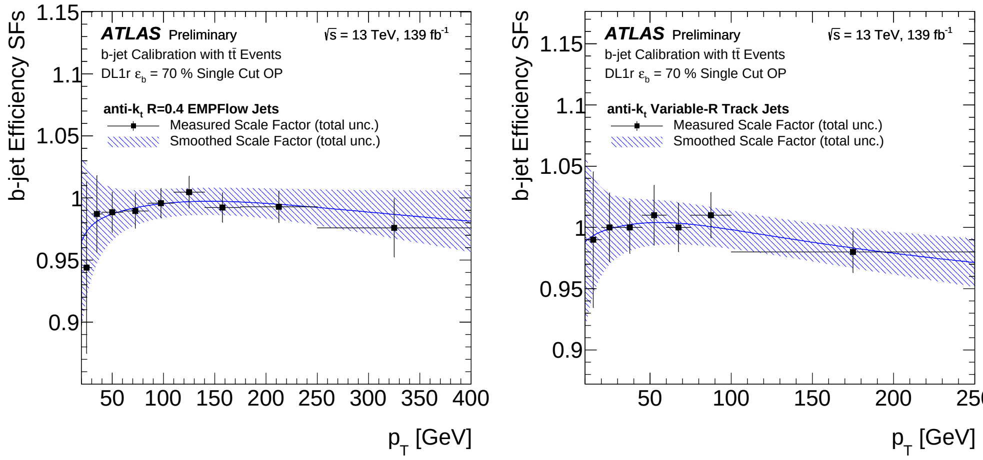

Figure 4.9: PFlow jets (left) and VR jets (right) efficiency scale factors for DL1r tagger at 70% working point[77].

4.5 Missing Transverse Momentum

The missing energy can arise from multiple sources, such as non-interacting particles like neutrinos, particles beyond the Standard Model (BSM), mis-reconstructed objects due to detector inefficiencies or poor resolution, and particles that are not reconstructed because they travel outside of the acceptance of the ATLAS detector. Since the initial beam has zero or negligible transverse momentum, the transverse missing energy, denoted as E_T^{miss}, represents the missing energy and is reconstructed indirectly by applying the law of conservation of energy or momentum in the transverse plane (the x-y plane).

$$\begin{aligned} E_{x(y)}^{\text{miss}} &= -\sum_{\text{Hard Objects}} E_{x(y)}^{\text{miss}} - \sum_{\text{SoftTerms}} E_{x(y)}^{\text{miss}}, \\ E_T^{\text{miss}} &= \sqrt{(E_x^{\text{miss}})^2 + (E_y^{\text{miss}})^2}. \end{aligned} \tag{4.12}$$

The E_T^{miss} is computed as the magnitude of the negative vector sum of the hard objects and the remaining soft terms. The hard objects include reconstructed particles such as electrons, muons, photons, τ-leptons, and jets. The soft terms include the tracks and clusters that are not used. The missing transverse energy is defined as:

$$E_T^{\text{miss}} = -\sum_{\text{sel. } e} p_T^e - \sum_{\text{acc. } \gamma} p_T^\gamma - \sum_{\text{acc. } \tau} p_T^{\tau_{\text{had}}} - \sum_{\text{sel. } \mu} p_T^\mu - \sum_{\text{acc. } j} p_T^{\text{jet}} - \sum_{\text{unus. trk}} p_T^{\text{track}}. \tag{4.13}$$

Chapter 5 Search for heavy right-handed Majorana neutrinos in $t\bar{t}$ decays with the ATLAS detector

This chapter presents the main analysis of this thesis, focusing on the search for heavy neutral leptons (HNL) in the $t\bar{t}$ process. Section 5.1 describes the data and Monte Carlo samples used in the HNL analysis. The general object selection criteria have already been described in Chapter 4, while Section 5.2 details the specific object and event selection criteria applied in this study. As discussed in Section 5.3, selected events are categorized into different regions. Section 5.4 introduces the multivariate analysis employed in the HNL search. A comprehensive estimation of different sources of systematic uncertainties is provided in Section 5.5, followed by a discussion of the statistical treatment in Section 5.6. Finally, the results are presented in Section 5.7.

5.1 Data and Simulated Samples

The search is based on the pp collision data recorded by the LHC at $\sqrt{s}$ = 13 TeV, collected with the ATLAS detector. Data quality criteria are applied to ensure that all detector components are fully operational [78]. The resulting dataset corresponds to an integrated luminosity of 140 fb^{-1}, complemented by measurements from the inner detector and calorimeters [79].

Simulated Monte Carlo events are used to model both the signal and the SM backgrounds. Detector effects are incorporated through a simulation of the ATLAS detector [80] obtained with the Geant4 program [81], or via a faster method using parameterized showers in the calorimeter. The impact of additional pp collisions from the same or nearby bunch crossings (pile-up) is modeled by overlaying minimum bias events, simulated using Pythia 8.1 [82] with the A3 tune, onto hard-scatter events [83]. MC events are reweighted to match the observed distribution of the average number of interactions per bunch crossing in the data.

All samples simulated with Powheg Box [84–87] and MadGraph5_aMC@NLO [88] are interfaced to Pythia 8 for parton showering, fragmentation, and the underlying event simulation, using the A14 tune [89] and the NNPDF2.3LO [90] parton distribution function set. Samples using PYTHIA 8 and HERWIG 7 [91, 92] model heavy-flavor hadron decays with EVTGEN [93]. The masses of the top quark and the Higgs boson are set to $m_t = 172.5$ GeV and $m_H = 125$ GeV, respectively. Both data and simulated events are processed with the same reconstruction and analysis algorithms.

5.1.1 Signal modelling

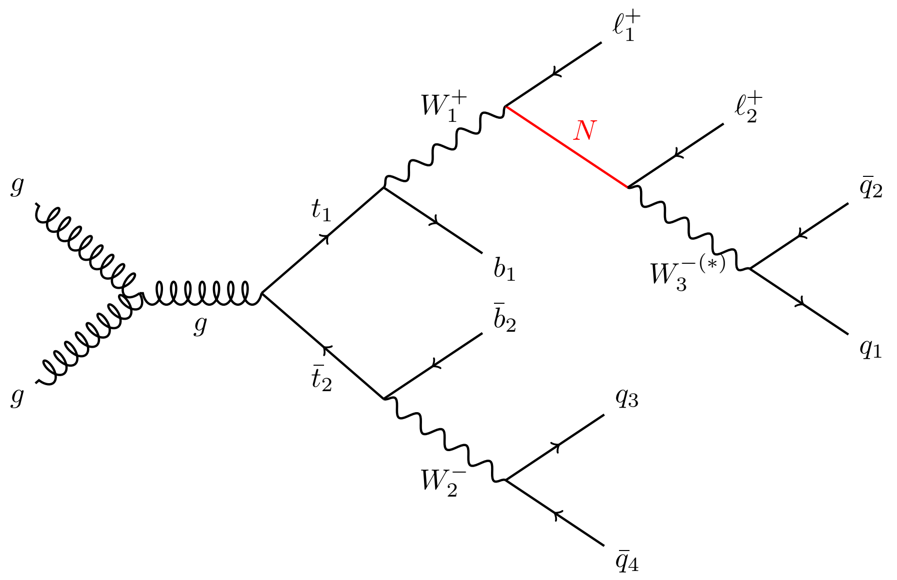

Figure 5.1: Feynman diagram of a possible heavy neutrino production process in proton-proton collisions. The diagram includes gluons (g), top quarks ($t_1, \bar{t}_2$), bottom quarks ($b_1, \bar{b}_2$), charged leptons (ℓ_1^+, ℓ_2^+), W bosons (W_1^+, W_2^-, W_3^- is a off-shell boson), a heavy right-handed Majorana neutrino (N, in red), and final-state quarks ($q_1, q_2, q_3, \bar{q}_4$).

Figure 5.1 shows an example Feynman diagram of the signal process, with the final state used in this search. The signal represents a Beyond the Standard Model process and is simulated using an extension of the Minimal Standard Model. This model is implemented as a Universal FeynRules Output (UFO) model called HEAVYN [94].

A simplified benchmark model is assumed that proposes a single HNL candidate N, which couples with either electrons, muons, or τ-leptons through a mixing with the corresponding neutrinos. In this model, the mass m_N and couplings $V_{\ell,N}$ of this new particle are free parameters. These couplings can be expressed through a mixing matrix,

$$V_{\ell,N} = \begin{pmatrix} V_{e,N} & 0 & 0 \\ 0 & V_{\mu,N} & 0 \\ 0 & 0 & V_{\tau,N} \end{pmatrix}, \tag{5.1}$$

where only one of the three diagonal terms can be non-zero at a time.

The width of the HNL is automatically computed by the MadGraph5_aMC@NLO generator, which provides matrix elements at next-to-leading order in QCD using the NNPDF3.0nlo [95] PDF set, and uses the five-flavor scheme. The QCD factorization (μ_{F}) and renormalization (μ_{R}) scales are set to be equal [96], given by the dynamical expression $\frac{1}{4}\sum_i \sqrt{m_i^2 + p_{\mathrm{T},i}^2}$, where the sum runs over all the particles generated in the matrix element calculation, and the mass and transverse momentum of each particle are denoted by m_i and $p_{\mathrm{T},i}$, respectively.

The decay of the top quarks is simulated using the MadSpin [97, 98] module, allowing three-body off-shell decays. The parton shower, the hadronization, and the decay of the τ-leptons are simulated using Pythia 8 with the A14 set of tuned parameters.

Two other dynamical scales are tested again using the three mass points (HNL15, HNL45, HNL75) to cover the low/middle/high regimes. These scales are $H_T/2$ and $m_t + H_T/2$, and they yield about 10-12% uncertainty whereas the chosen scale of $H_T/4$ yields a smaller uncertainty of 5–9% as shown in Figure 5.2. The decay of top quarks has been achieved using the MadSpin module with the ”set spinmode=none” option, which allows for 3-body off-shell decays. MadSpin calculates widths at LO, therefore, it is recommended to set the NLO width for the W boson by hand to avoid the LO precision given by MadSpin. This method is implemented. Parton shower and hadronization steps are achieved by interfacing generated events with Pythia 8.244 using the A14 set of tuned parameters.

A validation study has been conducted by creating an SM $t\bar{t}$ single lepton sample by turning off the BSM parameters and comparing it to an ATLAS reference $t\bar{t}$ sample (DSID: 410464, MG5 + PY8). However, at the time of these studies, there were no SM $t\bar{t}$ samples available, generated with the same Athena release (21.6). Therefore, samples from release 19.2 were used. Good agreement between the distributions is observed.

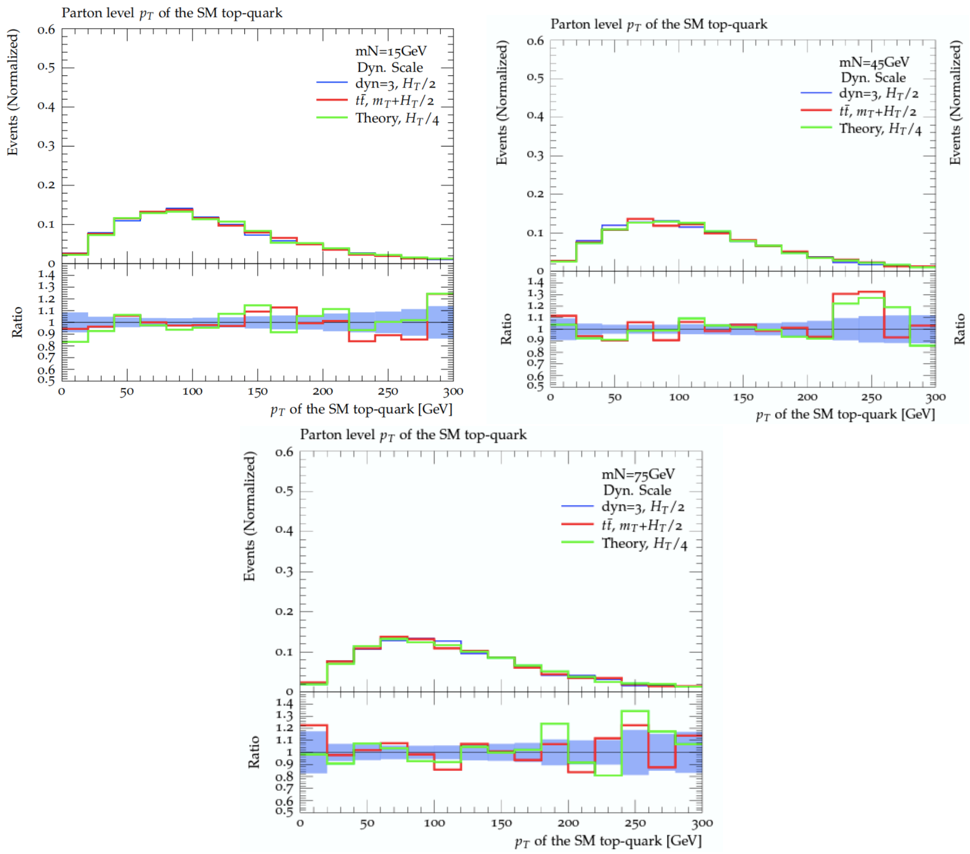

Figure 5.2: The comparison between different dynamical scale choices for the top transverse momentum (p_{T}) distribution. The selected choice for the dynamical scale (based on theory) is $H_T/4$, while the other two choices are $H_T/2$ (dyn=3 choice) and $m_t + H_T/2$ ($t\bar{t}$ choice). In comparison to the $H_T/2$ and $m_t + H_T/2$ choices, the $H_T/4$ scale demonstrates a smaller uncertainty. The HNL15 (top left), HNL45 (top right), and HNL75 (bottom) have been tested to cover the low/middle/high regimes.

Signal samples

Table 5.1 shows the list of signal simulation samples. The signal samples are generated with AltFastII (AFII) simulation at different mass points: 15, 25, 35, 40, 45, 50, 55, 60, 70, 75 GeV.

Our analysis specifically targets the final states with two same-sign, same-flavor leptons. However, during the reconstruction and simulation processes, we take into account all possible decays of the W bosons involving leptons from both the top Standard Model decay leg and the top Beyond Standard Model leg sides. This comprehensive consideration is necessary because some leptons may not be successfully reconstructed or may fail to pass the pre-selection criteria. As a result, only the two leptons that pass the pre-selection are retained for further analysis.

5.1.2 Background processes

Samples of events generated using Monte Carlo simulations were produced using different event generators interfaced to various shower/hadronization generators within the MC16a/d/e (for 2015 + 2016, 2017, and 2018 datasets) production campaigns.

Considering the signal process and the final states described in the previous section, we required two same-sign same-flavor leptons, two b-tagging jets, and four light jets to select the signal events. So there are those known physics processes that can mimic the process that interests this search. These processes, known as backgrounds, are simulated with some accuracy and since this analysis is statistically limited, we trusted these simulations to evaluate the known component of our data. The main backgrounds are $t\bar{t}$, $t\bar{t}Z$, $t\bar{t}W$, $t\bar{t}\gamma$, and $t\bar{t}H$ and account for more than 85% of events surviving the selection.

The $t\bar{t}$ process is simulated with Powheg-Box v2, a next-to-leading order matrix element generator [85–87] with the NNPDF3.0 NLO PDF set. This generator was then interfaced with Pythia8 (v8.210) with the NNPDF2.3 LO PDF set and the A14 tune for parton shower, hadronization, and underlying event modelling. In the Powheg configuration, the h_{damp} parameter, which gives a cut-off scale for the first gluon emission, was set to $\frac{3}{2}m_t$, where the m_t is the mass of the top quark. And the factorisation and renormalisation scales were set to $\mu_F = \mu_R = \sqrt{m_t^2 + p_{\mathrm{T},t}^2}$, where the top quark pT is evaluated before radiation [99].

The associated production of a top-quark-antiquark pair with a leptonically decaying Z boson is modelled using the MadGraph5_aMC@NLO v2.8.1 generator, which provides matrix elements at next-to-leading order in the strong coupling constant α_{s} with the NNPDF3.0NLO PDF set. The functional form of the renormalization and factorization scales (μ_{r}, μ_{f}) is set to the default scale $0.5 \times \sum_i \sqrt{m_i^2 + p_{T,i}^2}$, where the sum runs over all the particles generated from the matrix element calculation. Top quarks are decayed at LO using MADSPIN [97, 98] to preserve all spin correlations. The top-quark mass is set to 172.5 GeV. The events are interfaced with Pythia8 (v8.244) [100] for the parton shower and hadronization, using the A14 set of tuned parameters and the NNPDF2.3LO

DSID	name	full-name
503947	HNL15m	aMCPy8EG_A14NNPDF3NLO_ttbar_HNL_ML_m_15
503948	HNL15p	aMCPy8EG_A14NNPDF3NLO_ttbar_HNL_ML_p_15
507680	HNL25m	aMCPy8EG_A14NNPDF3NLO_ttbar_HNL_ML_m_25
507681	HNL25p	aMCPy8EG_A14NNPDF3NLO_ttbar_HNL_ML_p_25
503949	HNL35m	aMCPy8EG_A14NNPDF3NLO_ttbar_HNL_ML_m_35
503950	HNL35p	aMCPy8EG_A14NNPDF3NLO_ttbar_HNL_ML_p_35
503951	HNL40m	aMCPy8EG_A14NNPDF3NLO_ttbar_HNL_ML_m_40
503952	HNL40p	aMCPy8EG_A14NNPDF3NLO_ttbar_HNL_ML_p_40
503953	HNL45m	aMCPy8EG_A14NNPDF3NLO_ttbar_HNL_ML_m_45
503954	HNL45p	aMCPy8EG_A14NNPDF3NLO_ttbar_HNL_ML_p_45
503955	HNL50m	aMCPy8EG_A14NNPDF3NLO_ttbar_HNL_ML_m_50
503956	HNL50p	aMCPy8EG_A14NNPDF3NLO_ttbar_HNL_ML_p_50
503957	HNL55m	aMCPy8EG_A14NNPDF3NLO_ttbar_HNL_ML_m_55
503958	HNL55p	aMCPy8EG_A14NNPDF3NLO_ttbar_HNL_ML_p_55
503959	HNL60m	aMCPy8EG_A14NNPDF3NLO_ttbar_HNL_ML_m_60
503960	HNL60p	aMCPy8EG_A14NNPDF3NLO_ttbar_HNL_ML_p_60
503961	HNL70m	aMCPy8EG_A14NNPDF3NLO_ttbar_HNL_ML_m_70
503962	HNL70p	aMCPy8EG_A14NNPDF3NLO_ttbar_HNL_ML_p_70
503963	HNL75m	aMCPy8EG_A14NNPDF3NLO_ttbar_HNL_ML_m_75
503964	HNL75p	aMCPy8EG_A14NNPDF3NLO_ttbar_HNL_ML_p_75
508692	HNLlep15m	aMCPy8EG_A14NNPDF3NLO_ttbar_HNLfullLep_ML_m_15
508693	HNLlep15p	aMCPy8EG_A14NNPDF3NLO_ttbar_HNLfullLep_ML_p_15
508694	HNLlep25m	aMCPy8EG_A14NNPDF3NLO_ttbar_HNLfullLep_ML_m_25
508695	HNLlep25p	aMCPy8EG_A14NNPDF3NLO_ttbar_HNLfullLep_ML_p_25
508696	HNLlep35m	aMCPy8EG_A14NNPDF3NLO_ttbar_HNLfullLep_ML_m_35
508697	HNLlep35p	aMCPy8EG_A14NNPDF3NLO_ttbar_HNLfullLep_ML_p_35
508698	HNLlep40m	aMCPy8EG_A14NNPDF3NLO_ttbar_HNLfullLep_ML_m_40
508699	HNLlep40p	aMCPy8EG_A14NNPDF3NLO_ttbar_HNLfullLep_ML_p_40
508700	HNLlep45m	aMCPy8EG_A14NNPDF3NLO_ttbar_HNLfullLep_ML_m_45
508701	HNLlep45p	aMCPy8EG_A14NNPDF3NLO_ttbar_HNLfullLep_ML_p_45
507673	HNLlep50m	aMCPy8EG_A14NNPDF3NLO_ttbar_HNLfullLep_ML_m_50
507674	HNLlep50p	aMCPy8EG_A14NNPDF3NLO_ttbar_HNLfullLep_ML_p_50
508702	HNLlep55m	aMCPy8EG_A14NNPDF3NLO_ttbar_HNLfullLep_ML_m_55
508703	HNLlep55p	aMCPy8EG_A14NNPDF3NLO_ttbar_HNLfullLep_ML_p_55
508704	HNLlep60m	aMCPy8EG_A14NNPDF3NLO_ttbar_HNLfullLep_ML_m_60
508705	HNLlep60p	aMCPy8EG_A14NNPDF3NLO_ttbar_HNLfullLep_ML_p_60
508706	HNLlep70m	aMCPy8EG_A14NNPDF3NLO_ttbar_HNLfullLep_ML_m_70
508707	HNLlep70p	aMCPy8EG_A14NNPDF3NLO_ttbar_HNLfullLep_ML_p_70
508708	HNLlep75m	aMCPy8EG_A14NNPDF3NLO_ttbar_HNLfullLep_ML_m_75
508709	HNLlep75p	aMCPy8EG_A14NNPDF3NLO_ttbar_HNLfullLep_ML_p_75

Table 5.1: For each signal mass point, the ”m”, ”p” tag mean the two different decay syntaxes of (-,-) and (+,+) for the two same-sign leptons sharing the vertex with HNL. The additional ”lep” tag is used to distinguish the hadronic or leptonic decay W boson coming from the Standard Model decay leg.

PDF set. The decays of bottom and charm hadrons are simulated using the EVTGEN 1.7.0 program.

For top-quark-antiquark pair production with a W boson ($t\bar{t}W$), the Sherpa 2.2.10 generator and default parton shower are used at NLO accuracy in QCD, with multi-leg merging of up to 1 additional parton at NLO and up to 2 additional partons at LO (MEPS@NLO setup with a merging scale of 30 GeV). Additionally, a LO EW sample also generated with Sherpa 2.2.10 but for the $t\bar{t}Wj$ final state is used to emulate electroweak corrections to $t\bar{t}W$ production. Following the recommendations of the LHC Top and Higgs Working Groups, the cross sections of these QCD and EWK $t\bar{t}W$ samples are scaled separately to the reference predictions of Ref. [101] (corresponding to cross section of $674.7\,\text{fb}^{-1}$ and $47.7\,\text{fb}^{-1}$, respectively).

The $t\bar{t}\gamma$ process was generated with MadGraph_aMC@NLO v2.3.3.p1 tool and the parton shower used Pythia8 (v8.212). An overlap removal was implemented based on the procedure used by the charge asymmetry analysis of the $t\bar{t}\gamma$ process [102].

Two different $t\bar{t}H$ samples are used, one corresponding to semileptonic Higgs-boson decays, the other to dileptonic Higgs-boson decays. All $t\bar{t}H$ samples are generated at NLO with POWHEG with the NNPDF3.0 NLO PDF set [95]. The Higgs-boson decay, as well as hadronisation, parton shower, and the underlying event, are simulated with PYTHIA 8.

In addition, we also consider the "Electroweak" background composed of the processes V+jets, diboson (VV), and triboson (VVV).

V+jets: The production of V+jets is simulated with the Sherpa 2.2.1 [103] generator using NLO-accurate matrix elements for up to two jets, and LO-accurate matrix elements for up to four jets calculated with the Comix [104] and OpenLoops [105, 106] libraries. They are matched with the Sherpa parton shower [107] using the MEPS@NLO prescription [108–111] using the set of tuned parameters developed by the Sherpa authors. The NNPDF3.0 NNLO set of PDFs [95] is used and the samples are normalised to a next-to-next-to-leading order prediction [112].

VV: Samples of diboson final states are simulated with the Sherpa 2.2.1 or 2.2.2 generator, depending on the process. Fully leptonic final states and semileptonic final states, where one boson decays leptonically and the other hadronically are generated using matrix elements at NLO accuracy in QCD for up to one additional parton and at LO accuracy for up to three additional partons emissions. Samples for the loop-induced processes $gg \to VV$ are generated using LO-accurate matrix elements for up to one additional parton emission for both cases of fully leptonic and semileptonic final states. The matrix element calculations are matched and merged with the Sherpa parton shower based on Catani-Seymour dipole factorisation [104, 107] using the MEPS@NLO prescription [108–111]. The virtual QCD corrections are provided by the openloops library [105, 106]. The NNPDF3.0 NNLO set of PDFs is used [95], along with the dedicated set of tuned parton-shower parameters developed by the Sherpa authors.

VVV: The production of triboson events is simulated with the Sherpa 2.2.2 [103] generator using factorised gauge boson decays. Matrix elements, accurate at NLO for the inclusive process and at LO for up to two additional parton emissions, are matched and merged with the Sherpa parton shower based on Catani-Seymour dipole factorisation [104, 107] using the MEPS@NLO prescription [108–111]. The virtual QCD correction for matrix elements at NLO accuracy is provided by the openloops library [105, 106].

And all these “Electroweak” backgrounds are labelled as “V EW”.

Several other backgrounds are studied with smaller contributions (about 10% on all regions), which are much smaller than the main backgrounds. They are the production of 3/4 top quarks, tZq, tWZ diagram removal, single-top (three channels: s, t, Wt), and other rare top processes as below:

Single-top: Single-top tW associated production is modelled using the Powheg-Box [87] v2 generator at NLO in QCD in the five-flavour scheme with the NNPDF3.0 NLO PDF set. The diagram removal scheme [113] was employed to handle the interference with $t\bar{t}$ production. Single-top t-channel production is modelled using the Powheg-Box,[87] v2 generator at NLO in QCD in the four-flavour scheme with the NNPDF3.0 NLOnf4 PDF set. Single-top s-channel production is modelled using the Powheg-Box [87] v2 generator at NLO in QCD in the five-flavour scheme with the NNPDF3.0 NLO PDF set. For all single-top processes, the events are interfaced with Pythia using the A14 tune and the NNPDF2.3 LO PDF set.

tWZ and tZq: Rare top quark processes namely the production of tZq and tWZ

are modelled using the MadGraph5_aMC@NLO generator at NLO interfaced with Pythia using the A14 tune.

$t\bar{t}t$ and $t\bar{t}t\bar{t}$: The production of $t\bar{t}t$ is modelled using the MadGraph5_aMC@NLO v2.2.2.p6 generator at NLO interfaced with Pythia v8.186 using the A14 tune in the five flavour scheme and The production of $t\bar{t}t\bar{t}$ is modelled same with the MadGraph5_aMC@NLO v2.2.2.p6 generator at NLO interfaced with Pythia v8.186 using the A14 tune in the five flavour scheme.

Other rare top processes : Additionally, the production of a top quark, a Higgs boson, and either an additional jet or a W boson is considered. Moreover, the production of a top-quark pair in association with two W bosons is considered. All these samples are generated at NLO with aMC@NLO and interfaced with Pythia 8. Their contribution is almost negligible compared to other prompt lepton background sources, but for completeness's sake, they are included in this analysis. Other production of a top-quark pair in association with two vector bosons, one vector boson and one Higgs boson, two Higgs bosons are generated at LO with MadGraph and interfaced with Pythia 8. The production of a Higgs boson in association with either a W or a Z boson is also considered. The samples are produced with Pythia 8, assuming a Higgs-boson mass of 125 GeV. These VH samples have no contribution to the final states after the event selection.

These lesser background components, such as $t\bar{t}t/t\bar{t}t\bar{t}$, tWZ, tZq, $t\bar{t}WW$, and singletop, are merged under the label 'otherTop.' Other rare top processes, including tHW, tHq, and other $t\bar{t}$ XX samples, are merged under the label 't($t\bar{t}$)XX,' as all these samples use the AFII simulation. An inclusive approach involving total cross-section uncertainties is taken for these backgrounds. It's worth highlighting that the plots presented in the thesis amalgamate all these rare samples as part of the 'Top other' collective background category.

5.2 Object and Event Selection

The goal of this analysis is to study $t\bar{t}$ events, where one top quark decays through the Standard Model process, while the other decays via a chain involving a heavy neutrino, representing a beyond the Standard Model process. The signal of interest is characterized by a distinct final state with two same-sign leptons, a b-quark, and two light-flavor jets, which arise from the top BSM decay leg.

To search for this signature, a precise selection of objects and events is essential to ensure accurate reconstruction of the signal topology while minimizing contamination from SM backgrounds. The occurrence of two same-sign leptons is rare in SM $t\bar{t}$ decays, making this final state particularly useful for improving the analysis' sensitivity. A detailed phenomenological study of this process, including theoretical predictions for the decay of the heavy neutrino, is discussed in the theory paper [114].

In this section, the selection criteria for objects such as electrons, muons, jets, and b-jets are outlined, alongside the event selection methods used to isolate potential signal events. The event selection aims to suppress SM backgrounds while maintaining high efficiency for detecting the BSM signal. These strategies are vital for ensuring the analysis is sensitive to the possible presence of heavy neutrinos in top quark decays.

5.2.1 Analysis specific object selection

The specific object selection for this analysis was performed using the `AnalysisTop` software [115] (tag 21.2.259). This framework was utilized to guarantee consistent and precise object definitions throughout the analysis. The desired final state was selected by applying custom analysis code to the output ntuples generated by the Top Framework. This method facilitated the efficient identification of the relevant physics objects necessary for the signal topology, such as leptons, jets, and b-jets.

Electron selection

The Electron candidates are reconstructed from energy clusters in the electromagnetic calorimeter, which are linked to charged particle tracks reconstructed in the inner detector. Only candidates with $p_{\mathrm{T}} > 10$ GeV are considered. They must satisfy the condition $|\eta_{\mathrm{cluster}}| < 2.47$. Candidates in the transition region between different electromagnetic calorimeter components, $1.37 < |\eta_{\mathrm{cluster}}| < 1.52$, are excluded.

The transverse impact parameter of the electron candidates (d_0) is required to satisfy $|d_0/\sigma_{d_0}| < 5$, where σ_{d_0} is the uncertainty in d_0. The longitudinal impact

Feature	Criterion
Pseudorapidity range	$(\|\eta\| < 1.37) \quad \|\| \quad (1.52 < \|\eta\| < 2.47)$
Transverse momentum	$p_{\mathrm{T}} > 10\,\mathrm{GeV}$
Object quality	Not from a bad calorimeter cluster (`BADCLUSELECTRON`) Remove clusters from regions with EMEC bad HV (2016 data only)
Track to vertex association	$\|d_0\|/\sigma_{d_0} < 5$ $\|\Delta z_0^{\mathrm{BL}} \sin\theta\| < 0.5\,\mathrm{mm}$
Identification	(`TightLH`)
Isolation	`PLImprovedTight`
Loose isolation	`PLVLoose`
Extra selections	`ECIDS, ambiguity cuts`
Triggers 2015	e24_lhmedium_L1EM20VH, e60_lhmedium, e120_lhloose
Triggers 2016-18	e26_lhtight_nod0_ivarloose, e60_lhmedium_nod0, e140_lhloose_nod0

Table 5.2: Electron selection criteria.

parameter (z_0) must satisfy $|z_0 \sin\theta| < 0.5$. Electrons are calibrated according to the method outlined in Ref. [116].

Electrons selected for this analysis are required to meet the `TightLH` identification criteria and the `PLVLoose` isolation working points [117]. To enhance the rejection of non-prompt leptons, the lepton MVA tagger `PromptLeptonImprovedVeto` (PLIV) [118] is employed. Developed within the IFF CP group [117], this tagger provides superior performance over traditional cut-based selections that depend on impact parameters, isolation, and particle identification (PID). For a detailed description of the PLIV algorithm, see Ref. [119].

Additionally, electrons are tagged with `PLImprovedTight` (Prompt Lepton Improved Veto) if they meet the stricter `PLImprovedTight` isolation working points.

For specific regions of the analysis, additional criteria are applied to the electron selection. This includes the use of the ‘Electron Charge ID Selector Tool’ (ECIDS) [120], which enhances the rejection of electrons with misidentified charge. The tool uses a multivariate algorithm that combines various properties of the reconstructed electron/positron, providing a single calibrated working point with a cut of $BDT_{\mathrm{out}} > -0.337671$. This working point is calibrated across multiple isolation working points, including the `PLImprovedTight` WP used in this analysis.

Furthermore, for some analysis regions, cuts on the `DFCommonAddAmbiguity` and `ambiguityType` variables are applied, as defined by the ‘Electron Ambiguity Tool’ [121] within the E/gamma derivation framework. The requirement `ambiguityType = 0`, along with `DFCommonAddAmbiguity <= 0`, ensures the selection of electrons while rejecting candidates originating from internal/material photon conversions. This combination is referred to as the ”Ambiguity cut” and helps suppress electrons from photon conversions by excluding objects with multiple reconstructed tracks near the calorimeter cluster.

Each electron is assigned both ECIDS and ambiguity tags, indicating whether the lepton has passed the respective selection criteria. Furthermore, electrons must satisfy the un-prescaled single-electron triggers used during Run 2, as outlined in Table 5.2.

Muon selection

Feature	Criterion
Selection working point	`Medium`
Isolation	`PLImprovedTight`
Loose isolation	`PLVLoose`
Momentum calibration	Sagitta correction
p_{T} cut	$> 10\,\mathrm{GeV}$
$\lvert\eta\rvert$ cut	< 2.5
$\lvert d_0\rvert/\sigma_{d_0}$	< 3
$\lvert\Delta z_0 \sin\theta_\ell\rvert$ cut	$< 0.5\,\mathrm{mm}$
Triggers 2015	mu20_iloose_L1MU15, mu50
Triggers 2016-18	mu26_ivarmedium, mu50

Table 5.3: Muon selection criteria.

All muon candidates are required to have $p_{\mathrm{T}} > 10$ GeV and $\lvert\eta\rvert < 2.5$. The transverse impact parameter of the muon candidates must satisfy $\lvert d_0/\sigma_{d_0}\rvert < 3$, while the longitudinal impact parameter must meet the condition $\lvert z_0 \sin\theta\rvert < 0.5$. Muons selected for this analysis must fulfill the `Medium` identification criteria and the `PLVLoose` isolation working points.

Furthermore, muons are tagged with `PLImprovedTight` if they satisfy the stricter `PLImprovedTight` isolation working points. All muons are required to pass the single-muon triggers available during Run 2, as detailed in Table 5.3.

The procedures for muon reconstruction, identification, calibration, and scale factor extraction are discussed in Chapter 4.

Jets

Jets are reconstructed from particle flow objects using the anti-k_t algorithm with $R = 0.4$ (AntiKt4EMPFlowJets collection). The selection requires:

- Basic cuts: $p_{\mathrm{T}} > 20\,\mathrm{GeV}$ and $|\eta| < 4.5$
- Central jets ($|\eta| < 2.4$, $p_{\mathrm{T}} < 60\,\mathrm{GeV}$): JVT$>$ 0.5 (Tight working point) [122, 123]
- Forward jets ($2.5 < |\eta| < 4.5$, $p_{\mathrm{T}} < 120\,\mathrm{GeV}$): fJVT$<$ 0.4 plus timing requirement

b-tagged jets

Jets containing *b*-hadrons ("*b*-tagged") are tagged with the *DL1r* multivariate discriminant, which combines information from the impact parameters of displaced tracks and tertiary decay vertices reconstructed within the jet. For flavor tagging, the most recent Calibration Data Interface (CDI) at the time of analysis was used: `2020-21-13TeV-MC16-CDI-2021-04-16_v1.root`. Jets are considered *b*-tagged if they pass the DL1r efficiency working point of 85%.

Missing transverse momentum

Missing transverse momentum ($E_{\mathrm{T}}^{\mathrm{miss}}$) is used to apply additional selection criteria for the validation of background modeling. The missing transverse momentum vector is defined as the negative vector sum of the transverse momenta of all reconstructed and calibrated physics objects, along with the remaining unclustered energy. The $E_{\mathrm{T}}^{\mathrm{miss}}$ value for an event is taken as the magnitude of this vector.

The selection of missing transverse momentum is based on the default settings provided within `AnalysisTop`.

Overlap removal

The ASG overlap removal tool [124] is utilized within the `AnalysisTop` framework to ensure proper overlap removal of physics objects, preventing double-counting. Loose leptons and jets are considered in this procedure (see Table 5.2 and Table 5.3).

When object candidates passing selection cuts overlap, a classification is required to determine which of the overlapping objects to retain, while rejecting the others. The overlap removal procedure ensures that the same object is not counted twice, while allowing retention of distinct, nearby objects. The optimal overlap removal strategy applied in this analysis is as follows:

- **Electron/Muon OR**: Any muon sharing a track with an electron is removed, and any electron sharing a track with a muon is removed.
- **Electron/Jet OR**: If an electron and a jet are found within $\Delta R < 0.2$, the jet is removed. If they are within $\Delta R < 0.4$, the electron is removed.
- **Muon/Jet OR**: Jets with fewer than three tracks associated with them, found within $\Delta R < 0.2$ of a muon, or jets with fewer than three tracks and a muon inner-detector track ghost-associated with them, are removed. Muons found within $\Delta R < 0.4$ of a jet are removed.

This overlap removal is applied before all other object selections described above. The final results in the analysis are obtained using the `AnalysisTop` software.

5.2.2 Event preselection

The `AnalysisTop` framework defines the object selection described above, which is then used in the analysis code. Subsequently, event selection is applied to these different physics objects.

The event must contain exactly two same-sign, same-flavor light leptons (ee or $\mu\mu$). Both leptons are required to meet the isolation selection criteria of `PLVLoose`, and each electron will be assigned labels based on the results of the ECIDS and ambiguity filtering, as described in the electron object selection section.

The leading lepton must have $p_{\mathrm{T}}^{\ell_1} > 27$ GeV to ensure consistency across all data-taking periods after trigger matching.

Central jets must satisfy $p_{\mathrm{T}} > 20$ GeV and $|\eta| < 2.5$, while forward jets must lie within the pseudorapidity range $2.5 < |\eta| < 4.5$ and have $p_{\mathrm{T}} > 35$ GeV.

The b-tagging selection is also tightened: b-tagged jets must have $p_{\mathrm{T}}^{b} > 25$ GeV. Events must contain at least two b-tagged jets and at least four non-b-tagged jets.

Additionally, the invariant mass of the lepton pair, $m_{\ell\ell}$, must satisfy $m_{\ell\ell} > 12$ GeV to suppress contributions from the Drell-Yan process.

5.2.3 Event reconstruction

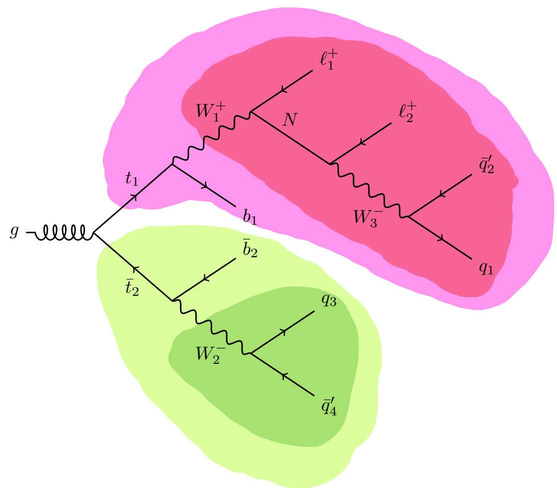

Figure 5.3: Feynman diagram of the signal production marked with different objects reconstruction.

Figure 5.3 The leading-order signal for this analysis is shown. It consists of a top quark pair, where one top quark decays as predicted by the Standard Model ($t_2 \to b_2 W_2 \to q_3 \bar{q}_4'$), and the other top quark decays to a b-quark (b_1) and a W boson (W_1). The W_1 boson subsequently decays via a heavy neutral lepton: $W_1 \to \ell_1 \ell_2 q_1 \bar{q}_2'$. This process provides four mass constraints (from the two top quarks and the two W bosons), and a χ^2 minimization approach is used to determine the origin of each final state particle.

In this notation, the indices 1 and 2 denote the Beyond-the-Standard-Model and Standard Model top quarks and W bosons, respectively. Each quark q_k is associated with a jet j_k, and each b_l is associated with a b-jet. The four masses involved are defined as follows: :

$$m(t_1) \equiv m(b_1\, \ell_1\, \ell_2\, j_1\, j_2), \tag{5.2}$$

$$m(W_1) \equiv m(\ell_1\, \ell_2\, j_1\, j_2), \tag{5.3}$$

$$m(t_2) \equiv m(b_2\, j_3\, j_4), \tag{5.4}$$

$$m(W_2) \equiv (\, j_3\, j_4). \tag{5.5}$$

Then, all the possible combinations of the available objects are used and the "match" association will be the one that minimizes χ^2 defined as:

$$\chi^2 = \sum_{i=1}^{n} \frac{(O_i - E_i)^2}{\sigma_i^2},$$

where:

χ^2 is the χ-squared value,

O_i is the observed value of the i-th data point,

E_i is the expected value of the i-th data point,

σ_i is the standard deviation (error) associated with the i-th data point,

n is the total number of data points.

The chi-squared (chi^2) algorithm is a common method for finding the best match between measured(observed) and expected values. In theory, the denominator should be the squared sigma of the measurement result. However, given that the measured sigma is initially unknown, we opt for an initial denominator setup employing the masses of the top quark (M_t) and the W boson (M_W), as exemplified in Equation 5.6, with their respective values of 172.69 GeV and 80.377 GeV, as defined in the Particle Data Group (PDG) [125]. Given that the χ^2 algorithm exhaustively searches for the minimum values across feasible combinations, we hold the belief that it will not exert a significant impact on reconstruction efficiency.

Upon acquiring the measured outcomes from the preliminary iteration, we have the option to integrate actual sigma values extracted from the invariant mass distributions of $m(t_1), m(t_2), m(W_1)$, and $m(W_2)$, as depicted in Figure 5.3.

It's important to note that at the truth level, our focus is on the final states comprising four light jets, two same-sign leptons, and two b-jets. Yet, reconstructing all jets decayed from the Beyond the Standard Model off-shell W boson at the reconstruction level can prove challenging, especially for low/high mass point signals. Consequently, there may arise instances of incorrect jet combinations when attempting to reconstruct the top quark and W boson. In summary, due to the complexities inherent in simulation, reconstruction, and object selection efficiencies, achieving ideal distributions proves to be a difficult task. Hence, we prefer fitting a Gaussian distribution to the core area to obtain a relatively reasonable sigma value for the second iteration. In the second iteration, we can use the sigma squares taken from the distributions of $m(t_1), m(t_2), m(W_1), m(W_2)$ as denominators, like the equation 5.7 shows.

$$\chi^2 = \frac{(m(t_1) - M_t)^2}{M_t} + \frac{(m(W_1) - M_W)^2}{M_W} + \frac{(m(t_2) - M_t)^2}{M_t} + \frac{(m(W_2) - M_W)^2}{M_W} \tag{5.6}$$

$$\chi^2 = \frac{(m(t_1) - M_t)^2}{\sigma_t^2} + \frac{(m(W_1) - M_W)^2}{\sigma_W^2} + \frac{(m(t_2) - M_t)^2}{\sigma_t^2} + \frac{(m(W_2) - M_W)^2}{\sigma_W^2} \tag{5.7}$$

The reconstructed distributions of the top and W masses are minimally influenced by alterations in the denominator, regardless of whether the top and W masses or their mass resolution values are employed. The relevant studies are included in the Appendix A.

Given that we possess σ values originating from distinct mass points within the signal, we have the option to utilize the averaged σ^2 values (36 GeV for σ_t and 27 GeV for σ_W), acquired from all mass points with equal weighting, as the unified denominators within the χ^2 formula (Equation 5.7).

5.3 Signal regions and control regions definition

5.3.1 IFF classification method

A crucial aspect of this analysis is the handling of backgrounds involving non-prompt leptons. These leptons primarily arise from b/c-hadron decays, where a lepton in the decay process is detected outside the jet cone and is misidentified as a prompt lepton. Additionally, charge misidentification in electrons and photon conversions significantly impacts the 2LSS final state.

Since accurately predicting the non-prompt lepton rates with simulated samples is challenging, a template fit method is employed to estimate their contribution. This approach assumes that the event kinematics are modeled well by the MC samples. The non-prompt lepton background rate is fitted to observed data in control regions enriched with such backgrounds, while IFF classification assists in identifying non-prompt leptons based on their different origins.

In this study, we require exactly two same-sign leptons, where one lepton is classified as "prompt" and the other is assigned according to the *IFF Truth Classifier*. The classification system described below is based on the README documentation for IFF classes, as detailed in reference [126].

0 *Unknown*: Leptons are categorized as `Unknown` (IFF class 0) when they cannot be assigned to any of the other classes described below. In the selected backgrounds/samples, no leptons fall into this class.

1 *KnownUnknown*: The `KnownUnknown` category (IFF class 1) refers to leptons that could potentially be classified, but where classification fails due to missing information. This background is treated as static during the fit.

2 *IsoElectron*: An electron classified as prompt (IFF class 2) corresponds to an isolated electron in the truth-type, or originates from prompt quarkonium decays (e.g. $c\bar{c}/b\bar{b} \rightarrow e^+e^-$).

3 *ChargeFlipIsoElectrons*: This category (IFF class 3) applies to electrons with charge misidentification. As our analysis requires same-sign leptons, this background is treated separately when evaluating the fake $t\bar{t}$ background.

4 *PromptMuon*: A muon is considered prompt (IFF class 4) if its truth-type corresponds to an isolated muon and it originates from a prompt source

such as W/Z, top, or Higgs bosons.

5 *PromptPhotonConversion*: Electrons originating from the conversion of prompt photons (IFF class 5) are identified based on their truth-type, corresponding to a background electron or photon from a prompt photon conversion.

6 *ElectronFromMuon*: Electrons classified as originating from muons (IFF class 6) are those where the electron' s truth-type corresponds to a non-isolated electron or photon, and the truth-origin is a muon.

7 *TauDecay*: Non-isolated electrons and muons from hadronic tau decays (IFF class 7) are identified by their truth-type, corresponding to non-isolated muons or electrons from tau leptons.

8(9) *B(C)HadronDecay*: Electrons and muons from heavy-flavor decays are classified as coming from either b-hadrons (IFF class 8) or c-hadrons (IFF class 9), based on their truth-origin.

10 *LightFlavourDecay*: Leptons produced by light-flavor jets (IFF class 10) are identified by their truth-type.

IFF categories are widely used in ATLAS to investigate lepton origins. The backgrounds considered in this analysis assume that at least one lepton is prompt, meaning it belongs to either IFF category 2 (prompt electron) or 4 (prompt muon).

The analysis labels events where the second lepton originates from photon conversion (IFF class 5) as "$t\bar{t}$ γ-conv", which includes processes like $t\bar{t}\gamma$ and $t\bar{t}$. This background is combined after removing events from the inclusive $t\bar{t}$ sample.

The label "$t\bar{t}$ Q-flip" is used for events where the second lepton arises from charge-flip misidentification (IFF class 3).

The label "$t\bar{t}$ dec" is assigned to events where the second lepton originates from a decay of either a heavier lepton or a hadron (IFF classes 7/8/9/10).

Finally, if the second lepton from the $t\bar{t}$ sample does not fit into any of the aforementioned backgrounds, it is labeled "$t\bar{t}$ other" (IFF class 0/1).

5.3.2 Analysis regions definition

In this section, the definitions of all regions passing the event selection criteria are outlined. A detailed analysis was performed on events that passed the selection criteria described in Section 5.2. These events feature two same-sign, same-flavor leptons (either electrons or muons), two b-tagged jets with an 85% efficiency working point, and at least four additional light-flavor jets. These jets and leptons provide the necessary variables for further event reconstruction and background rejection.

The leptons must pass the `PLVLoose` isolation working point, and each electron is further classified based on the results of the ECIDS and ambiguity filtering criteria. Leptons that pass the "Ambiguity cut" veto photon conversion candidates, while those failing indicate a possible photon conversion background. Electrons that pass the "ECIDS cut" indicate a misidentified charge, and those that fail are considered to have no charge misidentification. Additionally, a Z-boson mass veto is applied, excluding events with $|m_{ee} - m_Z| < 10$ GeV to suppress contributions from $Z \to ee$ events.

The following sections outline the event selection strategy for both the electron and muon channels, defining signal regions (SR) and multiple control regions to isolate various background processes.

Electron Channel

In the electron channel, events are selected based on a combination of lepton isolation, invariant mass of the two leptons, the ambiguity cut, and the ECIDS cut. This allows for the definition of a signal region and four control regions, each targeting a different background source, through flexible combinations of selection criteria.

- **Signal Region:** To define the signal region, two tight isolation cuts are applied to the same-sign leptons, along with the requirement that the invariant mass of the two leptons, $m_{\ell\ell}$, is less than 80 GeV. This selection maximizes the contribution of the heavy neutral lepton signal process, enabling the extraction of the signal strength, μ(HNL).

- **Control Region for $t\bar{t}$ W ($t\bar{t}W$ CR):** To control the background from $t\bar{t}W$ events and reduce contamination from the Z-boson mass peak, the opposite side of the $m_{\ell\ell}$ spectrum is selected, requiring $m_{\ell\ell} > 100$ GeV. Additionally, the $t\bar{t}W$ control region from the electron channel is merged with the corresponding region from the muon channel to improve statistical power.

- **Control Region for Fake Leptons (CRHF):** Fake leptons are controlled by selecting events where at least one of the two leptons, after passing the `PLVLoose` isolation, fails the tighter `PLIVTight` isolation. To further reduce signal contamination, a selection of $m_{\ell\ell} > 75$ GeV is applied.

- **Control Region for Electron Charge Flip (CRCF):** Events, where one of the two leptons passes the ECIDS cut, are used to define the electron charge flip control region. A veto on $Z \to ee$ events is applied by excluding events in the Z mass window, and a selection of $m_{\ell\ell} > 60$ GeV is added to reduce the signal contribution.

- **Control Region for Photon Conversion (CRPC):** The ambiguity cut, which is applied in all other regions to suppress photon conversion contributions, is inverted in this control region to enhance the contribution from photon conversion processes. Additionally, a selection of $m_{\ell\ell} > 75$ GeV and the Z-boson veto are applied to minimize signal contamination.

Muon Channel

The muon channel follows a similar strategy to the electron channel, with the same cuts applied to define the signal region and control regions. The primary difference lies in the lepton type and minor adjustments to enhance background suppression specific to muon events.

- **Signal Region:** The signal region is defined by requiring two same-sign muons passing tight isolation criteria and an invariant mass $m_{\ell\ell} < 80$ GeV, following the same logic as in the electron channel.

- **Control Region for $t\bar{t}$ W ($t\bar{t}W$ CR):** The $t\bar{t}W$ control region is defined similarly, by selecting events where $m_{\ell\ell} > 100$ GeV. As mentioned earlier, the $t\bar{t}W$ control region is merged with the electron channel's region to increase statistics.

- **Control Region for Fake Leptons (CRHF):** Events with at least one lepton passing the `PLVLoose` isolation but failing `PLIVTight`, along with a selection of $m_{\ell\ell} > 75$ GeV, are used to define the fake lepton control region in the muon channel.

5.3.3 Summary of Region Definitions

All of the cuts and selection criteria, including the Z-boson mass veto and the invariant mass thresholds on $m_{\ell\ell}$, are designed to enhance the contribution from targeted backgrounds in the control regions while ensuring signal event contamination in each control region is smaller than 1% of the total signal events.

In summary, Table 5.4 provides an overview of the selections applied to define the signal and control regions, ensuring statistical orthogonality across all regions.

Table 5.4: Definition of different signal regions and control regions.

Region	$\ell_1 - \ell_2$ flavour	Isolation cut	Ambiguity cut	ECIDs cut	Other
SR(ee)	e-e	PLIVTight & PLIVTight	Pass & Pass	!Pass & !Pass	$m_{\ell\ell} < 80$ GeV
CR(e_{ttW})	e-e	PLIVTight & PLIVTight	Pass & Pass	!Pass & !Pass	$m_{\ell\ell} > 100$ GeV and merged with CR(μ_{ttW})
CR(e_{HF})	e-e	!(PLIVTight & PLIVTight)	Pass & Pass	!Pass & !Pass	$m_{\ell\ell} > 75$ GeV
CR(e_{PC})	e-e	-	!(Pass & Pass)	!Pass & !Pass	$m_{\ell\ell} > 75$ GeV and veto Z
CR(e_{CF})	e-e	-	Pass & Pass	Pass | Pass	$m_{\ell\ell} > 60$ GeV and veto Z
SR($\mu\mu$)	μ-μ	PLIVTight & PLIVTight	-	-	$m_{\ell\ell} < 80$ GeV
CR(μ_{ttW})	μ-μ	PLIVTight & PLIVTight	-	-	$m_{\ell\ell} > 80$ GeV and merged with CR(e_{ttW})
CR(μ_{HF})	μ-μ	!(PLIVTight & PLIVTight)	-	-	$m_{\ell\ell} > 75$ GeV

The analysis defines two signal regions and six control regions, with the $t\bar{t}W$ control region shared between the electron and muon channels. The performance of the signal regions is evaluated using the BDTG score obtained from multivariate analysis (MVA) training, as detailed in Section 5.4. This approach enhances the discrimination between signal and background processes.

Simulated events are categorized based on the presence of non-prompt or fake leptons using the IFFTruthClassifier and MCTruthClassifier packages. Further details on these classification tools are provided in Section 5.3.1. The primary sources of misidentified leptons in the signal regions include heavy-flavor fake leptons (IFF classes 7/8/9/10) and electrons from photon conversions (IFF class 5), predominantly originating from $t\bar{t}$ and $t\bar{t}\gamma$ events. A minor contribution arises from charge-flip backgrounds (IFF class 3). A dedicated $t\bar{t}W$ control region is defined for both the electron and muon channels. The composition of lepton sources in the signal and control regions is illustrated in Figure 5.4.

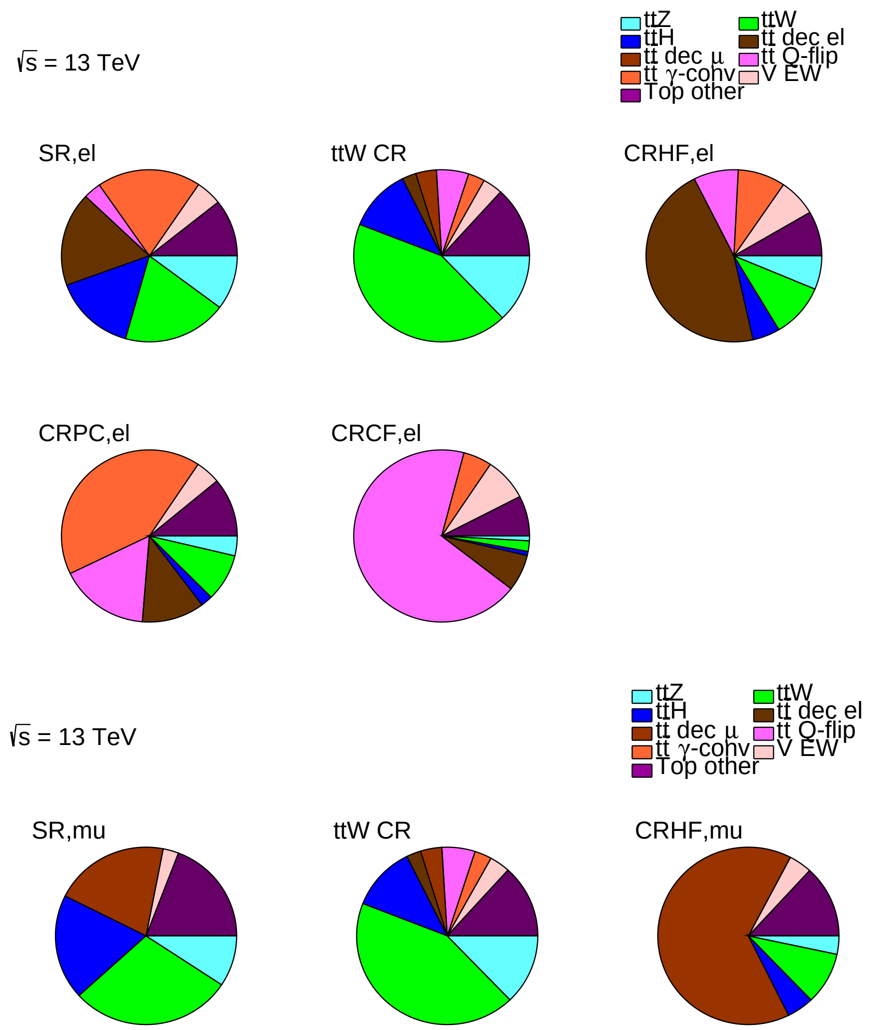

Figure 5.4: The compositions of the different background sources in the SR and CRs from the ee (upper) / $\mu\mu$ (lower) channel are shown here. The $t\bar{t}W$ control region is used both on the $ee/\mu\mu$ channel, while two CRHF regions are used to control the heavy flavor fake leptons from $ee/\mu\mu$ channel. CRPC and CPCF are used to control the photon conversion and charge flip background contributions, respectively. All the control regions effectively constrain the target composition.

The category labeled as Top other" in Figure 5.4 encompasses contributions from $t\bar{t}t/t\bar{t}t\bar{t}$, tWZ, tZq, single-top, tHq, tHW, ttXX, and non-photon conversions from $t\bar{t}\gamma$, as well as $t\bar{t}$ other. The "V EW" category includes contributions from V+jets and VV/VVV processes.

5.3.4 Pre-fit plots displayed with the IFF classification

The two signal regions and five control regions are employed, with the $t\bar{t}W$ control region shared between the electron and muon channels. These control regions are designed to constrain various background processes. Specifically, the $t\bar{t}W$ control region targets the $t\bar{t}W$ process, while the heavy-flavor fake lepton control regions address contributions from heavy-flavor fake leptons. Additional control regions, such as those for photon conversions and charge-flip backgrounds, further mitigate the impact of the leptons from the photon conversion and the misidentified leptons. The pre-fit plots are shown in Figure 5.5 and Figure 5.6.

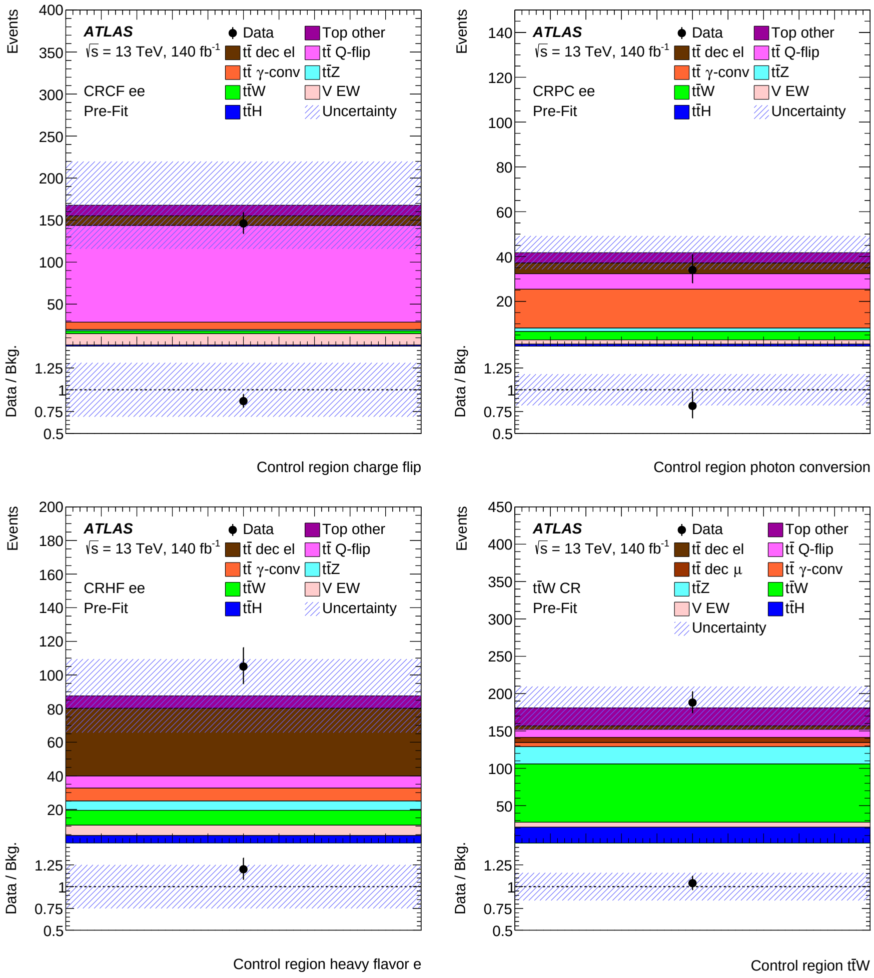

Figure 5.5: These pre-fit plots illustrate the different sources of lepton background estimation in the *ee* channel. The disagreement between data and MC prediction is due to the backgrounds not being normalized to data here (no NFs applied in these pre-fit plots). The uncertainty band includes the effects of all statistical and systematic uncertainties.

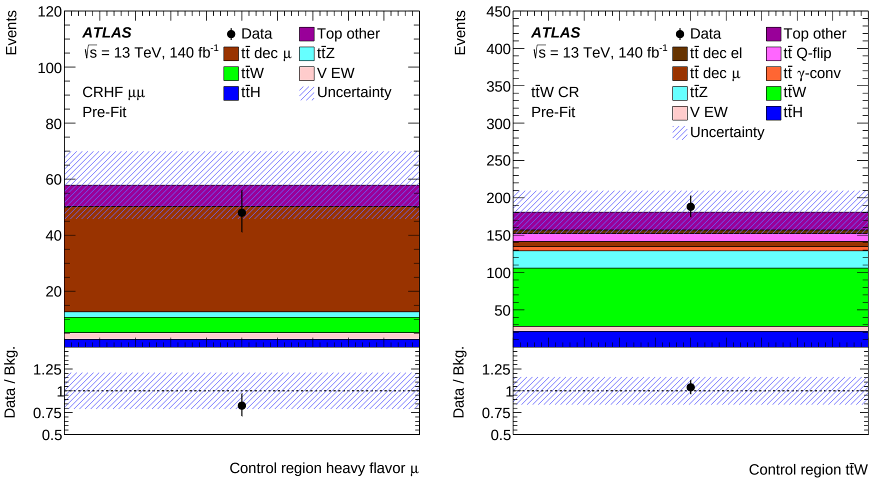

Figure 5.6: Pre-fit plots of the CRs in the $\mu\mu$ channel, which are essential for the Template Fit Method used to extract the normalization factors. These plots illustrate the different sources of lepton background estimation in the $\mu\mu$ channel. In each control region, the target backgrounds have the dominant composition, as expected. The disagreement between data and MC prediction is due to the backgrounds not being normalized to data here (no NFs applied in these pre-fit plots). The uncertainty band includes the effects of all statistical and systematic uncertainties from the backgrounds.

5.4 Multi-Variate Analysis

In high-energy physics, distinguishing between signal and background events in complex datasets often requires sophisticated analytical techniques. One such technique is the Multi-Variate Analysis, which leverages machine learning algorithms to enhance the separation power between different event types. This section outlines the application of MVA in our analysis, focusing on the use of Gradient Boosted Decision Trees (BDTG) for classification tasks.

5.4.1 Setting of the MVA

Following a cut-based selection, we defined two distinct signal regions for the $ee/\mu\mu$ channel. These regions were characterized by stricter isolation criteria and a low invariant mass cut $m_{\ell\ell} < 80$ GeV, as described in Section 5.3.

MVA Framework and Implementation

To implement the MVA, we employed the `mva-trainer` framework [127], which integrates machine learning libraries such as PyTorch [128], PyG [129], and scikit-learn [130]. Specifically, we utilized the `GradientBoostingClassifier` from `scikit-learn` for binary classification, enabling effective discrimination between signal and background events.

Signal Mass Point Grouping

Given the limited statistics for individual mass points, we grouped the 10 signal mass points (ranging from HNL 15 to HNL 75) into two categories: the high-mass region (HNL 45 to HNL 75) and the low-mass region (HNL 15 to HNL 40). This grouping strategy was guided by the recommendations in Table 5.6. The MVA studies were conducted separately for these aggregated mass sets, utilizing all background samples from the full Run-2 dataset. The resulting BDT scores were subsequently used as kinematic variables in the signal regions for the fitting process.

To address potential inconsistencies in kinematic distributions between the high and low mass regions, we explored three distinct approaches:

1. Assigning individual training weights to each mass point.

2. Assigning training weights from two single representative mass points (signal mass at 25 GeV and 50 GeV).

3. Assigning training weights from two sets of merged signal mass points

The latter two approaches, aimed at simplifying the training model, did not significantly impact the final significance in the signal regions. However, combining the signal sets enhanced statistical power and mitigated overtraining issues. Detailed performance evaluations of these approaches are provided in Appendix B.

Cross-Validation and Training Strategy

For robust validation, we implemented a 2-fold cross-validation procedure. The dataset was partitioned based on the `eventNumber` variable, with even and odd event numbers defining the training and testing sets for each fold. Additionally, 10% of the training events were reserved for validation to monitor validation loss and prevent overfitting. The BDT training outputs from the two folds were integrated into the Ntuples, with fold1's results applied to odd events and fold2's results applied to even events.

Handling Negative Weights

Negative weights in training events can pose challenges for machine learning algorithms. To address this, we tested two approaches:

1. Discarding events with negative weights.

2. Retaining events with absolute weights.

After comparing variable distributions and training outcomes, we opted for the second approach, which improved statistical robustness and reduced the risk of overtraining without compromising the significance of the results. Further details on this methodology are provided in Appendix C.

Background Normalization and Parameter Optimization

All background events were normalized to the actual luminosity to ensure accurate comparisons with signal events. During the BDT training, we evaluated various combinations of training parameters, with the number of estimators and tree depth being the most critical. By comparing test/training outputs and loss function plots (as shown in Figures 5.7 and 5.8), we identified the optimal parameter settings. A summary of the six trainable parameters and their descriptions is presented in Table 5.5.

Training Dataset

The BDT training utilized approximately 60,000 background events and 80,000 signal events in the high-mass region, along with 56,000 signal events in the low-mass region. This dataset provided a robust foundation for training and validation, ensuring reliable performance in the signal regions.

Option	Value	Description
nEstimators	50	Number of boosting stages to be performed during the training of a BDT.
MaxDepth	2	Maximum depth of the individual estimators of a BDT.
MaxFeatures	4	The number of features to consider when looking for the best split in a BDT.
MinSamplesSplit	0.1	The minimum number of samples required to split an internal node in a BDT.
MinSamplesLeaf	0.1	The minimum number of samples required to be at a leaf node in a BDT.
LearningRate	0.1	Initial learning rate for the training.

Table 5.5: Optimized BDT options. Both low and high-mass channels share the same settings. Performance is evaluated by comparing AUC values, test/training ratio plots (to assess overtraining), and loss function checks between the training and validation sets.

5.4.2 Optimization of the MVA

In Section 5.2.2, we select events containing two same-sign, same-flavour leptons, at least two b-tagged jets, and at least four light jets. Applying the χ^2 algorithm allows us to reconstruct key objects originating from the decay of the two top quarks. We extract 17 kinematic variables relevant to the top quark pair decay model and use them as inputs for the multivariate analysis:

- $p_{\mathrm{T}}^{\ell_1}$: p_{T} of the leading one among the same sign leptons.
- $p_{\mathrm{T}}^{\ell_2}$: p_{T} of the sub-leading one among the same sign leptons.
- η_{ℓ_1} : η of the leading one among the same sign leptons.

(a) Training vs. testing output with 100 estimators

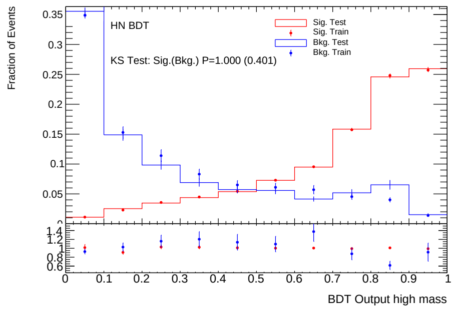

(b) Training vs. testing output with 50 estimators

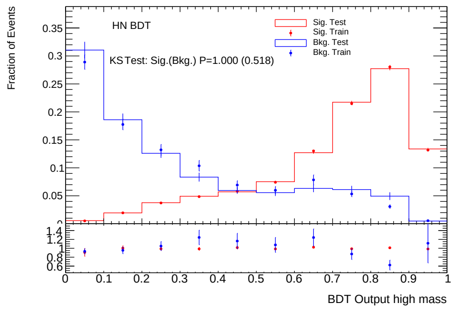

(c) Loss function with 100 estimators

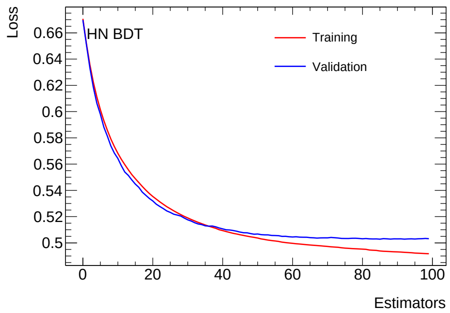

(d) Loss function with 50 estimators

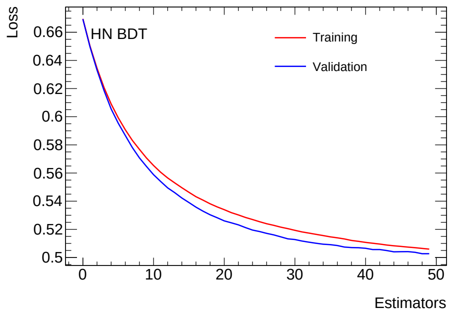

Figure 5.7: The training/testing and the loss function comparison with different estimators are shown here. Increasing the number of estimators can lead to overfitting. Therefore, we chose to set the number of estimators to 50.

(a) Training vs. testing output with depth = 3

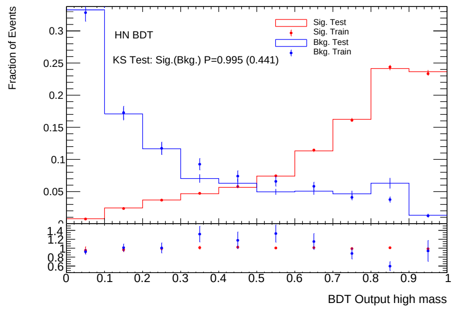

(b) Training vs. testing output with depth = 2

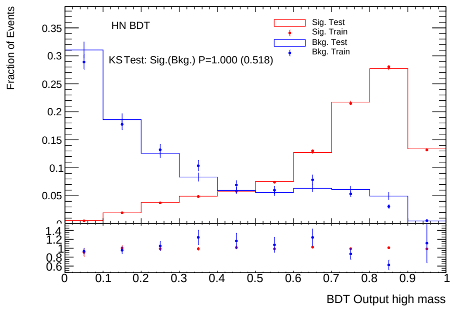

(c) Loss function with depth = 3

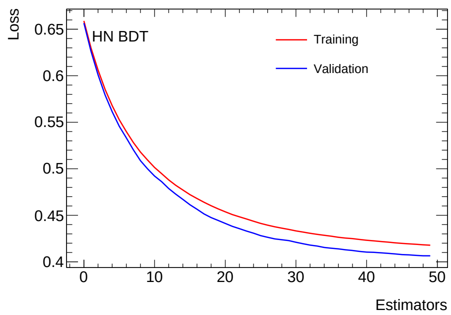

(d) Loss function with depth = 2

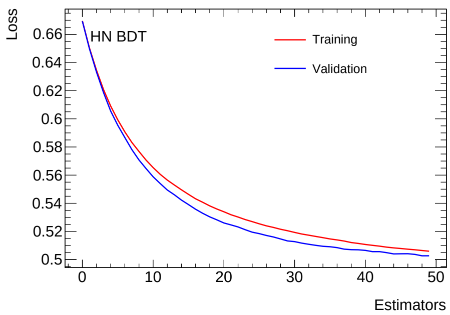

Figure 5.8: The training/testing and the loss function comparison with different training depths are shown here. A depth of 2 resulted in fewer overfitting issues compared to deeper trees, which exhibited more overfitting.

- η_{ℓ_2} : η of the sub-leading one among the same sign leptons.
- E_{T}^{miss} : Missing transverse momentum
- H_T : Scalar sum of the pT of all leptons and jets.
- $\Delta R_{\ell\ell}$: Angular separation of two same sign leptons
- $m_{\ell\ell}$: Invariant mass of two same sign leptons.
- $p_{\mathrm{T}}^{J_1}$: p_{T} of the leading Jet.
- N_{jet}: Number of all different types of jets (including b-tagging jets).
- N_{bjet}: Number of b-tagging jets.
- m_{smT}: Invariant mass of Top with SM decay.
- m_{smW}: Invariant mass of W decayed from SM Top.
- m_{bsmT}: Invariant mass of Top with BSM decay.
- m_{bsmW}: Invariant mass of W decayed from BSM Top.
- m_{bsmN1}: Invariant mass of HNL reconstructed with lepton1 and two jets decayed from off-shell W.
- m_{bsmN2}: Invariant mass of HNL reconstructed with lepton2 and two jets decayed from off-shell W.

In the GradientBoostingClassifier algorithm within Scikit-Learn, feature importance is computed based on the accumulated information gain produced by each feature during the tree splitting process. This cumulative information gain serves as a measure of each feature's contribution to the model's performance. The initial importance of all the input variables is listed in Figure 5.9, and the corresponding correlation matrix is shown in Figure 5.10. There are lots of variables that have a very high correlation matrix with others due to the similarity in composition.

To optimize the BDT, we applied several principles. Firstly, we aimed to decorrelate all variables to avoid multicollinearity issues and reduce the redundancy of information. Secondly, we compare the gain in significance (AUC value) to decorrelate and reduce the low-importance variables, thereby improving the signal-to-background separation. Lastly, we selected only the most significant variables as input to the BDT to further improve its performance. By applying these principles, we were able to reduce the number of input variables from 17 to 4 without significant loss of signal efficiency. The difference between the training with 17 variables and the 4 optimization variables is shown in Figure 5.11. These four variables are listed below:

- $p_{\mathrm{T}}^{\ell_2}$: p_{T} of the sub-leading one among the same sign leptons.
- $m_{\ell\ell}$: Invariant mass of two same sign leptons.
- E_{T}^{miss} : Missing transverse momentum
- m_{bsmW}: Invariant mass of W decayed from BSM Top.

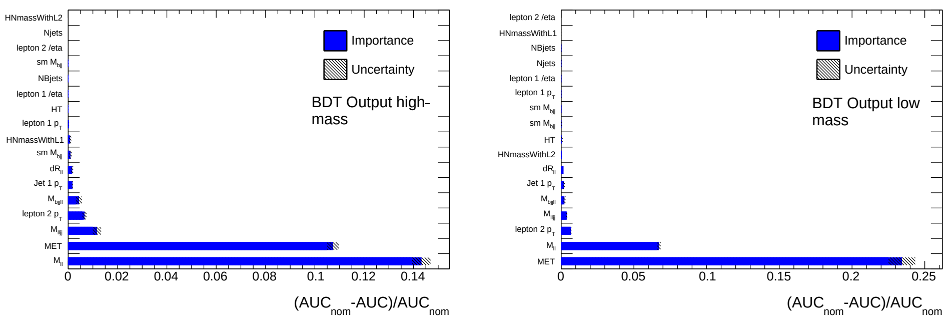

Figure 5.9: The most significant variables are the $p_{\mathrm{T}}^{\ell_2}$, $m_{\ell\ell}$, E_{T}^{miss}, m_{bsmW} both in high (left) and low (right) mass region, which is shown in the importance ranking plots.

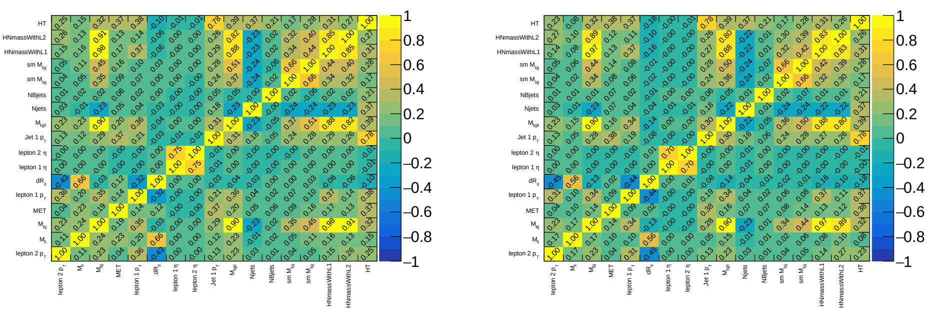

Figure 5.10: Correlation matrix of the variables in high (left) and low (right) mass region, decorrelation studies are performed and ordered by gain in significance.

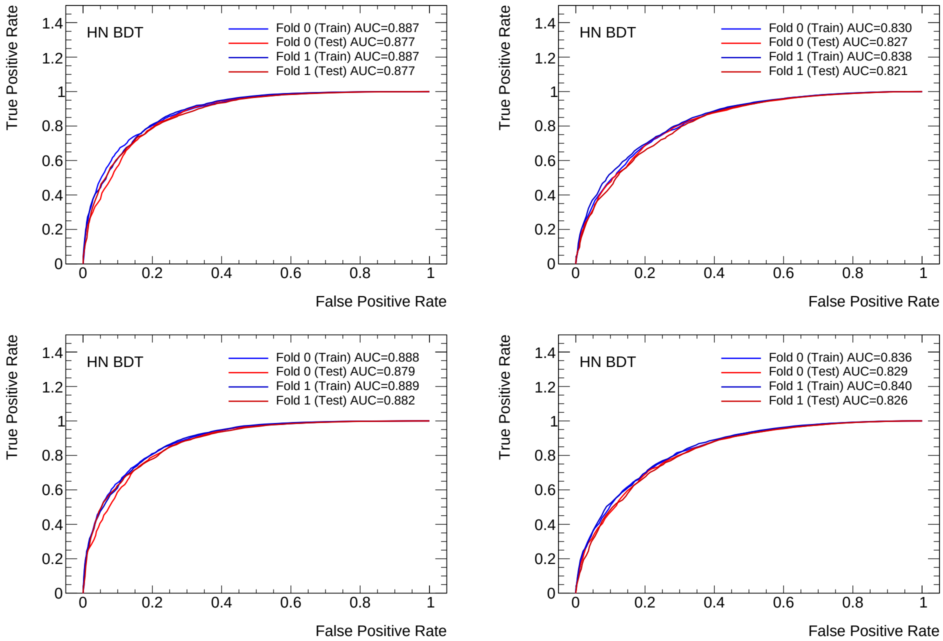

Figure 5.11: The optimization on the different numbers of input variables for training is presented here(ee channel (left) and $\mu\mu$ channel (right)). The training results with 4 variables (upper row) have almost the same signal efficiency as those with all 17 variables (lower row).

5.4.3 Modelling check for the input variables

To ensure the inclusion of all necessary background samples, a thorough comparison between data and Monte Carlo simulations is performed in the control regions. This validation utilizes four key kinematic variables, which are highly discriminative in the multivariate analysis: the missing transverse energy ($E_{\mathrm{T}}^{\mathrm{miss}}$), the invariant mass of the two leptons ($m_{\ell\ell}$), the transverse momentum of the subleading lepton (p_T^{l2}), and the invariant mass of the reconstructed beyond the Standard Model W boson (m_W). The distributions of these variables are illustrated in Figure 5.12 to Figure 5.15.

A control region only (CR-only) fit is conducted, focusing exclusively on the control regions defined in Table 5.4. In this fit, the normalization factors for the primary background contributions are allowed to vary freely. The post-fit results demonstrate good agreement between data and MC predictions, with no significant discrepancies observed in the modeling.

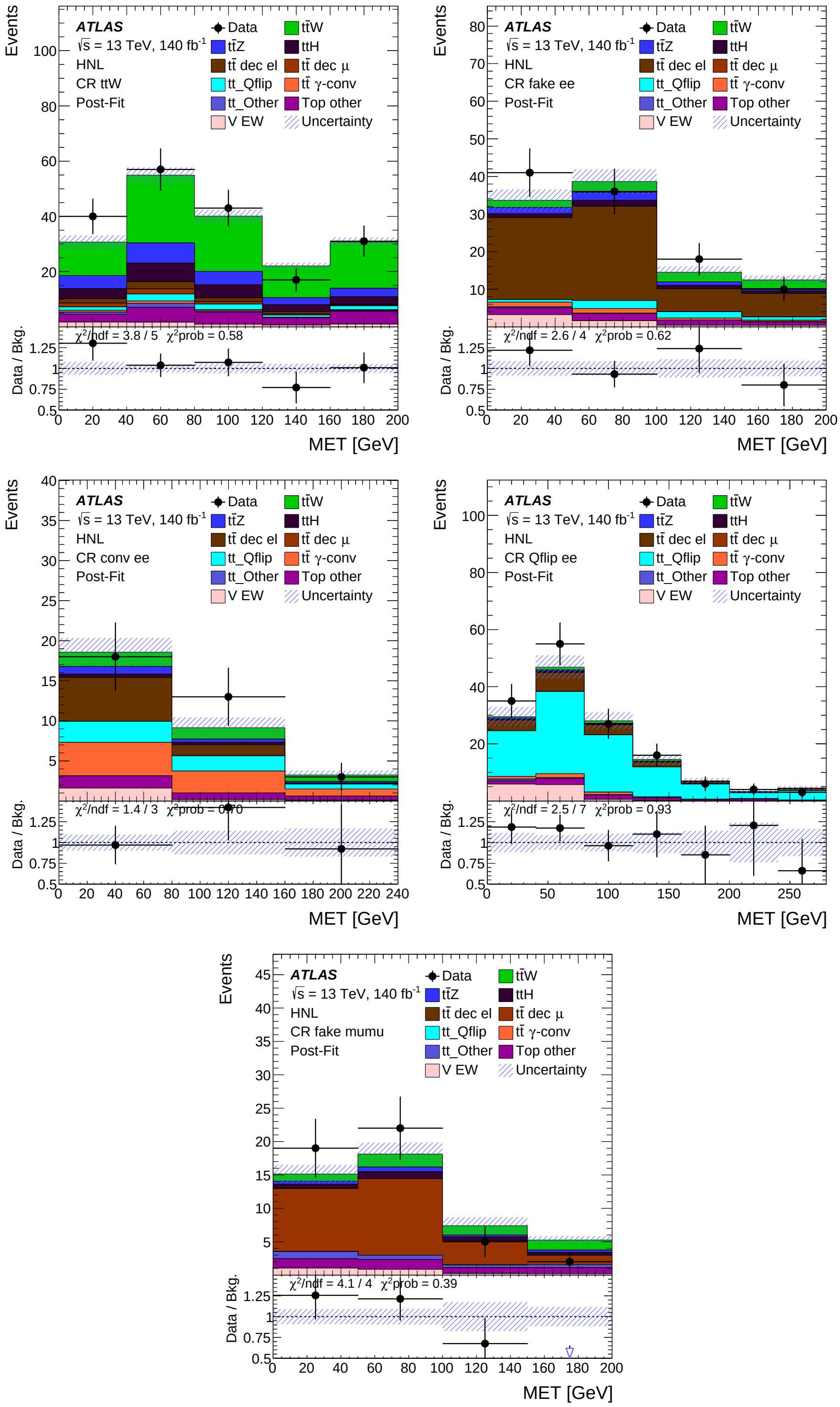

Figure 5.12: Modelling check for the missing transverse energy in all control regions. Normalization factors taken from the CR-only fit are applied to the target backgrounds, and the uncertainty bands incorporate both statistical and systematic uncertainties. The χ^2 values are provided for each region to quantify the agreement between data and MC predictions.

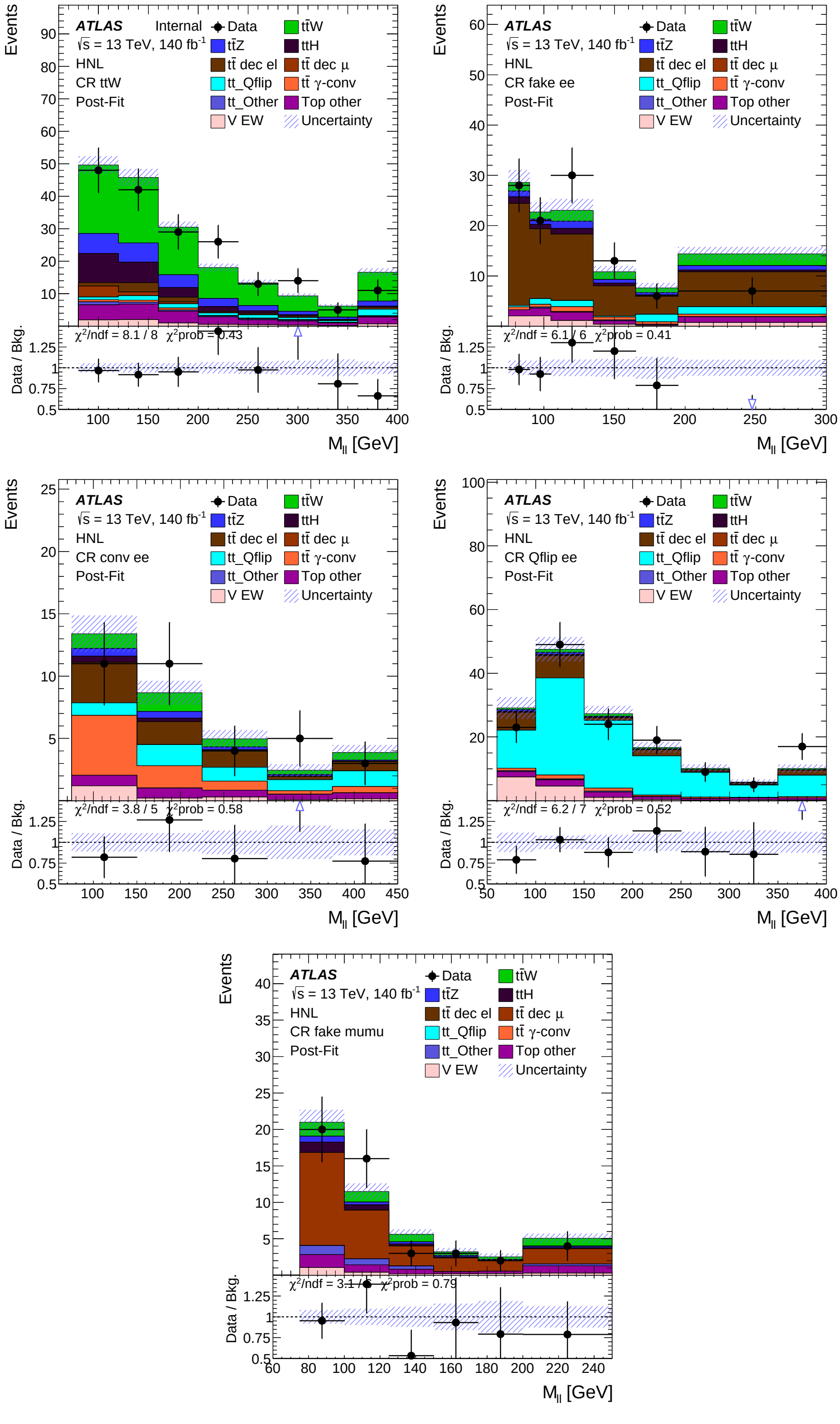

Figure 5.13: Modelling check for the invariant mass of the two leptons ($m_{\ell\ell}$) in all control regions. Normalization factors taken from the CR-only fit are applied to the target backgrounds, and the uncertainty bands include both statistical and systematic uncertainties. The χ^2 values are displayed to assess the level of agreement between data and MC predictions.

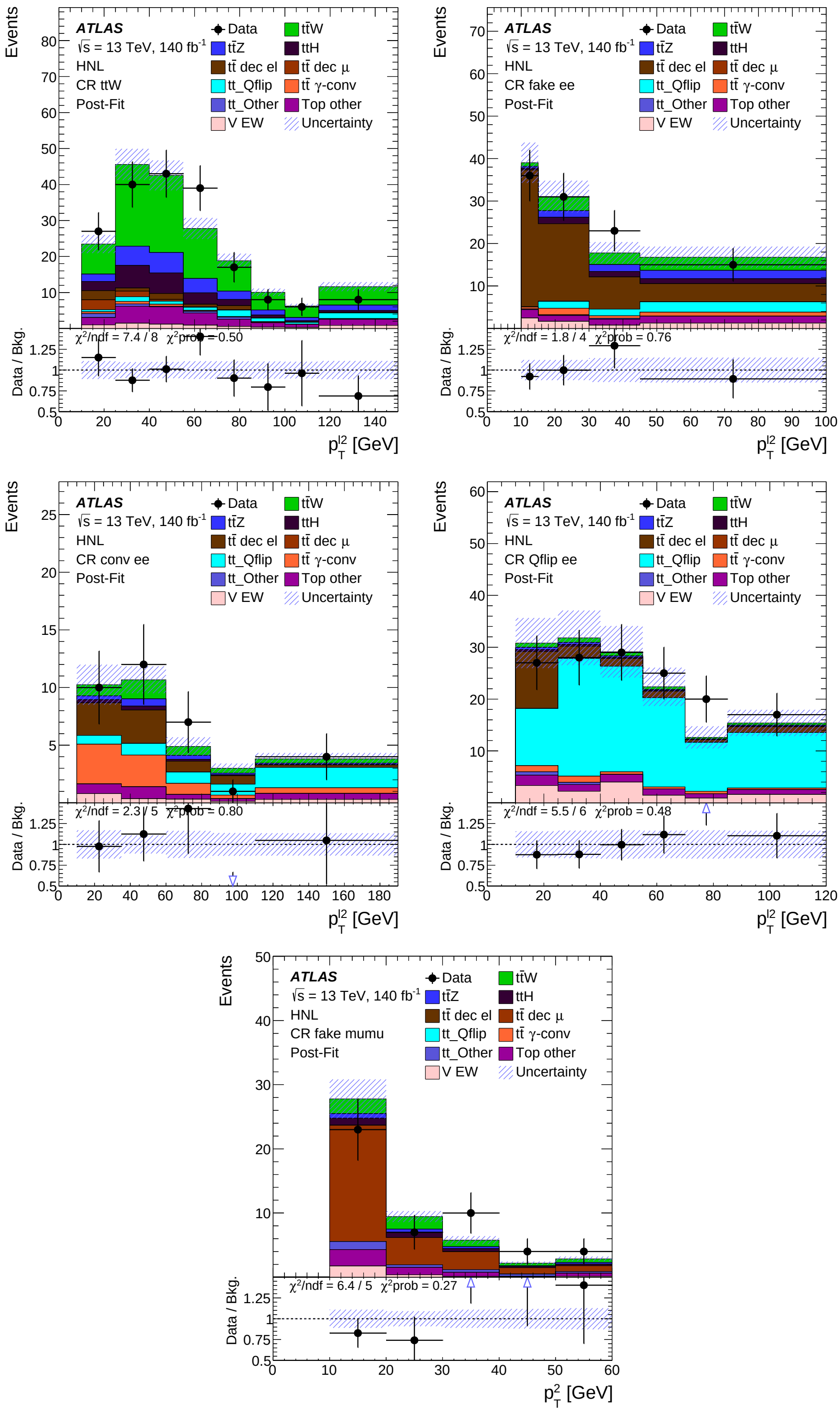

Figure 5.14: Modelling check for the subleading lepton transverse momentum in all control regions. Normalization factors taken from the CR-only fit are applied to the target backgrounds, and the uncertainty bands include both statistical and systematic uncertainties. The χ^2 values are provided for reference.

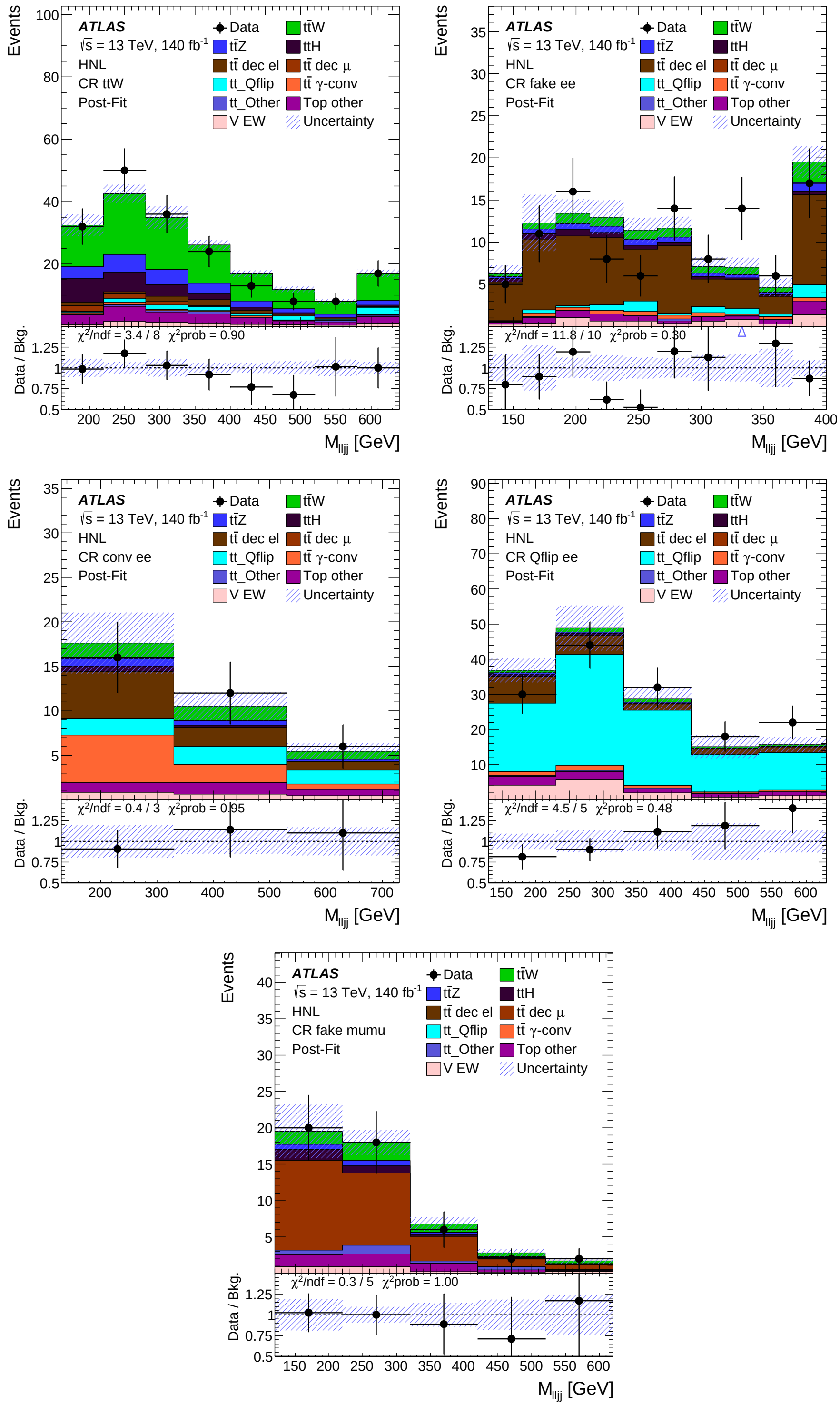

Figure 5.15: Modelling check for the invariant mass of the reconstructed BSM W boson (m_W) in all control regions. Normalization factors taken from the CR-only fit are applied to the target backgrounds, and the uncertainty bands include both statistical and systematic uncertainties. The χ^2 values are provided for each control region to quantify the agreement between data and MC predictions.

5.4.4 MVA training results

Due to the sufficiently discriminative variable distribution between the signal and the background, four variables shown in Section 5.4.3 are used in the 2LSS channel after optimization from the initial pool.

Figure 5.16 displays the distributions of the four most influential variables, showcasing their significant capability to distinguish between the merged signal mass and the assorted backgrounds under consideration. The distributions of the isolated signal mass points versus background variables' distributions are presented in Appendix B.

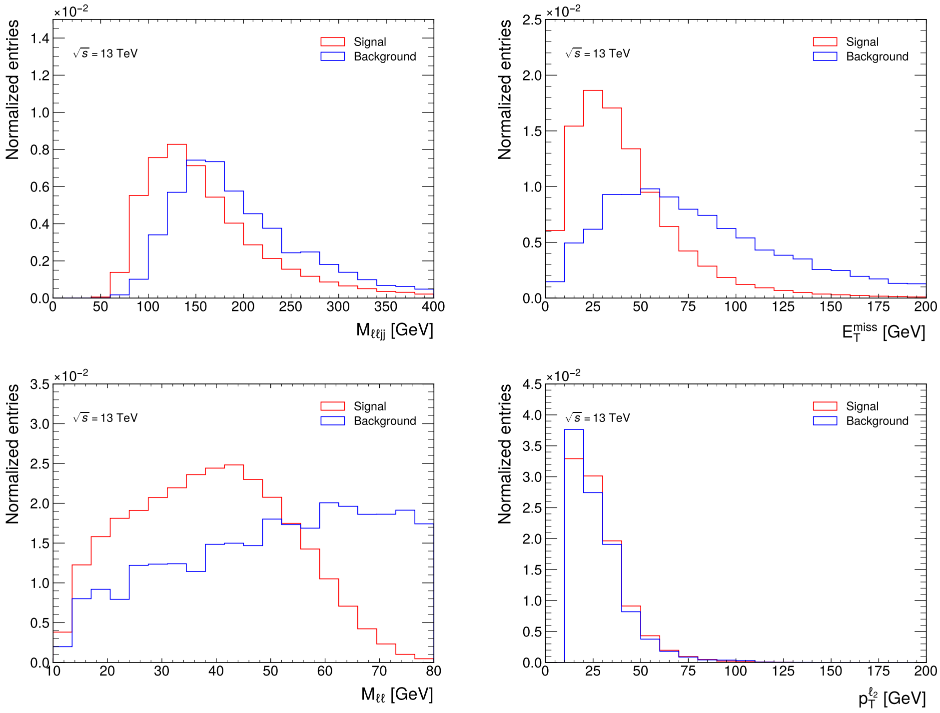

Figure 5.16: The distributions of the 4 input variables trained in MVA are shown here, and the signal events are combined with all the signal mass points.

The response distributions of the Boosted Decision Tree for both signals and backgrounds in the training and testing samples are presented in Figure 5.18. Train/test overtraining checks are also performed with the final optimized binning in the Signal Region. The distributions demonstrate excellent separation between the signal and background, indicating the robustness of the BDT approach in discriminating between the two. Refer to the plotting results of the training/testing comparison with uniform binning/final binning and the P-value of the Kolmogorov-Smirnov (KS) test to demonstrate that there is no apparent

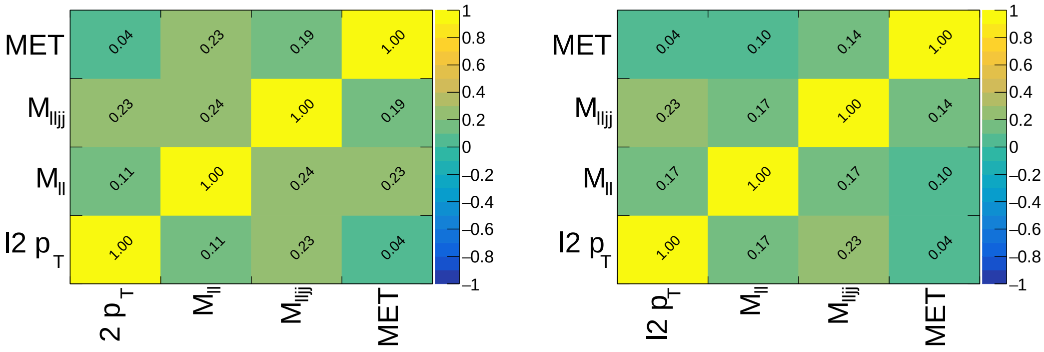

Figure 5.17: The correlation matrix of the selected 4 variables is shown here, and no correlation is higher than 0.25.

overtraining situation.

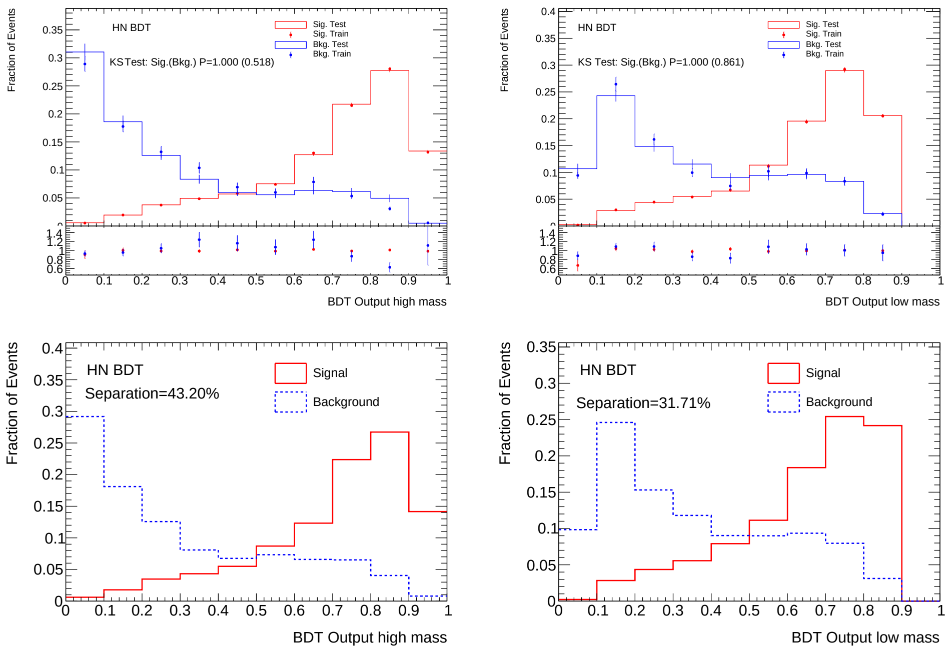

Figure 5.18: The BDT response (upper) of different mass sets of the signal is shown. There is good separation (lower) between signal and backgrounds, and no obvious overtraining issues were found.

To make sure the high/low mass sets are enough and properly describe all the mass points of the signal, we made a significant comparison between different MVA training models. Table 5.6 listed the stat-only expected significance results. The significance of the signal region is shown for different mass points in the first row, where each model is trained separately with all backgrounds. The second and third rows display the significance for different mass points, but each model is trained with the HNL50 and HNL25 vs backgrounds, respectively. The difference in significance between high and low mass regions is small, less than 6%. Due to limited statistics for signal masses (HNL15 - HNL75), we merge the $ee/\mu\mu$ channels and define two sets of MVA training for high and low-mass regions. For the high-mass region, the HNL45 - HNL75 signal samples are used, while the HNL15 - HNL40 signal samples are used for the low-mass region. The output from the high mass training is used to inject HNL45-HNL75 signal samples, and the output from the low mass training is used to inject HNL15 - HNL40 signal samples.

Signal mass in ee channel (GeV)	75	60	55	50	45	40	45	25	15
Significance(σ) results with their own weights	3.3	9.7	10.9	11.7	11.8	12.1	11.3	8.8	5.5
Significance(σ) results with weights from HNL50	3.1	9.6	11.0	11.7	11.9	11.9	11.0	7.8	4.6
Significance(σ) results with weights from HNL25						11.9	11.4	8.8	5.6
Significance(σ) results with weights from high mass set	3.3	9.9	11.4	11.7	11.8				
Significance(σ) results with weights from low mass set						11.5	11.1	9.2	5.3
Signal mass in $\mu\mu$ channel (GeV)	75	60	55	50	45	40	45	25	15
Significance(σ) results with their own weights	6.8	16.6	19.1	20.0	18.8	19.2	18.1	14.0	9.7
Significance(σ) results with weights from HNL50	6.4	16.2	19.1	20.0	19.0	18.5	17.5	12.6	8.4
Significance(σ) results with weights from HNL25						18.5	18.4	14.0	10.3
Significance(σ) results with weights from high mass set	6.7	16.9	19.4	20.5	19.4				
Significance(σ) results with weights from low mass set						18.1	17.9	14.6	9.5

Table 5.6: Expected significance performance with different bookMVA methods. The first row shows the significance from the signal region for different mass points, with each model trained independently on its corresponding signal and backgrounds. The second and third rows present significance scores using a fixed signal for training: HNL50 and HNL25, respectively. The last two rows repeat this but with a merged high/low mass signal.

5.4.5 Signal Region Definition with Multivariate Analysis Techniques

The signal region for this analysis is defined by requiring at least two same-sign same-flavor (SSSF) leptons, at least two b-tagged jets passing the 85% working point, and at least four light jets. This selection criterion ensures a robust signal region for the 2ℓSS (two same-sign leptons) channel, optimized for sensitivity to the signal while effectively suppressing background contributions.

The analysis was performed using `TRExFitter`, a widely-used tool within the ATLAS collaboration, which incorporates both experimental and theoretical uncertainties for signal and background processes, as detailed in Section 5.5. To optimize the binning of kinematic distributions, we employed the automatic binning method transformation D (with $Z_b = 3$ and $Z_s = 3$) across all regions. This method ensures that the bin-by-bin Monte Carlo statistical uncertainty of the backgrounds remains below 20%. Additionally, to maintain sufficient statistical power, we imposed a minimum background yield of 3 events (reweighted sum of events) per bin after automatic classification. In cases where the signal contribution was negligible in the first few bins, these bins were merged to ensure that the signal events in the first bin constituted more than 3% of the total signal events.

The pre-fit event yields for the HNL50 signal in the ee and $\mu\mu$ channels are presented in Table 5.7 and Table 5.8, respectively. The pre-fit results for the 2ℓSS channel signal region using the BDTGscore variable for all mass points can be found in Appendix D.

SS2L ee	
HNL 50 N1	59 ± 8
Top other	5.4 ± 2.2
$t\bar{t}$ decay el	9 ± 4
$t\bar{t}$ Q-flip	1.6 ± 1.1
$t\bar{t}\gamma$ conv	9.6 ± 2.5
$t\bar{t}Z$	5.1 ± 1.1
$t\bar{t}W$	9.6 ± 2.7
V EW	2.4 ± 0.9
$t\bar{t}H$	7.6 ± 1.3

Table 5.7: The pre-fit event yields in ee channel with the signal mass at 50 GeV. The $t\bar{t}$ IFF categories contribute approximately half of the total background events. Signal events are normalized to a cross-section of 0.05 pb.

SS2L $\mu\mu$	
HNL 50 N2	125 ± 16
Top other	6.5 ± 3.3
$t\bar{t}$ other	12 ± 4
$t\bar{t}$ decay mu	12 ± 7
$t\bar{t}Z$	5.6 ± 1.1
$t\bar{t}W$	17 ± 5
V EW	1.7 ± 1.3
$t\bar{t}H$	11.6 ± 1.9

Table 5.8: The pre-fit event yields in the $\mu\mu$ channel with the signal mass at 50 GeV. Compared to the ee channel, a larger contribution is observed from the $t\bar{t}W$ and $t\bar{t}Z$ samples. Signal events are normalized to a cross-section of 0.05 pb.

5.5 Systematic uncertainties

In this analysis, we implement the systematic uncertainties affecting the ATLAS multi-lepton searches, focusing on both experimental and theoretical aspects. The experimental uncertainties arise from lepton reconstruction and identification, jet calibration, energy scales, and missing transverse energy. These uncertainties are calibrated using Monte Carlo simulations, with scale factors applied to correct for potential mis-modelling of the detector. For jets, individual components of the jet energy scale and resolution are treated as separate nuisance parameters (NPs), accounting for pile-up effects, flavour dependence, and detector calibration accuracy. The theoretical uncertainties related to Monte Carlo modelling include variations in parton distribution functions, renormalization, and factorization scales, with particular emphasis on background processes such as $t\bar{t}$ and their associated uncertainties. The symmetrisation and smoothing of uncertainties are applied to improve the stability and reliability of the analysis. Symmetrisation ensures that systematic uncertainties affecting different regions of phase space do not introduce artificial asymmetries, which could bias the final results. Smoothing helps reduce statistical fluctuations in the uncertainty estimates, preventing overfitting to statistical noise in limited data regions. These steps provide a more robust and interpretable uncertainty treatment, ensuring that variations in the results are driven by genuine systematic effects rather than statistical artifacts. The symmetrisation and smoothing details are described in

Section 5.5.4.

5.5.1 Experimental systematics

The uncertainty in the combined integrated luminosity for the 2015–2018 data-taking period, corresponding to $140\,\mathrm{fb}^{-1}$, is 0.83% [131].

Lepton efficiency includes reconstruction, identification, isolation, and trigger efficiencies. In Monte Carlo simulations, these efficiencies are corrected using scale factors, calculated as the ratio of efficiencies measured in data and simulations. The tag-and-probe method in $Z \to ee$ decays for electrons [132] and $Z \to \mu\mu$ decays for muons [133] is employed to determine these scale factors. The SFs, which depend on E_{T}^{miss} and η, are varied by one standard deviation up and down to assess the uncertainty's impact on lepton efficiency.

Lepton energy (momentum) is calibrated using Monte Carlo-based techniques, with corrections derived from studies of Z boson dileptonic decays. These correction factors account for detector mis-modeling and are also varied by one standard deviation to evaluate lepton energy (momentum) scale uncertainties. For electrons, the energy scale and resolution are combined with those of photons and referred to as the e/γ scale and resolution [132]. For muons, corrections are applied for momentum scale and resolution uncertainties, which include combined uncertainties from the Muon Spectrometer and the Inner Detector tracking system. Additional uncertainties address charge-dependent corrections (the "sagitta bias") applied in the data [134].

The SFs for lepton trigger efficiencies, as detailed in Table 5.2 and Table 5.3, are provided by the `TrigGlobalEfficiencyCorrection` package [135]. The associated uncertainties arise from the individual trigger SFs, which are derived similarly to the identification and isolation SFs for both electrons and muons.

Uncertainties in the MET soft-track component (the "soft term"), which cannot be attributed to any reconstructed or calibrated physics object (the "hard term"), are derived from data-MC comparisons of the p_{T} balance between the hard and soft MET components [136]. The scale and resolution uncertainties of the soft term are treated as separate nuisance parameters [137].

Among the systematic uncertainties, those related to jet calibration (e.g., JES, JER, JVT, and fJVT) and the MET soft-track terms are particularly large and influential. The total uncertainty in the jet energy scale includes terms derived from in situ measurements, pile-up effects, flavor dependence, and other estimates, as summarized in Table 5.10. Most of these terms originate from in situ measurements, covering effects from analysis selection cuts, event topology, and Monte Carlo mis-modeling, as well as statistical limitations. These also include uncertainties related to the calibration of electrons, muons, and photons.

For JES uncertainty, information from test beam data, LHC collision data, and simulations is utilized. Data from collisions at $\sqrt{s} = 13\,\text{TeV}$ help calibrate the residual JES uncertainty [138, 139]. The “Category Reduction” uncertainty set [140] used here consists of 30 independent NPs, each with up/down variations depending on jet p_{T} and η.

For η inter-calibration [141], six NPs are derived: one covers modeling effects, one covers statistical uncertainties, and four parameterize non-closure. Pile-up effects are described by four NPs, accounting for offsets and p_{T} dependence in $< \mu >$ and N_{PV}, as well as event topology dependence of the density metric ρ.

Flavor dependence uncertainties, based on simulations, account for differences in jet response between quark-, gluon-, and b-initiated jets. The punch-through uncertainty addresses mis-modeling in Global Sequential Calibration [141], while the high-p_{T} single-particle uncertainty covers regions beyond 2.4 TeV, based on individual hadron response studies. For AFII-simulated MC samples, a non-closure uncertainty accounts for jet response differences compared to full detector simulations.

Accurate jet energy resolution is essential for detailed measurements of SM jet production. The “Full JER” smearing model [140] introduces 13 NPs, including terms for fast-simulation and full-simulation samples. To align the simulation with data, two types of smearing procedures are applied, depending on the detector simulation type.

Jet vertex track and forward JVT uncertainties are handled via the `JetJvtEfficiency` package [123] by applying event weights.

For b-jets, b-tagging distinguishes between jets from b-quarks and light-flavor jets. Each jet is assigned a working point, and the b-tagging uncertainties for each jet type are determined by varying calibration SFs up and down. These uncertainties are decomposed into independent components using the eigenvector method, resulting in 45 NPs for b-jets, and 20 NPs each for c-jets and light-flavor jets [68].

In summary, the ATLAS performance groups evaluate experimental systematic treatments, which are incorporated in the multi-lepton analysis either as event re-weighting (e.g., b-tagging and pile-up) or as rescaling/smearing of object energy and momentum for scale and resolution uncertainties.

The list of lepton- and b-tagging-related systematics is provided in Table 5.9 and Table 5.11, along with their type, description, and corresponding workspace name. The "Application" row indicates the method used in the analysis (Event Weight or p_{T} Weight).

Experimental Systematics on Leptons			
Type	Description	Systematics Name	Application
		Muons	
Efficiencies	Reconstruction and identification	MU_SF_ID_[STAT,SYST]	Event Weight
	Reconstruction and Identification (low p_{T})	MU_SF_ID_[STAT,SYST]_LOWPT	Event Weight
	Isolation	MU_SF_Isol_[STAT,SYST]	Event Weight
	Track To Vertex Association	MU_SF_TTVA_[STAT,SYST]	Event Weight
	Trigger	MU_SF_Trigger_[STAT,SYST]	Event Weight
p_{T} Scale	p_{T} Scale	MUONS_SCALE	p_{T} Correction
Resolution	Momentum Resol.	MUONS_CB	p_{T} Correction
	MS Momentum Resol. (charge dependent)	MUONS_SAGITTA_[RHO,DATASTAT]	p_{T} Correction
		Electrons	
Efficiencies	Reconstruction	EL_SF_ID	Event Weight
	Identification	EL_SF_Reco	Event Weight
	Isolation	EL_SF_Isol	Event Weight
	Trigger	EL_SF_Trigger	Event Weight
Scale Factor	Energy Scale	EG_SCALE_ALL	Energy Correction
		EG_SCALE_AF2	Energy Correction
Resolution	Energy Resolution	EG_RESOLUTION_ALL	Energy Correction

Table 5.9: Summary of experimental systematics to be included in the analysis for muons and electrons. The type, description, name of systematics, and the mode of application are listed from left to right.

Experimental Systematics on Jets and $E_{\mathrm{T}}^{\mathrm{miss}}$			
Type	Origin	Systematics Name	Application
Jets			
Jet Vertex Tagger		JVT	Event Weight
Forward Jet Vertex Tagger		FJVT	Event Weight
Energy Scale	Calibration Method	JET_EffectiveNP_Detector[1,2]	p_{T} Correction
		JET_EffectiveNP_Mixed[1,3]	p_{T} Correction
		JET_EffectiveNP_Modelling[1,4]	p_{T} Correction
		JET_EffectiveNP_Statistical[1,6]	p_{T} Correction
	η inter-calibration	JET_EtaIntercalibration_Modelling	p_{T} Correction
		JET_EtaIntercalibration_NonClosure ($\times 4$)	p_{T} Correction
		JET_EtaIntercalibration_TotalStat	p_{T} Correction
	High p_{T} jets	JET_SingleParticle_HighPt	p_{T} Correction
	Pile-Up	JET_Pileup_OffsetNPV	p_{T} Correction
		JET_Pileup_OffsetMu	p_{T} Correction
		JET_Pileup_PtTerm	p_{T} Correction
		JET_Pileup_RhoTopology	p_{T} Correction
	Non Closure	JET_PunchThrough_MC16	p_{T} Correction
		JET_PunchThrough_AFII	p_{T} Correction
		JET_RelativeNonClosure_AFII	p_{T} Correction
	Flavour	JET_Flavor_Response	p_{T} Correction
		JET_BJES_Response	p_{T} Correction
		JET_Flavor_Composition	p_{T} Correction
Resolution		JET_JER_EffectiveNP_[1,11]	p_{T} Correction
		JET_JER_EffectiveNP_12restTerm	p_{T} Correction
		JET_JER_DataVsMC_MC16	p_{T} Correction
		JET_JER_DataVsMC_AFII	p_{T} Correction
$E_{\mathrm{T}}^{\mathrm{miss}}$			
Soft Tracks Terms	Resolution	MET_SoftTrk_ResoPerp	p_{T} Correction
	Resolution	MET_SoftTrk_ResoPara	p_{T} Correction
	Scale	MET_SoftTrk_Scale	p_{T} Correction

Table 5.10: The $E_{\mathrm{T}}^{\mathrm{miss}}$ systematics are included here, but no selection of it in our analysis. Jet systematics take into account the effects of jets calibration method, η inter-calibration, high p_{T} jets, pile-up, non-closure, flavor response, JER variations. The effects from ATLAS fast simulation also show on the JER and jet PunchThrough/RelativeNonClosure. They are all identified as effective parameters.

Experimental Systematics on b-jets and Pile-up Reweighting		
Type	Origin	Systematics Name
b-tagging		
Scale Factors	DL1r b-tagger efficiency on b-originated jets	bTagSF_DL1r_Continuous_B[0-44]
	DL1r b-tagger efficiency on c-originated jets	bTagSF_DL1r_Continuous_C[0-19]
	DL1r b-tagger efficiency on light-flavoured jets	bTagSF_DL1r_Continuous_Light[0-19]
Pile-up Reweighting		
Pile-up Reweighting		weight_pileup

Table 5.11: Summary of experimental systematics for b-tagged jets in the analysis, using the DL1r tagging algorithm at the 85% Working Point. All b-tagging-related systematics on $b/c/$light jets are applied as event weights. Their type, description, and name of the systematic are listed from left to right.

5.5.2 Theoretical uncertainties

Systematic effects from MC modeling are evaluated by comparing different generators or varying event generation parameters.

For the HNL signal samples generated using MadGraph+Pythia8, the following modeling systematics are incorporated:

- The uncertainty on parton distribution functions is propagated according to the PDF4LHC15 prescription [142], utilizing 30 nuisance parameters. The systematic uncertainty is computed by comparing the PDF variations to the PDF4LHC15 baseline prediction and symmetrizing them. Each of the 30 PDF variations is treated as an individual nuisance parameter, with one-sided symmetrization applied.

- Independent variations of the renormalization and factorization scales (μ_R and μ_F) are taken into account during signal production. Events are reweighted using internal weights where μ_R and μ_F are varied by factors of two from their nominal values. The MadGraph generator is effective in describing the kinematics of signal events, as outlined in Section 5.1.1. Two-sided symmetrization is applied.

The dominant background for this search is non-allhadronic $t\bar{t}$. The nominal $t\bar{t}$ sample (DSID 410470) is generated with Powheg-Box V2, interfaced with Pythia8 for parton showering. The uncertainties considered for this background are:

- Two additional samples estimate uncertainties related to the matrix-element-to-parton-shower matching scale in $t\bar{t}$ production. One sample uses the *hdamp* parameter set to $3 \times m_t$, keeping all other generator settings the same as the nominal sample. Another sample uses the *pThard* parameter set to 1. One-sided symmetrization is applied.

- To estimate uncertainties from the parton shower and hadronization model choice, the Powheg+Pythia8 sample is compared to a Powheg+Herwig7.2.1 sample. One-sided symmetrization is applied.

- Independent variations of the renormalization and factorization scales (μ_R and μ_F) are included to account for missing higher-order corrections in the matrix element calculation. Events are reweighted using internal weights in which μ_R and μ_F are varied by factors of two from their nominal values. Two-sided symmetrization is applied.

- PDF uncertainties are propagated using the PDF4LHC15 prescription, with 30 nuisance parameters. Each variation is treated as a separate nuisance parameter, with one-sided symmetrization applied.

- Uncertainties in initial-state radiation are estimated by comparing the nominal Powheg+Pythia8 sample to event weights produced with higher and lower radiation scenarios, using the Pythia A14 *var3c* eigentune. Two-sided symmetrization is applied.

- Final-state radiation modeling is evaluated using the following weights:

  – `isr:muRfac=1.0_fsr:muRfac=2.0`

  – `isr:muRfac=1.0_fsr:muRfac=0.5`

  These correspond to variations of μ_R for QCD emissions in the final-state shower. Two-sided symmetrization is applied.

For the modeling of $t\bar{t}W$:

- Nominal: Sherpa-2.2.10 (QCD+EWK).

- Shower systematics: The difference between Powheg+Pythia and Powheg+Herwig is applied to the nominal Sherpa 2.2.10 sample. One-sided symmetrization is applied.

- Generator systematics: Sherpa-2.2.10 is compared to a MadGraph5_aMC@NLO + Pythia8 sample using the FxFx merging scheme. One-sided symmetrization is applied.

- PDF and scale variations: Independent variations of the renormalization and factorization scales (μ_R and μ_F) by factors of two. The PDF uncertainty is propagated using PDF4LHC15 with 30 nuisance parameters. Each variation is treated as a separate nuisance parameter. One-sided symmetrization is applied.

- Scale variations: Independent variations of μ_R and μ_F by factors of two. Two-sided symmetrization is applied.

For the modeling of $t\bar{t}Z$:

- Nominal: MadGraph5_aMC@NLO + Pythia8.

- Shower systematics: MadGraph5_aMC@NLO + Herwig7 is considered, with one-sided symmetrization applied.
- Alternative scale variation: MadGraph5_aMC@NLO + Pythia8 with A14Var3 for the A14 shower tune variation. Two-sided symmetrization is applied.
- Scale variations: Independent variations of μ_R and μ_F by factors of two. Two-sided symmetrization is applied.

For the modeling of $t\bar{t}H$:

- Nominal: Powheg + Pythia8.
- Additional samples estimate uncertainties from matrix element choice, generated with the *pThard* parameter set to 1 (the default is 0). One-sided symmetrization is applied.
- Uncertainties from the parton shower and hadronization model choice are estimated by comparing the Powheg+Pythia8 sample to a Powheg+Herwig7 sample. One-sided symmetrization is applied.
- Independent variations of μ_R and μ_F account for missing higher-order corrections in the matrix element calculation. Events are reweighted using internal weights where μ_R and μ_F are varied by factors of two. Two-sided symmetrization is applied.
- PDF uncertainties are propagated using the PDF4LHC15 prescription with 30 nuisance parameters. Each variation is treated as a separate nuisance parameter. One-sided symmetrization is applied.
- ISR uncertainties are estimated by comparing the nominal Powheg+Pythia8 sample to event weights produced with higher and lower radiation scenarios using the Pythia A14 *var3c* eigentune. Two-sided symmetrization is applied.
- FSR modeling is evaluated using the following weights:
  - `isr:muRfac=1.0_fsr:muRfac=2.0`
  - `isr:muRfac=1.0_fsr:muRfac=0.5`

  These correspond to variations of μ_R for QCD emissions in the final-state shower. Two-sided symmetrization is applied.

5.5.3 Background Normalisation Uncertainties

Uncertainties of 12% and 10% are included for the $t\bar{t}Z$ and $t\bar{t}H$ production cross sections respectively [143].

For the "V EW" background, which includes half of the Z+jets events (with a recommended 20% uncertainty derived from measurements of the Z boson cross section [144]) and half of the VV/VVV events (with uncertainties of 60%/50% respectively, derived from [145]), a 30% cross-section uncertainty is set as a weighted average consideration.

The "KnownUnknown" IFF category from the $t\bar{t}$ sample is labeled as the "tt_other" sample and is assigned a 50% cross-section uncertainty as a conservative approach, given its non-negligible contribution to the muon channel (about 7%).

For other minor backgrounds labeled as "otherTop" and "t(tt)XX", which includes the production of three or four top quarks, $t\bar{t}+WW$, tZq, tWZ, single-top (in three channels: s, t, Wt), tHW, tHq, and ttXX ($ttWZ$, $ttHH$, $ttWZ$, $ttZZ$) and the not discussed IFF category classes in Section 5.3.1 from $t\bar{t}\gamma$, a relatively large uncertainty of 50% is assigned as a conservative approach. This value is based on previous analyses in a similar final state [146, 147] and is conservative enough to cover the predictions.

5.5.4 Symmetrisation and smoothing of the uncertainties

For systematic uncertainties featuring both 'up' and 'down' variations, the "TWOSIDED" symmetrization method is applied. The content of each bin is computed by taking the variation of (up − down)/2, which is then mirrored.

In cases where a one-sided variation is present (e.g., modeling uncertainties from an alternative generator), the "ONESIDED" symmetrization method is used. Here, the variation is mirrored around the mean value in each bin.

The systematic uncertainties related to leptons and b-tagging, detailed in Table 5.9 and Table 5.11, undergo "TWOSIDED" symmetrization. The same applies to jet and MET-related uncertainties, as demonstrated in Table 5.10, except for the soft-track component resolution of MET, which employs "ONESIDED" symmetrization.

The default "MAXVARIATION smoothing" procedure, implemented in TRExFitter, is applied to reduce the impact of Monte Carlo statistical fluctuations on the systematic templates. It is employed on all uncertainties with large statistical fluctuations to ensure that the impact on the pull/constraints of these nuisance parameters is not spurious.

5.6 Statistical Treatment

The TRExFitter is used as our main limit-setting framework. It uses a global likelihood function for all bins and nuisance parameters:

$$\mathcal{L}(\vec{n}, \vec{\Theta}^0|\mu, \vec{\Theta}) = \prod_{i\in\text{bins}} P\left(n_i|\mu S(\vec{\Theta}) + B(\vec{\Theta})\right) \cdot \underbrace{\prod_{j\in\text{NP}} G(\Theta_j^0|\Theta_j)}_{\text{systematics}}. \tag{5.8}$$

P and G are Poisson and Gaussian distributions, n the number of events, Θ the nuisance parameters, S and B are the signal and background predictions, and μ is the parameter of interest (POI, signal strength).

The one-sided profile likelihood ratio $\lambda(\mu)$ is used as the test statistic q_μ, which is the ratio between the maximized likelihood for a given μ and the maximized likelihood for all μ (conditional likelihood $\mathcal{L}(\mu, \hat{\hat{\theta}}_\mu)$ divided by unconditional likelihood $\mathcal{L}(\hat{\mu}, \hat{\theta}_\mu)$) as:

$$q_\mu = -2\ln\lambda(\mu), \tag{5.9}$$

with

$$\lambda(\mu) = \frac{\mathcal{L}(\mu, \hat{\hat{\theta}}_\mu)}{\mathcal{L}(\hat{\mu}, \hat{\theta}_\mu)}, \tag{5.10}$$

where $\hat{\mu}$ and $\hat{\theta}$ are the values of the parameters that maximize the likelihood function and $\hat{\hat{\theta}}$ are the values of the nuisance parameters that maximize the likelihood function for a given value of μ. The test statistic is evaluated with the `RooStats` package [148] and is used in the modified frequentist (CL_S) method [149] to obtain upper limits on the signal strength. The corresponding confidence levels are calculated as follows:

$$\text{CL}_{s+b} = \int_{q_{obs}}^{\infty} f(q|\mu)dq, \tag{5.11}$$

$$\text{CL}_b = \int_{q_{obs}}^{\infty} f(q|0)dq. \tag{5.12}$$

TRExFitter uses the CLs method to test the signal hypothesis. The CL_s value is defined as the ratio between the signal-plus-background CL and the background-only CL:

$$\mathrm{CL}_s = \frac{\mathrm{CL}_{s+b}}{\mathrm{CL}_b}. \tag{5.13}$$

The 95% confidence limit on the signal strength can be found by solving the equation:

$$\mathrm{CL}_s(\mu_{\mathrm{Limit}}) = 0.05. \tag{5.14}$$

Moreover, our main observable is the BDTGscore, trained in Section 5.4, which is evaluated in the signal regions using profile likelihood functions. As detailed in Section 5.1.2, all background samples and uncertainties are taken into consideration.

The following three subsections present the results of the **background-only fit in the control region**, the **fit to the Asimov data in both the signal and control regions**, and the **fit to real data in both the signal and control regions**. Each of these fits serves a distinct purpose in the analysis and is essential for ensuring the robustness and reliability of the final results.

The background-only fit in Section 5.6.1 could help to check the data/MC agreement in the control regions, and the post-fit values of the NPs obtained from this fit could be used to improve the background modeling in the signal region, ensuring a reliable background estimation.

The fit to the Asimov data in Section 5.6.2 is performed using a pseudo-dataset generated from the expected signal and background models, covering both the signal region and control region. This fit evaluates the sensitivity of the analysis, tests the statistical procedures, and estimates the expected significance of a potential signal. The Asimov dataset is constructed using the post-fit NPs from the background-only fit, ensuring consistent propagation of systematic uncertainties.

The fit to the real data in Section 5.6.3 is performed using the actual experimental data in both the signal region and control region. This fit simultaneously extracts the signal strength and constrains the background contributions while accounting for systematic uncertainties. The results are used to determine the presence or absence of a signal, set limits on the signal strength, and provide the final physics results.

5.6.1 Background-only fit in CRs

The background-only fit is performed across all control regions to constrain the normalization factors of the studied background processes. These include the heavy-flavor fake leptons (HF_fake_el and HF_fake_μ), charge misidentification (charge flip), photon conversions, and the $t\bar{t}W$ background, as detailed in Section 5.3.

In the fitting procedure, the normalization factors for all backgrounds associated with the IFF categories and the $t\bar{t}W$ process are left free to float. To maintain fit stability and avoid over-parameterization, systematic uncertainties with minimal impact—specifically those contributing less than 1% to the shape variation or less than 1% to the overall normalization—are pruned during the background-only fit.

Given that independent fits are conducted for the dielectron (ee) and dimuon ($\mu\mu$) channels, the normalization factors are extracted channel-by-channel:

- For the **ee channel**, the fit determines the normalizations of HF_fake_el, charge flip, photon conversions, and $t\bar{t}$ +W backgrounds using the corresponding templates.

- For the $\mu\mu$ **channel**, the normalizations of HF_fake_μ and $t\bar{t}$ +W are derived from their respective templates.

The pre-fit and post-fit comparisons are illustrated in Figures 5.19, 5.20, and 5.21. Due to limited statistics in the control regions, a one-bin fitting strategy is adopted for all CRs. This approach focuses on scaling the background predictions to match the observed data yields while remaining insensitive to potential mismodeling of kinematic distributions in the Monte Carlo simulations. The one-bin method provides a robust normalization constraint without introducing shape-dependent biases that could arise from low-statistics bins.

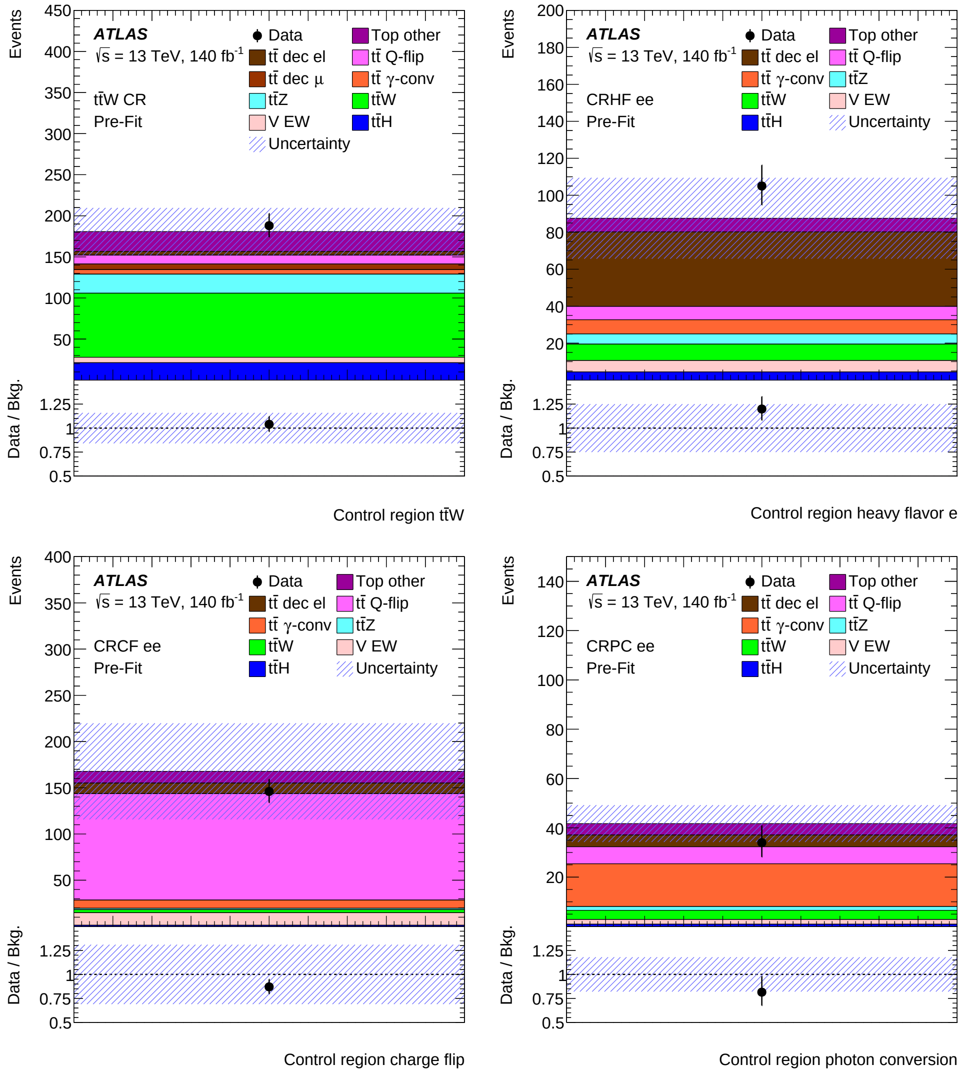

Figure 5.19: Pre-fit distributions in the four control regions in the ee channel. The uncertainty band includes Monte Carlo statistical uncertainties and all systematic uncertainties.

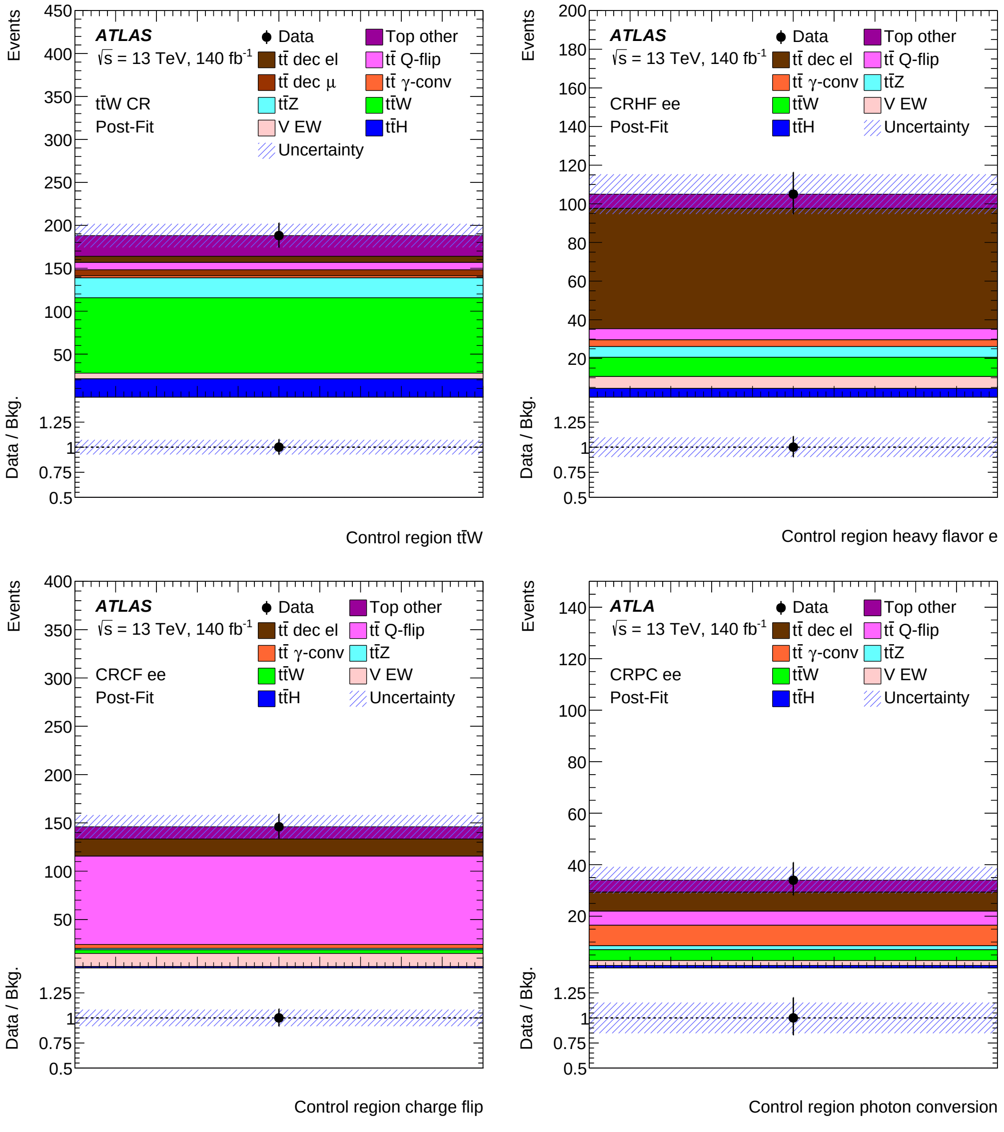

Figure 5.20: Post-fit distributions of the CR-only fit for the four control regions in the *ee* channel. The uncertainty band includes Monte Carlo statistical uncertainties and all systematic uncertainties.

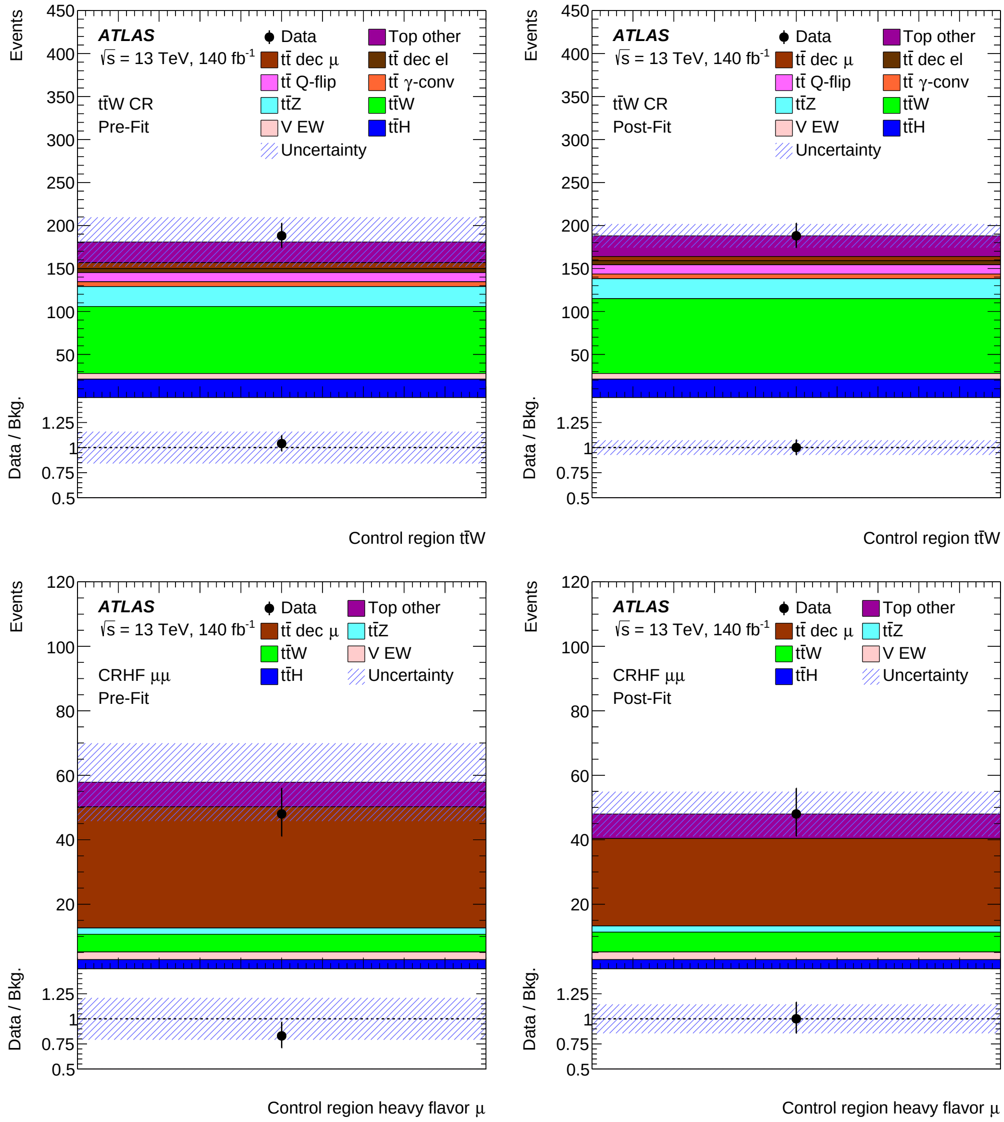

Figure 5.21: The pre-fit distributions (left side) and post-fit distributions under CR-only fit (right side) in $\mu\mu$ channel. The uncertainty bands include the Monte Carlo statistical uncertainty and all systematic uncertainties.

A summary of the resulting normalization factors from the CR-only fit can be seen in figures 5.22.

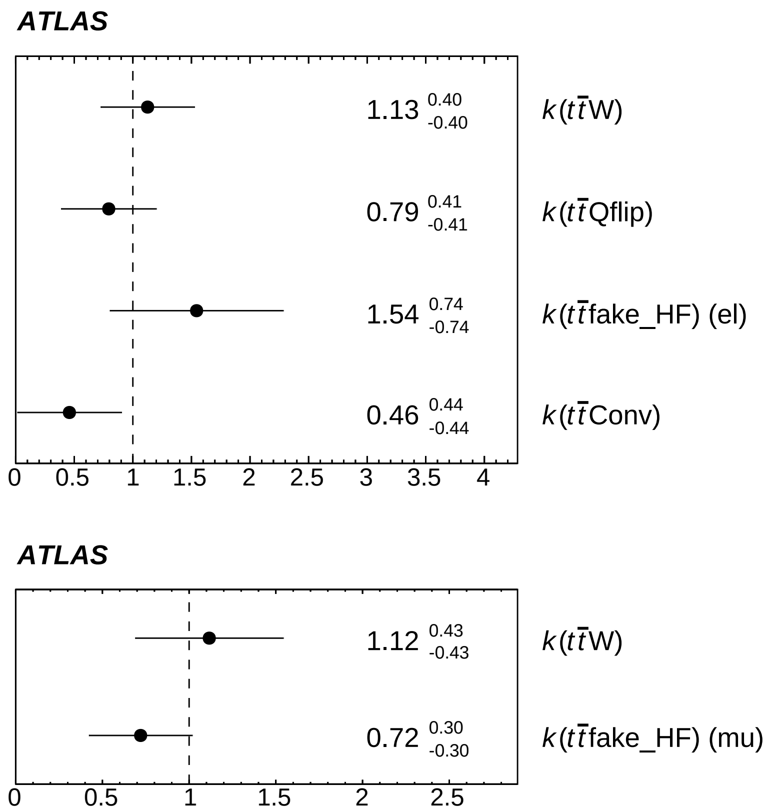

Figure 5.22: Summary of the normalization factors in the CR-only fit for the ee channel(upper) and $\mu\mu$ channel (lower). A similar NF result of the $t\bar{t}W$ is seen for the two channels.

Figures 5.23 display relevant constraints and pulls. The fit converged very successfully, and no NPs were over-pulled or over-constrained.

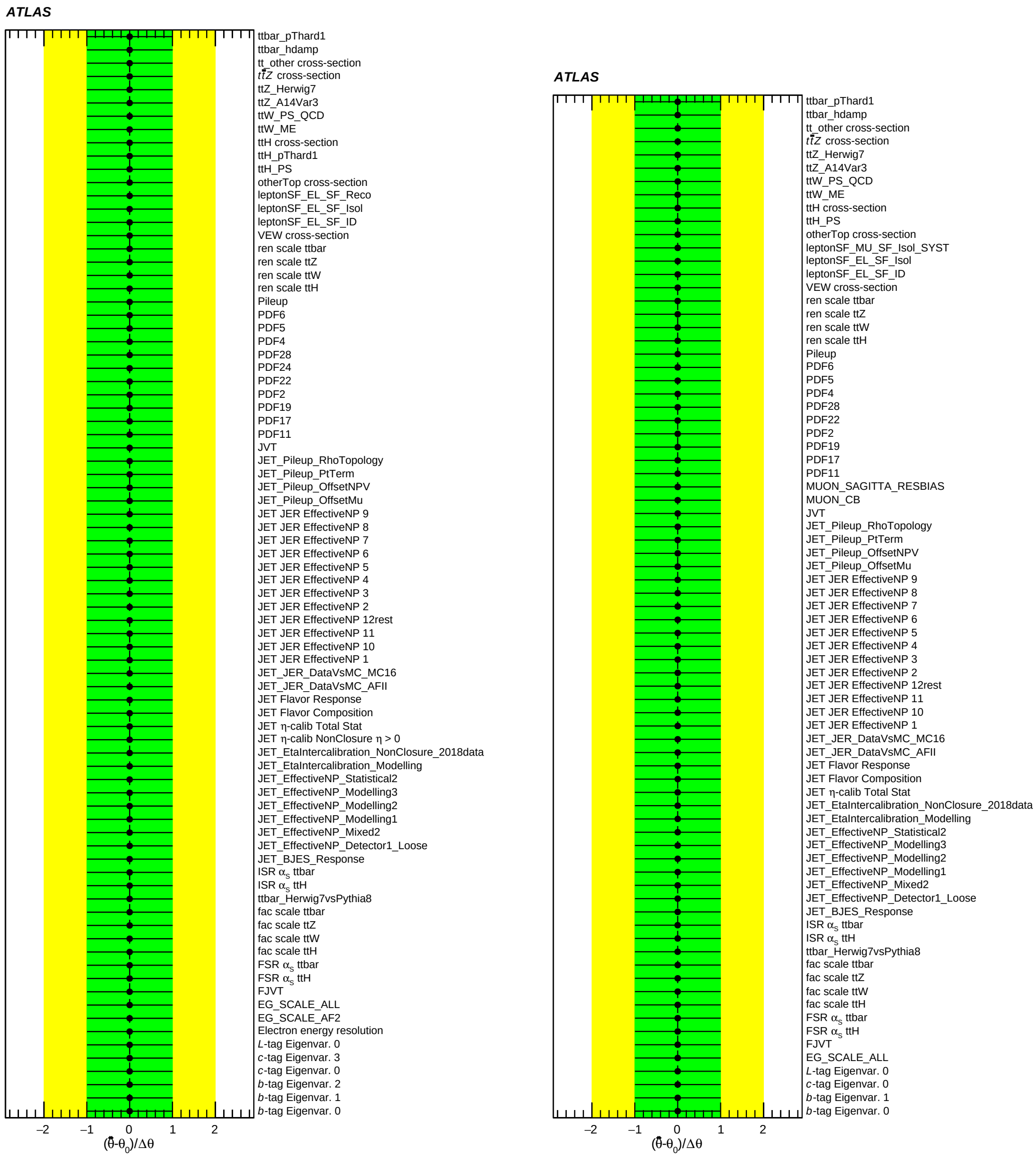

Figure 5.23: The pulls and constraints observed in the CR-only fit for the nuisance parameters related to all uncertainties are shown for the ee channel(left) and $\mu\mu$ channel (right).

5.6.2 The fit to the Asimov data (SR + CR)

This section presents the results of the fit to the Asimov data. All signal samples are normalized to 0.05 pb in the pre-fit stage, which does not affect the final limit-setting results. The fit to the Asimov data is performed in the SRs and CRs simultaneously. We treat signal plus background as the Asimov data, where data is generated using the post-fit values of all NPs obtained from the background-only fit described in the Section 5.6.1.

For the fit to the Asimov data

In Figure 5.24, it presents the post-fit signal region results with the signal mass at 50 GeV. The plots in the CRs should be consistent with the background-only results.

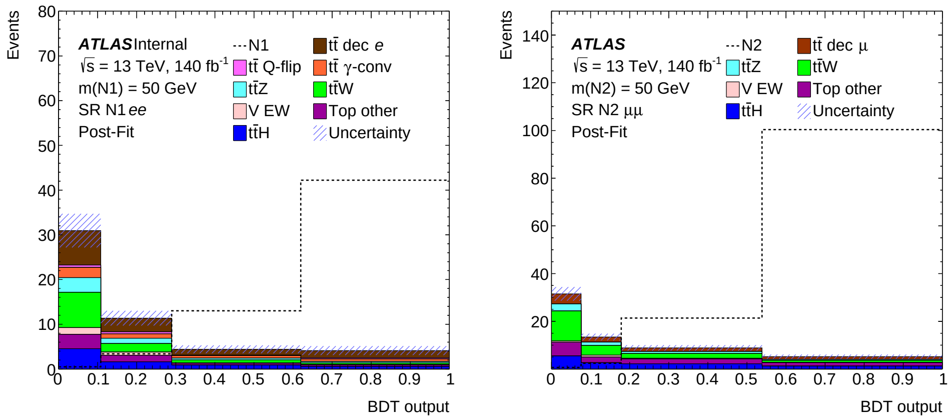

Figure 5.24: The post-fit result in BDTG score distribution in the ee channel (left) and $\mu\mu$ channel (right) with the signal mass points at 50 GeV. The signal cross-section is normalized to 0.05 pb. The uncertainty band includes the MC statistical uncertainties and all systematic uncertainties.

To account for all uncertainties and neglect those with negligible impact, we apply several pruning threshold cuts (0.5%, 1%, 5%) on the shape and overall uncertainties. If we set the threshold higher than 1% on shape, the number of nuisance parameters will be reduced by half. After checking the expected upper limit on the signal strength between different choices, we find that decreasing the 5% to 1% threshold on overall uncertainties results in a 1% drop in the limit, whereas there is almost no difference between 1% and 0.5% (less than 0.1%).

Simultaneously, an extremely low threshold (0.01% for both shape and overall) is tested and could lead to a substantial runtime increase without affecting the upper limit results compared to the 1% threshold. As a result, we opt to trim systematic uncertainties that are less than 1% for shape and 1% for overall uncertainties.

The pulls and constraints in Figure 5.25 display the best-fit values and associated uncertainties for all systematics that pass the pruning. There are no over pull/constrain issues observed.

After reviewing the correlation and pruning plots, the analysis indicates that the theoretical modeling uncertainties of the $t\bar{t}$ background and normalization factors have the most significant impact on the signal strength. The detailed plots could be seen in Appendix G

Expected limit on signal strength from fit to the Asimov data

The upper exclusion limit at 95% confidence level of the signal strength is shown in Table 5.12. To estimate the impact of the low statistics, we also added stat-only checks and a comparison of using toys to calculate the limit. The results are shown in Appendix E.

m_{N} [GeV]	15	25	35	40	45	50	55	60	70	75
Upper limit results on μ (ee)	0.42	0.19	0.14	0.14	0.13	0.13	0.14	0.17	0.36	0.70
Stat-only fit results (ee)	0.37	0.17	0.13	0.13	0.12	0.12	0.13	0.16	0.34	0.64
Upper limit results on μ ($\mu\mu$)	0.19	0.10	0.08	0.07	0.07	0.06	0.07	0.08	0.17	0.31
Stat-only fit results ($\mu\mu$)	0.17	0.09	0.07	0.07	0.06	0.06	0.06	0.07	0.15	0.28

Table 5.12: The upper limits on the signal strength for the split ee and $\mu\mu$ channels are extracted from the fit to the Asimov data and presented here. These limits are derived from the Boosted Decision Tree (BDTG) output, and the highest sensitivity is observed for the expected upper limits on the signal strength in the $ee/\mu\mu$ channel, specifically for the HNL50 case. For comparison, the corresponding results from the stat-only fit are also included, revealing an approximately 10% reduction in the limit results.

The stat-only fit to the Asimov data leads to an approximate 11% reduction in the upper limit results on the signal strength of the electron channel(9% on muon channel), which is also shown in Table 5.12. The interesting uncertainties in performance are shown on Appendix F.

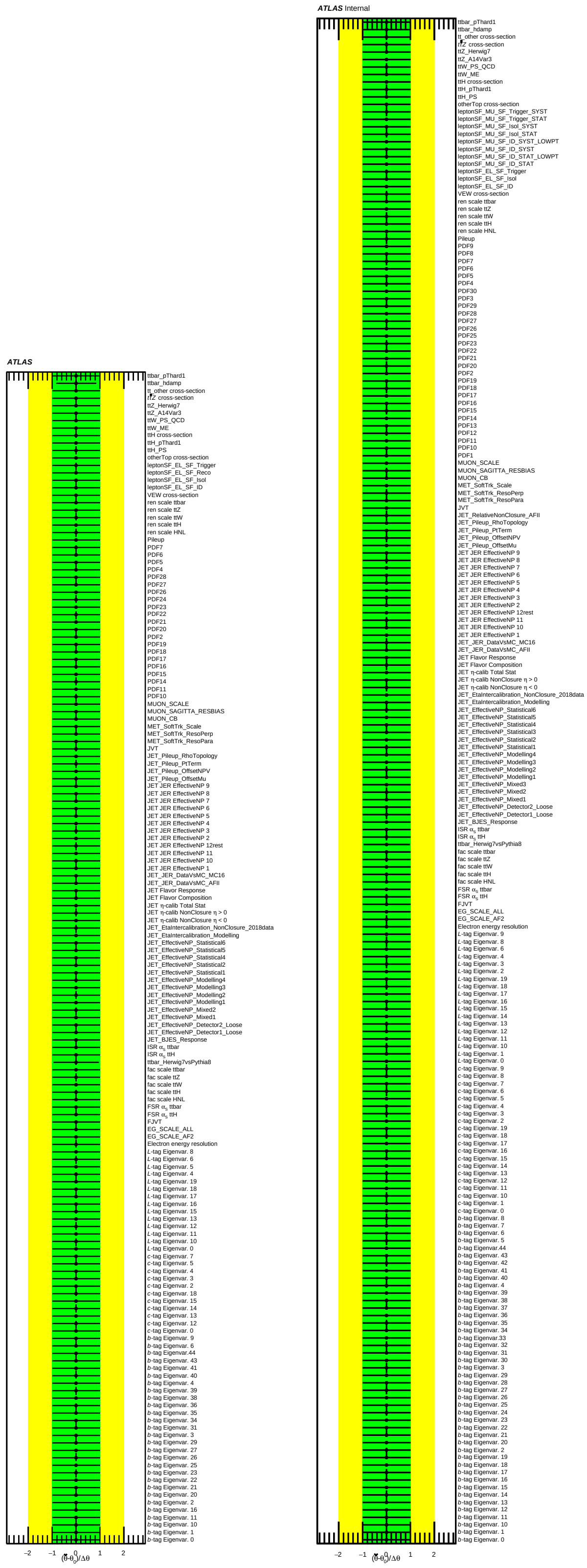

Figure 5.25: All nuisance parameters in the fit to Asimov data with signal mass at 50 GeV for ee channel (left plot) and the $\mu\mu$ channel (right plot).

The best sensitivity of the expected upper limits on the signal strength is the signal mass at 50 GeV on the ee/ $\mu\mu$ channel.

5.6.3 The fit to the real data (SR + CR)

This chapter presents the final fit results of the analysis. The full fit to real data described in this chapter was only performed once the b-only fit and fit to the Asimov data were found to be stable and produce consistent results.

For the fit to the real data

The pre-fit and post-fit plots of all the regions from the signal mass at 50 GeV are presented in Figure 5.26, Figure 5.27 and 5.28. All control regions are implemented using a one-bin strategy.

A summary of the resulting normalization factors can be seen in Figure 5.29. First and foremost, the signal normalisation can be seen to be compatible with Zero. Additionally, it can be observed that the other NFs are scaled up/down compared to the nominal normalisation. This observation is in agreement with the background-only fit results.

The post-fit event yields results in the fits to the real data, with the signal mass at 50 GeV is shown in Table 5.13 and Table 5.14

The pulls and constraints in Figure 5.30 display the best-fit values from all associated systematics uncertainties that pass the pruning.

Aside from the pulls and constraints of NPs in the fit, their impact on the obtained signal normalisation μ is of interest. This can be estimated by fixing a given NP to a certain value (either the up or down-variation using the pre- or post-fit uncertainty). Figure 5.31 presents the Top 20 ranking of the nuisance parameters in the fit to the real data.

The correlation matrix of the nuisance parameters from the fit to the real data is shown in Figures 5.32 and 5.33.

Expected and observed limit on signal strength from the fit to the real data

The expected and observed upper exclusion limit at 95% confidence level of the signal strength is shown in Table 5.15.

SS2L ee	
HNL 50 N1	3.1 ± 4.0
Top other	5.5 ± 2.2
$t\bar{t}$ decay el	13 ± 6
$t\bar{t}$ Q-flip	1.4 ± 1.0
$t\bar{t}$ conv	3.3 ± 2.9
$t\bar{t}\gamma$ conv	1.4 ± 1.2
$t\bar{t}Z$	5.1 ± 1.1
$t\bar{t}W$	10.5 ± 2.6
V EW	2.4 ± 0.9
ttH	7.6 ± 1.3
Total prediction	53 ± 6
Data	52

Table 5.13: Post-fit event yields of the fit to the real data with signal mass at 50 GeV, where all $t\bar{t}$ IFF categories contribute about half of the total background events.

SS2L $\mu\mu$	
HNL 50 N2	0.5 ± 3.1
Top other	11 ± 4
$t\bar{t}$ decay mu	7.9 ± 3.2
$t\bar{t}Z$	5.6 ± 1.1
$t\bar{t}W$	18 ± 5
V EW	1.9 ± 1.5
ttH	11.3 ± 1.9
Total prediction	56 ± 5
Data	51

Table 5.14: Post-fit event yields of the fit to the real data with signal mass at 50 GeV in $\mu\mu$ channel. More events are coming from the $t\bar{t}W$ and $t\bar{t}Z$ samples, compared with ee channel.

m_{N} [GeV]	15	25	35	40	45	50	55	60	70	75
Exp.Upperlimit results on μ (ee)	0.54	0.22	0.16	0.14	0.14	0.13	0.14	0.17	0.37	0.72
Obs.Upperlimit results on μ (ee)	0.94	0.38	0.25	0.21	0.21	0.19	0.20	0.24	0.52	1.04
Exp.Upperlimit results on μ ($\mu\mu$)	0.23	0.11	0.08	0.07	0.06	0.06	0.06	0.08	0.16	0.30
Obs.Upperlimit results on μ ($\mu\mu$)	0.20	0.11	0.07	0.07	0.06	0.06	0.07	0.08	0.17	0.30

Table 5.15: The upper limits on the signal strength for the split ee and $\mu\mu$ channels are extracted from the fit to the real data and presented here. These limits are derived from the Boosted Decision Tree output, and the highest sensitivity is observed for the expected upper limits on the signal strength in the $ee/\mu\mu$ channel, specifically for the signal mass at 50 GeV case.

The best sensitivity of the expected/observed upper limits on the signal strength is the signal mass at 50 GeV on the ee/ $\mu\mu$ channel, consistent with the fit to the Asimov data results.

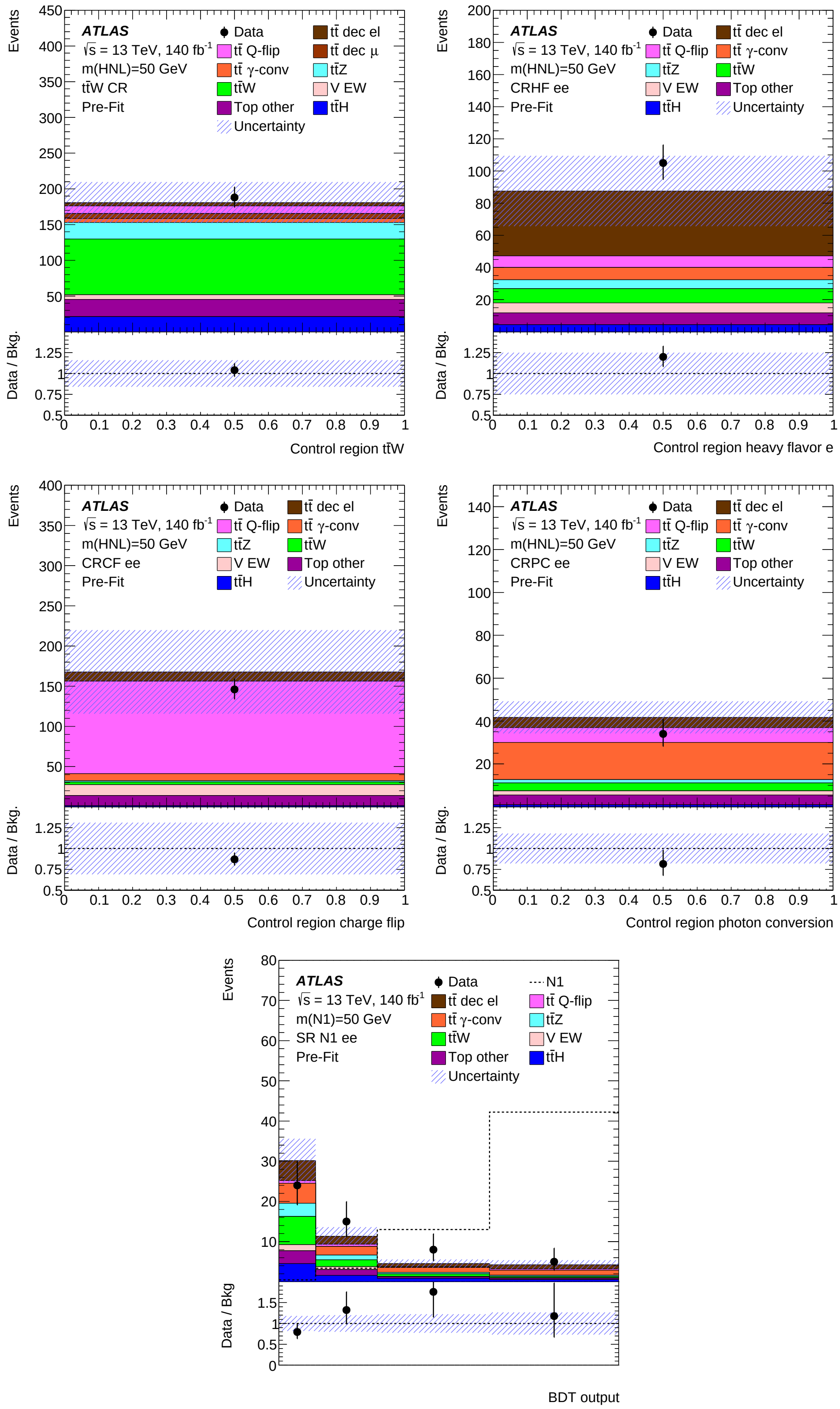

Figure 5.26: Pre-fit distributions of the fit to the real data in the four control regions and the signal region of the *ee* channel. The uncertainty band includes Monte Carlo statistical uncertainties and all systematic uncertainties.

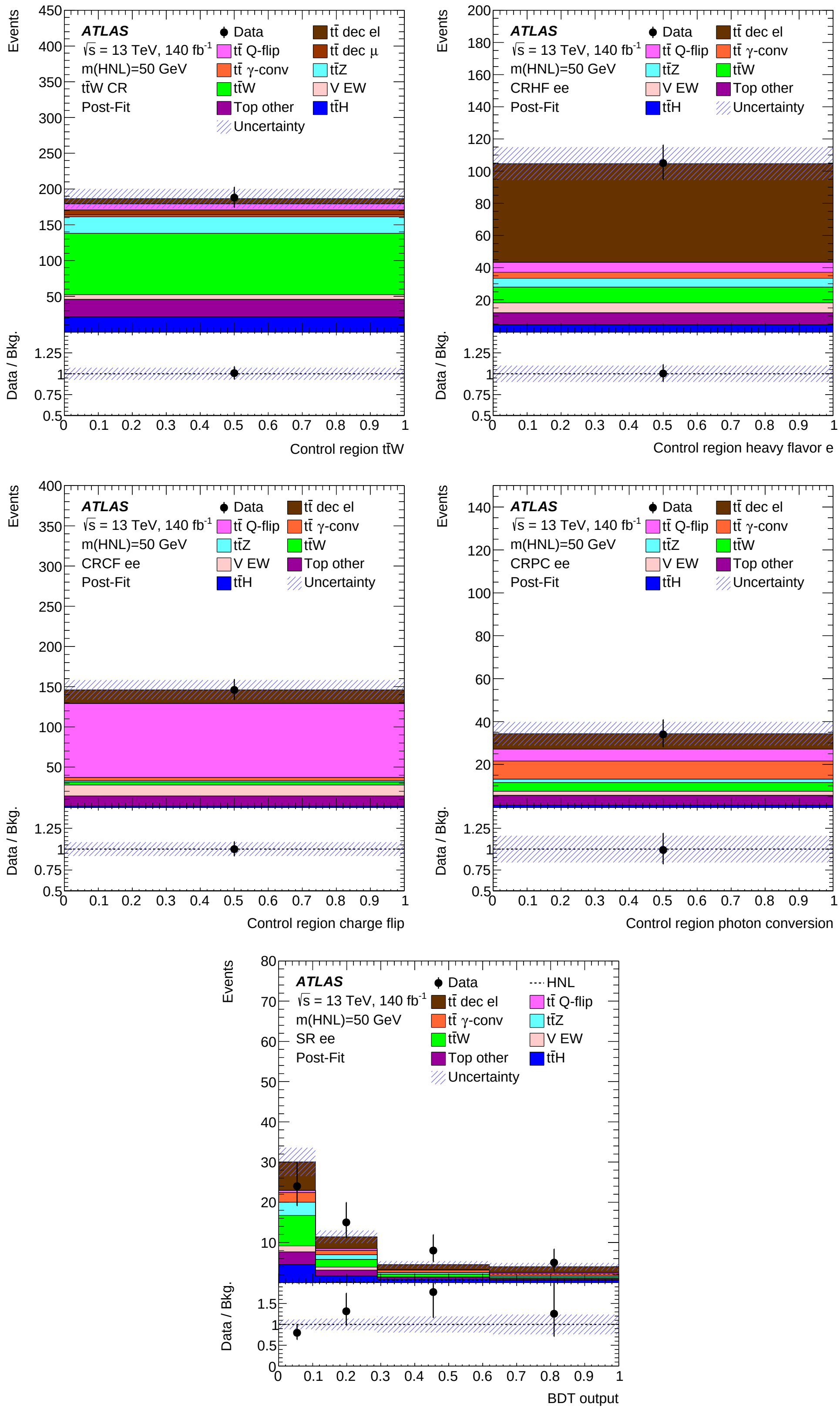

Figure 5.27: Post-fit distributions in 4 control regions and the signal region for the *ee* channel for the fit to the real data. The uncertainty band includes Monte Carlo statistical uncertainties and all systematic uncertainties.

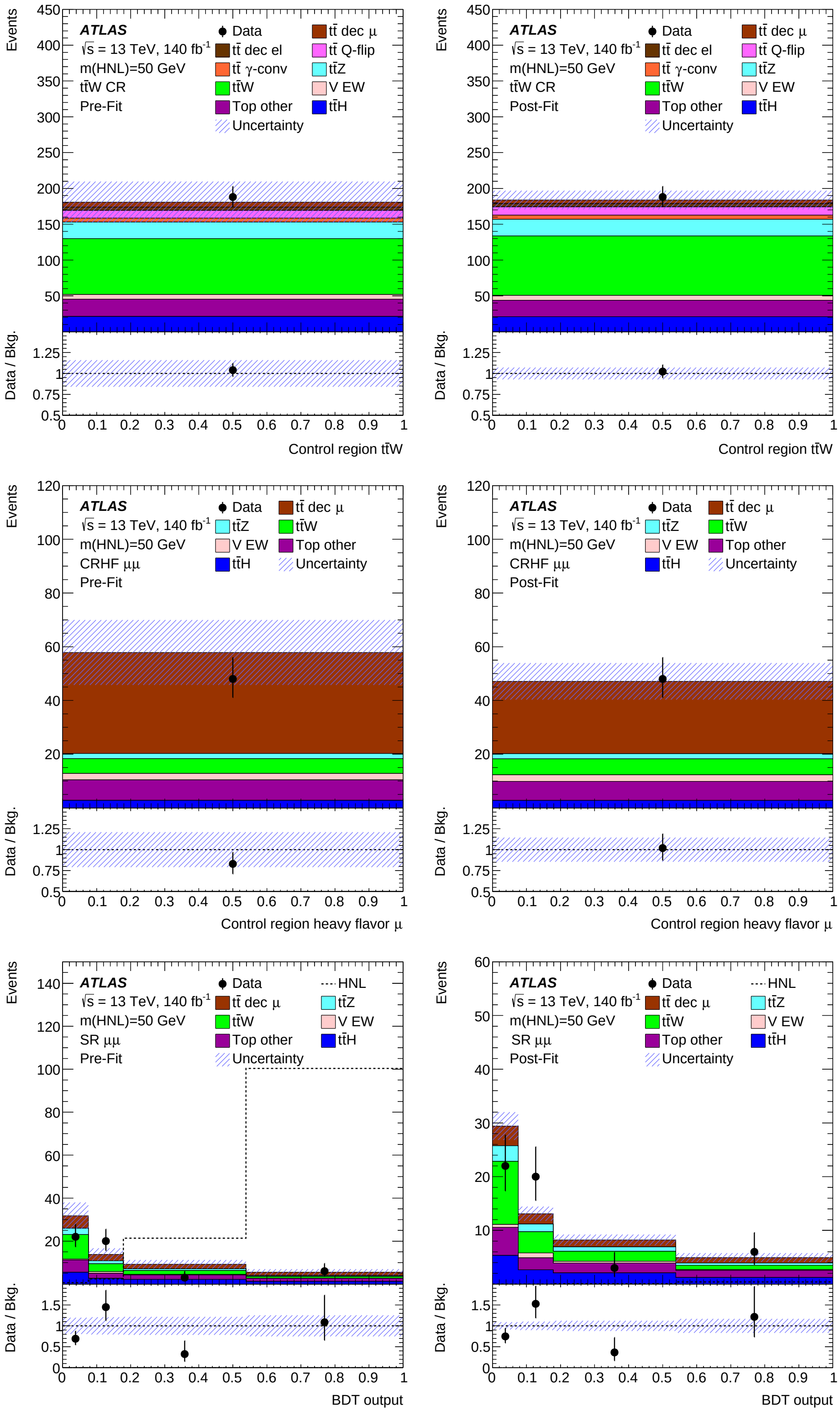

Figure 5.28: Pre-fit (left side) and Post-fit (right side) distributions in 2 control regions and the signal region for the $\mu\mu$ channel for the fit to the real data. The uncertainties band includes the Monte Carlo statistical uncertainty and all systematic uncertainties.

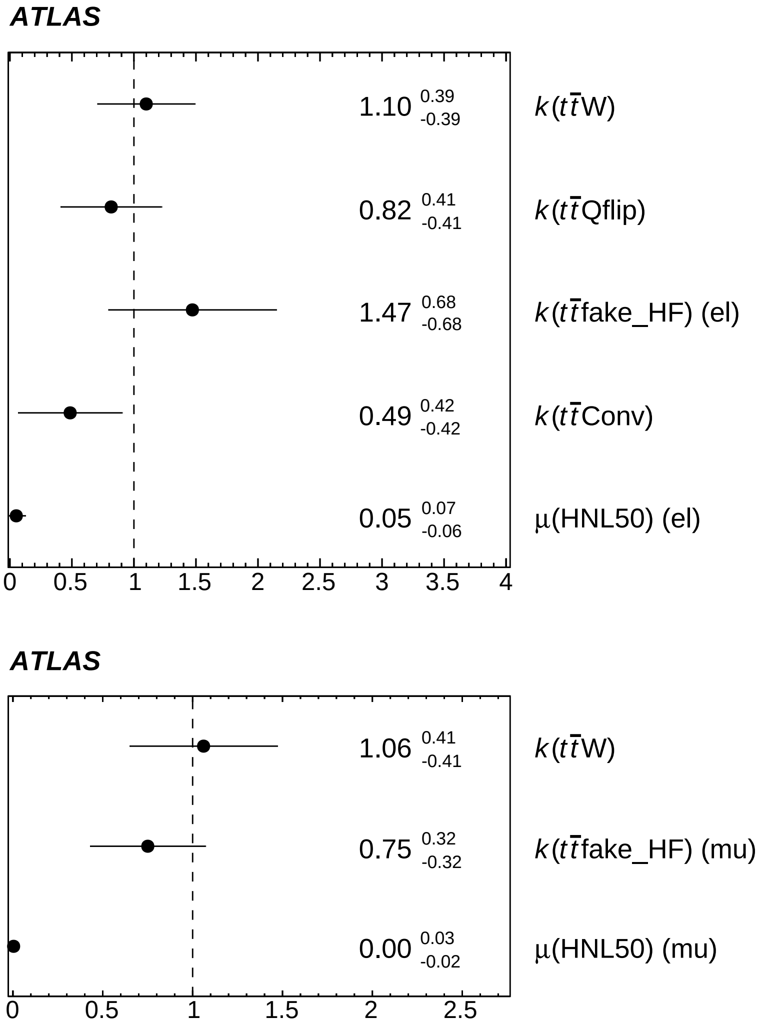

Figure 5.29: Summary of the normalization factors in the fit to the real data on both the signal and control regions for the ee channel(upper) and $\mu\mu$ channel (lower) with the signal mass at 50 GeV.

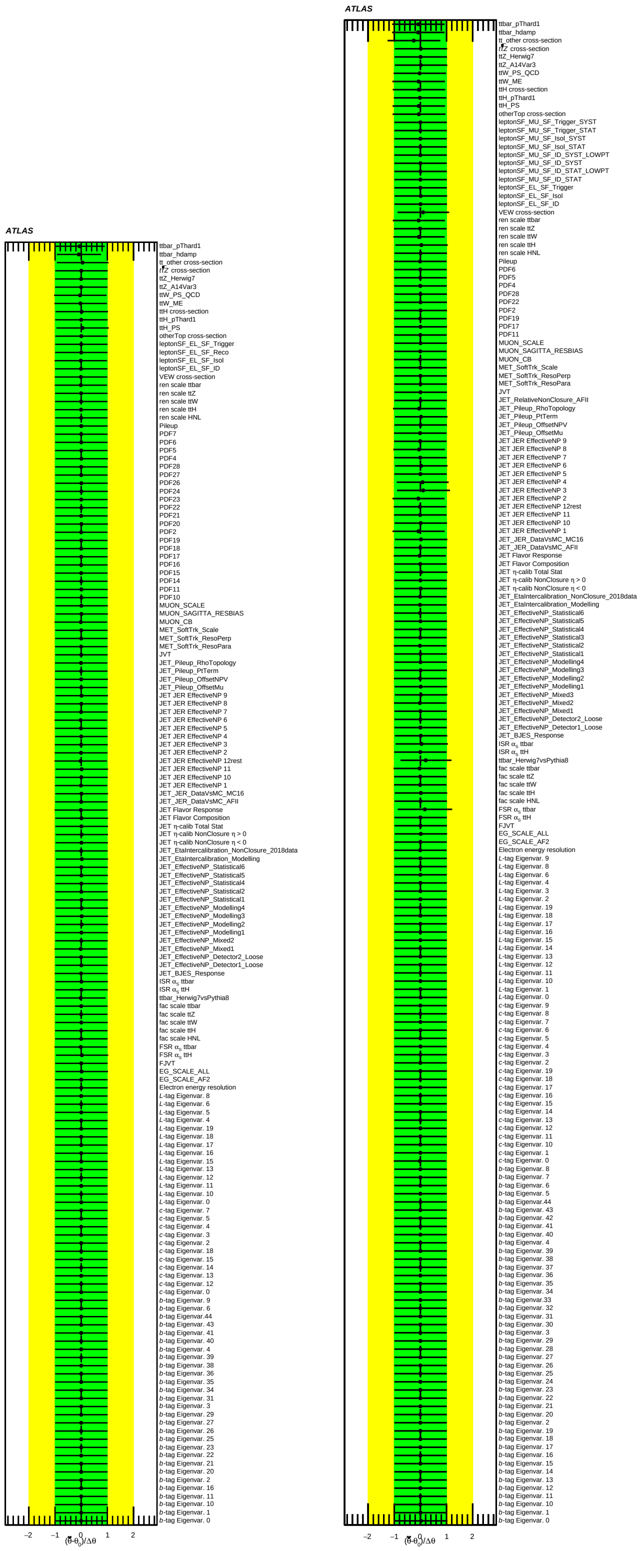

Figure 5.30: Pull distributions of all nuisance parameters in the ee channel (left) and the mm channel (right) for the signal with mass at 50 GeV. They show all the nuisance parameters passing the pruning, including all the theoretical uncertainties and experimental uncertainties.

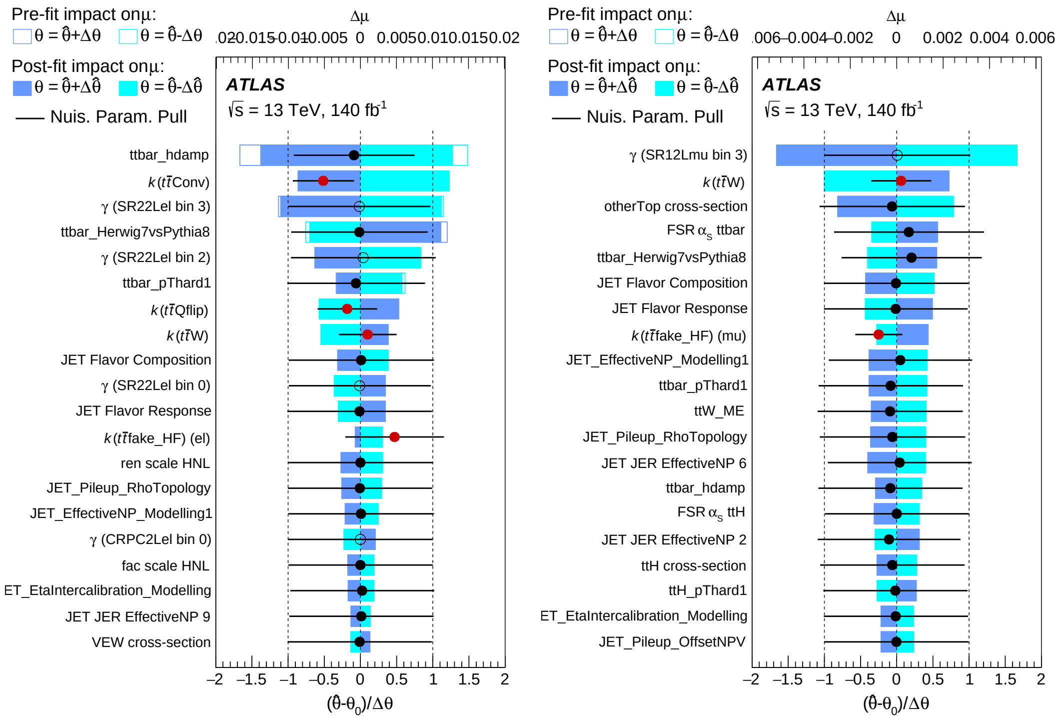

Figure 5.31: The top 20 ranking nuisance parameters for the fit to real data in the ee (left)/$\mu\mu$ (right) channel with signal mass at 50 GeV.

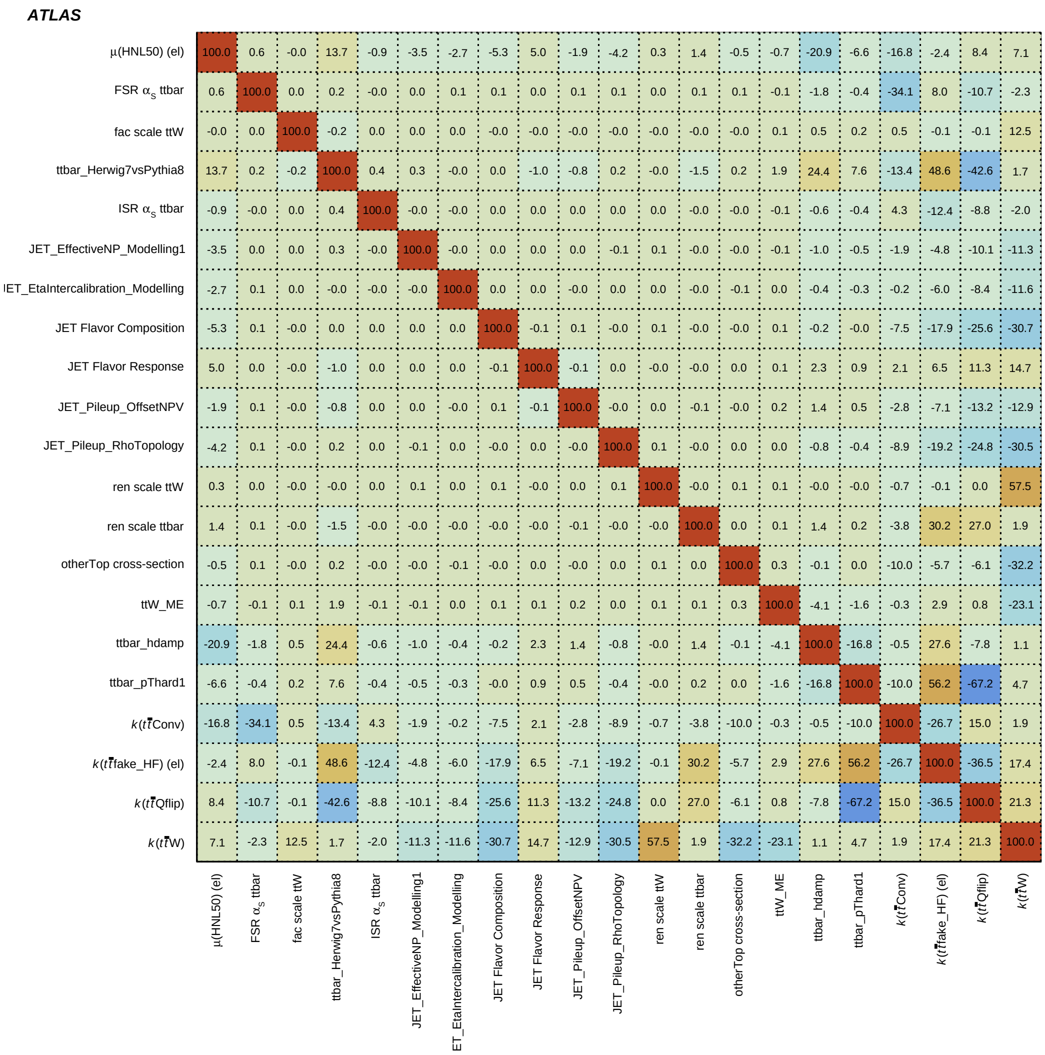

Figure 5.32: The correlation matrix for the fit to real data for the *ee* channel with signal mass at 50 GeV (only NPs with at least one coefficient above 10 are displayed).

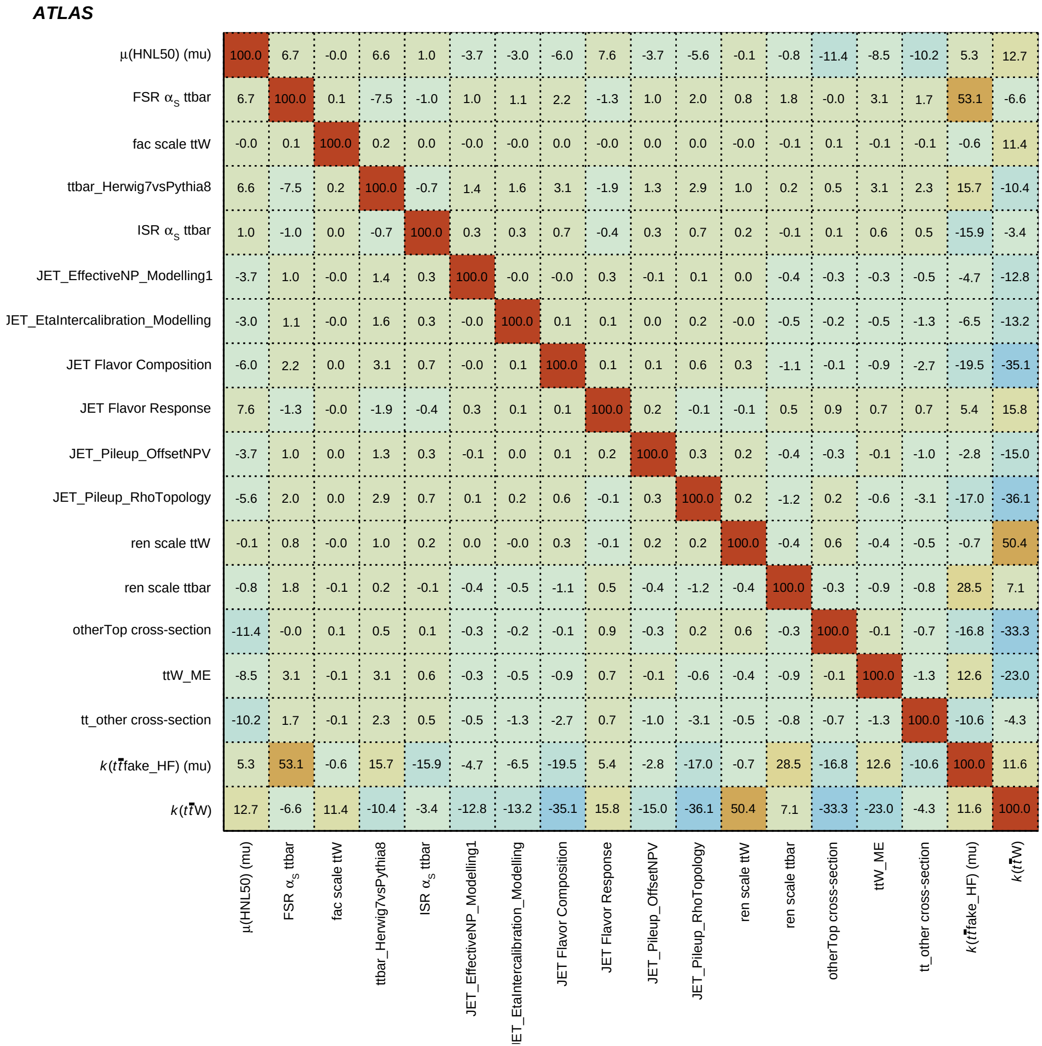

Figure 5.33: The correlation matrix for the fit to real data for the $\mu\mu$ channel with signal mass at 50 GeV (only NPs with at least one coefficient above 10 are displayed).

5.7 Results for the mixing parameter

To better compare with previous experiments, we can obtain the corresponding sensitivity on the mixing parameter through the signal strength.

The upper limits on the signal cross-sections are translated into upper limits on the mixing parameters using the following equation:

$$\sigma_{\ell,N} = 2 \cdot \sigma_{t\bar{t}} \cdot |V_{\ell,N}|^2 \cdot \mathcal{B}(W^+ \to N_{|V_{\ell,N}|=1}\ell^+) \cdot \mathcal{B}(N \to \ell^+ W^-), \tag{5.15}$$

where $\mathcal{B}(W^+ \to N_{|V_{\ell,N}|=1}\ell^+)$ is the branching ratio of the $W^+ \to N\ell^+$ decay, for $|V_{\ell,N}| = 1$. The value of $\mathcal{B}(N \to \ell^+W^-)$ does not depend on the mixing parameter $V_{\ell,N}$ and varies from 36% to 39% in the mass range considered.

These values are derived from the associated theoretical decay models and Monte Carlo generation log files, ensuring a robust estimation of the mixing constraints. The calculation involves evaluating the theoretical cross-sections for the production and decay of the heavy neutral leptons while incorporating the latest electroweak corrections and parton distribution functions. These theoretical inputs are crucial in correctly translating the experimental upper limits on cross-sections into mixing parameter constraints.

Figure 5.34 shows the upper limits on the electron and muon mixing parameters as functions of the HNL mass. The observed upper limits for $|V_{e,N}|^2$ and $|V_{\mu,N}|^2$ are comparable across the whole mass range, with $|V_{\mu,N}|^2$ being slightly more stringent. This is expected due to the different reconstruction efficiencies of electron and muon channels, as well as the distinct background contributions affecting each lepton flavor. The observed upper limits from some of the previous searches for HNLs in W boson decays are shown as colored dashed lines. The discontinuities seen in the solid red line originate from the different optimization strategies applied in different mass regions.

Nevertheless, these limits are weaker compared to some of the previous results, as shown in this figure. The discrepancy arises primarily due to differences in analysis techniques, dataset sizes, and background estimation methodologies.

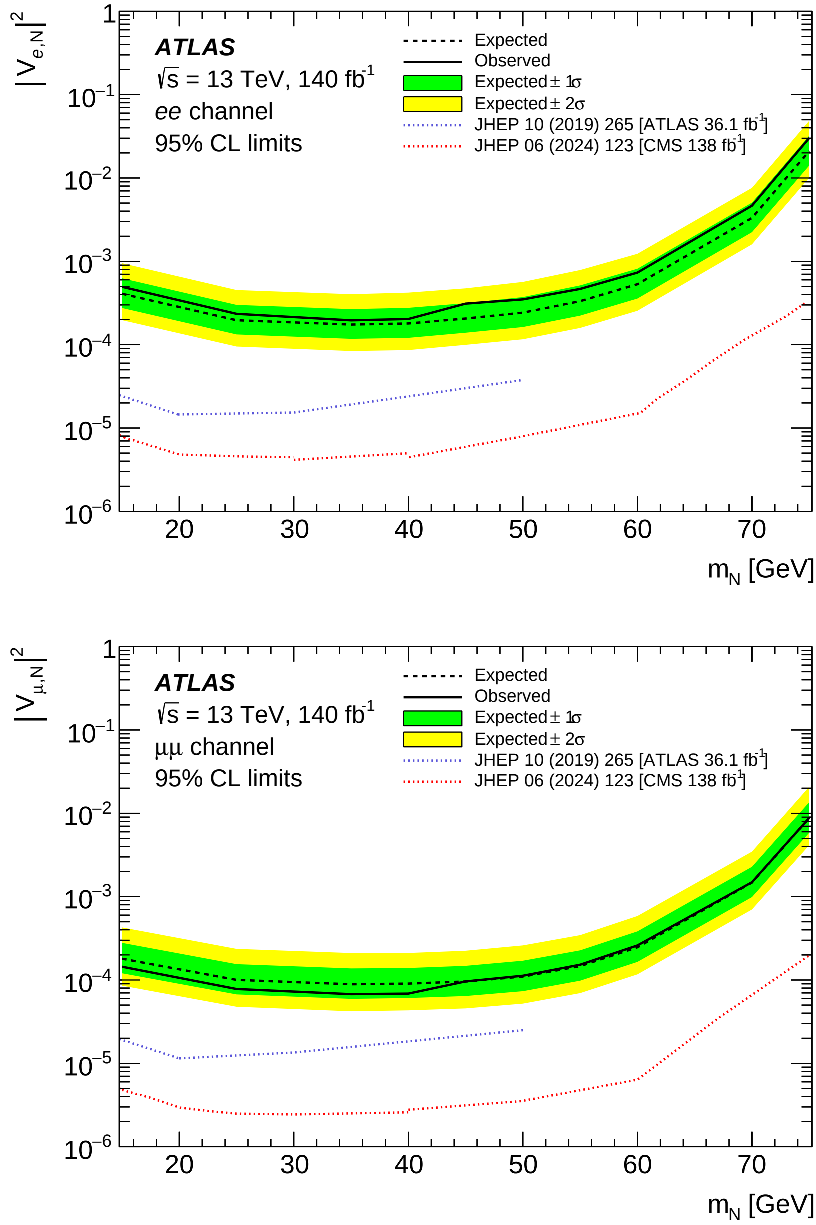

Figure 5.34: Expected (dashed black lines) and observed (solid black lines) upper limits on the strength of HNL mixing with electrons (top) and muons (bottom) at 95% CL, along with the 1σ (green) and 2σ (yellow) uncertainty bands. The small discontinuity after 40 GeV reflects the use of a different BDT beyond this mass point. The observed upper limits from some of the previous searches for HNLs in W boson decays are shown as colored dashed lines [150, 151].

Chapter 6 Conclusion

A study is conducted to search for heavy neutral leptons in $t\bar{t}$ events featuring dileptonic final states. The analysis utilizes 140 fb^{-1} of proton-proton collision data collected at a center-of-mass energy of 13 TeV by the ATLAS detector at the LHC. This is the first search for heavy neutral leptons with $t\bar{t}$ events, using the unique signature of same-sign di-leptons ($ee/\mu\mu$) in the final state.

No significant deviation from the Standard Model expectation is observed, and the search results are presented as 95% CL upper limits on the mixing parameters $|V_{e,N}|^2$ and $|V_{\mu,N}|^2$ as functions of the mass of the heavy neutral lepton.

The analysis primarily focuses on HNL mixing with the first two lepton generations. The most stringent upper bounds in the analyzed parameter space are $|V_{e,N}|^2 < 2.0 \times 10^{-4}$ and $|V_{\mu,N}|^2 < 6.8 \times 10^{-5}$. While these limits are roughly an order of magnitude weaker than those reported in a prior ATLAS investigation of HNLs arising from W boson decays [152], this analysis extends the ATLAS search for heavy neutral leptons coupling to the first- and second-generation leptons to higher mass ranges, probing $m_N > 50$ GeV up to 75 GeV.

From the Figure 6.1, a comparison study is performed for the observed upper limits on the mixing parameter between the results of this analysis and those from previous ATLAS and CMS studies. Our analysis yields higher upper limits on the mixing parameters compared to other experiments, indicating that our constraints are less stringent.

Although the sensitivity of this channel is 2 – 3 orders of magnitude lower than channels where W bosons are directly produced in proton-proton collisions, searches for unconventional couplings in top-quark decays remain crucial. The final states explored in this analysis may arise in alternative theoretical frameworks, such as effective field theory (EFT) models incorporating lepton-number violation and complex five-fermion interactions.

With the upcoming Run-3 dataset [153] and the anticipated High-Luminosity LHC (HL-LHC) era, the potential for precise measurements and the discovery of new phenomena will be significantly enhanced. The cumulative luminosity as a function of time, recorded up to 2024, is shown in Figure 6.2. The increased luminosity will improve statistical precision and enhance sensitivity to rare processes,

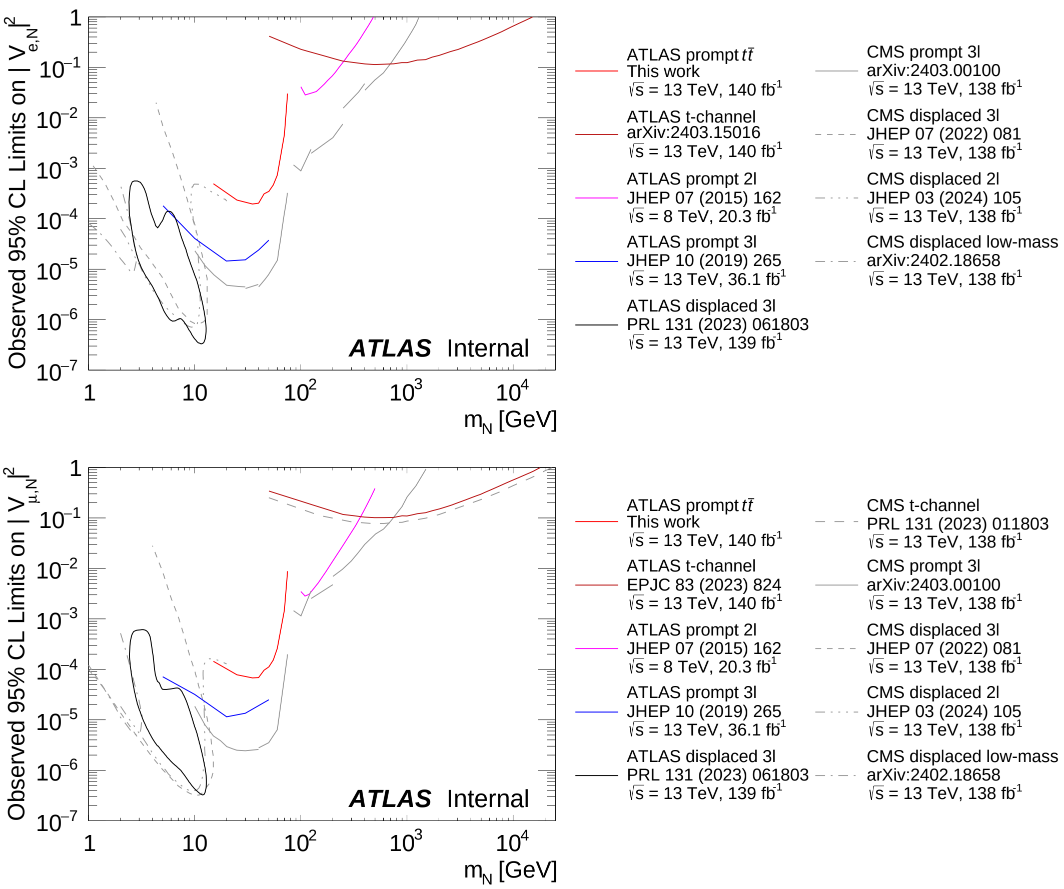

Figure 6.1: The comparison of the observed upper limits obtained from the different searches for HNL mixing with (upper) electron neutrinos and (lower) muon neutrinos. This analysis is shown in solid, red lines.

providing new opportunities to explore physics beyond the Standard Model.

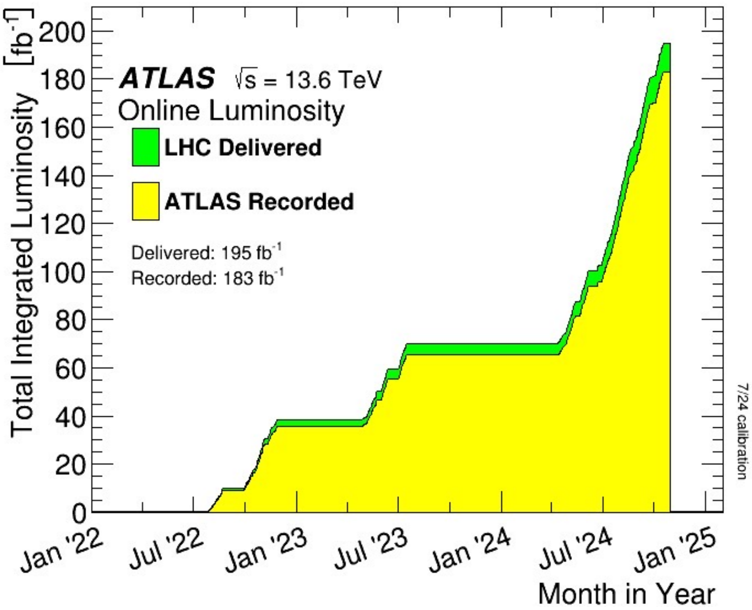

Figure 6.2: Cumulative luminosity versus time delivered to (green) and recorded by ATLAS (yellow) during stable beams for p-p collisions at 13.6 TeV center-of-mass energy in LHC Run 3 (2022-2024).

References

[1]J. Harvey, D. Reiss, and P. Ramond. "Mass relations and neutrino oscillations in an SO(10) model". In: *Nuclear Physics B* 199.2 (1982), pp. 223–268. ISSN: 0550-3213. DOI: https://doi.org/10.1016/0550-3213(82)90346-7. URL: https://www.sciencedirect.com/science/article/pii/0550321382903467.

[2]S. Dimopoulos, L. J. Hall, and S. Raby. "Predictive framework for fermion masses in supersymmetric theories". In: *Phys. Rev. Lett.* 68 (13 May 1992), pp. 1984–1987. DOI: 10.1103/PhysRevLett.68.1984. URL: https://link.aps.org/doi/10.1103/PhysRevLett.68.1984.

[3]L. J. Hall and S. Raby. "Complete supersymmetric SO(10) model". In: *Physical Review D* 51.11 (June 1995), pp. 6524–6531. DOI: 10.1103/physrevd.51.6524. URL: https://doi.org/10.1103%2Fphysrevd.51.6524.

[4]Y. Zhang and B. Zhang. "A potential scenario for Majorana neutrino detection at future lepton colliders". In: *Journal of High Energy Physics* 2019.2 (Feb. 2019). DOI: 10.1007/jhep02(2019)175. URL: https://doi.org/10.1007%2Fjhep02%282019%29175.

[5]I. Dorsner, P. F. Pérez, and R. G. Felipe. "Phenomenological and cosmological aspects of a minimal GUT scenario". In: *Nuclear Physics B* 747.1-2 (July 2006), pp. 312–327. DOI: 10.1016/j.nuclphysb.2006.05.006. URL: https://doi.org/10.1016%2Fj.nuclphysb.2006.05.006.

[6]I. Dorš ner, P. F. Pérez, and G. Rodrigo. "Fermion masses and the UV cutoff of the minimal realistic SU(5)". In: *Physical Review D* 75.12 (June 2007). DOI: 10.1103/physrevd.75.125007. URL: https://doi.org/10.1103%2Fphysrevd.75.125007.

[7]P. Minkowski. "$\mu \to e\gamma$ at a rate of one out of 10^9 muon decays?" In: *Physics Letters B* 67.4 (1977), pp. 421–428. ISSN: 0370-2693. DOI: https://doi.org/10.1016/0370-2693(77)90435-X. URL: https://www.sciencedirect.com/science/article/pii/037026937790435X.

[8]E. Ma. "Neutrino Masses and Leptogenesis from R Parity Violation". In: *Dark Matter in Astro- and Particle Physics*. Ed. by H. V. Klapdor-Kleingrothaus. Berlin, Heidelberg: Springer Berlin Heidelberg, 2001, pp. 448–454. ISBN: 978-3-642-56643-1.

[9]R. N. Mohapatra, familyi=c., given=Goran, giveni=G., „ and. "Neutrino Mass and Spontaneous Parity Nonconservation". In: *Phys. Rev. Lett.* 44 (14

Apr. 1980), pp. 912–915. DOI: 10.1103/PhysRevLett.44.912. URL: https://link.aps.org/doi/10.1103/PhysRevLett.44.912.

[10] J. Schechter and J. W. F. Valle. "Neutrino masses in SU(2) $\bigotimes$ U(1) theories". In: *Phys. Rev. D* 22 (9 Nov. 1980), pp. 2227–2235. DOI: 10.1103/PhysRevD.22.2227. URL: https://link.aps.org/doi/10.1103/PhysRevD.22.2227.

[11] T. Asaka, S. Blanchet, and M. Shaposhnikov. "The vMSM, dark matter and neutrino masses". In: *Physics Letters B* 631.4 (2005), pp. 151–156. ISSN: 0370-2693. DOI: https://doi.org/10.1016/j.physletb.2005.09.070. URL: https://www.sciencedirect.com/science/article/pii/S0370269305013675.

[12] Z.-z. Xing. "Naturalness and Testability of TeV Seesaw Mechanisms". In: *Progress of Theoretical Physics Supplement* 180 (Apr. 2009), pp. 112–127. ISSN: 0375-9687. DOI: 10.1143/PTPS.180.112. URL: https://doi.org/10.1143/PTPS.180.112.

[13] A. Ibarra, E. Molinaro, and S. T. Petcov. "TeV scale see-saw mechanisms of neutrino mass generation, the Majorana nature of the heavy singlet neutrinos and ()0-decay". In: *Journal of High Energy Physics* 2010.9 (Sept. 2010). DOI: 10.1007/jhep09(2010)108. URL: https://doi.org/10.1007%2Fjhep09%282010%29108.

[14] R. Adhikari and A. Raychaudhuri. "Light neutrinos from massless texture and below TeV seesaw scale". In: *Phys. Rev. D* 84 (3 Aug. 2011), p. 033002. DOI: 10.1103/PhysRevD.84.033002. URL: https://link.aps.org/doi/10.1103/PhysRevD.84.033002.

[15] A. Samanta et al. "The Low-Scale Approach to Neutrino Masses". In: *Advances in High Energy Physics* 2014 (2014), p. 831598. DOI: 10.1155/2014/831598. URL: https://doi.org/10.1155/2014/831598.

[16] H. Zhou and P.-H. Gu. "From high-scale leptogenesis to low-scale one-loop neutrino mass generation". In: *Nuclear Physics B* 927 (2018), pp. 184–195. ISSN: 0550-3213. DOI: https://doi.org/10.1016/j.nuclphysb.2017.12.016. URL: https://www.sciencedirect.com/science/article/pii/S0550321317304017.

[17] S. Davidson, E. Nardi, and Y. Nir. "Leptogenesis". In: *Physics Reports* 466.4-5 (2008), pp. 105–177.

[18] W. H. Furry. "On Transition Probabilities in Double Beta-Disintegration". In: *Phys. Rev.* 56 (12 Dec. 1939), pp. 1184–1193. DOI: 10.1103/PhysRev.56.1184. URL: https://link.aps.org/doi/10.1103/PhysRev.56.1184.

[19] M. Doi and T. Kotani. “Neutrinoless Modes of Double Beta Decay”. In: *Progress of Theoretical Physics* 89.1 (Jan. 1993), pp. 139–159. ISSN: 0033-068X. DOI: 10.1143/ptp/89.1.139. eprint: https://academic.oup.com/ptp/article-pdf/89/1/139/5207768/89-1-139.pdf. URL: https://doi.org/10.1143/ptp/89.1.139.

[20] G. Aad et al. “Search for Majorana neutrinos in same-sign WW scattering events from pp collisions at $\sqrt{s} = 13$ TeV”. In: *The European Physical Journal C* 83.9 (2023), p. 824. DOI: 10.1140/epjc/s10052-023-11915-y. URL: https://doi.org/10.1140/epjc/s10052-023-11915-y.

[21] A. M. Sirunyan et al. “Search for heavy Majorana neutrinos in same-sign dilepton channels in proton-proton collisions at $\sqrt{s} = 13$ TeV”. In: *Journal of High Energy Physics* 2019.1 (2019), p. 122. DOI: 10.1007/JHEP01(2019)122. URL: https://doi.org/10.1007/JHEP01(2019)122.

[22] A. M. Sirunyan et al. “Search for Heavy Neutral Leptons in Events with Three Charged Leptons in Proton-Proton Collisions at $\sqrt{s} = 13$ TeV”. In: *Phys. Rev. Lett.* 120 (22 May 2018), p. 221801. DOI: 10.1103/PhysRevLett.120.221801. URL: https://link.aps.org/doi/10.1103/PhysRevLett.120.221801.

[23] G. Aad et al. “Search for heavy neutral leptons in decays of W bosons produced in 13 TeV pp collisions using prompt and displaced signatures with the ATLAS detector”. In: *Journal of High Energy Physics* 2019.10 (2019). DOI: 10.1007/jhep10(2019)265. URL: https://doi.org/10.1007%2Fjhep10%282019%29265.

[24] ATLAS Collaboration. “Search for Heavy Neutral Leptons in Decays of W Bosons Using a Dilepton Displaced Vertex in $\sqrt{s} = 13$ TeV pp Collisions with the ATLAS Detector”. In: *Phys. Rev. Lett.* 131 (2023), p. 061803. DOI: 10.1103/PhysRevLett.131.061803. arXiv: 2204.11988 [hep-ex].

[25] ATLAS Collaboration. “Search for Majorana neutrinos in same-sign WW scattering events from pp collisions at $\sqrt{s} = 13$ TeV”. In: *Eur. Phys. J. C* 83.9 (2023), p. 824. DOI: 10.1140/epjc/s10052-023-11915-y. arXiv: 2305.14931 [hep-ex].

[26] ATLAS Collaboration. *Search for heavy Majorana neutrinos in $e^{\pm}e^{\pm}$ and $e^{\pm}\mu^{\pm}$ final states via WW scattering in pp collisions at $\sqrt{s} = 13$ TeV with the ATLAS detector*. 2024. arXiv: 2403.15016 [hep-ex].

[27] S. Bar-Shalom et al. “Majorana neutrinos and lepton-number-violating signals in top-quark and W-boson rare decays”. In: *Physics Letters B* 643.6

(2006), pp. 342–347. ISSN: 0370-2693. DOI: https://doi.org/10.1016/j.physletb.2006.10.060. URL: https://www.sciencedirect.com/science/article/pii/S0370269306013761.

[28] H. Yuan et al. "Lepton-number violating four-body decays of heavy mesons". In: *Journal of High Energy Physics* 2013.8 (2013), p. 66. DOI: 10.1007/JHEP08(2013)066. URL: https://doi.org/10.1007/JHEP08(2013)066.

[29] W. N. Cottingham and D. A. Greenwood. *An introduction to the Standard Model of particle physics*. University of Bristol, UK: Cambridge University Press, 2007.

[30] C. Patrignani and Particle Data Group. "Review of Particle Physics". In: *Chinese Physics C* 40 (2016), p. 100001. URL: http://stacks.iop.org/1674-1137/40/i=10/a=100001.

[31] ATLAS Collaboration. "Observation of a new particle in the search for the Standard Model Higgs boson with the ATLAS detector at the LHC". In: *Phys. Lett. B* 716 (2012), p. 1. DOI: 10.1016/j.physletb.2012.08.020. arXiv: 1207.7214 [hep-ex].

[32] CMS Collaboration. "Observation of a new boson at a mass of 125 GeV with the CMS experiment at the LHC". In: *Phys. Lett. B* 716 (2012), p. 30. DOI: 10.1016/j.physletb.2012.08.021. arXiv: 1207.7235 [hep-ex].

[33] MissMJ. *Standard Model of Elementary Particles*. https://en.wikipedia.org/wiki/File:Standard_Model_of_Elementary_Particles.svg. Licensed under CC BY-SA 3.0, Accessed: 2025-05-16. 2006.

[34] S. Weinberg. "A model of leptons". In: *Phys. Rev. Lett.* 19 (1967), pp. 1264–1266. DOI: 10.1103/PhysRevLett.19.1264.

[35] A. Salam. "Electromagnetic and weak interactions". In: *Phys. Rev. Lett.* 13 (1964), p. 168.

[36] A. Collaboration. *Standard Model Summary Plots October 2023*. Tech. rep. Geneva: CERN, 2023.

[37] R. Placakyte. "Parton Distribution Functions". In: *Proceedings, 31st International Conference on Physics in collisions (PIC 2011): Vancouver, Canada, August 28-September 1, 2011*. 2011. arXiv: 1111.5452 [hep-ph].

[38] ATLAS Collaboration. *Determination of the parton distribution functions of the proton from ATLAS measurements of differential W and Z/γ^* boson and $t\bar{t}$ cross sections*. ATL-PHYS-PUB-2018-017. 2018. URL: https://cds.cern.ch/record/2633819.

[39]A. Buckley et al. “General-purpose event generators for LHC physics”. In: *Phys. Rep.* 504.5 (2011), pp. 145–233.

[40]W. Lukas. “Fast Simulation for ATLAS: Atlfast-II and ISF”. In: *Journal of Physics: Conference Series* 396.2 (2012), p. 022031. URL: http://stacks.iop.org/1742-6596/396/i=2/a=022031.

[41]L. Evans and P. Bryant. “LHC Machine”. In: *JINST* 3 (2008), S08001. DOI: 10.1088/1748-0221/3/08/S08001.

[42]*ALTAS Experiment Luminosity Public Results Run 2*. URL: https://twiki.cern.ch/twiki/bin/view/AtlasPublic/LuminosityPublicResultsRun2.

[43]ATLAS Collaboration. “The ATLAS Inner Detector commissioning and calibration”. In: *Eur. Phys. J. C* 70 (2010), p. 787. DOI: 10.1140/epjc/s10052-010-1366-7. arXiv: 1004.5293 [hep-ex].

[44]ATLAS Collaboration. *ATLAS Insertable B-Layer Technical Design Report*. ATLAS-TDR-19; CERN-LHCC-2010-013. 2010. URL: https://cds.cern.ch/record/1291633.

[45]G. Aad et al. “Readiness of the ATLAS Liquid Argon Calorimeter for LHC Collisions”. In: *Eur. Phys. J.* C70 (2010), pp. 723–753. DOI: 10.1140/epjc/s10052-010-1354-y. arXiv: 0912.2642 [physics.ins-det].

[46]G. Aad et al. “Readiness of the ATLAS Tile Calorimeter for LHC collisions”. In: *Eur. Phys. J.* C70 (2010), pp. 1193–1236. DOI: 10.1140/epjc/s10052-010-1508-y. arXiv: 1007.5423 [physics.ins-det].

[47]ATLAS Collaboration. *ATLAS Level-1 Trigger: Technical Design Report*. ATLAS-TDR-12; CERN-LHCC-98-014. 1998. URL: https://cds.cern.ch/record/381429.

[48]ATLAS Collaboration. *ATLAS High-Level Trigger, Data Acquisition and Controls: Technical Design Report*. ATLAS-TDR-16; CERN-LHCC-2003-022. 2003. URL: https://cds.cern.ch/record/616089.

[49]ATLAS Collaboration. *Performance of the ATLAS Inner Detector Track and Vertex Reconstruction in High Pile-Up LHC Environment*. ATLAS-CONF-2012-042. 2012. URL: https://cds.cern.ch/record/1435196.

[50]R. Fruhwirth. “Application of Kalman filtering to track and vertex fitting”. In: *Nucl. Instrum. Meth. A* 262 (1987), pp. 444–450. DOI: 10.1016/0168-9002(87)90887-4.

[51]ATLAS Collaboration. “Reconstruction of primary vertices at the ATLAS experiment in Run 1 proton-proton collisions at the LHC”. In: *Eur. Phys.*

J. C77.5 (2017), p. 332. DOI: 10.1140/epjc/s10052-017-4887-5. arXiv: 1611.10235 [physics.ins-det].

[52]ATLAS Collaboration. *Improving jet substructure performance in ATLAS using Track-CaloClusters.* ATL-PHYS-PUB-2017-015. 2017. URL: https://cds.cern.ch/record/2275636.

[53]ATLAS Collaboration. "Jet reconstruction and performance using particle flow with the ATLAS Detector". In: *Eur. Phys. J. C* 77 (2017), p. 466. DOI: 10.1140/epjc/s10052-017-5031-2. arXiv: 1703.10485 [hep-ex].

[54]ATLAS Collaboration. "Topological cell clustering in the ATLAS calorimeters and its performance in LHC Run 1". In: *Eur. Phys. J. C* 77 (2017), p. 490. DOI: 10.1140/epjc/s10052-017-5004-5. arXiv: 1603.02934 [hep-ex].

[55]ATLAS Collaboration. "Electron reconstruction and identification efficiency measurements with the ATLAS detector using the 2011 LHC proton–proton collision data". In: *Eur. Phys. J. C* 74 (2014), p. 2941. DOI: 10.1140/epjc/s10052-014-2941-0. arXiv: 1404.2240 [hep-ex].

[56]ATLAS Collaboration. "Electron reconstruction and identification in the ATLAS experiment using the 2015 and 2016 LHC proton–proton collision data at $\sqrt{s} = 13\,\text{TeV}$". In: *Eur. Phys. J. C* 79 (2019), p. 639. DOI: 10.1140/epjc/s10052-019-7140-6. arXiv: 1902.04655 [hep-ex].

[57]W. Lampl et al. *Calorimeter Clustering Algorithms: Description and Performance.* ATL-LARG-PUB-2008-002. 2008. URL: https://cds.cern.ch/record/1099735.

[58]ATLAS Collaboration. *Electron efficiency measurements with the ATLAS detector using the 2015 LHC proton–proton collision data.* ATLAS-CONF-2016-024. 2016. URL: https://cds.cern.ch/record/2157687.

[59]A. Collaboration. *Electron efficiency measurements in 2017 data and electron identification discriminating variables from 2016 data.* Tech. rep. Technical report, available at: https://atlas.web.cern.ch/Atlas/GROUPS/PHYSICS/PLOTS/EGAM-2018-002/index.html. ATLAS Collaboration, 2018.

[60]ATLAS Collaboration. "Muon reconstruction performance of the ATLAS detector in proton–proton collision data at $\sqrt{s} = 13\,\text{TeV}$". In: *Eur. Phys. J. C* 76 (2016), p. 292. DOI: 10.1140/epjc/s10052-016-4120-y. arXiv: 1603.05598 [hep-ex].

[61]A. Collaboration. *Muon identification and reconstruction efficiencies in full Run-2 dataset.* Tech. rep. Technical report, available at: https://atlas.

web.cern.ch/Atlas/GROUPS/PHYSICS/PLOTS/MUON-2019-03/index.html. ATLAS Collaboration, 2019.

[62]M. Cacciari, G. P. Salam, and G. Soyez. "The anti-k_t jet clustering algorithm". In: *JHEP* 04 (2008), p. 063. DOI: 10.1088/1126-6708/2008/04/063. arXiv: 0802.1189 [hep-ph].

[63]S Catani et al. "Longitudinally-invariant $k_\perp$-clustering algorithms for hadron-hadron collisions". In: *Nucl. Phys. B* 406.CERN-TH-6775-93. LU-TP-93-2 (1993), 187–224. 38 p. DOI: 10.1016/0550-3213(93)90166-M.

[64]ATLAS Collaboration. *Selection of jets produced in* 13 *TeV proton–proton collisions with the ATLAS detector*. ATLAS-CONF-2015-029. 2015. URL: https://cds.cern.ch/record/2037702.

[65]ATLAS Collaboration. "Performance of pile-up mitigation techniques for jets in pp collisions at $\sqrt{s} = 8$ TeV using the ATLAS detector". In: *Eur. Phys. J. C* 76.11 (2016), p. 581. DOI: 10.1140/epjc/s10052-016-4395-z. arXiv: 1510.03823 [hep-ex].

[66]ATLAS Collaboration. *Forward jet vertex tagging using the particle flow algorithm*. ATL-PHYS-PUB-2019-026. 2019. URL: https://cds.cern.ch/record/2683100.

[67]ATLAS Collaboration. *Performance of the ATLAS Secondary Vertex b-tagging Algorithm in* 7 *TeV Collision Data*. ATLAS-CONF-2010-042. 2010. URL: https://cds.cern.ch/record/1277682.

[68]ATLAS Collaboration. *Optimisation and performance studies of the ATLAS b-tagging algorithms for the 2017-18 LHC run*. ATL-PHYS-PUB-2017-013. 2017. URL: https://cds.cern.ch/record/2273281.

[69]ATLAS Collaboration. *Secondary vertex finding for jet flavour identification with the ATLAS detector*. ATL-PHYS-PUB-2017-011. 2017. URL: https://cds.cern.ch/record/2270366.

[70]ATLAS Collaboration. *Topological b-hadron decay reconstruction and identification of b-jets with the JetFitter package in the ATLAS experiment at the LHC*. ATL-PHYS-PUB-2018-025. 2018. URL: https://cds.cern.ch/record/2645405.

[71]A. Sciandra. *Development of a new Soft Muon Tagger for the identification of b-jets in ATLAS*. Tech. rep. Geneva: CERN, 2018. DOI: 10.22323/1.314.0768.

[72]ATLAS Collaboration. "ATLAS b-jet identification performance and efficiency measurement with $t\bar{t}$ events in pp collisions at $\sqrt{s} = 13$ TeV". In: *Eur.

Phys. J. C 79 (2019), p. 970. DOI: 10.1140/epjc/s10052-019-7450-8. arXiv: 1907.05120 [hep-ex].

[73]ATLAS Collaboration. "Measurements of b-jet tagging efficiency with the ATLAS detector using $t\bar{t}$ events at $\sqrt{s} = 13\,\text{TeV}$". In: *JHEP* 08 (2018), p. 089. DOI: 10.1007/JHEP08(2018)089. arXiv: 1805.01845 [hep-ex].

[74]ATLAS Collaboration. *Calibration of the ATLAS b-tagging algorithm in $t\bar{t}$ semileptonic events.* ATLAS-CONF-2018-045. 2018. URL: https://cds.cern.ch/record/2638455.

[75]ATLAS Collaboration. *Calibration of the performance of b-tagging for c and light-flavour jets in the 2012 ATLAS data.* ATLAS-CONF-2014-046. 2014. URL: https://cds.cern.ch/record/1741020.

[76]ATLAS Collaboration. *Calibration of light-flavour b-jet mistagging rates using ATLAS proton–proton collision data at $\sqrt{s} = 13$ TeV.* ATLAS-CONF-2018-006. 2018. URL: https://cds.cern.ch/record/2314418.

[77]A. Collaboration. "ATLAS b-jet identification performance and efficiency measurement with $t\bar{t}$ events in pp collisions at $\sqrt{s} = 13$ TeV". In: *Eur. Phys. J. C* 79.11 (2019), p. 970. arXiv: 1907.05120.

[78]ATLAS Collaboration. "ATLAS data quality operations and performance for 2015–2018 data-taking". In: *JINST* 15 (2020), P04003. DOI: 10.1088/1748-0221/15/04/P04003. arXiv: 1911.04632 [physics.ins-det].

[79]ATLAS Collaboration. "Luminosity determination in pp collisions at $\sqrt{s} = 13\,\text{TeV}$ using the ATLAS detector at the LHC". In: (2022). arXiv: 2212.09379 [hep-ex].

[80]ATLAS Collaboration. "The ATLAS Simulation Infrastructure". In: *Eur. Phys. J. C* 70 (2010), p. 823. DOI: 10.1140/epjc/s10052-010-1429-9. arXiv: 1005.4568 [physics.ins-det].

[81]GEANT4 Collaboration, S. Agostinelli, et al. "GEANT4 – a simulation toolkit". In: *Nucl. Instrum. Meth. A* 506 (2003), p. 250. DOI: 10.1016/S0168-9002(03)01368-8.

[82]T. Sjöstrand, S. Mrenna, and P. Skands. "A brief introduction to PYTHIA 8.1". In: *Comput. Phys. Commun.* 178 (2008), pp. 852–867. DOI: 10.1016/j.cpc.2008.01.036. arXiv: 0710.3820 [hep-ph].

[83]ATLAS Collaboration. *The Pythia 8 A3 tune description of ATLAS minimum bias and inelastic measurements incorporating the Donnachie–Landshoff diffractive model.* ATL-PHYS-PUB-2016-017. 2016. URL: https://cds.cern.ch/record/2206965.

[84]S. Frixione, G. Ridolfi, and P. Nason. “A positive-weight next-to-leading-order Monte Carlo for heavy flavour hadroproduction”. In: *JHEP* 09 (2007), p. 126. DOI: 10.1088/1126-6708/2007/09/126. arXiv: 0707.3088 [hep-ph].

[85]P. Nason. “A new method for combining NLO QCD with shower Monte Carlo algorithms”. In: *JHEP* 11 (2004), p. 040. DOI: 10.1088/1126-6708/2004/11/040. arXiv: hep-ph/0409146.

[86]S. Frixione, P. Nason, and C. Oleari. “Matching NLO QCD computations with parton shower simulations: the POWHEG method”. In: *JHEP* 11 (2007), p. 070. DOI: 10.1088/1126-6708/2007/11/070. arXiv: 0709.2092 [hep-ph].

[87]S. Alioli et al. “A general framework for implementing NLO calculations in shower Monte Carlo programs: the POWHEG BOX”. In: *JHEP* 06 (2010), p. 043. DOI: 10.1007/JHEP06(2010)043. arXiv: 1002.2581 [hep-ph].

[88]J. Alwall et al. “The automated computation of tree-level and next-to-leading order differential cross sections, and their matching to parton shower simulations”. In: *JHEP* 07 (2014), p. 079. DOI: 10.1007/JHEP07(2014)079. arXiv: 1405.0301 [hep-ph].

[89]ATLAS Collaboration. *ATLAS Pythia 8 tunes to* 7 *TeV data*. ATL-PHYS-PUB-2014-021. 2014. URL: https://cds.cern.ch/record/1966419.

[90]R. D. Ball et al. “Parton distributions with LHC data”. In: *Nucl. Phys. B* 867 (2013), p. 244. DOI: 10.1016/j.nuclphysb.2012.10.003. arXiv: 1207.1303 [hep-ph].

[91]M. Bähr et al. “Herwig++ physics and manual”. In: *Eur. Phys. J. C* 58 (2008), p. 639. DOI: 10.1140/epjc/s10052-008-0798-9. arXiv: 0803.0883 [hep-ph].

[92]J. Bellm et al. “Herwig 7.0/Herwig++ 3.0 release note”. In: *Eur. Phys. J. C* 76.4 (2016), p. 196. DOI: 10.1140/epjc/s10052-016-4018-8. arXiv: 1512.01178 [hep-ph].

[93]D. J. Lange. “The EvtGen particle decay simulation package”. In: *Nucl. Instrum. Meth. A* 462 (2001), p. 152. DOI: 10.1016/S0168-9002(01)00089-4.

[94]C. Degrande et al. “Fully automated precision predictions for heavy neutrino production mechanisms at hadron colliders”. In: *Phys. Rev. D* 94.5 (2016), p. 053002. DOI: 10.1103/physrevd.94.053002. arXiv: 1602.06957 [hep-ph].

[95] R. D. Ball et al. "Parton distributions for the LHC run II". In: *JHEP* 04 (2015), p. 040. DOI: 10.1007/JHEP04(2015)040. arXiv: 1410.8849 [hep-ph].

[96] R. Frederix, D. Pagani, and M. Zaro. "Large NLO corrections in $t\bar{t}W^{\pm}$ and $t\bar{t}t\bar{t}$ hadroproduction from supposedly subleading EW contributions". In: *JHEP* 02 (2018), p. 031. DOI: 10.1007/JHEP02(2018)031. arXiv: 1711.02116 [hep-ph].

[97] S. Frixione et al. "Angular correlations of lepton pairs from vector boson and top quark decays in Monte Carlo simulations". In: *JHEP* 04 (2007), p. 081. DOI: 10.1088/1126-6708/2007/04/081. arXiv: hep-ph/0702198.

[98] P. Artoisenet et al. "Automatic spin-entangled decays of heavy resonances in Monte Carlo simulations". In: *JHEP* 03 (2013), p. 015. DOI: 10.1007/JHEP03(2013)015. arXiv: 1212.3460 [hep-ph].

[99] ATLAS Collaboration. *Studies on top-quark Monte Carlo modelling for Top2016*. ATL-PHYS-PUB-2016-020. 2016. URL: https://cds.cern.ch/record/2216168.

[100] T. Sjöstrand et al. "An introduction to PYTHIA 8.2". In: *Comput. Phys. Commun.* 191 (2015), p. 159. DOI: 10.1016/j.cpc.2015.01.024. arXiv: 1410.3012 [hep-ph].

[101] R. Frederix and I. Tsinikos. "On improving NLO merging for $\mathrm{t\bar{t}W}$ production". In: *JHEP* 11 (2021), p. 029. DOI: 10.1007/JHEP11(2021)029. arXiv: 2108.07826 [hep-ph].

[102] a. Diez Pardos Carmen et. "Measurements of top quark pair charge asymmetry $t\bar{t}\gamma$ production at 13 TeV with the ATLAS detector". In: *ANA-TOPQ-2021-29-INT1* (2021).

[103] E. Bothmann et al. "Event generation with Sherpa 2.2". In: *SciPost Phys.* 7.3 (2019), p. 034. DOI: 10.21468/SciPostPhys.7.3.034. arXiv: 1905.09127 [hep-ph].

[104] T. Gleisberg and S. Höche. "Comix, a new matrix element generator". In: *JHEP* 12 (2008), p. 039. DOI: 10.1088/1126-6708/2008/12/039. arXiv: 0808.3674 [hep-ph].

[105] F. Cascioli, P. Maierhöfer, and S. Pozzorini. "Scattering Amplitudes with Open Loops". In: *Phys. Rev. Lett.* 108 (2012), p. 111601. DOI: 10.1103/PhysRevLett.108.111601. arXiv: 1111.5206 [hep-ph].

[106] A. Denner, S. Dittmaier, and L. Hofer. "COLLIER: A fortran-based complex one-loop library in extended regularizations". In: *Comput. Phys. Commun.*

212 (2017), pp. 220–238. DOI: 10.1016/j.cpc.2016.10.013. arXiv: 1604.06792 [hep-ph].

[107]S. Schumann and F. Krauss. "A parton shower algorithm based on Catani–Seymour dipole factorisation". In: *JHEP* 03 (2008), p. 038. DOI: 10.1088/1126-6708/2008/03/038. arXiv: 0709.1027 [hep-ph].

[108]S. Höche et al. "A critical appraisal of NLO+PS matching methods". In: *JHEP* 09 (2012), p. 049. DOI: 10.1007/JHEP09(2012)049. arXiv: 1111.1220 [hep-ph].

[109]S. Höche et al. "QCD matrix elements + parton showers. The NLO case". In: *JHEP* 04 (2013), p. 027. DOI: 10.1007/JHEP04(2013)027. arXiv: 1207.5030 [hep-ph].

[110]S. Catani et al. "QCD Matrix Elements + Parton Showers". In: *JHEP* 11 (2001), p. 063. DOI: 10.1088/1126-6708/2001/11/063. arXiv: hep-ph/0109231.

[111]S. Höche et al. "QCD matrix elements and truncated showers". In: *JHEP* 05 (2009), p. 053. DOI: 10.1088/1126-6708/2009/05/053. arXiv: 0903.1219 [hep-ph].

[112]C. Anastasiou et al. "High-precision QCD at hadron colliders: Electroweak gauge boson rapidity distributions at next-to-next-to leading order". In: *Phys. Rev. D* 69 (2004), p. 094008. DOI: 10.1103/PhysRevD.69.094008. arXiv: hep-ph/0312266.

[113]S. Frixione et al. "Single-top hadroproduction in association with a W boson". In: *JHEP* 07 (2008), p. 029. DOI: 10.1088/1126-6708/2008/07/029. arXiv: 0805.3067 [hep-ph].

[114]N. Liu et al. "Top quark as a probe of heavy Majorana neutrino at the LHC and future collider". In: *Phys. Rev. D* D.101 (2020). https://arxiv.org/abs/1910.00749, p. 071701.

[115]ATLAS Collaboration. *Introduction of the AnalysisTop21.2.X*. https://twiki.cern.ch/twiki/bin/view/AtlasProtected/AnalysisTop21. 2021.

[116]ATLAS Collaboration. "Electron and photon energy calibration with the ATLAS detector using 2015–2016 LHC proton–proton collision data". In: *JINST* 14 (2019), P03017. DOI: 10.1088/1748-0221/14/03/P03017. arXiv: 1812.03848 [hep-ex].

[117]ATLAS Collaboration. *Recommended Lepton Isolation Working Points*. 2022. URL: https://twiki.cern.ch/twiki/bin/view/AtlasProtected/RecommendedIsolationWPs.

[118]ATLAS Collaboration. *Definition of Prompt Lepton Improved Veto*. 2022. URL: https://twiki.cern.ch/twiki/bin/view/AtlasProtected/PLImprovedWPs.

[119]T. Baroncelli et al. *Measurement of the Higgs boson production cross section in association with a vector boson and decaying into WW^* with the ATLAS detector at $\sqrt{s} = 13\,\text{TeV}$*. Tech. rep. Geneva: CERN, 2021. URL: https://cds.cern.ch/record/2765898.

[120]ATLAS Collaboration. *Electron Charge ID Selector Tool*. 2022. URL: https://twiki.cern.ch/twiki/bin/view/AtlasProtected/ElectronChargeFlipTaggerTool.

[121]ATLAS Collaboration. *EGamma ambiguity tool in analysis*. 2022. URL: https://twiki.cern.ch/twiki/bin/view/AtlasProtected/EGammaIdentificationRun2#Using_the_Ambiguity_tool_in_anal.

[122]ATLAS Collaboration. *Tagging and suppression of pileup jets with the ATLAS detector*. ATLAS-CONF-2014-018. 2014. URL: https://cds.cern.ch/record/1700870.

[123]ATLAS Collaboration. *Jet Vertex Tagger for Run 2 in reco and analysis*. 2021. URL: https://twiki.cern.ch/twiki/bin/view/AtlasProtected/JetVertexTaggerTool.

[124]ATLAS Collaboration. *Recommended setup for overlap removal*. https://twiki.cern.ch/twiki/bin/view/AtlasProtected/TopRecoObjTwikiModel#Overlap_Removal. https://twiki.cern.ch/twiki/bin/view/AtlasProtected/TopRecoObjTwikiModel#Overlap_Removal. 2021.

[125]P. A. Zyla et al. "Review of Particle Physics". In: *PTEP* 2020.8 (2020), p. 083C01. DOI: 10.1093/ptep/ptaa104.

[126]ATLAS Collaboration. *Readme for the usage of the IFF classes*. https://gitlab.cern.ch/atlas/athena/-/blob/21.2/PhysicsAnalysis/AnalysisCommon/TruthClassification/README.md. 2021.

[127]ATLAS Collaboration. *MVA Trainer Documentation*. 2023. URL: https://mva-trainer-docs-site.docs.cern.ch/.

[128]PyTorch Developers. *PyTorch*. 2023. URL: https://pytorch.org/.

[129]PyTorch Geometric Developers. *PyTorch Geometric*. 2023. URL: https://pytorch-geometric.readthedocs.io/en/latest/.

[130]Scikit-learn Developers. *Scikit-learn*. 2023. URL: https://scikit-learn.org/stable/.

[131]A. Collaboration. *Luminosity determination in pp collisions at $\sqrt{s} = 13$ TeV using the ATLAS detector at the LHC*. 2022. arXiv: 2212.09379 [hep-ex].

[132]ATLAS Collaboration. *Electron Efficiencies for Run 2 (scale factors and uncertainties)*. 2021. URL: https://twiki.cern.ch/twiki/bin/view/AtlasProtected/ElectronEfficiencyRun2.

[133]ATLAS Collaboration. *MCP Analysis Guidelines for MC16*. 2021. URL: https://twiki.cern.ch/twiki/bin/view/AtlasProtected/MCPAnalysisGuidelinesMC16.

[134]ATLAS Collaboration. "Muon reconstruction and identification efficiency in ATLAS using the full Run 2 *pp* collision data set at $\sqrt{s} = 13$ TeV". In: *Eur. Phys. J. C* 81 (2021), p. 578. DOI: 10.1140/epjc/s10052-021-09233-2. arXiv: 2012.00578 [hep-ex].

[135]ATLAS Collaboration. *TrigGlobalEfficiencyCorrectionTool twiki*. 2022. URL: https://twiki.cern.ch/twiki/bin/viewauth/Atlas/TrigGlobalEfficiencyCorrectionTool.

[136]ATLAS Collaboration. "Performance of missing transverse momentum reconstruction with the ATLAS detector using proton–proton collisions at $\sqrt{s} = 13$ TeV". In: *Eur. Phys. J. C* 78 (2018), p. 903. DOI: 10.1140/epjc/s10052-018-6288-9. arXiv: 1802.08168 [hep-ex].

[137]ATLAS Collaboration. *MET Soft track Systematics Recommendations R21*. 2021. URL: https://twiki.cern.ch/twiki/bin/view/AtlasProtected/MissingETSystematics#Soft_track_uncertainties.

[138]ATLAS Collaboration. "Jet energy scale measurements and their systematic uncertainties in proton–proton collisions at $\sqrt{s} = 13$ TeV with the ATLAS detector". In: *Phys. Rev. D* 96 (2017), p. 072002. DOI: 10.1103/PhysRevD.96.072002. arXiv: 1703.09665 [hep-ex].

[139]ATLAS Collaboration. "Jet energy scale and resolution measured in proton–proton collisions at $\sqrt{s} = 13$ TeV with the ATLAS detector". In: *Eur. Phys. J. C* 81 (2020), p. 689. DOI: 10.1140/epjc/s10052-021-09402-3. arXiv: 2007.02645 [hep-ex].

[140]ATLAS Collaboration. *JetEtMiss Recommendations for Release 21 MC16 (2015-2018)*. 2021. URL: https://twiki.cern.ch/twiki/bin/view/AtlasProtected/JetEtmissRecommendationsR21.

[141]A. Collaboration. "Jet energy scale and resolution measured in proton-proton collisions at $\sqrt{s} = 13$ TeV with the ATLAS detector". In: *Phys. Rev. C* 81

(2021), p. 689. DOI: 10.1140/epjc/s10052-021-09402-3. URL: https://doi.org/10.1140/epjc/s10052-021-09402-3.

[142]J. Butterworth et al. "PDF4LHC recommendations for LHC Run II". In: *J. Phys. G* 43 (2016), p. 023001. DOI: 10.1088/0954-3899/43/2/023001. arXiv: 1510.03865 [hep-ph].

[143]D. de Florian and A. Collaboration. *Handbook of LHC Higgs Cross Sections: 4. Deciphering the Nature of the Higgs Sector*. CERN Yellow Reports: Monographs. 869 pages, 295 figures, 248 tables and 1645 citations. Working Group web page: https://twiki.cern.ch/twiki/bin/view/LHCPhysics/LHCHXSWG. 2016. DOI: 10.23731/CYRM-2017-002. URL: https://cds.cern.ch/record/2227475.

[144]M. Aaboud et al. "Measurements of the production cross section of a Z boson in association with jets in pp collisions at $\sqrt{s} = 13$ TeV with the ATLAS detector". In: *The European Physical Journal C* 77 (2017), p. 4900. DOI: 10.1140/epjc/s10052-017-4900-z. URL: https://doi.org/10.1140/epjc/s10052-017-4900-z.

[145]ATLAS Collaboration. "Measurement of $W^{\pm}Z$ production cross sections and gauge boson polarisation in pp collisions at $\sqrt{s} = 13\,\text{TeV}$ with the ATLAS detector". In: *Eur. Phys. J. C* 79 (2019), p. 535. DOI: 10.1140/epjc/s10052-019-7027-6. arXiv: 1902.05759 [hep-ex].

[146]ATLAS Collaboration. "Observation of four-top-quark production in the multilepton final state with the ATLAS detector". In: *The European Physical Journal C* 83.6 (2023), p. 496. DOI: 10.1140/epjc/s10052-023-11573-0. URL: https://doi.org/10.1140/epjc/s10052-023-11573-0.

[147]ATLAS Collaboration. "Measurements of inclusive and differential fiducial cross-sections of $t\bar{t}$ production with additional heavy-flavour jets in proton-proton collisions at $\sqrt{s} = 13$ TeV with the ATLAS detector". In: *JHEP* 2019.4 (2019), p. 046. ISSN: 1029-8479. DOI: 10.1007/JHEP04(2019)046. URL: http://dx.doi.org/10.1007/JHEP04(2019)046.

[148]L. Moneta et al. "The RooStats project". In: *PoS* ACAT2010 (2011), p. 057. DOI: 10.22323/1.093.0057. arXiv: 1009.1003 [physics.data-an].

[149]A. L. Read. "Presentation of search results: the CL_s technique". In: *J. Phys. G* 28.10 (2002), p. 2693. DOI: 10.1088/0954-3899/28/10/313.

[150]P. Abreu et al. "Search for neutral heavy leptons produced in Z decays". In: *Z. Phys. C* 74 (1997). [Erratum: Z.Phys.C 75, 580 (1997)], pp. 57–71. DOI: 10.1007/s002880050370.

[151]CMS Collaboration. *Search for heavy neutral leptons in final states with electrons, muons, and hadronically decaying tau leptons in proton-proton collisions at* $\sqrt{s}$ *=13 TeV*. 2024. arXiv: 2403.00100 [hep-ex].

[152]ATLAS Collaboration. "Search for heavy neutral leptons in decays of W bosons produced in 13 TeV pp collisions using prompt and displaced signatures with the ATLAS detector". In: *JHEP* 10.10 (2019), p. 265. DOI: 10.1007/jhep10(2019)265. arXiv: 1905.09787 [hep-ex].

[153]ATLAS Collaboration. *ATLAS Luminosity Public Results for Run 3*. [Online; accessed 22-Mar-2025]. 2025. URL: https://twiki.cern.ch/twiki/bin/view/AtlasPublic/LuminosityPublicResultsRun3.

Acknowledgement

很难想象，我终于有一天要离开山大这片土地，并且以一名博士的身份昂首挺胸地离开。从 2014 年踏入山大校园，开始我的本科生涯，连我自己也没有想到，我会在这里奉献人生中最美好的 11 年。从本科到硕博，这里留下了我精彩而又热烈的青春记忆。从郁郁葱葱的洪家楼到碧海青天的鳌山卫，从济南中心校区的小树林到瑞士美丽的日内瓦湖，从逸夫楼内的自习室到德国锡根的会议厅，我仿佛什么都没变，依然像 10 年前那样求知若渴；但我又焕然一新，已经在属于自己的领域贡献出了一份独特的光亮。回首往事，感慨良多，这一路的辛酸曲折，也只有自己才知。唯有以感恩之心，献给一路以来支持我的亲朋好友、尊师贵人。

首先，我想感谢一路指引我学术道路的导师马连良教授和张学尧教授。依稀记得，报考研究生时，我正迷茫在人生的十字路口，对粒子物理几乎一知半解。是马老师用他的热情和耐心，让我坚定了走入粒子物理领域的决心。尽管由于工作原因，马老师与学生们总是聚少离多，但他总能在关键时刻为我们指点迷津，化解学术上的困惑。在学术之外，他又如慈父密友一般关心我们的日常生活，教导我们如何劳逸结合、享受生活，让我们的科研生涯既充实又充满欢乐。独自做科研的道路难免枯燥乏味，但有了马老师的指导和引领，我始终信心倍增。后来，在博士阶段，我有幸加入张学尧教授的课题组，在他的悉心指导下，我的科研能力得到了进一步的提升。张老师严谨治学的态度令我受益匪浅，他不但给予我充分的学术自由，又能在重要问题上提供精准指导。张老师课题组内开放的学术氛围，使我在研究过程中不仅提升了专业能力，也收获了宝贵的协作经验。能够在马老师和张老师的指导下完成我的学术研究，我深感幸运。他们不仅是我科研道路上的引路人，更是我人生中的良师益友。他们的教诲将一直激励我在未来的学术旅程中再接再厉，勇攀高峰。

其次，我想感谢在德国锡根大学联合培养期间给予我帮助的外导和同事们。我的外导 Markus Cristinziani 教授是一位专业、严谨、热情而又不失幽默的意大利学者。初到德国时，面对种种不便与慌乱，是 Markus 用他沉稳而温暖的态度让我放松身心，并调动一切资源为我解决生活中的琐事。在学术道路上，他也为我化解了无数的挫折与困难。我还要感谢在这里遇到的巴西同事 Gabriel、意大利同事 Beatrice 和德国同事 Katharina。他们的热情、包容以及在生活中的相互鼓励与支持，让我在德国的科研生活不再枯燥乏味。他们是我这辈子难以忘怀的好朋友。

此外，衷心感谢在我科研期间提供帮助的师兄师姐们。特别感谢 Mário José

Sousa 博士后，他在我科研初期帮助我构建了分析框架，并承担了最艰苦的开荒工作。没有 Mário 师兄的帮助，我不知会花费多少时间在入门阶段。感谢杜东硕、赵永柯、李通和徐钟煜坤师兄，在 CERN 交流期间，他们周末带我购物、出游、烹饪美食。在异国他乡，有这些知心伙伴相伴，为我的海外生活增添了别样的色彩。

同时，感谢同组的兄弟姐妹们——李直、贾琛、韩靖宜、陶泽和韩路。无数次的组会见证了我们的思维碰撞，也建立了不可磨灭的同窗情谊。当然，还有数不清的 ATLAS 科研同事，没有他们的共同努力，绝不会有我今天的成就。

在这里，我还要由衷感谢我的爱人。读博是一段漫长而艰苦的旅程，尤其是像我这样奔赴海外的科研工作者。是我的妻子从始至终坚定地支持我，甚至奋不顾身地出国工作，给了我无尽的动力和前进的方向。她永远是我科研道路上最坚实的后盾。

还要由衷感谢我的父母。虽然他们不懂什么是高能物理和粒子加速器，但他们始终相信，他们的儿子在做一件很了不起的事情并无给予条件支持和信任。我永远是他们的骄傲。

最后，感谢我自己。在这场艰苦的博士战役中，我从未退缩，直至抵达胜利的终点。

Appendices

Appendix A Chi-Squared Reconstruction Technique and Strategy

Basically, the object reconstruction technique employed in our analysis aims to create some useful variables for MVA training, rather than achieving high precision. It suffices to distinguish between the signal and background. And the chi-squared algorithm is a common method for finding the best match between measured and expected values. The original denominator should be the squared error of the measurement result showed on Equation (5.7). For initial values, we choose the mass of the top quark and the W boson as the denominator (strategy 1). Given that the chi^2 algorithm seeks the lowest values across all possible combinations, we believe it won't significantly impact reconstruction efficiency.

Once we obtain measured results from the initial iteration, we can employ the actual sigma value extracted from the distributions of invariant mass(strategy 2)by fitting a Gaussian distribution to the core area. The plots are shown in Figure A.1

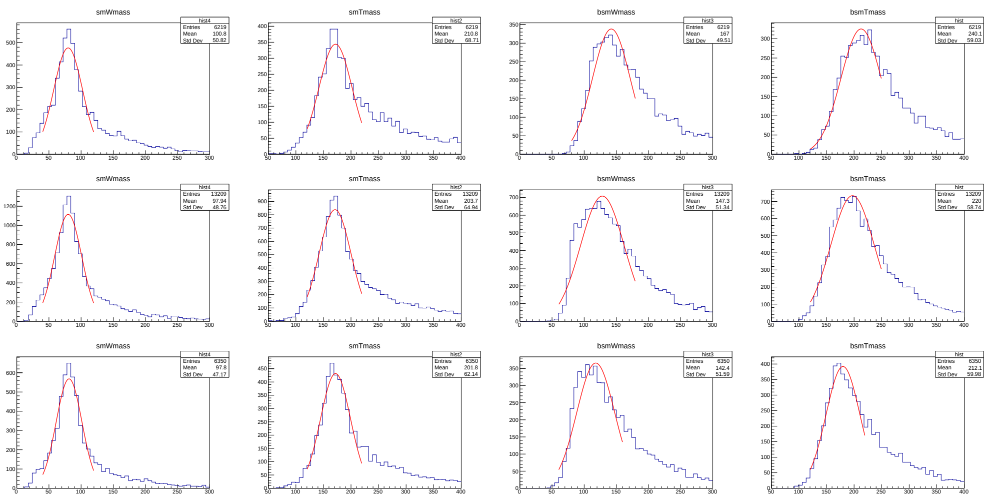

Figure A.1: The Gaussian fit results in the invariant mass of the reconstructed top (t_1,t_2) and W boson(W_1,W_2). The tails in the distributions allow us only to fit the core part. Here show 3 mass points of signal, the fit results of HNL15 (top), HNL50 (middle) and HNL75 (bottom), we will consider all the mass points of signal and take their average of sigma for χ^2 algorithm.

Interestingly, the reconstructed invariant mass distribution is not overly sensitive to the choice of the denominator value. We also tested using the standard deviation value from the entire distribution of the four invariant mass (strategy 3) instead of the sigma from the core area. Remarkably, the output distribution maintains the same statistical parameters, such as the mean and standard deviation values shown on Table A.1.

By fitting the Gaussian distribution to the fixed core area of these three strategies and examining the mean and sigma values of the Gaussian distribution, we can solidify our confidence that the reconstructed invariant mass remains minimally influenced by the choice of sigma value. The invariant mass distribution of different strategies are shown on Figure A.2 and σ value information taken from the Gaussian fit are attached. Thus, using the squared average value as the denominator for chi^2 calculations across all signals and backgrounds is a natural choice.

With HNL50 signal mass point					
Reconstructed object	σ^2 choice	t_2	W_2	t_1	W_1
Strategy 1	use M_t, M_W taken from PDG	Mean:202 Std Dev: 65	Mean:98 Std Dev:48	Mean:216 Std Dev:59	Mean:146 Std Dev:50
Strategy 2	σ is taken from Gaussian fit on the core area	Mean:202 Std Dev:64	Mean:98 Std Dev:48	Mean:216 Std Dev:59	Mean:146 Std Dev:50
Strategy 3	σ is the Std Dev value taken from whole distribution	Mean:202 Std Dev:64	Mean:98 Std Dev:48	Mean:216 Std Dev:59	Mean:146 Std Dev:50

Table A.1: The summary table of different chi^2 choice strategy effects on the distribution of the four invariant masses we are interested. Here the mean value and the standard deviation of the whole distribution are listed and there are tiny difference.

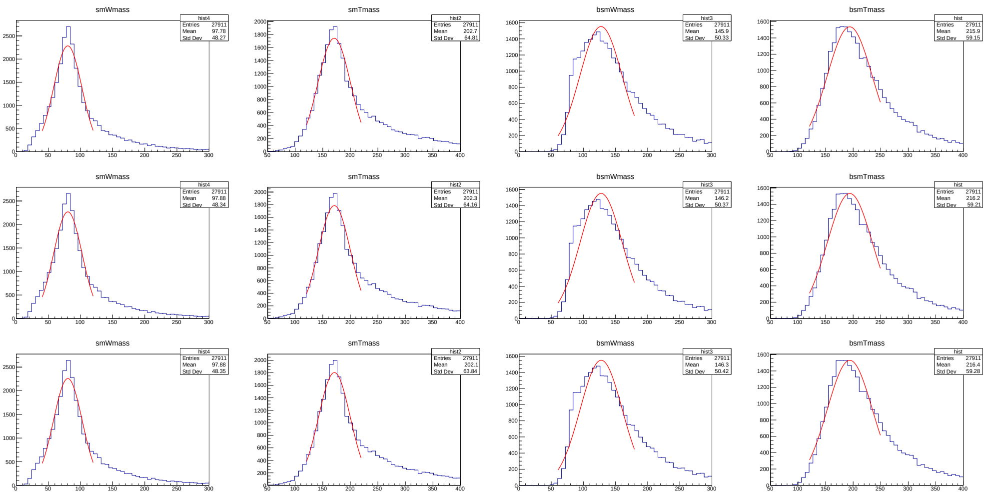

Figure A.2: A Gaussian fit was performed on the invariant mass distributions of the reconstructed top particles (t_1, t_2) and W bosons (W_1, W_2) for three different strategies. The σ values obtained from the Gaussian fit for strategy 1 are shown at the top, strategy 2 in the middle, and strategy 3 at the bottom. The x-axis range for fitting was held constant across all strategies.

Appendix B Studies of the evaluation methods on the BDT output

This section offers a comprehensive breakdown of the details highlighted in Table 5.6. The presented plots, spanning from Figure B.1 to Figure B.4, illustrate the variable distribution. These plots depict observations derived from the independent signal mass point versus background BDT training, carried out separately for the ee/$\mu\mu$ channels. When examining the various mass points, subtle variations in variable distribution become evident, particularly at the extreme mass points. This distinction is the motivation behind our decision to adopt two separate sets to encompass all signal mass points.

By implementing consistent BDT settings and parameters, Figure B.5 represents our final strategy, employing high/low mass sets for signal versus backgrounds training distribution. This strategy helps mitigate bias arising from the low statistics associated with independent signal mass points. The signal variables distribution become flater than the separately signal mass point distribution.

In Figure B.6 and Figure B.7, we visually portray the AUC performance arising from the independent signal mass points. The AUC values between training and testing stages tend to exhibit significant fluctuations, varying notably across different mass points. This phenomenon often gives rise to pronounced overtraining issues, as evident in Figure B.8, where we examine HNL15/HNL50/HNL75 samples for test/train overtraining assessment.

However, the high/low mass set approach consistently maintains a relatively stable performance in both test/train plots and AUC performance, as demonstrated in Figure 5.18.

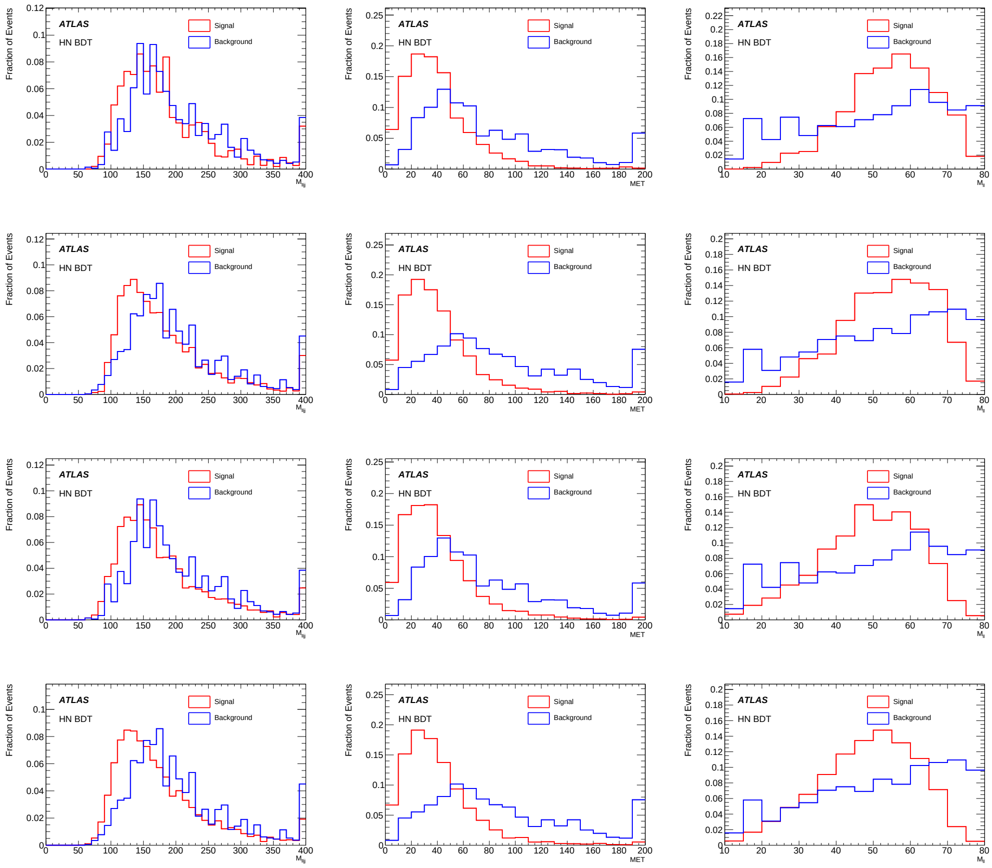

Figure B.1: Distributions of the training variables from the independent mass points of HNL15 and HNL25 compared to backgrounds, shown separately for the ee and $\mu\mu$ channels. Subfigures (a)–(c) show m_{bsmW}, E_{T}^{miss}, and $m_{\ell\ell}$ distributions for HNL15 in the ee channel; (d)–(f) for HNL15 in the $\mu\mu$ channel; (g)–(i) for HNL25 in the ee channel; and (j)–(l) for HNL25 in the $\mu\mu$ channel.

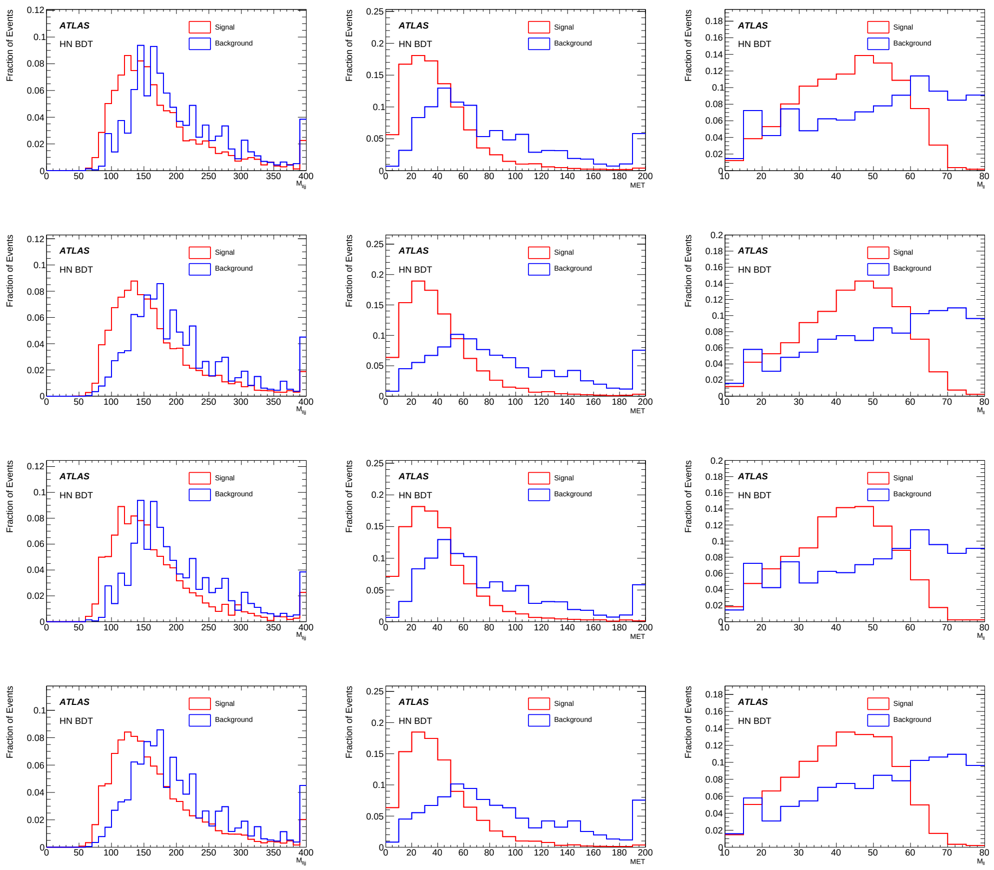

Figure B.2: Distributions of the training variables from the independent mass points of HNL35 and HNL40 compared to backgrounds, shown separately for the ee and $\mu\mu$ channels. Subfigures (a)–(c) show m_{bsmW}, E_{T}^{miss}, and $m_{\ell\ell}$ distributions for HNL35 in the ee channel; (d)–(f) for HNL35 in the $\mu\mu$ channel; (g)–(i) for HNL40 in the ee channel; and (j)–(l) for HNL40 in the $\mu\mu$ channel.

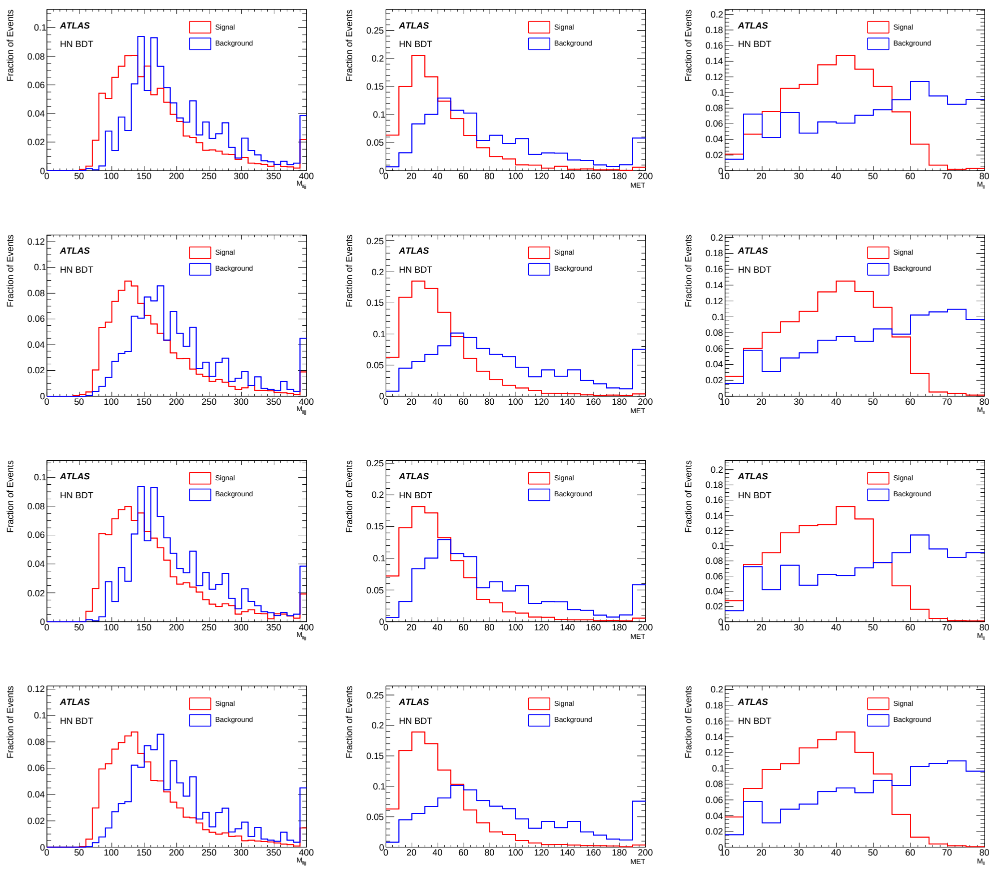

Figure B.3: Distributions of the training variables from the independent mass points of HNL45 and HNL50 compared to backgrounds, shown separately for the ee and $\mu\mu$ channels. Subfigures (a)–(c) show m_{bsmW}, E_{T}^{miss}, and $m_{\ell\ell}$ distributions for HNL45 in the ee channel; (d)–(f) for HNL45 in the $\mu\mu$ channel; (g)–(i) for HNL50 in the ee channel; and (j)–(l) for HNL50 in the $\mu\mu$ channel.

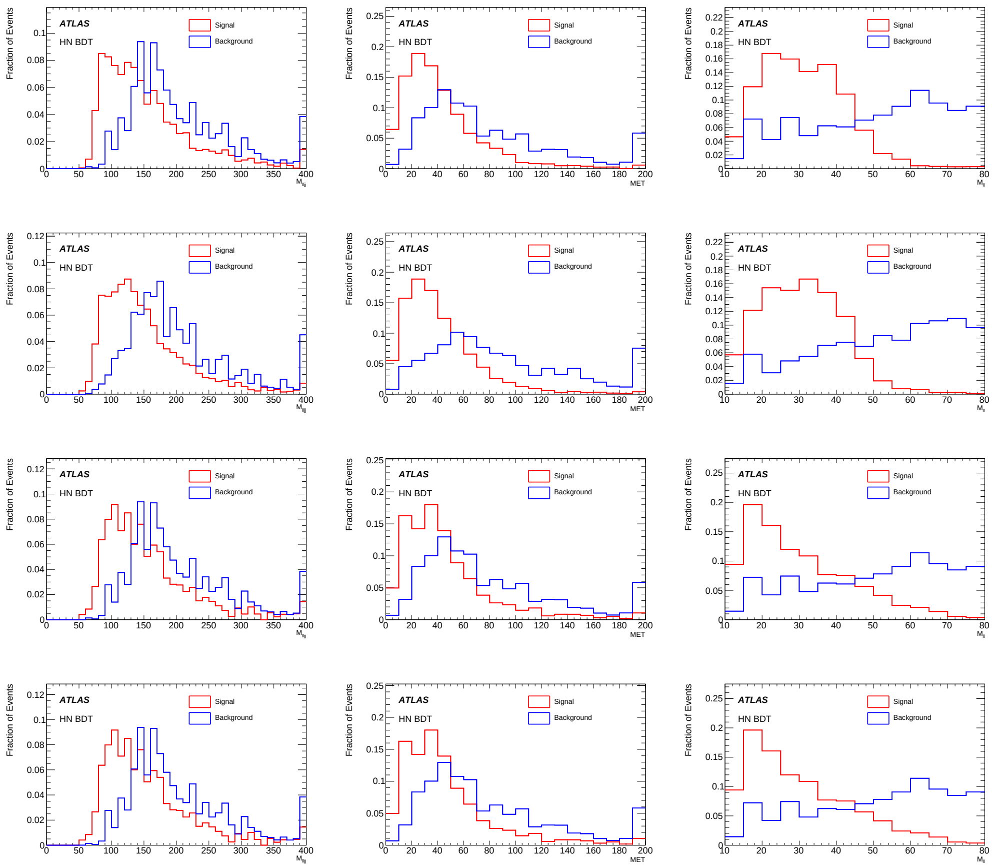

Figure B.4: Distributions of the training variables from the independent mass points of HNL60 and HNL75 compared to backgrounds, shown separately for the ee and $\mu\mu$ channels. Subfigures (a)–(c) show m_{bsmW}, E_{T}^{miss}, and $m_{\ell\ell}$ distributions for HNL60 in the ee channel; (d)–(f) for HNL60 in the $\mu\mu$ channel; (g)–(i) for HNL75 in the ee channel; and (j)–(l) for HNL75 in the $\mu\mu$ channel.

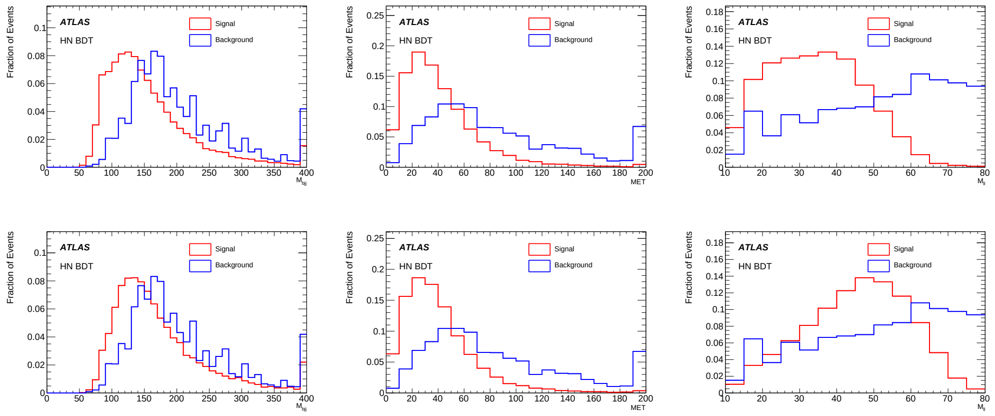

Figure B.5: Distributions of the training variables from the high and low mass sets compared to backgrounds. The first row shows the distributions for the high mass set, while the second row shows the distributions for the low mass set, including m_{bsmW}, E_{T}^{miss}, and $m_{\ell\ell}$.

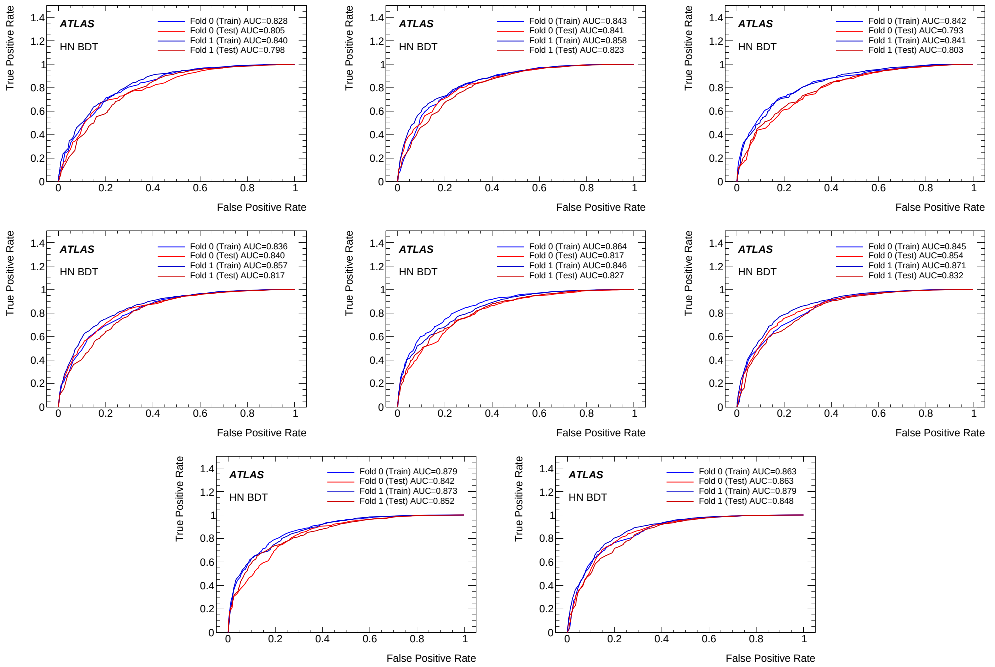

Figure B.6: ROC performance of various HNL mass signals (HNL15, HNL25, HNL35, HNL40) against background events in both ee and $\mu\mu$ channels.

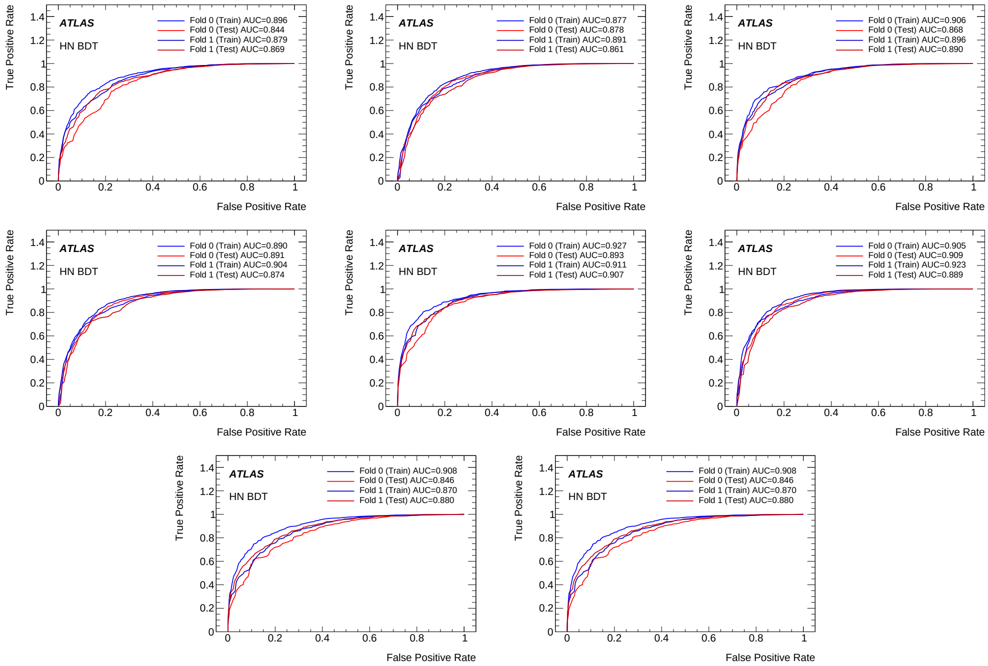

Figure B.7: ROC performance of HNL45, HNL50, HNL60, and HNL75 signals against background events in both ee and $\mu\mu$ channels.

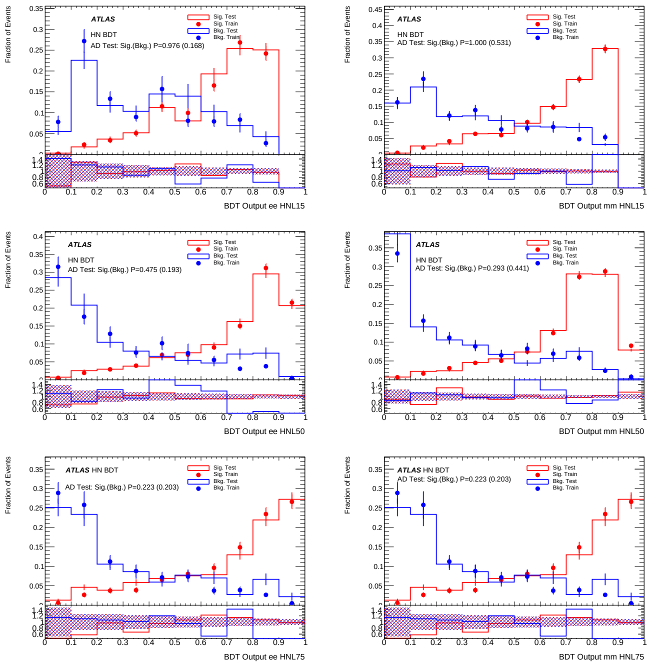

Figure B.8: Test/train comparison for HNL15, HNL50, and HNL75 signals against backgrounds in both ee and $\mu\mu$ channels, showing significant overtraining due to low statistics.

Appendix C Negative weights treatment

During the training process, it was observed that events with negative weights, which occurred in approximately 30% of Sherpa generated samples, could potentially cause issues. To address this, the shapes of input variables were compared between events with negative weights and those with positive weights, as shown in Figure C.1. The ROC and BDT output comparison is shown in Figure C.2. The BDT performance was found to be very similar between the two weighting options. Therefore, the absolute weight option was selected as it improved the statistics and minimized overtraining issues.

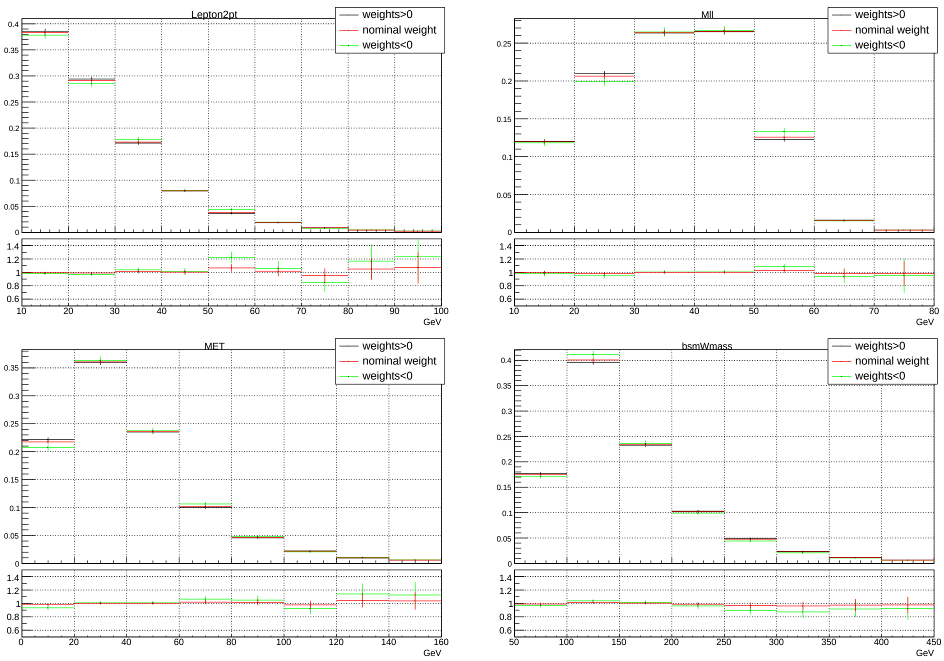

Figure C.1: The distribution of input variables for the signal sample, normalized with respect to positive, negative, and absolute weights. The shapes of the distributions do not fluctuate significantly with different weighting options.

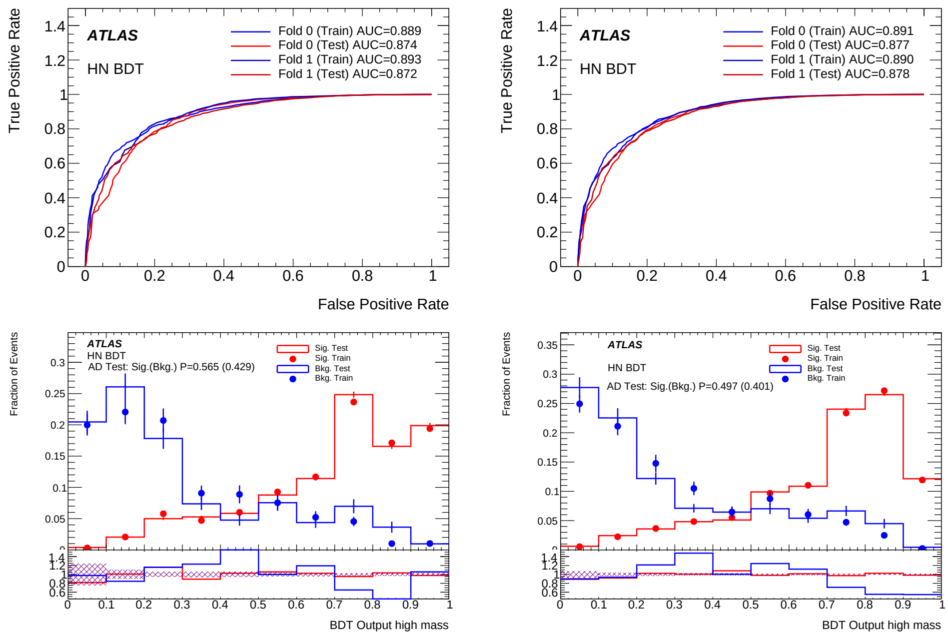

Figure C.2: Comparison of MVA performance using two weight options: positive weights (only positive events) and absolute weights (considering both positive and negative events, reversed to positive during training). The ROC curves show similar results, with the absolute weights option resulting in less overtraining due to increased statistics.

Appendix D Pre-fit distribution with BDTscore

From Figure D.1 to Figure D.5 presents the pre-fit results for the 2ℓSS channel signal region (Blinded) using the BDTGscore variable for all mass points.

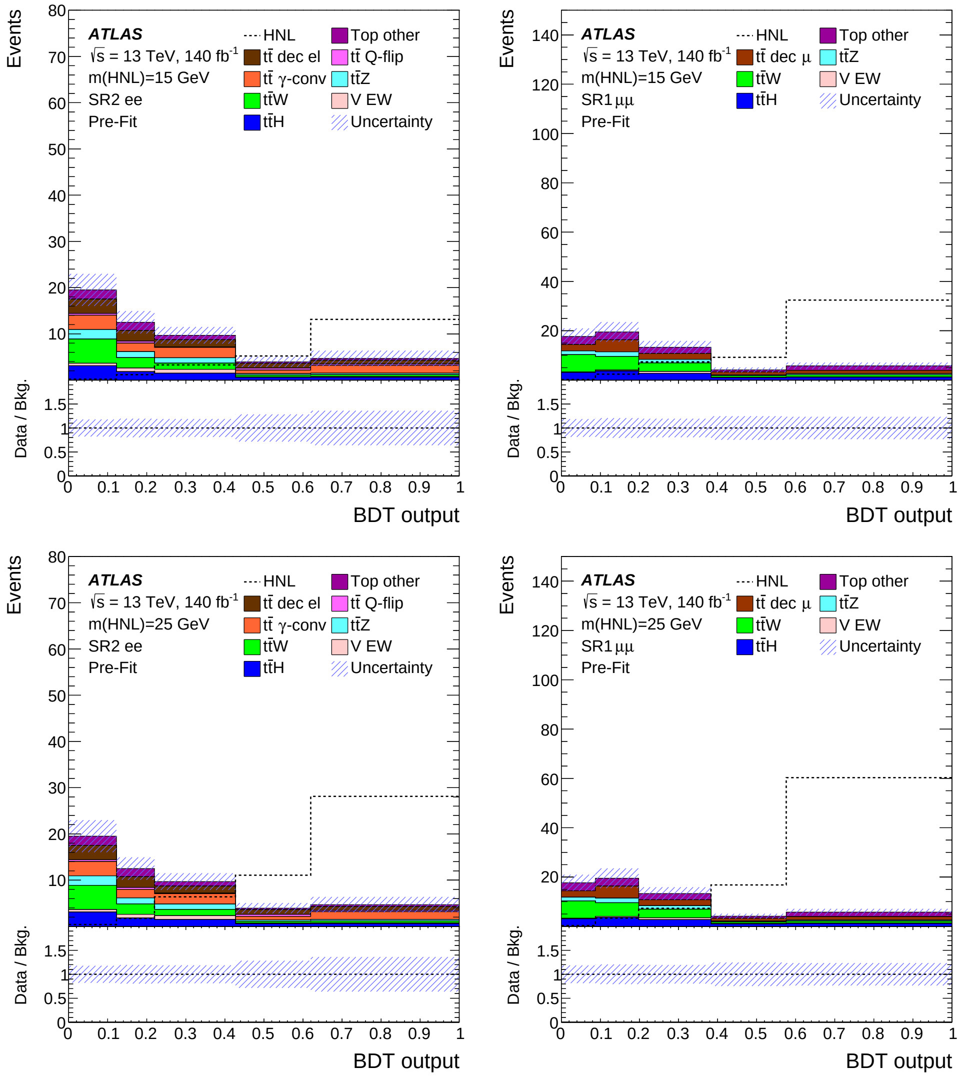

Figure D.1: The pre-fit result in BDTG score distribution in the ee channel (left column) and $\mu\mu$ channel (right column) signal regions for 2 different mass points of 15 GeV and 25 GeV, respectively. The uncertainty band includes the MC statistical uncertainties and all the other systematic uncertainties.

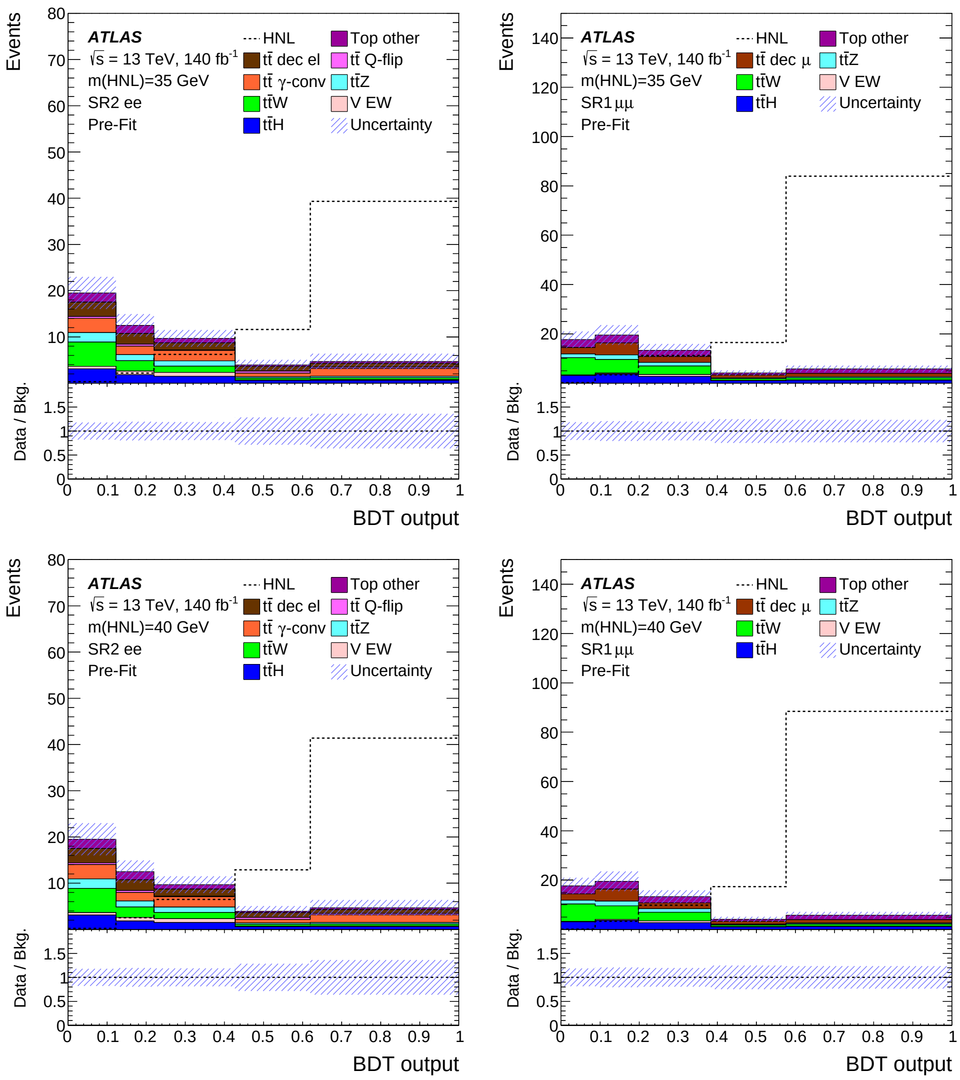

Figure D.2: The pre-fit result in BDTG score distribution in the ee channel (left column) and $\mu\mu$ channel (right column) signal regions for 2 different mass points of 35 GeV and 40 GeV, respectively. The uncertainty band includes the MC statistical uncertainties and all the other systematic uncertainties.

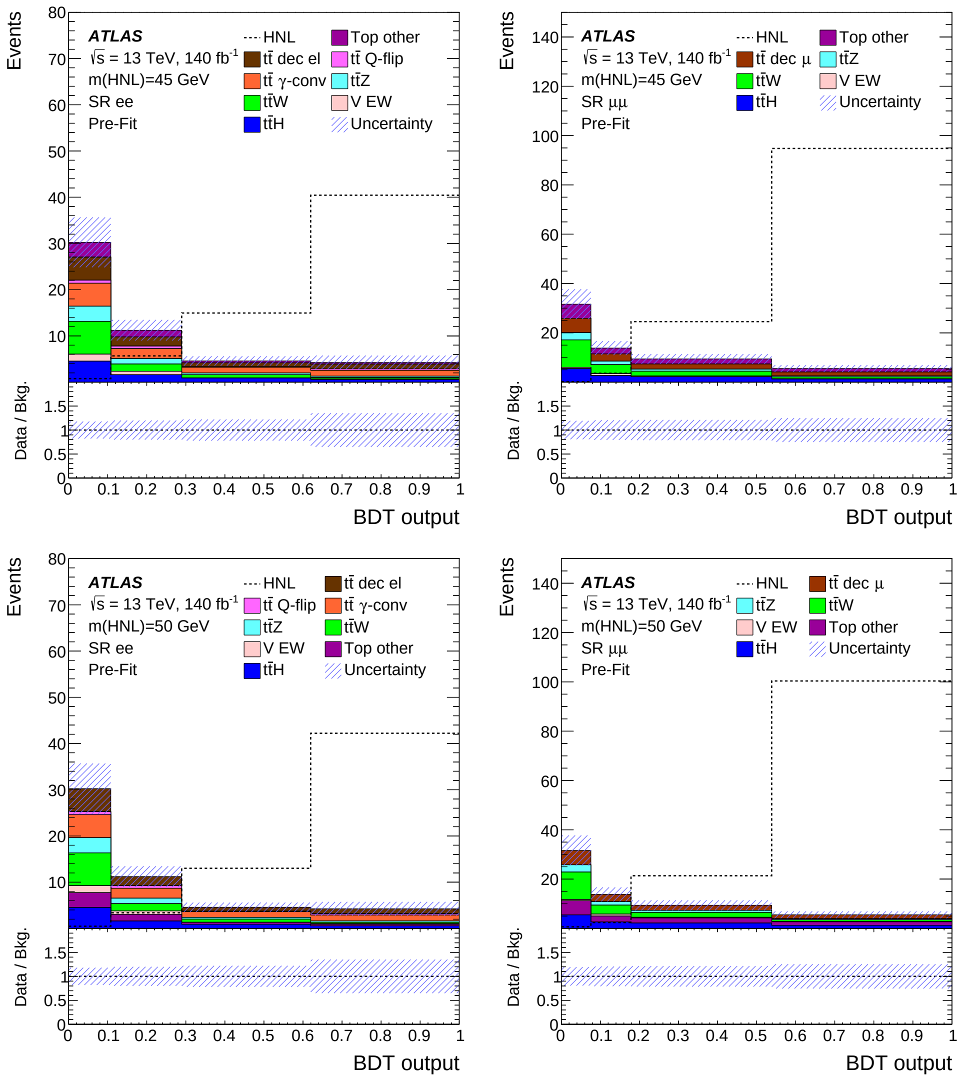

Figure D.3: The pre-fit result in BDTG score distribution in the ee channel (left column) and $\mu\mu$ channel (right column) signal regions for 2 different mass points of 45 GeV and 50 GeV, respectively. The uncertainty band includes the MC statistical uncertainties and all the other systematic uncertainties.

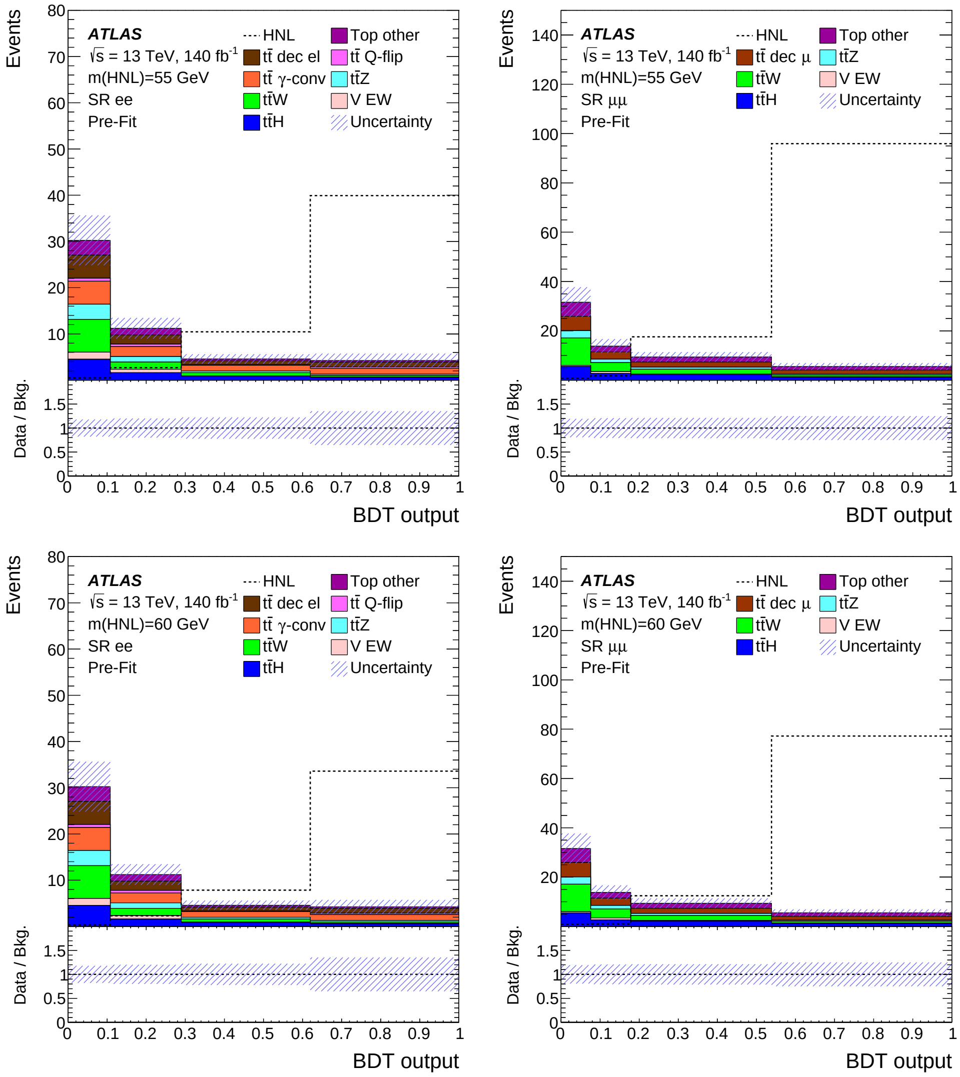

Figure D.4: The pre-fit result in BDTG score distribution in the ee channel (left column) and $\mu\mu$ channel (right column) signal regions for 2 different mass points of 55 GeV and 60 GeV, respectively. The uncertainty band includes the MC statistical uncertainties and all the other systematic uncertainties.

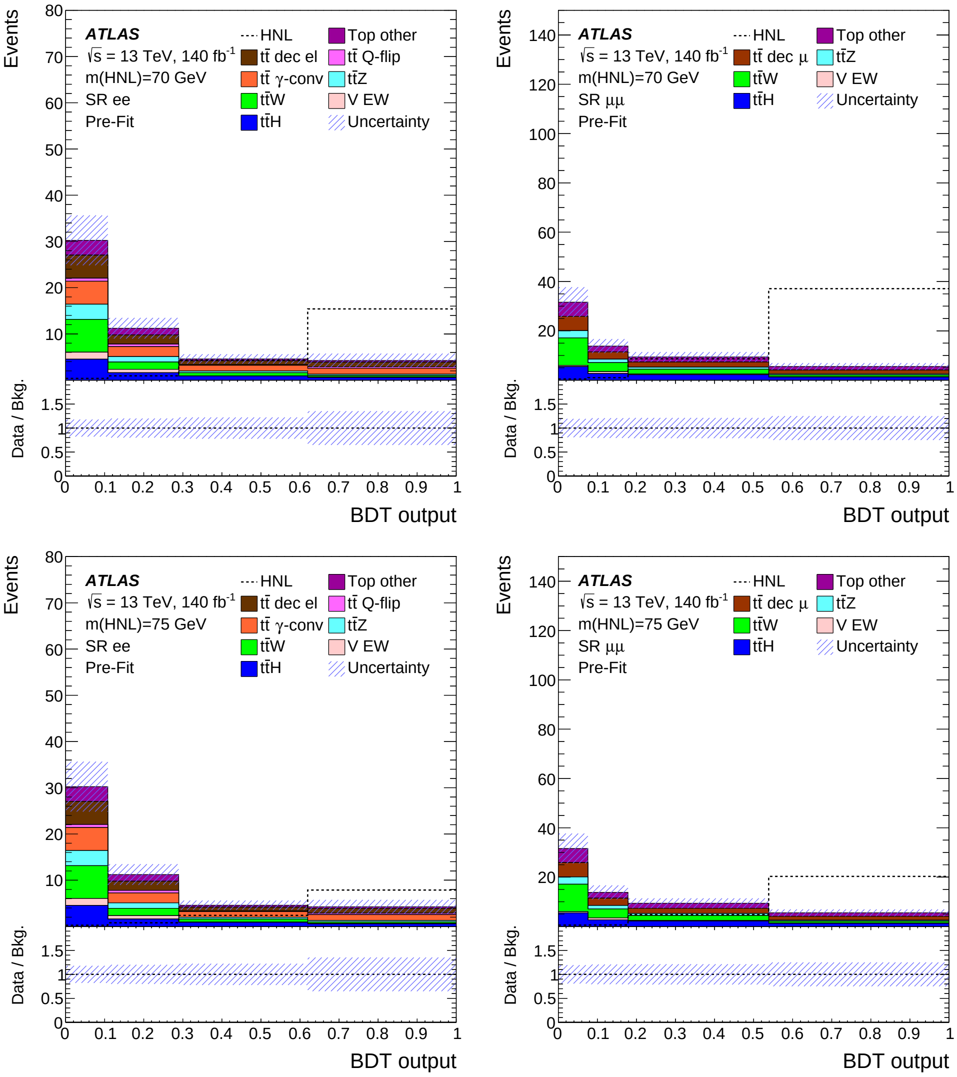

Figure D.5: The pre-fit result in BDTG score distribution in the ee channel (left column) and $\mu\mu$ channel (right column) signal regions for 2 different mass points of 70 GeV and 75 GeV, respectively. The uncertainty band includes the MC statistical uncertainties and all the other systematic uncertainties.

Appendix E Stat-only limit with toys calculation

The expected upper limit results on μ of stat-only fit are 0.120 (ee channel) and 0.055 ($\mu\mu$ channel) under the Asymptotic calculation, since some bins have very low statistics from our BDTscore distribution. We tested the limit estimation with 6k toys to check that the limits setting statistics used are behaving well. The upper limit scan results are shown in Figure E.1, which indicate the upper limit results of 0.121 (ee channel) and 0.057 ($\mu\mu$ channel). There is a very small difference compared to the asymptotic results, thus we can have confidence in the current Asymptotic limit setting method.

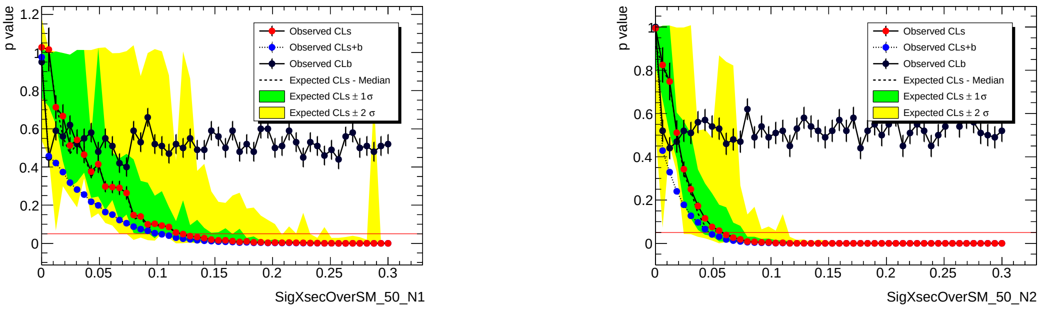

Figure E.1: Upper limit scans for the ee and $\mu\mu$ channels using 6k toys for a stat-only upper limit scan. A very small difference (less than 4%) was observed in the upper limit results compared to the asymptotic calculation.

Appendix F The variations of the main theoretical uncertainties

This appendix presents the primary systematic variations of the nuisance parameters (NPs) that hold a prominent position and have an asymmetric impact on the signal strength μ.

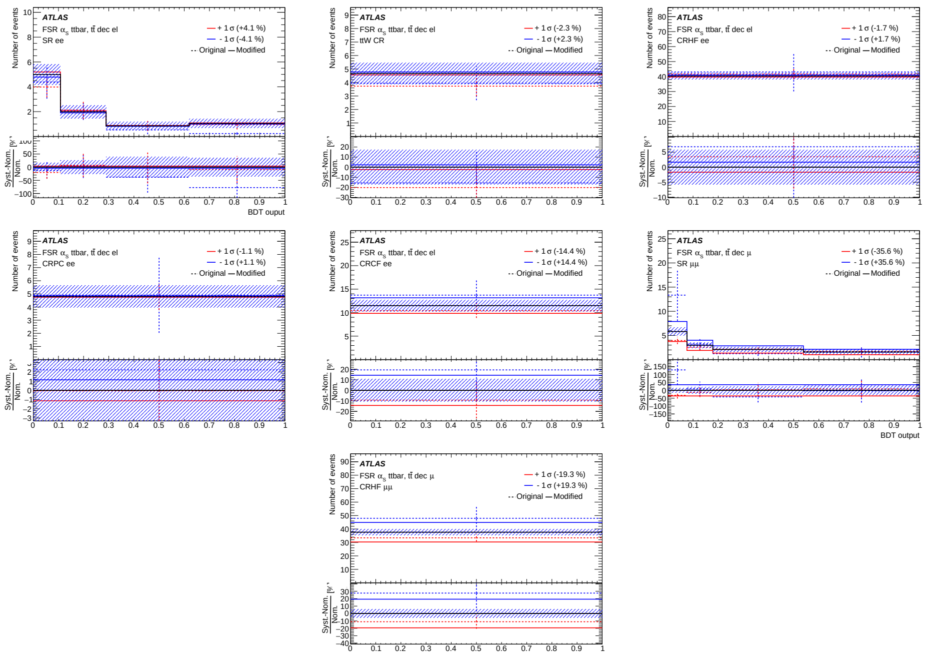

Figure F.1: The FSR modeling from the $t\bar{t}$ heavy flavor (HF) category in the signal region and control regions. Dashed lines represent the systematics derived from the yields, while solid lines show the systematics after smoothing.

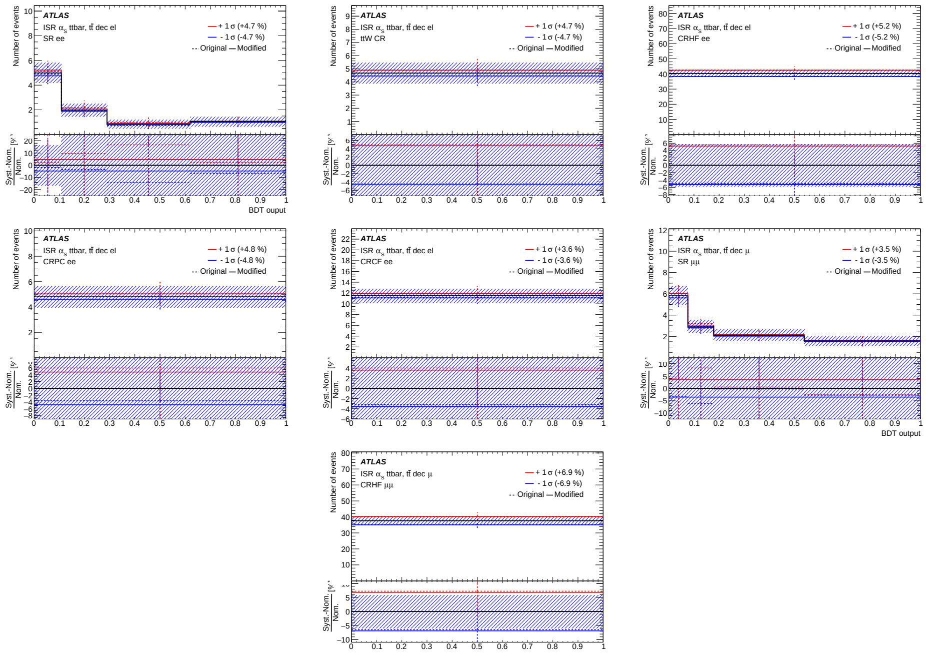

Figure F.2: The ISR modeling from the $t\bar{t}$ heavy flavor (HF) category in the signal region and control regions. Dashed lines represent systematics derived from yields, while solid lines show the systematics after smoothing.

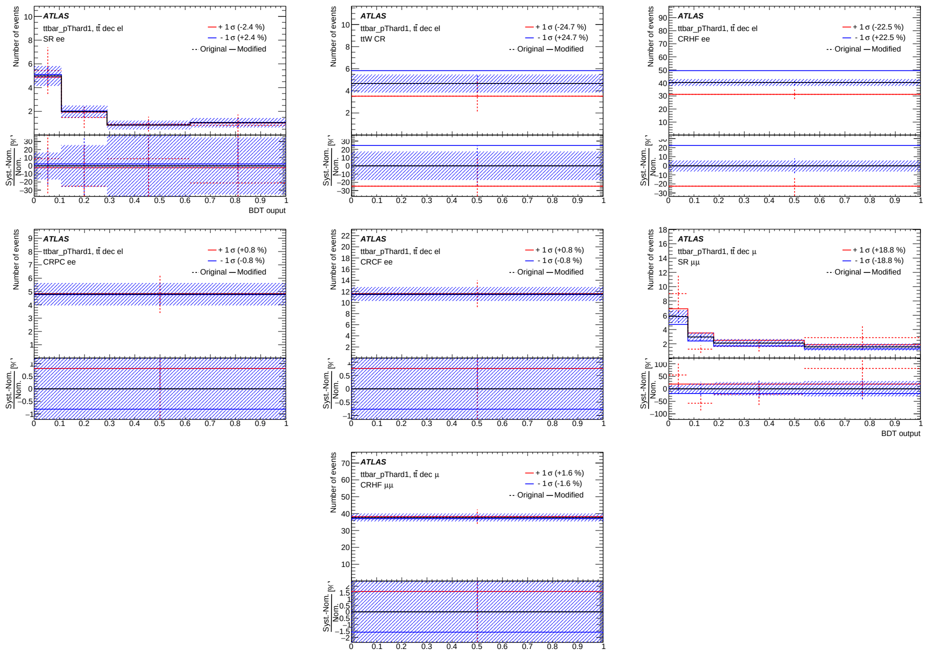

Figure F.3: The pThard1 alternative sample provided modeling uncertainties from the $t\bar{t}$ heavy flavor (HF) category in the signal region and control regions. Dashed lines represent systematics derived from yields, while solid lines show the systematics after smoothing.

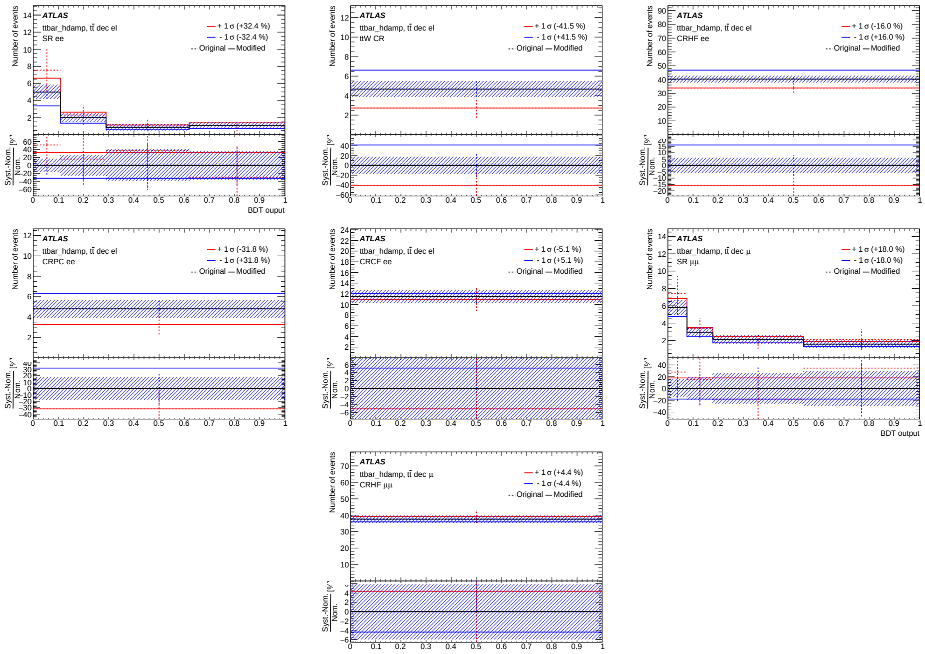

Figure F.4: The hdamp=3 alternative sample provided modeling uncertainties from the $t\bar{t}$ heavy flavor (HF) category in the signal region and control regions. Dashed lines represent systematics derived from yields, while solid lines show the systematics after smoothing.

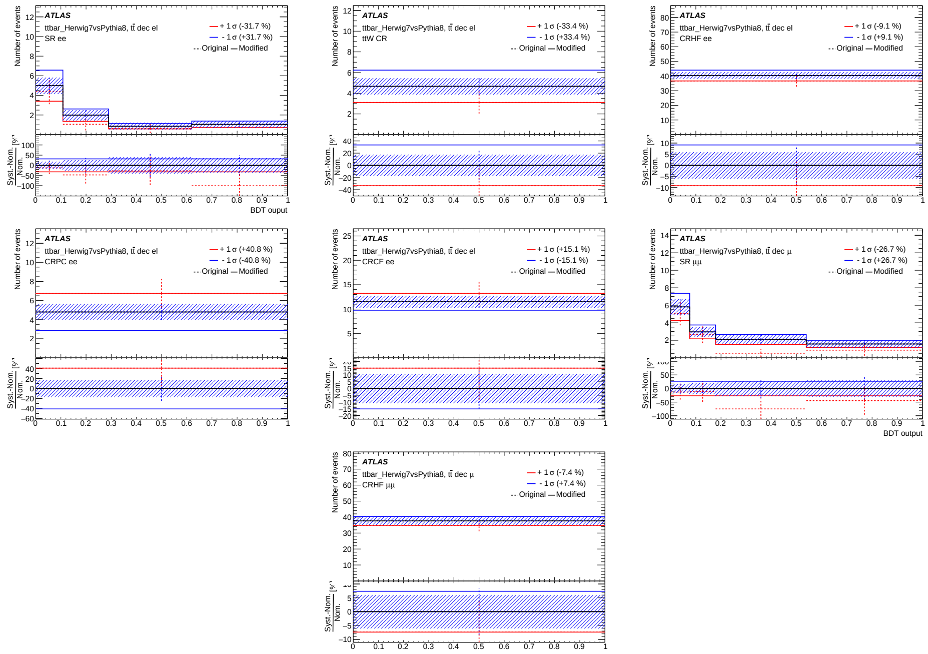

Figure F.5: The Herwig7 vs. Pythia8 alternative PS sample provided modeling uncertainties from the $t\bar{t}$ heavy flavor (HF) category in the signal region and control regions. Dashed lines represent systematics derived from yields, while solid lines show the systematics after smoothing.

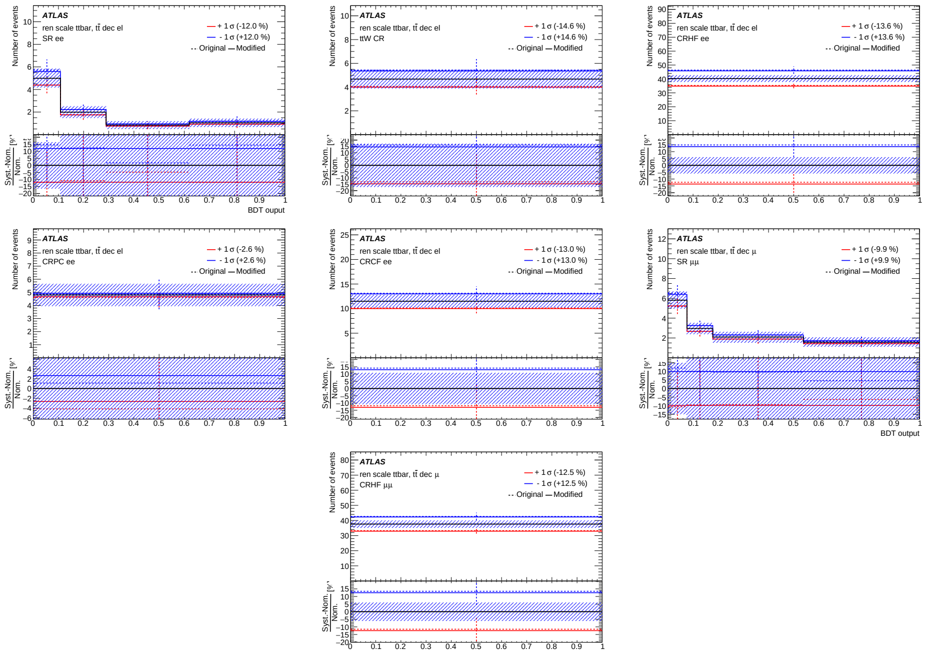

Figure F.6: The renormalization scale variations provided modeling uncertainties from the $t\bar{t}$ heavy flavor (HF) category in the signal region and control regions. Dashed lines represent systematics derived from yields, while solid lines show the systematics after smoothing.

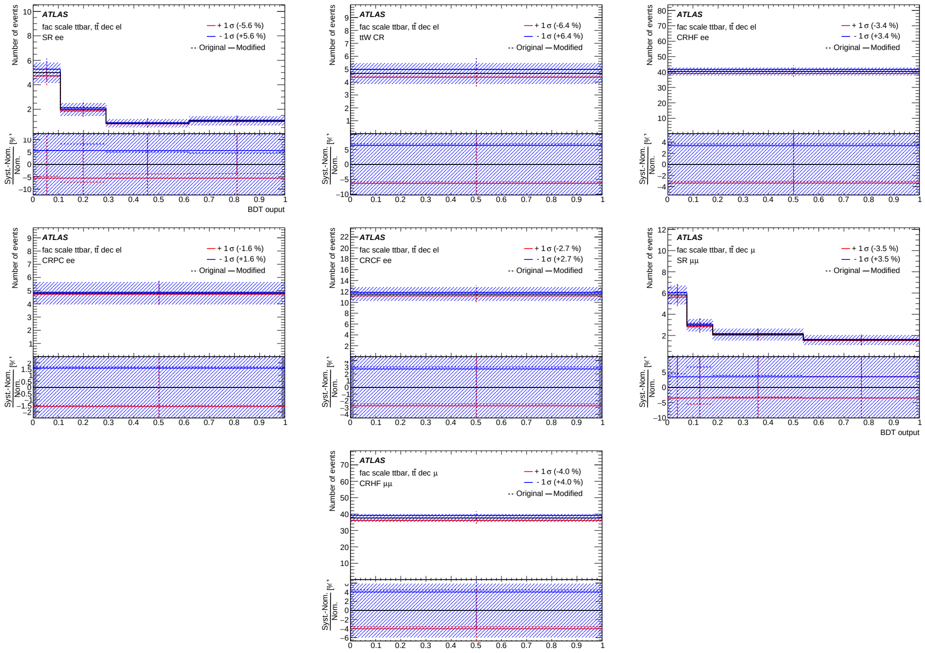

Figure F.7: The factorization scale variations provided modeling uncertainties from the $t\bar{t}$ heavy flavor (HF) category in the signal region and control regions. Dashed lines represent systematics derived from yields, while solid lines show the systematics after smoothing.

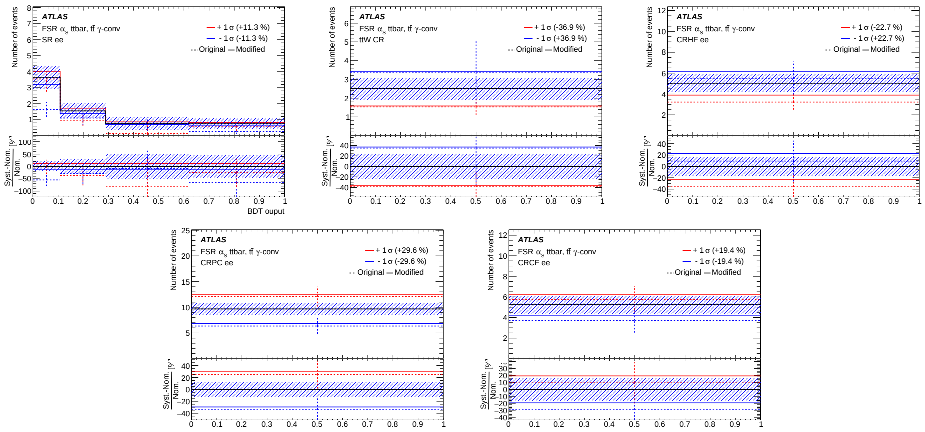

Figure F.8: The FSR modeling from the $t\bar{t}$ photon conversion (PC) category in the signal region and control regions. Dashed lines represent systematics derived from yields, while solid lines show the systematics after smoothing.

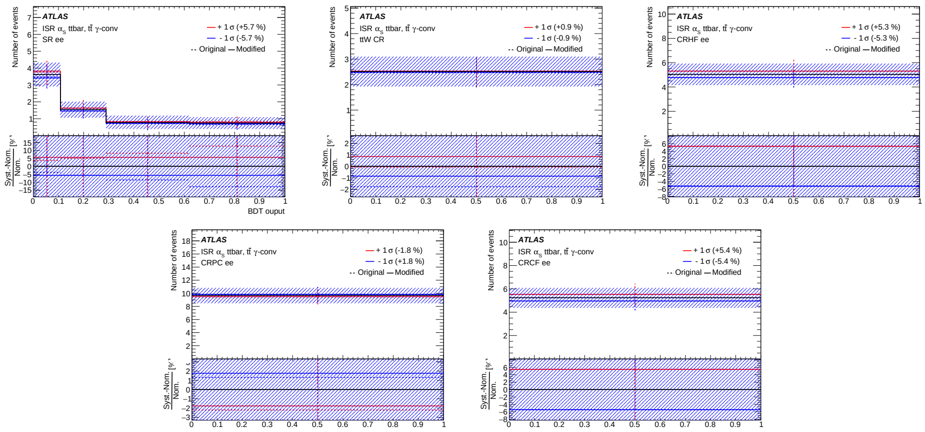

Figure F.9: The ISR modeling from the $t\bar{t}$ photon conversion (PC) category in the signal region and control regions. Dashed lines represent systematics derived from yields, while solid lines show the systematics after smoothing.

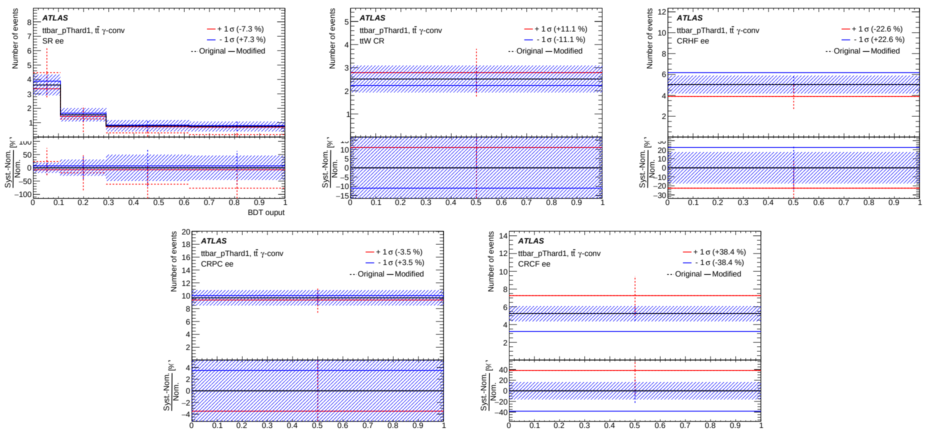

Figure F.10: The pThard1 alternative sample provided modeling uncertainties from the $t\bar{t}$ photon conversion (PC) category in the signal region and control regions. Dashed lines represent systematics derived from yields, while solid lines show the systematics after smoothing.

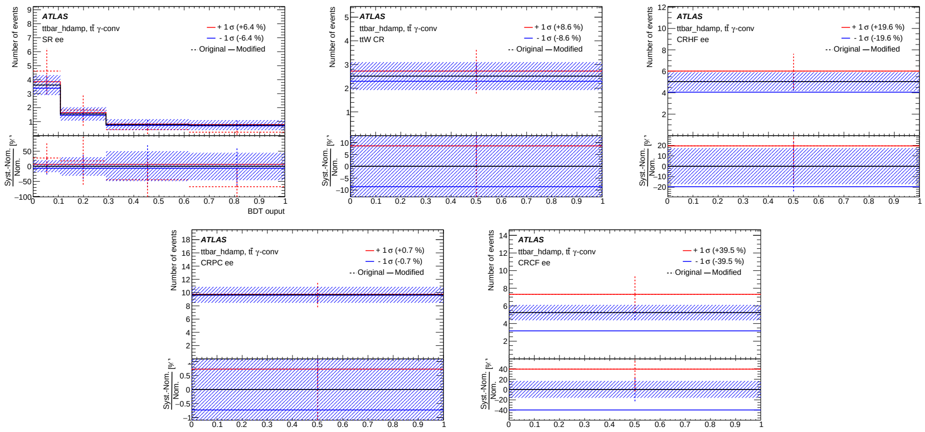

Figure F.11: The hdamp=3 alternative sample provided modeling uncertainties from the $t\bar{t}$ photon conversion (PC) category in the signal region and control regions. Dashed lines represent systematics derived from yields, while solid lines show the systematics after smoothing.

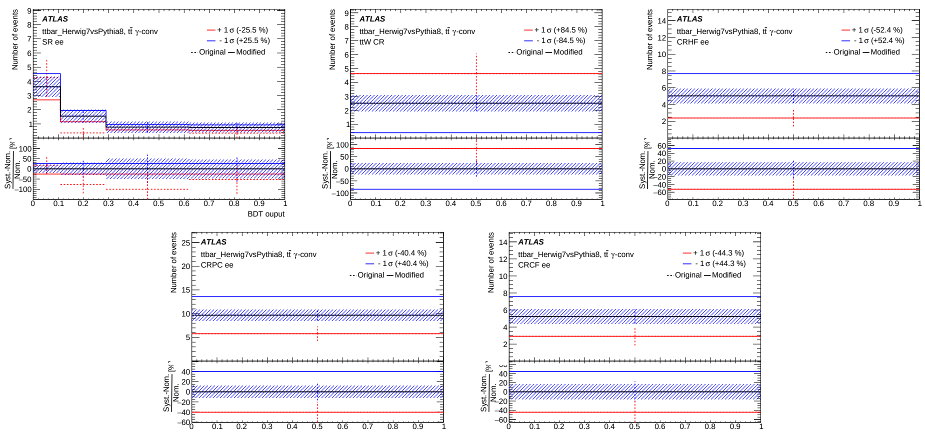

Figure F.12: The Herwig7 vs. Pythia8 alternative PS sample provided modeling uncertainties from the $t\bar{t}$ photon conversion (PC) category in the signal region and control regions. Dashed lines represent systematics derived from yields, while solid lines show the systematics after smoothing.

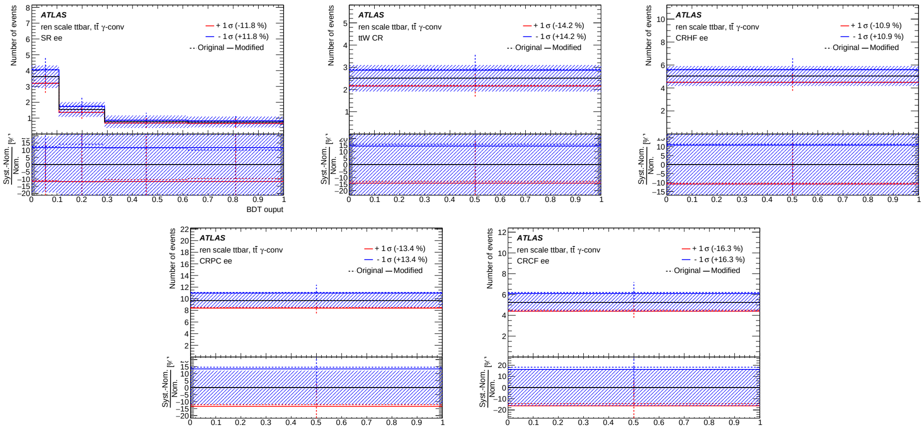

Figure F.13: The variations of the renormalisation uncertainties from the $t\bar{t}$ photon conversion (PC) category in the signal region and control regions. Dashed lines represent systematics derived from yields, while solid lines show the systematics after smoothing.

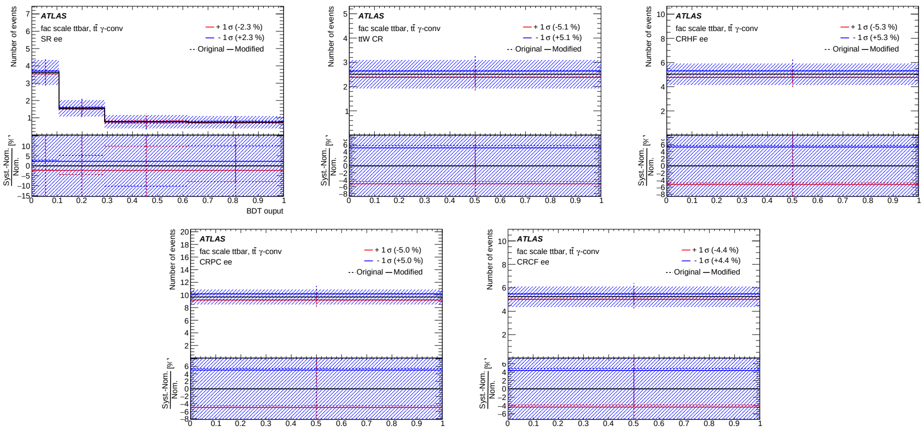

Figure F.14: The variations of the factorization uncertainties from the $t\bar{t}$ photon conversion (PC) category in the signal region and control regions. Dashed lines represent systematics derived from yields, while solid lines show the systematics after smoothing.

Appendix G Supplement to Asimov fit plots

This appendix presents key plots from the fit to the Asimov data.

A summary of the normalization factors fit to the Asimov data is shown in Figure G.1.

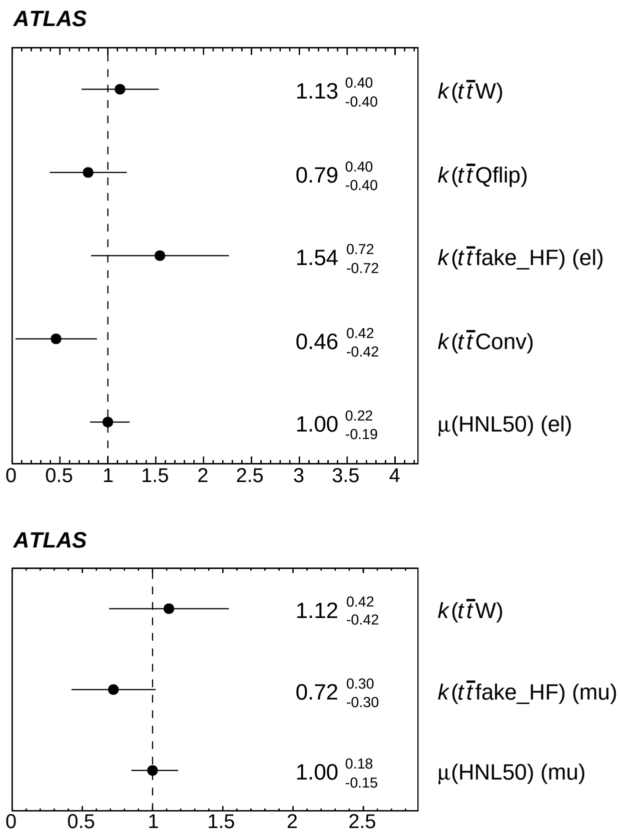

Figure G.1: Summary of the normalization factors in the fit to the Asimov data on both the signal and control regions for the ee channel (upper) and $\mu\mu$ channel (lower). The NFs of the backgrounds are consistent with the background-only fit results.

The list of the systematic that is dropped from the fit to Asimov data is shown in Figure Figure G.2 for both channels.

The correlation matrix for the fit to the Asimov data is depicted in Figures G.3 and G.4.

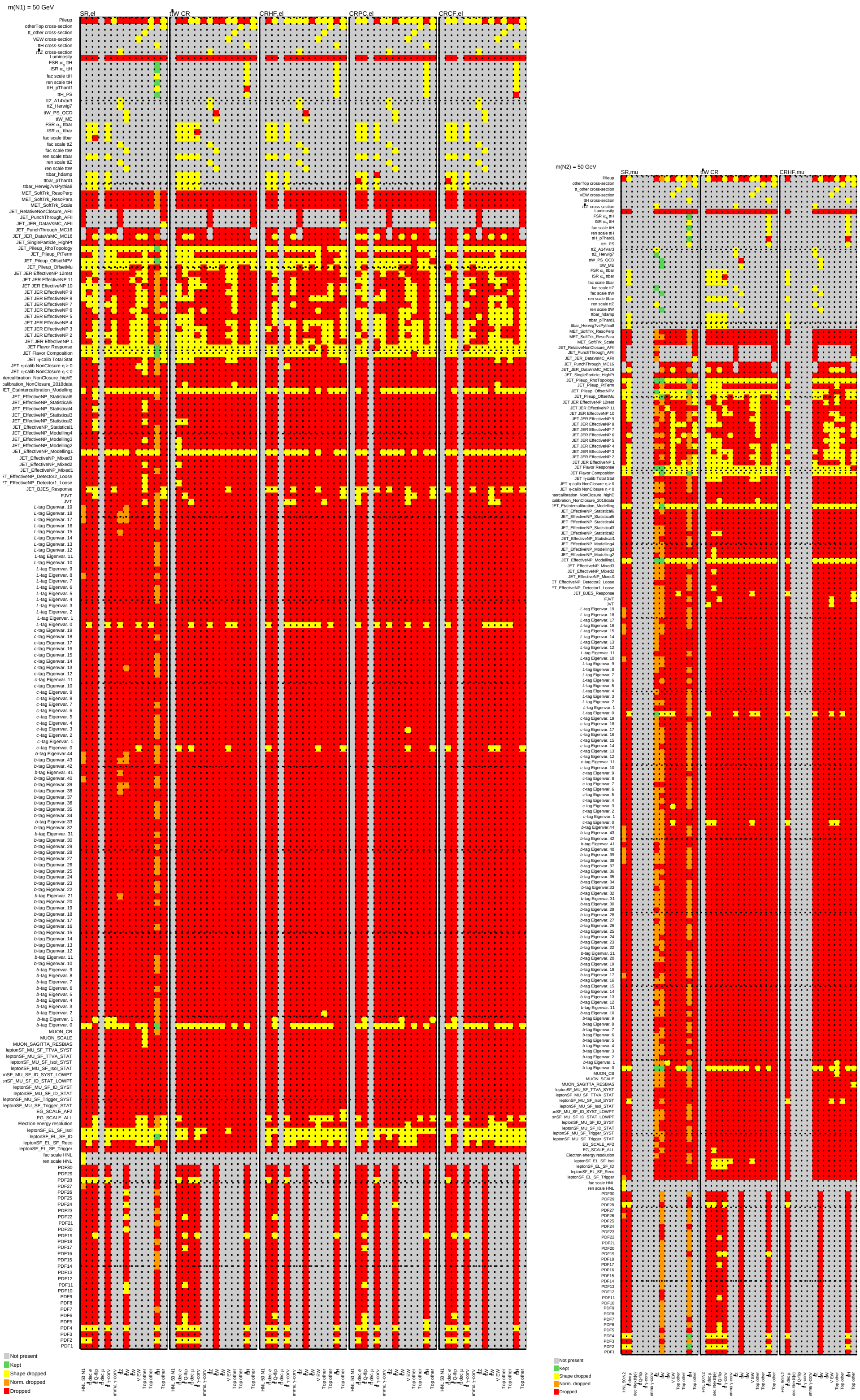

Figure G.2: The Asimov fit pruning of all nuisance parameters in the split $ee/\mu\mu$ channel with the signal mass at 50 GeV is shown here. The pruning thresholds for both overall/shape uncertainties are 1%.

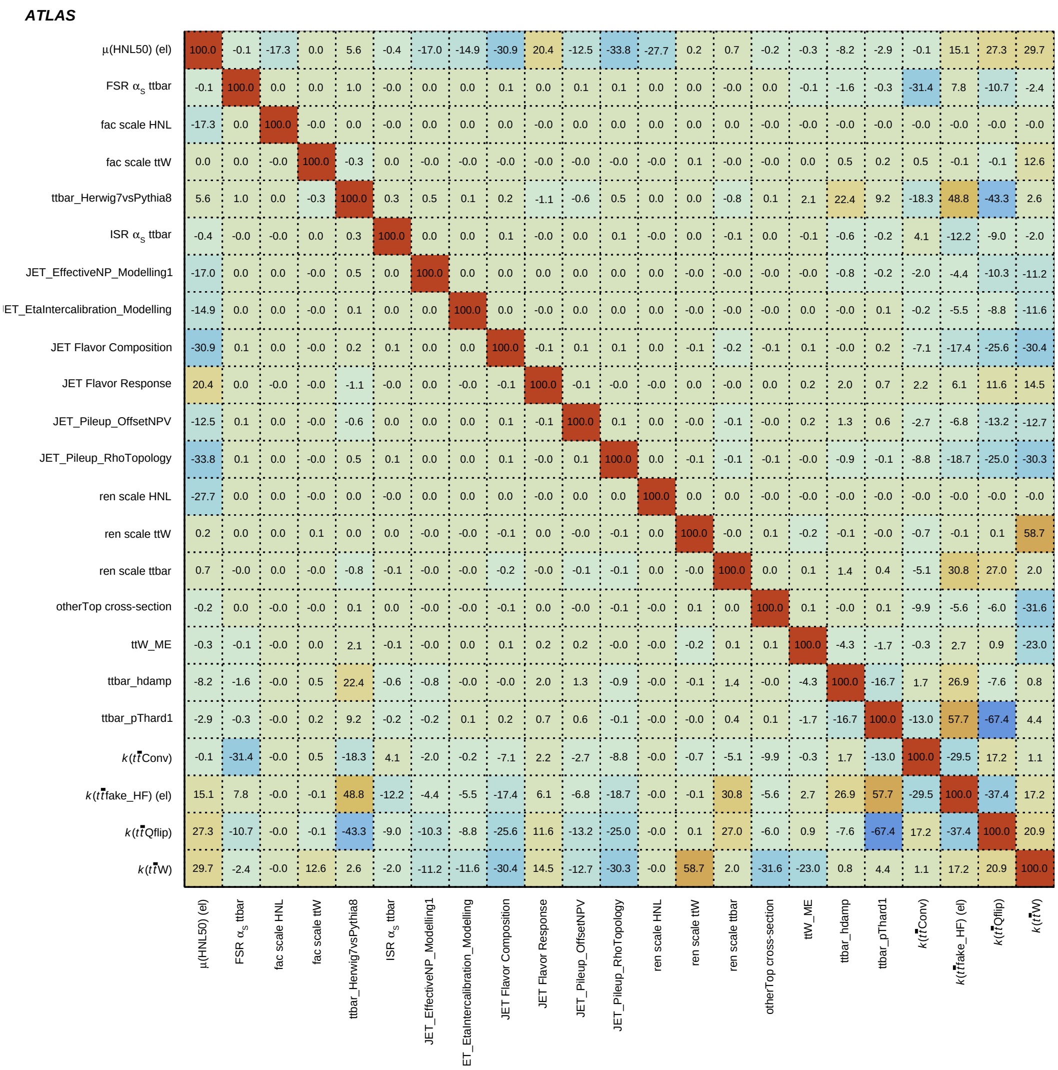

Figure G.3: Correlation matrix in the *ee* channel for the fit to the Asimov data with signal mass at 50 GeV (only NPs with at least one coefficient above 10 are displayed).).

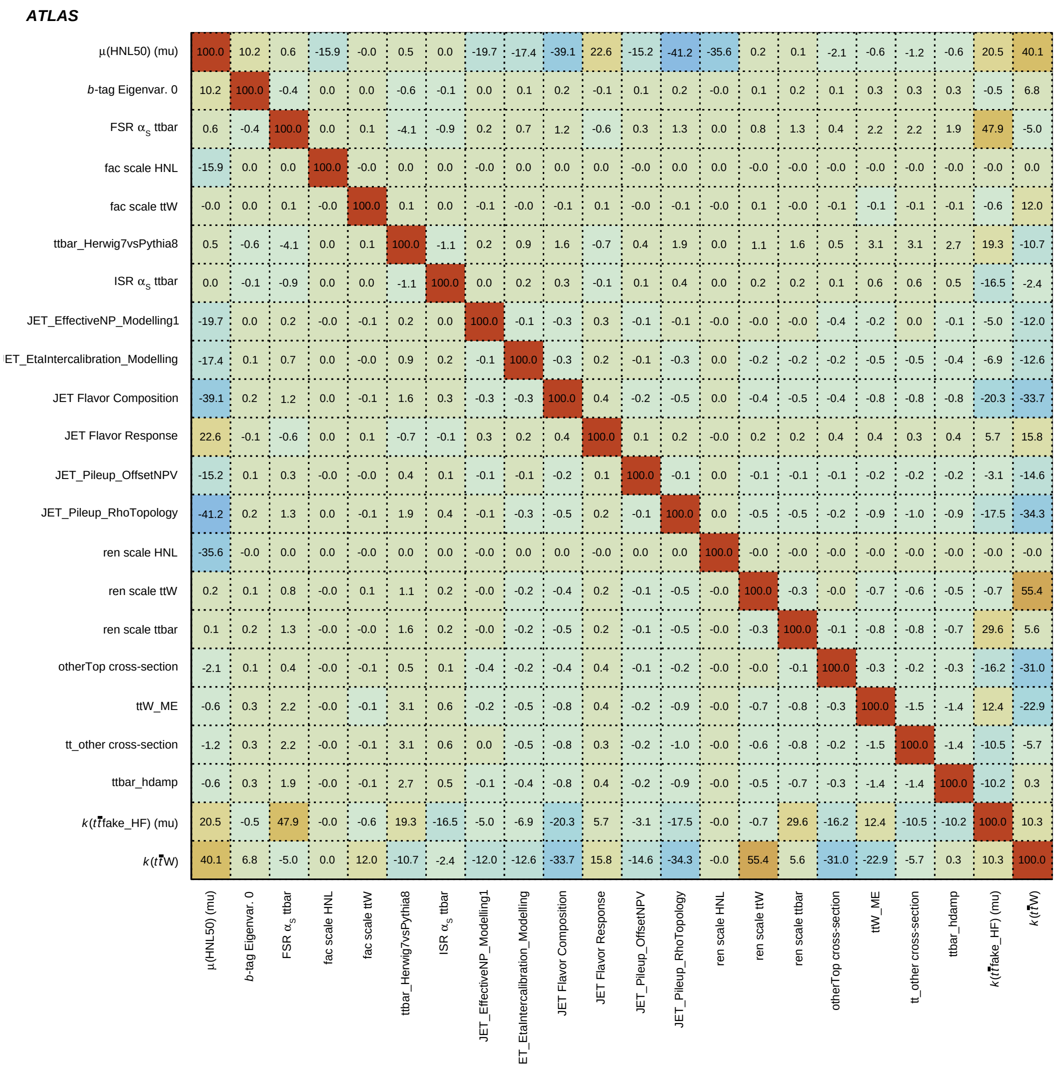

Figure G.4: Correlation matrix in the $\mu\mu$ channel for the fit to the Asimov data with signal mass at 50 GeV (only NPs with at least one coefficient above 10 are displayed).